University of Alberta

Design, Development, and Implementation of a High Adaptability Whole Body Counting System

by

Stephen Steciw

A thesis submitted to the Faculty of Graduate Studies and Research in partial fulfillment of the requirements for the degree of Doctor of Philosophy

in

Medical Sciences – Radiology and Diagnostic Imaging

Edmonton, Alberta

Fall 2001

National Library of Canada
Acquisitions and Bibliographic Services
395 Wellington Street
Ottawa ON K1A 0N4
Canada

Bibliothèque nationale du Canada
Acquisitions et services bibliographiques
395, rue Wellington
Ottawa ON K1A 0N4
Canada

Your file Votre référence

Our file Notre référence

The author has granted a non-exclusive licence allowing the National Library of Canada to reproduce, loan, distribute or sell copies of this thesis in microform, paper or electronic formats.

L'auteur a accordé une licence non exclusive permettant à la Bibliothèque nationale du Canada de reproduire, prêter, distribuer ou vendre des copies de cette thèse sous la forme de microfiche/film, de reproduction sur papier ou sur format électronique.

The author retains ownership of the copyright in this thesis. Neither the thesis nor substantial extracts from it may be printed or otherwise reproduced without the author's permission.

L'auteur conserve la propriété du droit d'auteur qui protège cette thèse. Ni la thèse ni des extraits substantiels de celle-ci ne doivent être imprimés ou autrement reproduits sans son autorisation.

0-612-68997-2

Canada

University of Alberta

Library Release Form

Name of Author: Stephen Steciw

Title of Thesis: Design, Development, and Implementation of a High Adaptability Whole Body Counting System.

Degree: Doctor of Philosophy

Year this Degree Granted: 2001

Permission is hereby granted to the University of Alberta Library to reproduce single copies of this thesis and to lend or sell such copies for private, scholarly, or scientific research purposes only.

The author reserves all other publication and other rights in association with the copyright in the thesis, and except as hereinbefore provided, neither the thesis nor any substantial portion thereof may be printed or otherwise reproduced in any material form whatever without the author's prior written permission.

Stephen Steciw
Driftwood Road
Box 2665
Smithers B.C.
V0J 2N0

Dated: July 23rd, 2001

University of Alberta

Faculty of Graduate Studies and Research

The undersigned certify that they have read, and recommend to the Faculty of Graduate Studies and Research for acceptance, a thesis entitled **"Design, Development, and Implementation of a High Adaptability Whole Body Counting System"**, submitted by Stephen Steciw in partial fulfillment of the requirements for the degree of Doctor of Philosophy in Medical Sciences (Radiology & Diagnostic Imaging).

Dr. L.J. Filipow (Supervisor)

Dr. M.E. Hoskinson

Dr. A.J.B. McEwan

Dr. J.L. Pinfold

Dr. H.R. Hooper

Dr. G.H. Kramer
(External Examiner)

Dated: 23 July 2001

Присвячую моїм любим родичам.

To my loving parents.

"All religions, arts and sciences are branches of the same tree. All these aspirations are directed toward ennobling man's life, lifting it from the sphere of mere physical existence and leading the individual towards freedom."

Albert Einstein

Abstract

A unique whole-body gamma ray counter has been designed that is capable of accommodating all subject sizes, and all subject activities. Detailed design criteria and comprehensive simulations of it's response are presented in this work.

Sixty-four (1.5" x 3") NaI(Tl) crystals from a decommissioned Positron Emission Tomography scanner were used in the counter. The detector responses were modeled using a ray-tracing computer simulation, which, in conjunction with experimental data, was used to optimize all aspects of the counter. In order to accommodate variable subject sizes, a moving detector gantry was incorporated into the counter's design. Retracting detectors and variable aperture 'shutters' prevent the counter from becoming saturated in the presence of high activity. A unique 'semi-empirical-regression' algorithm was also developed, so that the entire counter could be modeled, and very accurate performance specifications determined.

A "shadow-shielded" scanning-bed configuration was chosen for the whole body counter. Sufficient lead shielding (in addition to graded shielding) was instituted to ensure that the whole body counter is properly shielded from background radiation. As a result of these design efforts, subject sizes ranging from newborn infants to full-grown adults will be accommodated, and subject activities ranging from natural body background to several GBq will be accurately measured. A minimum detectable activity of 181 Bq (for 1.46 MeV photons) for the 50^{th} percentile man is expected, with a quantification uncertainty of only 8.8%. Lateral and AP regional 2D information will be available with an expected resolution of approximately 20 cm, and 10 cm respectively.

Optimization of this whole body counter using computer simulations enabled a

unique counter design to be developed that will provide more quantitative and regional information, for the widest range of subject sizes and activities, than any other existing system.

Acknowledgments

I would like to thank my supervisor, Dr. Larry Filipow for the help and direction that he gave me over the course of my project. I am truly grateful for the chance he has given me to pursue my interests. Dr. Filipow's expertise, wit, and humor made every conversation a memorable learning experience, and I thank him for being a mentor and friend. I would like to thank Dr. Sandy McEwan, Dr. Stuart Jackson, and Dr. Lawrence Le for their support and guidance over the years. Their interest in my project was invaluable, and was greatly appreciated. My sincere thanks to the Cross Cancer Institute machinists, Mr. Gary Morrison and Mr. Ken Hennig for machining the experimental apparatus seen in this thesis. Their craftsmanship was vital to the completion of my project. A special thank you to Mr. Chris Ediss, who spent a lot of time designing the preamplifier electronics for this project, and helped me with its construction. I would like to thank Dr. John Duke from the SLOWPOKE reactor site for sharing his knowledge, offering his advice, and always taking the time to help me. My sincere thanks to Dr. Peter Dozzi for volunteering his time in verifying the structural integrity of the superstructure / flooring designed in this project. I would like to thank the staff at the Department of Radiology & Diagnostic Imaging for offering such a welcoming environment for me to work in. Their encouragement, support, and sincere interest in my research did not go unnoticed. In particular, I would like to thank Mrs. Jan Dawson and Mrs. Helen Skolarchuk for their help and humor over the years. I would also like to thank Mr. Parminder Basran for his friendship, and for the help he offered me with Monte Carlo simulations. My sincere thanks to Mr. Collin Tobert, and Mr. Phil Fleury for their friendship, and for their constructive feedback while sitting in on several of my mock presentations. I would also like to thank Mr. Barton Pawluski for his contribution and commitment to this project.

Finally, I would like to express my sincerest thanks and gratitude to my parents and sister for their endless love and support over the years. They have been a source of inspiration. Thank you also to Mrs. Jeannie Stanley, who believed.

Table of Contents

1.0 Introduction 1

1.1 Overview of Whole Body Counting 1

1.2 Overview of Whole Body Counter Design 2

1.3 Outline of Thesis 4

2.0 Background Physics to Whole Body Counting 11

2.1 Photon Propagation Through Matter 11

Compton Scattering 11
Photoelectric Effect 13
Pair Production 15
X-ray Escape Peak 16
Attenuation 16

2.2 Sources of Radiation 17

Cosmic 18
Airborne 21
Terrestrial 22
Materials 22
Human Body 23
Experimentally Measured External Background Radiation Spectrum 24

2.3 Whole Body Counting 25

Basic Principles of Operation 25
Detector Types 26
Photomultipliers 29
Detector Efficiency 30
Energy Resolution 31
Electronics 32
Detector Stability 33
Shielding 36

3.0 Methods in Whole Body Counting 44

3.1 Configurations 44

Fixed versus Scanning Whole Body Counters 44
Chair 45
Large-Volume 46
Arc 46
Multi-Detector 47

3.2 Calibration 47

Phantom Calibration Method 48
Same-Element Calibration Method 50
Cadaver Calibration Method 51
Computer Methods in Calibration 52

3.3 Data analysis 52

Photopeak quantification 52
Radionuclide identification 56
Photopeak searching / imaging 57
Minimum Detectable Activity (MDA) 58

4.0 Hardware Considerations in Designing the WBC 62

4.1 History of an Old PET Scanner 62

4.2 Detector Characteristics 64

Detector efficiencies 64
Energy Resolution 65
Photopeak Position 66

4.3 Preamplifier Design 67

4.4 Testing the Preamplifier 71

Heat tests 71
Drift & Shift 72

4.5 Summing NIM 73

Summing Electronics 74
High-Low Gain 75

Summing NIM Schematic 76

4.6 Peripheral Electronics and WBC Software 78

Stepper motors and electronics 78
Top Gantry Movement Sensor 79
Other Electronics 80
Software 80

4.7 Electronic Configuration of the Counter 81

5.0 Theoretical Considerations in Designing the WBC 84

5.1 Ray-Tracing Computer Simulation 84

Overview of Simulations and their Shortcomings 84
The Semi-Empirical-Regression Method 85
Determining $W_{tot}(E,\theta,\phi)$ 87

5.2 Ray-Tracing Simulation: A First-Order Approximation 88

Development and Experimental Verification 89
Concerns About Build-Up and Quantification 94

5.3 WBC Optimization: Theoretical & Experimental Methods 99

Primary Shielding Thickness 100
Graded Shielding 103
Shadow versus Room Shielding 104
WBC Length Optimization 107
Detector Bank Configurations 110
Collimator Thickness Optimization 114
Collimator Design 117
Number and Location of the WBC's Detectors 121

5.4 Determining and Implementing $W_{tot}(E,\theta,\phi)$ 124

Mapping out $W_{tot}(E,\theta,\phi)$ for the WBC 125
Verification of the Semi-Empirical-Regression Method 141

6.0 High-Adaptability WBC Design and Function 148

6.1 The Physical Layout of the WBC 148

6.2 High-Sensitivity Mode 150

Top Gantry Movement 150
Top-Detector Movement 152
Infant Positioning in the WBC 153

6.3 Low-Sensitivity Mode 153

Detector Retraction & Shutters 154

6.4 WBC Drawings 155

7.0 Selecting Low-Background Conditions 158

7.1 WBC Manufacturing Considerations 158

Materials 158
K-40 PMT Contamination 160

7.2 Location 163

Desired Conditions 163
Conditions at the CCI 165

8.0 Expected Performance 171

8.1 Proposed Operation 171

8.2 Subject Count Rate 173

8.3 Minimum Detectable Activity 175

8.4 Flatness in the WBC's Response 179

8.5 Maximum Subject Activity 181

8.6 WBC 'Imaging' 183

9.0 Conclusions and Future Work 189

9.1 Conclusions 189

9.2 Future Work 190

Appendix A – Select WBC Drawings 193

Appendix B - Electronics 205

Preamplifier Schematics 206

Summing NIM Schematics 210

Appendix C – Program Listings 214

List of Figures

Figure 1-1	A horizontal rotational scanner used to detect the quantity and distribution of radiation in the body.	5
Figure 1-2	Whole body counter that uses water as shielding is under construction.	5
Figure 1-3	The improvised whole body counter used in Goiania.	6
Figure 2-1	The geometry of Compton scattering.	12
Figure 2-2	Compton edge and continuum shown on a typical NaI spectrum.	13
Figure 2-3	The photopeak and the photopeak area are shown on a typical NaI spectrum.	14
Figure 2-4	Single and double escape peaks on a typical NaI spectrum.	15
Figure 2-5	Attenuation of primary photon beam through a material of thickness t.	17
Figure 2-6	Sources of background radiation.	18
Figure 2-7	A star before and after super-nova.	19
Figure 2-8	Schematic diagram of cosmic ray shower.	20
Figure 2-9	Experimental sea level spectra for cosmic shower components.	20
Figure 2-10	Neutron-flux / solar-wind eleven year cycle.	21
Figure 2-11	Background radiation from the SLOWPOKE reactor site.	24
Figure 2-12	Schematic diagram of the basic components found in WBCs. In this example the two detector signals are summed.	25
Figure 2-13	Diagram showing the sodium iodide detector arrangement and the reflective action of the packing used in detector cans.	28
Figure 2-14	Background spectrum acquired from HPGe and NaI detectors (T=250000s).	29

Figure 2-15	Schematic of a typical photomultiplier tube.	30
Figure 2-16	The full-width-half-maximum of a spectrum peak.	31
Figure 2-17	Photopeak and the first pile-up peak in a typical NaI spectrum.	35
Figure 2-18	Characteristic x-rays from primary and graded shielding.	38
Figure 2-19	Cross-section illustration of room-shielded and shadow-shielded counter arrangements.	40
Figure 2-20	A large building used to create the cosmic ray 'shadow' affect.	41
Figure 3-1	Typical fixed-detector whole body counter orientation.	44
Figure 3-2	Typical scanning-detector whole body counter orientation.	45
Figure 3-3	Chair-type whole body counter configuration.	46
Figure 3-4	Large-volume whole body counter configuration.	46
Figure 3-5	Arc whole body counter configuration.	47
Figure 3-6	Bush phantom (a) and a bottle-type Bush emulating phantom (b).	49
Figure 3-7	Reference Man phantom (a) and BOMAB phantom (b).	49
Figure 3-8	Photopeak on a flat background (a) and on a sloped background (b).	53
Figure 3-9	Photopeak before smoothing (a) and after smoothing using DCT (b).	54
Figure 3-10	The superimposed and fitted Gaussian curves in a spectrum.	55
Figure 4-1	The decommissioned PET scanner with and without its cover on.	62
Figure 4-2	The salvaged components from the PET scanner (a), and one of six detector banks (b).	63
Figure 4-3	The relative efficiencies of the sixty six PET detectors.	64
Figure 4-4	The energy resolutions of the sixty six PET detectors	65
Figure 4-5	The photopeak position of the sixty six PET detectors.	66

Figure 4-6	The raw signal coming from a photomultiplier tube.	67
Figure 4-7	Schematic of the basic preamp designed for the whole body counter.	68
Figure 4-8	With and without pole-zero cancellation in an RC circuit.	69
Figure 4-9	The preamplifier designed for use in the WBC.	70
Figure 4-10	The signal coming from the preamplifier.	71
Figure 4-11	Photopeak position for a range of temperatures.	72
Figure 4-12	Opposing detectors in a WBC summed through a summing amp.	74
Figure 4-13	The probability of photon emission of various energies from natural body and clinically used radionuclides.	75
Figure 4-14	Circuit schematic for one of the summing sections in the summing NIM.	76
Figure 4-15	Proposed face for the two-wide summing NIM module.	77
Figure 4-16	Top-view of proposed subject profile sensor.	79
Figure 4-17	The electronic configuration of the high-adaptability WBC.	82
Figure 5-1	Geometry for a point-source ray entering a square cylindrical detector.	86
Figure 5-2	The original cylindrical crystal (a) and its rectangular modeled equivelant.	89
Figure 5-3	Theory versus experiment for a Co-60 point source on-axis.	89
Figure 5-4	Monte Carlo and first-order approximation detector responses.	90
Figure 5-5	The detector-collimator-source geometry for the fist-order approximation.	91
Figure 5-6	Path-lengths verified on paper for different source-detector positions.	92
Figure 5-7	Collimated and uncollimated detector responses from a homogeneous source.	92

Figure 5-8	Experimental setup for measuring the homogeneous source.	93
Figure 5-9	Theory and experimental detector responses for lateral movement.	93
Figure 5-10	Build-up in a detector from forward-scattered photons in a material.	95
Figure 5-11	Build-up in ROI from 1.46 MeV photons passed through 20 cm of air.	96
Figure 5-12	Build-up from 1.46 MeV photons passed through 11.3 cm of lead.	96
Figure 5-13	Fraction of ROI counts attributed to build-up from different materials.	97
Figure 5-14	Monte Carlo NaI spectrum for 1.46 MeV photons through 20 cm of air.	98
Figure 5-15	Monte Carlo NaI spectrum for 1.46 MeV photons through 11.3 cm of lead.	98
Figure 5-16	The fraction of calculated to actual photopeak counts for air, water, and lead.	99
Figure 5-17	Cosmic ray attenuation through various thicknesses of Al and Pb.	101
Figure 5-18	Decay schemes for Potassium-40.	102
Figure 5-19	Background radiation spectrum for the Edmonton region,	103
Figure 5-20	Lead shielding configured in a room-shielded arrangement.	104
Figure 5-21	Lead shielding configured in a shadow-shielded arrangement	105
Figure 5-22	Shadow and room shielded background spectra for ~2 cm of lead shielding.	106
Figure 5-23	Ideal subject-detector configuration for a scanning WBC.	108
Figure 5-24	The critical distances in shadow-shielded WBCs.	108
Figure 5-25	The relative detector response from a varying-length WBC.	109
Figure 5-26	Geometric efficiency iso-response curves for a single detector	110

Figure 5-27	A detector bank placed perpendicular to the subject.	111
Figure 5-28	Geometric efficiency iso-response curves for a detector bank.	111
Figure 5-29	Side-by-side (I), and shielding-separated (II) bank configurations.	112
Figure 5-30	Thick and thin collimator arrangements for the middle bank.	114
Figure 5-31	End-view of the shielding used to determine background attenuation.	116
Figure 5-32	Attenuation of background through different thicknesses of lead.	116
Figure 5-33	Optimization curve for lead collimator thickness.	117
Figure 5-34	Final collimator design for the whole body counter.	118
Figure 5-35	The central-collimator shielding design.	119
Figure 5-36	The neighboring-bank collimator shielding design (right side).	120
Figure 5-37	The geometric efficiency from two opposing detector banks.	121
Figure 5-38	The optimized detector arrangement and the WBC's graded shielding.	122
Figure 5-39	The geometric efficiency from all four detector banks.	123
Figure 5-40	Individual detector responses from several detector bank arrangements.	123
Figure 5-41	The bottom-middle detector bank used to map $W_{tot}(E,\theta,\phi)$.	125
Figure 5-42	The experimental setup used to map $W_{tot}(E,\theta,\phi)$.	126
Figure 5-43	The grid-detector orientation used to measure $W_{tot}(E,\beta_x,\beta_y)$.	126
Figure 5-44	The original versus the chosen data set and their regression curves.	128
Figure 5-45	The original versus the chosen data set and their regression curves.	128
Figure 5-46	The regression surface for one quadrant defining $W_{tot}(E,\beta_x,\beta_y)$ for –2.17 cm.	130

Figure 5-47	The regression surface for one quadrant defining $W_{tot}(E,\beta_x,\beta_y)$ for –1.73 cm.	131
Figure 5-48	The regression surface for one quadrant defining $W_{tot}(E,\beta_x,\beta_y)$ for –1.23 cm.	132
Figure 5-49	The regression surface for one quadrant defining $W_{tot}(E,\beta_x,\beta_y)$ for –0.57 cm.	133
Figure 5-50	The regression surface for one quadrant defining $W_{tot}(E,\beta_x,\beta_y)$ for –0.13 cm.	134
Figure 5-51	The regression surface for one quadrant defining $W_{tot}(E,\beta_x,\beta_y)$ for 0 cm.	135
Figure 5-52	The regression surface for one quadrant defining $W_{tot}(E,\beta_x,\beta_y)$ for +0.37 cm.	136
Figure 5-53	The regression surface for one quadrant defining $W_{tot}(E,\beta_x,\beta_y)$ for +0.57 cm.	137
Figure 5-54	The regression surface for one quadrant defining $W_{tot}(E,\beta_x,\beta_y)$ for +0.87 cm.	138
Figure 5-55	The regression surface for one quadrant defining $W_{tot}(E,\beta_x,\beta_y)$ for +1.14 cm.	139
Figure 5-56	The regression surface for one quadrant defining $W_{tot}(E,\beta_x,\beta_y)$ for +2.12 cm.	140
Figure 5-57	Water bottle with KCl solution placed in front of the detector arrangement.	141
Figure 5-58	Experimental versus theoretical photopeak detector responses.	142
Figure 5-59	Water bottle elevated and placed in front of the detector arrangement.	142
Figure 5-60	Experimental versus theoretical responses for an elevated water bottle.	143
Figure 5-61	Water bottle placed length-wise in front of the detector arrangement.	144
Figure 5-62	Experimental versus theoretical responses for the small bottle.	144

Figure 6-1	Illustration of the shadow-shielded scanning whole body counter.	148
Figure 6-2	Cut-away view of the shadow-shielded scanning whole body counter.	149
Figure 6-3	End view of the whole body counter, with an adult subject inside.	150
Figure 6-4	Side view of the counter, with the top gantry positioned for an adult.	151
Figure 6-5	Side view of the counter, with the top gantry positioned for a child.	151
Figure 6-6	The top gantry positioned far away and close to the bottom shielding.	152
Figure 6-7	Placement of a very small subject in the whole body counter.	153
Figure 6-8	The detector and shutter movement during low-sensitivity mode.	154
Figure 6-9	Side view of the counter in low-sensitivity mode for an adult subject.	155
Figure 7-1	The 11 cm thick lead shielding arrangement, half and fully shielded.	161
Figure 7-2	The NaI spectrum acquired over 48 hours in the 11 cm lead shielding.	162
Figure 7-3	Background contributions from a shielded NaI detector.	164
Figure 7-4	The worst-case background spectrum obtained from the CCI.	166
Figure 7-5	The total spectrum counts up to 400 keV acquired at the CCI over 5 days.	167
Figure 7-6	Shadow-shielded spectra from the CCI and the EDC, 2 day acquisition.	168
Figure 8-1	Flow-chart describing the proposed operation of the high-adaptability WBC.	171
Figure 8-2	The NaI and HPGe background spectra in the K-40 photopeak region.	177

Figure 8-3	Iso-response plot for one bottom-middle detector.	180
Figure 8-4	Iso-response curves for the middle detector banks of the WBC.	180
Figure 8-5	Iso-response curves for the end detector banks of the WBC.	181
Figure 8-6	Illustration of Rayleigh's criterion for the resolution of two peaks.	183
Figure 8-7	Lateral and longitudinal responses for the high-sensitivity position.	184
Figure 8-8	Lateral and longitudinal responses for the fully retracted detector.	184
Figure 8-9	Lateral and longitudinal responses for the half-shuttered detector.	185
Figure 8-10	Lateral and longitudinal responses for the detector placed behind a 1 cm hole.	185

List of Tables

Table 2-1	Experimentally measured gamma counts for common materials.	23
Table 2-2	Naturally occurring radionuclides found in the human body.	24
Table 5-1	Ratio of simulated to experimental detector responses.	94
Table 5-2	Relative activities for side-by-side and shielding-separated WBCs.	113
Table 7-1	K-40 activities from various parts of Hamamatsu PMTs.	161
Table 8-1	Summary of the detector responses simulated using seven different phantoms.	174
Table 8-2	The WBC's MDAs for a 30 minute scan, with and without PMT K-40 contamination.	175
Table 8-3	The WBC's MDA_qs for a 30 minute scan, with and without PMT K-40 contamination.	178
Table 8-4	Quantification errors for the WBC, with and without PMT K-40 contamination.	178
Table 8-5	The maximum subject activity for different detector and shutter positions.	182
Table 8-6	Summary of the lateral and longitudinal resolutions for various detector arrangements.	185

List of Abbreviations

CCI	-	Cross Cancer Institute
EDC	-	Education and Development Center (location of the main laboratory)
FOV	-	Field Of View
MCA	-	Multi-Channel Analyzer
MCB	-	Multi-Channel Buffer
MDA	-	Minimum Detectable Activity (required for detection)
MDA_q	-	Minimum Detectable Activity (required for quantification)
PTTR	-	Peak-To-Total-Ratio
SNR	-	Signal-to-Noise-Ratio
WBC	-	Whole Body Counter

Chapter 1

Introduction

1.1 Overview of Whole Body Counting

The task of accurately measuring radiation from within the human body, or "Whole Body Counting" began in conjunction with the development of the earliest radiation detectors. Photographic emulsions were the first radiation detectors, used in 1895 by Wilhelm Roentgen to detect x-rays. In 1908 the first gas counter was developed by Hans Geiger, making radiation detection and measurement much more practical. Twenty nine years later, in 1937, a gas counter was used by Robley Evans to develop the first whole body counter[1]. His counter was used to quantify the radium content and radium retention rates in radium watch dial painters.

Whole body counters (WBCs) are the instruments used to accurately quantify the amount of a radionuclide present within the human body. They are designed to measure very small, trace amounts of radiation including naturally occurring isotopes from full-grown adults[2]. There are however, counters made specifically for infant[3] and high activity studies[4,5]. To be able to measure naturally occurring isotopes, a whole body counter must be sensitive enough to detect sources as small as roughly thirty Bequerels of high-energy photons. To achieve this level of sensitivity, whole body counters must be shielded from cosmic, airborne, and terrestrial background radiation by using significant amounts of shielding[6]. The detectors used in a WBC must also exhibit good quantum detection efficiency for detecting high-energy gamma radiation. In theory, any radiation detector could be used in a WBC, but Sodium Iodide (NaI) and Germanium (Ge) detectors are most common[7]. They are either held in a static position around the subject or scanned past while data is collected. Because of the constraints associated with whole body counting, conventional systems and devices, including gamma cameras and survey

meters cannot be used in place of a WBC. Well counters can be used for high sensitivity work, but are restricted to measuring only very small objects.

Data from WBCs can be processed via nuclear spectroscopy, and the specific radionuclides present can be determined which provides the possibility for a wide variety of experiments and clinical tasks. Robley Evans developed the first whole body counter for the application of determining the extent of radioactive contamination of radium watch-dial painters, which was first recognized as a danger to workers in 1925[8]. Survivors of Hiroshima and Nagasaki, as well as accidentally contaminated individuals have had their internal doses determined and monitored using data from whole body counters. Since the 1950s, applications for whole body counters have become much more diverse. Current uses of whole body counters include a broad range of normal human sports medicine and physiological studies[9-27], body composition studies[9,28-37], determination of work[38,39], accidental[40-45], and post-therapy doses[46,47], animal studies[48-50], diagnosis of diseases[15,25-27], validation of tests/treatments[51], follow-up studies after thyroid therapy[52], and detection of carcinoma[53-55]. A very recent application is in the field of cancer research, where the pharmacokinetics of radiolabeled monoclonal antibodies[56,57] can be determined. Because of the extreme sensitivity required to conduct these studies, other detector devices cannot be used in place of whole body counters.

Although whole body counters are useful for a variety of tasks, there are only of the order of a hundred in the world[69,70], and only nine in Canada[58]; presently Western Canada does not have a whole body counter.

1.2 Overview of Whole Body Counter Design

The uses of whole body counters are very diverse and by virtue of this, many different types of WBCs have been constructed. Although diverse, all high-sensitivity WBCs implement massive amounts of shielding to shield against background radiation[59] since the minimum detectable activity (MDA) decreases as the detected background radiation is reduced[60]. Shielding can either be room-shielded[61] (present around the entire room in which the WBC sits), or the whole body counter can be shadow shielded[36]. Shadow-shielded WBCs only shield the direct, line-of-sight background radiation that would otherwise reach the detector.

With shadow-shielded whole body counters, shielding from background radiation is the single-most important and largest design obstacle, restricting the number, size, and placement of the detectors. These counters can be either scanning-bed[62] or constant-position[63] types. Because it is difficult to properly shadow shield several detectors or banks of detectors, most counters only contain one detector bank below and / or above the subject. The detectors are usually stationary or have little movement, therefore these types of counters are often restricted to a small range of subject sizes. With only one exception[5], none have been built that are capable of counting a wide range of activities. None to date have been built that accommodate all subject sizes. The advantage of shadow shielded whole body counters is that they are considerably less expensive to construct since much less shielding material is needed than with room-shielded counters.

When entire rooms are shielded from background radiation, the design constraints disappear. Multi-detector arrangements are available in either scanning[64] or constant-position[65] configurations. A wide range of innovative designs (see figure 1-1) are also available as compared to shadow-shielded WBCs, and can make use of atypical shielding including water[66] (see figure 1-2), chalk, and other materials. Whole body counters with moving gantries have been made, however only one exists that allows the counter to be used for a wide range of subject sizes[67]. None to date have been made that accommodate all subject activities. Despite the advantages of room-shielded counters, they are very costly to construct, and much effort must be taken in order to prevent contamination.

Two types of whole body counters have been designed that operate adequately with high-activity subjects. The first type is a shadow-shielded scanning counter[5] equipped with collimators that can significantly reduce the amount of radiation reaching the detectors. This WBC uses only two detectors, and was designed for use on adult subjects. The second type of WBC was built to assess the extent of radioactive contamination in Goiania[4], and has a single, stationary detector in a chair-type configuration (see figure 1-3). This WBC has no shielding, and was designed for measuring high activities only.

1.3 Outline of Thesis

The intent of this research is to develop a whole body counter that encompasses all of the benefits from shadow, room shielded, and high-activity counters into one, unique counter: a WBC that will accommodate a wide variety of subject sizes (newborn infants to adults) and a wide range of subject activity. No WBC has been designed with this dual capability. In addition, unique shadow shielding has been designed which allows for multiple detector banks to be implemented. The final product is a scanning, multi-detector shadow shielded WBC capable of providing quantitative and regional information[62] on gamma-emitting radionuclides with energies of up to 2 MeV which are emitted from the human body. Subject sizes ranging from newborn infants to full-grown adults will be accommodated, and subject activities ranging from natural body background[68] to several GBq will be accurately measured. The added versatility of variable subject size and detector sensitivity will make this whole body counter a unique, valuable and useful research and clinical tool.

In this thesis, all aspects of the background, theory, and development of the whole body counter are discussed. Following the introduction presented here, Chapter 2 briefly reviews the physics needed to design the whole body counter and to assess the detectors. Chapter 3 reviews the most common whole body counter configurations, the techniques used to calibrate them, and the methods used to analyze the data. Hardware considerations, including detectors and electronics are then discussed in Chapter 4. A ray-tracing computer simulator was constructed to assist in designing the WBC; its development and uses/results are explained in detail in Chapter 5. In Chapter 6, the WBC's physical design and function are discussed. Low-background conditions for construction and location are discussed in Chapter 7, and the expected performance of the whole body counter is then investigated in Chapter 8. The thesis concludes in Chapter 9, with a discussion on the completed high-adaptability WBC, and future work associated with it.

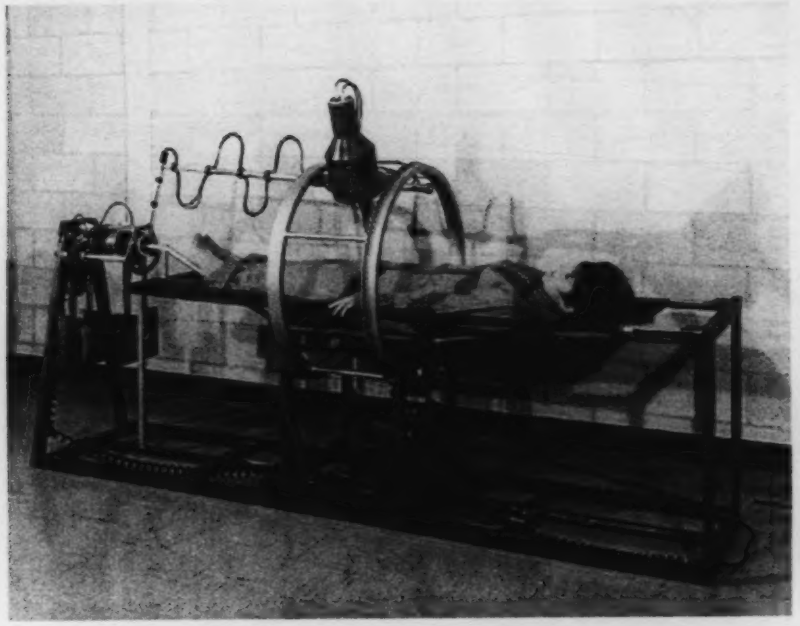

Figure 1-1. A horizontal rotational scanner used to detect the quantity and distribution of radiation in the body.

Figure 1-2. Whole body counter that uses water as shielding is under construction.

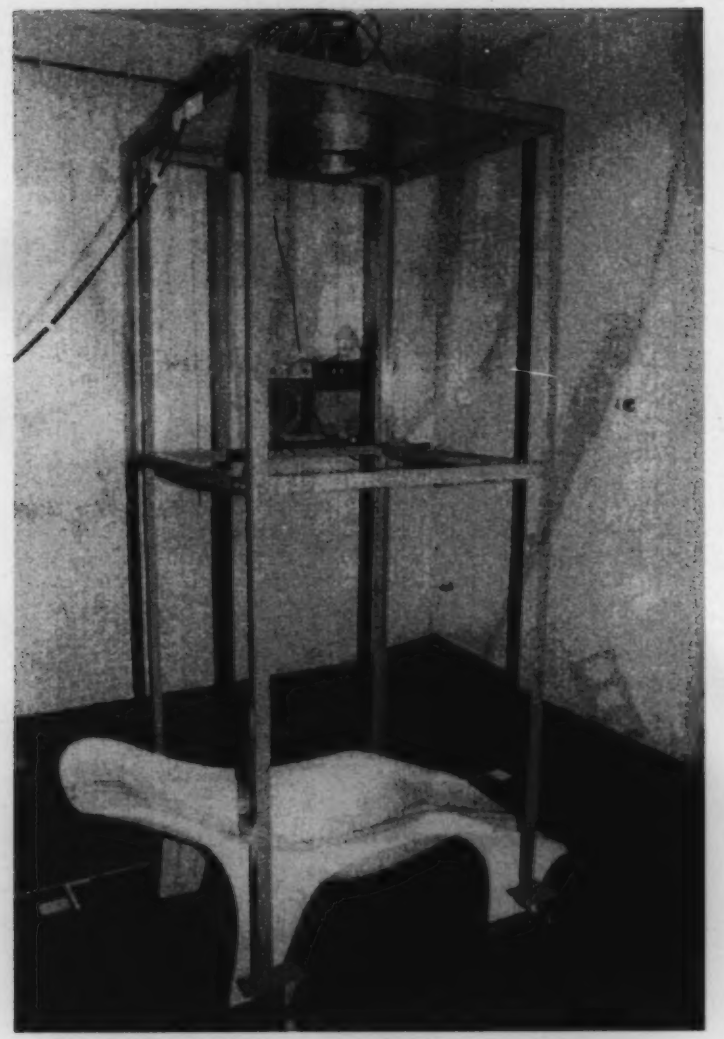

Figure 1-3. The improvised whole body counter used in Goiania.

References

[1] R.D. Evans. Radium poisoning II: the quantitative determination of the radium content and radium elimination rate of living persons. *Am. J. of Roentgenology*. **37**:368-378;1937.

[2] Y. Naversten, V. Lenger. Total body potassium determination using a whole-body counter. *Acta Radiologica-Oncology*. **22**(2):167-175;1983.

[3] D.W. Spady *et al*. Measurement of total body potassium in premature infants by means of a whole-body counter. *Journal of Pediatric Gastroenterology & Nutrition*. **5**(5):750-755;1986.

[4] The radiological Accident in Goiania. *International Atomic Energy Agency, Vienna*, 1988.

[5] C. Pirich *et al*. Monitoring of the biodistribution and biokinetics of dysprosium-165 ferric hydroxide with a shadow-shield whole-body counter. *European Journal of Nuclear Medicine*. **24**(4):398-402;1997.

[6] D.E. Watt, D. Ramsden. High sensitivity counting techniques. 31-33;1964.

[7] G.H. Kramer *et al*. Results of the 1993 Intercomparison/Intercalibration: Final Report. *The Canadian National Calibration Reference Center for In-Vivo Monitoring and the United States Department of Energy*. HMLTD-95-3.

[8] H.S. Martland *et al*. Unrecognized dangers in the use and handling of radioactive substances; with especial reference to storage of insoluble products of radium and mesothorium in reticulo-endothelial system. *The Journal of the American Medical Association*. **85**:1769-1776;1925.

[9] T. Smith, A.G. Cronquist. A versatile and economic whole-body counter based on liquid scintillation detector modules. *British Journal of Radiology* **50**(593):332-339;1977.

[10] F.T. Jensen *et al*. Calcium metabolism evaluated by ^{47}Ca kinetics. Methodologic aspects with optimization of a whole-body counter. *Acta Radiologica-Oncology* **23**(2-3):127-133;1984.

[11] B. Arvidson *et al*. A radionuclide technique for studies of zinc absorption in man. *Interventional Journal of Nuclear Medicine and Biology* **5**(2-3):104-109;1978.

[12] C.C. Shipp *et al*. Measurement of ^{47}Calcium retention with a whole-body counter. *Calcified Tissue International* **41**(6):307-312;1987.

[13] T. Smith, R. Hesp. Measurement of ^{57}Co-labelled vitamin B_{12} using a liquid scintillator whole-body counter. *British Journal of Radiology* **52**(622):832-835;1979.

[14] C.E. Tait, R. Hesp. Measurement of ^{57}Co-vitamin B_{12} uptake using a static whole-body counter. *British Journal of Radiology* **49**(587):948-950;1976.

[15] J.J. Marx. Mucosal uptake, mucosal transfer and retention of iron, measured by whole-body counting. *Scandinavian Journal of Haematology* **23**(4):293-302;1979.

[16] T. Hiraki *et al*. Whole body retention of radioxenon. *Journal of Nuclear Medicine* **18**(5):462-471;1977.

[17] S. Molloi *et al*. Whole body and regional retention of Tc-99m-labelled diphosphonates with a whole body counter: A study with normal males. *Calcified Tissue International* **44**(5):322-329;1989.

[18] J.J. Marx *et al*. Simultaneous measurement of ^{59}Fe and ^{51}Cr in iron absorption studies using a whole-body scanner and mobile shielding. *Nuklearmedizin* **19**(3):140-145;1980.

[19] L. Davidsson *et al.* Intrinsic and extrinsic labeling for studies of manganese absorption in humans. *Journal of Nutrition* **118**(12):1517-1521;1988.

[20] J.A. Cardarelli *et al.* Correction and attenuation in whole-body determination of Co-57 B_{12} absorption: Concise communication. *Journal of Nuclear Medicine* **24**(10):949-951;1983.

[21] S.P. Nielsen *et al.* Fractional intestinal absorption and retention of calcium measured by whole-body counting. Application of a power function model. *Scandinavian Journal of Clinical and Laboratory Investigation* **35**(3):197-203;1975.

[22] G.I. Lykken. A whole body counting technique using ultra low doses of ^{59}Fe and ^{65}Zn in absorption and retention studies in humans. *American Journal of Clinical Nutrition* **37**(4):652-662; 1983.

[23] L. Rosenthall, A. Arzoumanian. Total body retention measurements of Tc-99m MDP using a simple detector. *Clinical Nuclear Medicine* **8**(5):210-213;1983.

[24] R.E. Toohey *et al.* Measurement techniques for radium and the actinides in man at the center for human radiobiology. *Health Physics* **44**suppl 1:323-341;1983.

[25] P. Charles *et al.* Calcium metabolism evaluated by 47Ca kinetics: Estimation of dermal calcium loss. *Clinical Science* **65**(4):415-422;1983.

[26] P.K. Hansen *et al.* Cobalamin absorption determined by the stool spot test. *Scandinavian Journal of Gastroenterology* **21**(3):341-347;1986.

[27] A. Celada *et al.* Inorganic iron absorption in subjects with iron deficiency, anemia, achylia gastrica and alcoholic cirrhosis using a whole-body counter. *Acta Haematologica* **60**(3):182-192:1978.

[28] E. Havlik *et al.* Increased ^{137}Caesium whole body radioactivity in high-performance athletes. *International Journal of Sports Medicine* **11**(1):37-40;1990.

[29] N. Vaisman *et al.* Changes in body composition during refeeding of patients with anorexia nervosa. *Journal of Pediatrics* **113**(5):925-929;1988.

[30] Y. Naversten, V. Lenger. Total body potassium determination using a whole-body counter. *Acta Radiologica-Oncology* **22**(2):167-175;1983.

[31] M.D. Jensen *et al.* Measurement of body potassium with a whole-body counter: Relationship between lean body mass and resting energy expenditure. *Mayo Clinic Proceedings* **63**(9):864-868;1988.

[32] L.P. Novak *et al.* Estimation of total body potassium in normal adolescents by whole-body counting: age and sex differences. *Medicine and Science in Sports* **5**(3):147-155;1973.

[33] R.N. Pierson Jr. *et al.* Body potassium by four-pi ^{40}K counting: an anthropometric correction. *American Journal of Physiology* **246**(2Pt2):F234-239;1984.

[34] G.B. Forbes. Unmeasured losses of potassium in balance studies. *American Journal of Clinical Nutrition* **38**(3):347-348;1983.

[35] J.K. Haywood *et al.* A two-way scanning method for total body in vivo neutron activation analysis. *Physics in Medicine and Biology* **23**(5):865-867;1978.

[36] K. Boddy *et al.* A high-sensitivity dual-detector shadow-shield whole body counter with an 'invariant' response for total body in vivo neutron activation analysis. *Physics in Medicine and Biology* **20**(2):296-304;1975.

[37] G.L. Hill *et al.* A new method for the rapid measurement of body composition in critically ill surgical patients. *British Journal of Surgery* **65**(10):732-735;1978.

[38] F.X. Masse, M.M. Bolton Jr. Experience with a low-cost chair-type detector system for the determination of radioactive body burdens of MIT radiation workers. *Health Physics* **19**(1):27-35;1970.

[39] P.M.B. Pillai *et al.* Deposition and clearance of ^{212}Pb in humans. *Health Physics* **66**(3):343-345;1994.

[40] J.J. Estrada, G.R. Laurer. A method to obtain subject background for low-level in-vivo measurements of the head. *Health Physics* **65**(3):306-312;1993.

[41] L.E. Howard, J.F. Sommers. Xenon whole-body counting and dose determinations. *Health Physics* **38**(3):349-358;1980.

[42] N. Cohen *et al.* Body burden estimation of ^{32}P by measurement and calibration of bremsstrahlung radiation produced in the skull. *Health Physics* **44**(6):668-671;1983.

[43] C.D. Berger. The effectiveness of a whole body counter during and after an accident situation at nuclear facilities. *Health Physics* **40**(5):685-692;1981.

[44] T. Smith, C.J. Edmonds. Selenium 75 contamination in iodine 131 solutions. *British Journal of Radiology* **52**(614):145-147;1979.

[45] H. Nishiyama *et al.* Accidental Cs-137 contamination. *Radiology* **154**(2):513-517;1985.

[46] G.M. Blake *et al.* ^{89}Sr radionuclide therapy: Dosimetry and haematological toxicity in two patients with metastasising prostatic carcinoma. *European Journal of Nuclear Medicine* **13**(1):41-46;1987.

[47] T. Smith *et al.* Radiation absorbed dose from technetium-99m DTPA. *Journal of Nuclear Medicine* **28**(2):240-243;1987.

[48] A.G. Cronquist *et al.* A simple whole-body counter for measuring radionuclides in large dogs. *Physics in Medicine and Biology* **22**(6):1197-1201;1977.

[49] R.D. Lloyd *et al.* Design and calibration of a total-body counting system for measuring radioactivity in Beagles. *International Journal of Applied Radiation and Isotopes* **27**(2):103-111;1976.

[50] J.S. Morton *et al.* A convenient device for the determination of whole body radionuclide concentrations in live ducks. *Health Physics* **38**(2):234-236;1980.

[51] J.H. Phipps *et al.* Validation of a method of treating menorrhagia by endometrial solution. *Clinical Physics and Physiological Measurement* **13**(3):273-280;1992.

[52] C.J. Edmonds *et al.* Follow-up of thyroid carcinoma by whole-body counting. *British Journal of Radiology* **43**:868;1970.

[53] E.T. Korppi-Tommola *et al.* Double-tracer dosimetry of organs in assessment of bone marrow involvement by two monoclonal antibodies. *Acta Oncologica* **35**(3):357-365;1996.

[54] J.P. Edlin *et al.* Detection of recurrent colorectal carcinoma with In-111 CYT-103 scintigraphy in a patient with nondiagnostic MRI and CT. *Clinical Nuclear Medicine* **19**(11):1004-1007;1994.

[55] M.J. Blend *et al.* Uptake of In-111 GYK-DTPA B72.3 monoclonal antibody in metastatic squamous cell carcinoma. *Clinical Nuclear Medicine* **19**(10):912-913;1994.

[56] P.H. Brown *et al.* Primary lung cancer: Biodistribution and dosimetry of two In-111 labeled monoclonal antibodies. *Radiology* **173**(3):701-705;1989.

[57] B.B. Mittal *et al.* Phase I/II trial of combined 131I anti-CEA monoclonal antibody and hyperthermia in patients with advanced colorectal adrenocarcinoma. *Cancer* **78**(9):1861-1870;1996.

[58] G.H. Kramer. The Canadian whole body counting intercomparison program: a summary report for 1989 – 1993. *Health Physics*. **69**(4):560-565;1995.

[59] G.R. Meneeley, S.M. Linde. Radioactivity in Man, Second Symposium (Whole body counting and effects of internal gamma ray-emitting radioisotopes). *Charles C Thomas Publisher*. Copyright 1965.

[60] L.A. Currie. Limits for qualitative detection and quantitative determination. *Analytical Chemistry*. **44**(3):586-593;1968

[61] G.R.Laurer, M. Eisenbud. Low level in vivo measurement of I^{131} in humans. *Radioactivity in man – second symposium.* Charles C Thomas Publisher, Copyright 1965.

[62] R. Novario, L. Conte. A new method for calculating the distribution of radioactivity in man measured with a whole-body counter. *Health Physics* **58**(5):597-607;1990.

[63] M.E. Noz, Simple method for reducing shadow-shield background. *Health Physics* **39**(2):304-306;1980.

[64] G.J. Hine, *et al.* Geometrical and attenuation corrections for a two crystal whole body counter; body scanning with an 8 by 4 in. NaI crystal. *Radioactivity in man – second symposium.* Charles C Thomas Publisher, Copyright 1965.

[65] P. Mariss, *et al.* A whole body counter with an invariant response for whole body analysis. *European journal of nuclear medicine* **3**(2):129-135;1978.

[66] R.E. Peterson *et al.* Evaluation of a water shield whole body counter. *Radioactivity in Man, Second Symposium* (Whole body counting and effects of internal gamma ray-emitting radioisotopes). *Charles C Thomas Publisher*. Copyright 1965.

[67] K.L. Ellis, R.J. Shypailo. Whole body potassium measurements independent of body size. *Human Body Composition, Plenium Press,* 1992.

[68] J. Shapiro. Radiation protection – a guide for scientists and physicists. 2nd edition:55-56;1981.

[69] IAEA, Whole body counting. IAEA Vienna, STI/PUB/47, 1962

[70] IAEA, Directory of Whole body radioactivity monitors. IAEA Vienna, STI/PUB/213, 1970

Chapter 2

Background Physics to Whole Body Counting

2.1 Photon Propagation through Matter

An understanding of atomic interactions involved when photons propagate through matter is crucial when dealing with whole body counting. Radionuclides within the human body emit photons that propagate through and interact with subject tissue, air, and finally with the detector before giving rise to a measurable signal. Information on the interactions that take place along the photon's path can be obtained once the detector's signal is processed, and an energy spectrum is generated. With knowledge of photon-atomic interactions, the spectrograph can be properly analyzed and the quantity and types of radionuclides present can then be determined. In addition to spectral analysis, theoretical modeling of the spectrum in whole[1] or in part[2] can be done with the knowledge of photon-atomic interactions. Verification and predictions of experimental results and setups can then be made.

The following is a review of the atomic interactions that take place when photons propagate though matter. Only the essential physics is covered here for Compton scattering, photoelectric effect, and pair production. This review is in no way complete, but is presented here in order to give a basic understanding of atomic interactions relevant to this thesis.

Compton Scattering

During Compton scattering, a photon with original energy E_γ inelastically scatters with an outermost atomic electron. Some of the photon's energy is transferred to the electron, ejecting it from the atom with energy E_e, at an angle Φ. The photon experiences an energy loss of E_e plus the electron's binding energy, and is scattered at an angle θ. A pictorial representation of Compton scattering can be seen in figure 2-1.

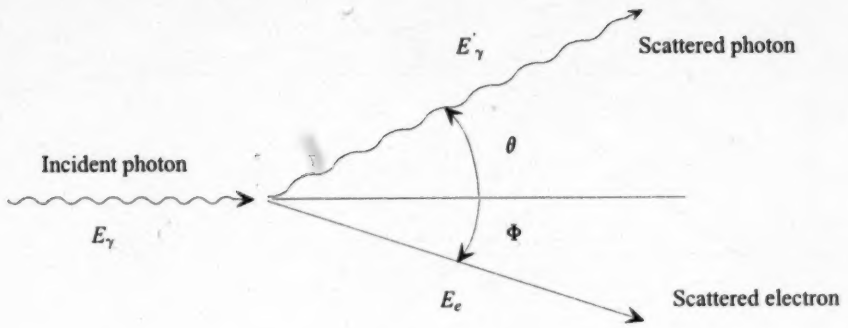

Figure 2-1. The geometry of Compton scattering.

Assuming that the electron's binding energy is negligible compared to E_γ, the Compton-scattering formula can be derived and is given in equation 2-1, where m is the rest mass of the electron. This formula describes the final photon energy (E_γ'), given the initial photon energy (E_γ) and the photon's scattering angle (θ).

$$E'_\gamma = \frac{E_\gamma}{1+(E_\gamma/mc^2)(1-\cos\theta)} \tag{2-1}$$

It is easy to see from the above equation that little or no energy is lost in a forward-scattered photon, and that a back-scattered photon would result in a minimum photon energy of $mc^2/2 \approx 0.25$ MeV for large incident photon energies (~5 MeV).

The probability of a photon being scattered off an atom of atomic number Z into an angle θ is given by the Klein-Nishina formula seen below. Here, $\alpha = E_\gamma/mc^2$, $r_o = e^2/4\pi\epsilon_o mc^2 = 2.818$ fm, and $d\sigma_c/d\Omega$ is the differential scattering cross section.

$$\frac{d\sigma_c}{d\Omega} = Z{r_o}^2\left[\frac{1}{1+\alpha(1-\cos\theta)}\right]^2\left[\frac{1+\cos^2\theta}{2}\right]\left[1+\frac{\alpha^2(1-\cos\theta)^2}{(1+\cos^2\theta)[1+\alpha(1-\cos\theta)]}\right] \tag{2-2}$$

Compton scattering appears as a continuum in the energy spectrum due to the range in possible photon scattering angles. The energy released to the detector is by way

of the scattered electron, and therefore the maximum energy on the Compton continuum or 'Compton Edge' is equal to $E_\gamma - E_\gamma$, or for high energy photons E_γ-0.25 MeV. The Compton continuum and Compton edge for a typical NaI spectrum is illustrated in figure 2-2.

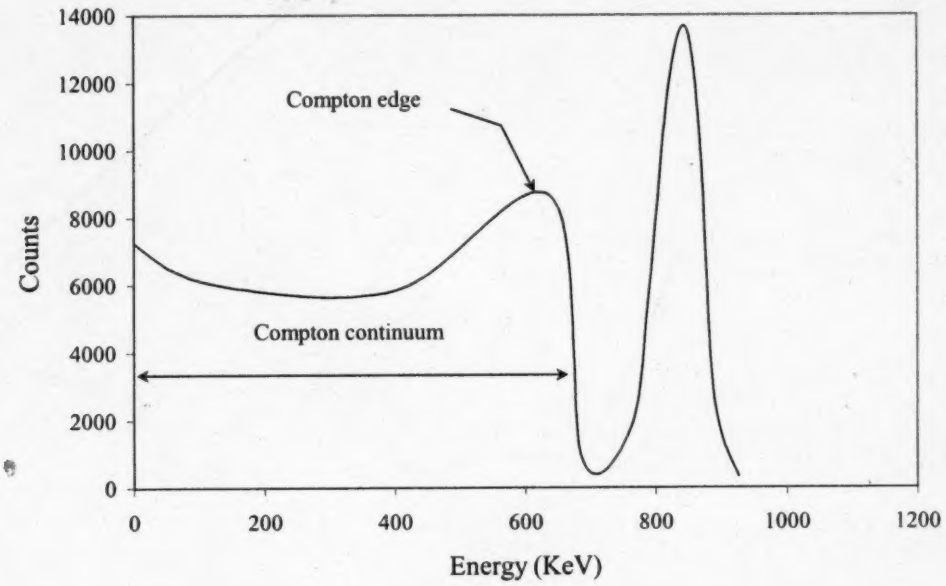

Figure 2-2. Compton edge and continuum shown on a typical NaI spectrum.

Photoelectric Effect

The photoelectric effect occurs when an atomic electron absorbs all of the energy from an incoming photon and is ejected from the atom. This process most often occurs with inner K and L shell atomic electrons, and the emitted electron or 'photoelectron' has a kinetic energy E_e equal to the photon's original energy E_γ minus the electron's binding energy E_B.

$$E_e = E_\gamma - E_B \tag{2-3}$$

The probability of a photoelectric interaction is highly dependent on the incoming photon's energy and the atomic number of the target atom. Its probability is approximately proportional to $(atomic\ number)^4/(photon\ energy)^3$.

This photoelectric effect can be seen in the spectrum as a single peak known as the photopeak. The counts computed from the area under the photopeak give the number of total absorption events that occurred in the detector over a given period of time. The position of the photopeak can be used to measure photon energies and identify radionuclides, while the photopeak area can be used to quantify the amount of the nuclide.

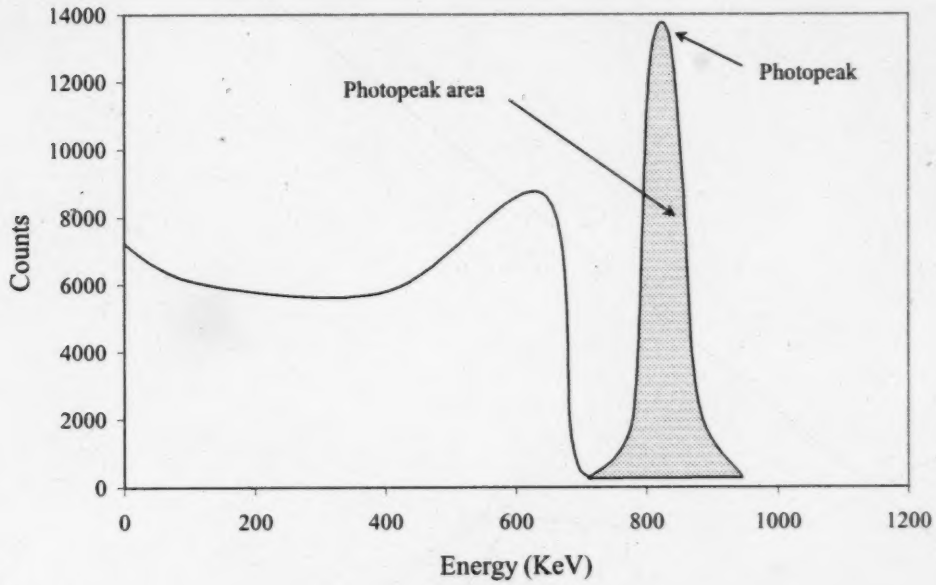

Figure 2-3. The photopeak and the photopeak area are shown on a typical NaI spectrum.

The amount of photopeak counts present in a NaI spectrum from a source can be expressed by the *peak-to-total ratio (PTTR)*. This ratio is defined as the net photopeak counts divided by the total number of counts in a given spectrum. PTTRs are only defined for mono-energetic point sources located on the NaI crystal axis. They are empirically determined, and each PTTR is very specific for a certain crystal size, and photon energy. Because the probability of the photoelectric effect is proportional to $(atomic\ number)^4/(photon\ energy)^3$, the PTTR reaches unity at low energies, and quickly falls off at higher energies.

Pair Production

The creation of an electron-positron pair can occur when a high-energy photon passes close to the nucleus of an atom. This interaction is called pair production, and can occur when threshold photon energies above 1.022 MeV are present, since the rest mass energy of each resulting particle is 0.511 MeV. The remainder of the photon's energy adds to the kinetic energy of the electron and the positron. The electron and its energy is absorbed in the detector, while the positron interacts with the detector until it recombines with an electron and produces two 0.511 MeV photons known as annihilation radiation.

The annihilation radiation is absorbed in the detector through one or more of the aforementioned interactions, and evidence of incomplete absorption can be seen in the resulting spectrum. When one of the annihilation photons escapes the detector, a single escape peak can be seen with an energy 0.511 MeV lower than the full-energy peak. Both of the annihilation photons can escape the detector, giving rise to a double escape peak with an energy 1.022 MeV below the full-energy peak. The effect of single and double escape peaks on the spectrum is illustrated in figure 2-4.

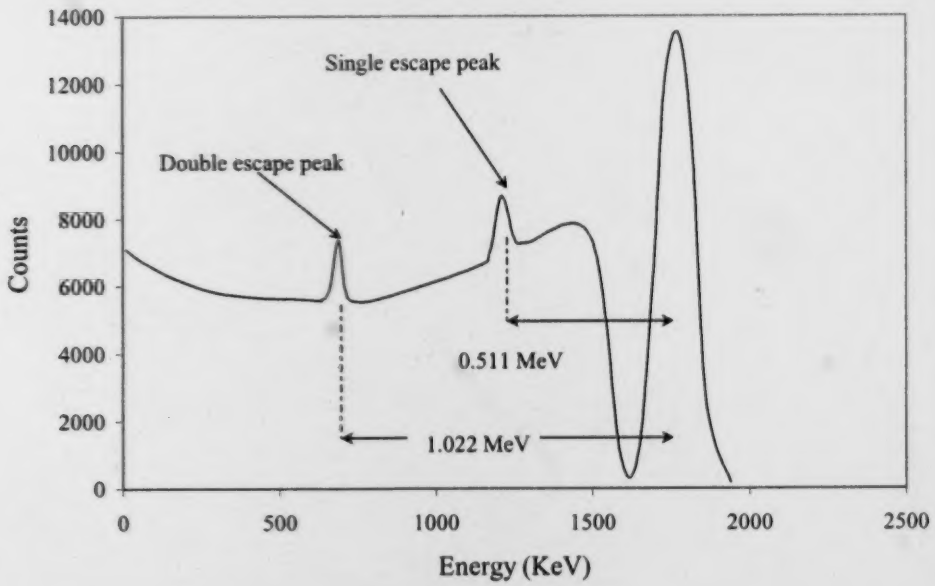

Figure 2-4. Single and double escape peaks on a typical NaI spectrum.

A variation of pair production can occur if the photon energy exceeds 2.044 MeV. In this case, pair production can occur when the photon passes near an atomic electron instead of the nucleus. As before, an electron-positron pair is created, however the total kinetic energy is now shared between the positron-electron pair and the atomic electron. Since the atomic electron is ejected from the atom, this process is called *triplet production.*

X-ray Escape Peak

Another type of escape peak that commonly appears in nuclear spectra is the x-ray escape peak. Immediately following a photoelectric interaction, an electron vacancy is created in the K or L shell of the atom. An electron from a higher-energy orbital quickly fills this vacancy, and emits an x-ray when moving to this lower-energy state. The x-ray that is emitted has an energy equal to the difference in the electron binding energies of the two states. Because the x-ray energies are dependent on the electron energy states, each element has its own specific x-rays that appear after photoelectric interactions, or its own *'characteristic x-rays'*. When the detector's own characteristic x-rays are not absorbed by the detector, an x-ray escape peak will be seen in the spectrum. X-ray escape peaks appear at an energy below the full-energy photopeak, shifted by an energy equal to that of the characteristic x-ray emitted. For NaI detectors, an escape peak from the iodine atom can be seen at approximately 28 keV below the photopeak. Lower-energy photons (<200 keV) have a higher probability of creating an x-ray escape peak, thus, at higher energies, iodine escape peaks are not seen in the NaI spectra.

Attenuation

As photons pass through a material, one or more of the previously mentioned processes can occur, reducing the photon's energy and/or deflecting the photon from its original path and thus creating secondary photons. The removal of primary photons from an initial photon beam is known as *attenuation*, and the probability of it occurring grows exponentially with material thickness such that:

$$N = N_o e^{-\mu t} \qquad (2\text{-}4)$$

Where N_o is the number of photons in the original photon beam, and N is the number of primary photons left after passing through a material of thickness t; figure 2-5 illustrates the concept.

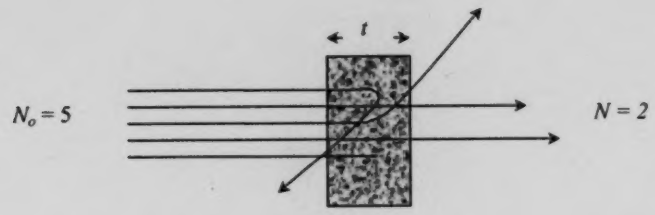

Figure 2-5. Attenuation of primary photon beam through a material of thickness t.

In equation 2-4, μ is known as the *linear attenuation coefficient*, and is defined as the probability that a photon will be attenuated per unit thickness of attenuating material. The value for μ is obtained by taking the sum of the linear attenuation coefficients for each type of interaction:

$$\mu = \mu_{PE} + \mu_{CS} + \mu_{pp} \qquad (2\text{-}5)$$

Here, μ_{PE}, μ_{CS}, and μ_{pp} are coefficients for photoelectric effect, Compton scattering, and pair production respectively. Values for the linear attenuation coefficients change with photon energy and material type.

2.2 Sources of Radiation

The environment in which we live is radioactive by nature. Many elements have one or more isotopes that are naturally radioactive, and one or more of these isotopes are found in almost all materials including natural and man-made objects, the air we breath, and even our very own bodies. Radiation from the cosmos is constantly bombarding the Earth, and is another substantial source of background radiation. The sources of background radiation and their dose equivalent contributions per year can be seen in figure 2-6. To put these doses in perspective, a single chest x-ray delivers 0.1 mSv, and flying at high altitude in a typical airliner for ten hours can produce 0.02 mSv [9].

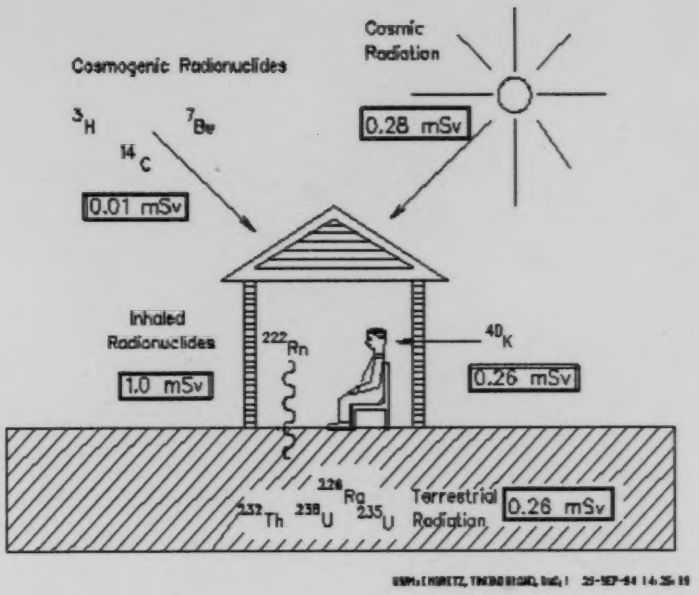

Figure 2-6. Sources of external background radiation[3].

An understanding of the types and sources of naturally occurring radiation affects the function and design of a whole body counter - shielding requirements, shielding type, room location, room ventilation requirements, pre-study preparation, and the types of studies that can be performed are all affected.

Cosmic

Cosmic radiation originates from the sun, stars, super novas, pulsars, and other cosmic events and is primarily made up of extremely high-energy charged nuclei, which include all elements from the periodic table.

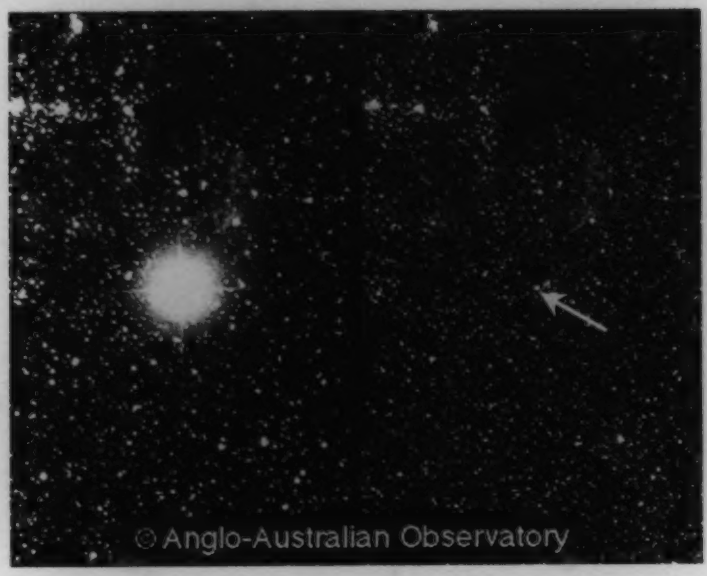

Figure 2-7. A star before and after super-nova[4].

Lighter elements are most predominant in cosmic radiation, with 89% made up from protons, 10% helium, and the remaining 1% from heavier elements. Cosmic ray particles have kinetic energies that range from 10^9 eV to 10^{20} eV. Cosmic radiation also contains small amounts of gamma rays and neutrinos as well.

A continuous flux of cosmic radiation 'rains' on the earth, 99% of which interacts with the earth's atmosphere. These interactions produce showers of lower energy particles (see figure 2-8), many of which are absorbed by the earth's atmosphere. The remaining particles from the showers that reach the earth's surface are produced from 3rd to 7th generation showers, and consist mostly of muons, photons, neutrons, electrons, protons, pions, and positrons of various energies. Figure 2-9 shows experimentally observed fluxes for neutrons, muons, protons, and pions at sea level.

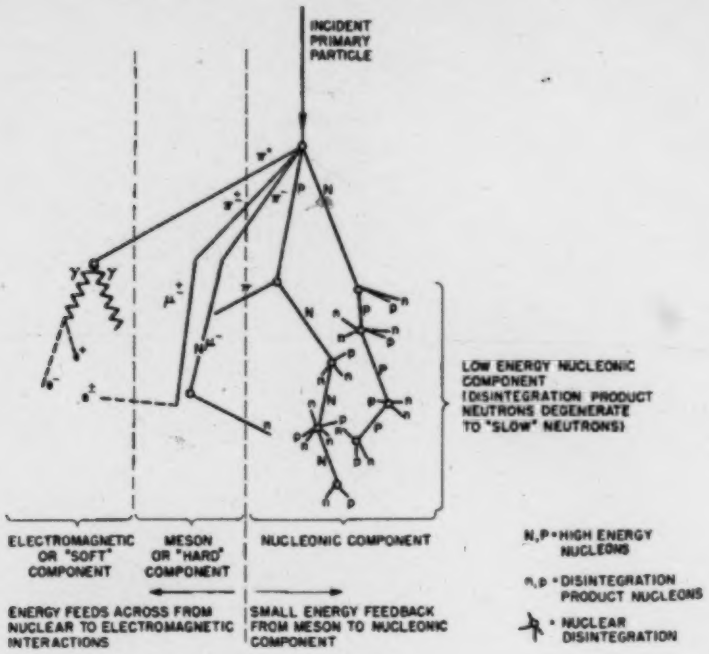
INCIDENT PRIMARY PARTICLE
LOW ENERGY NUCLEONIC COMPONENT (DISINTEGRATION PRODUCT NEUTRONS DEGENERATE TO "SLOW" NEUTRONS)
ELECTROMAGNETIC OR "SOFT" COMPONENT
MESON OR "HARD" COMPONENT
NUCLEONIC COMPONENT
ENERGY FEEDS ACROSS FROM NUCLEAR TO ELECTROMAGNETIC INTERACTIONS
SMALL ENERGY FEEDBACK FROM MESON TO NUCLEONIC COMPONENT
N,P = HIGH ENERGY NUCLEONS
n,p = DISINTEGRATION PRODUCT NUCLEONS
= NUCLEAR DISINTEGRATION

Figure 2-8. Schematic Diagram of Cosmic Ray Shower[5].

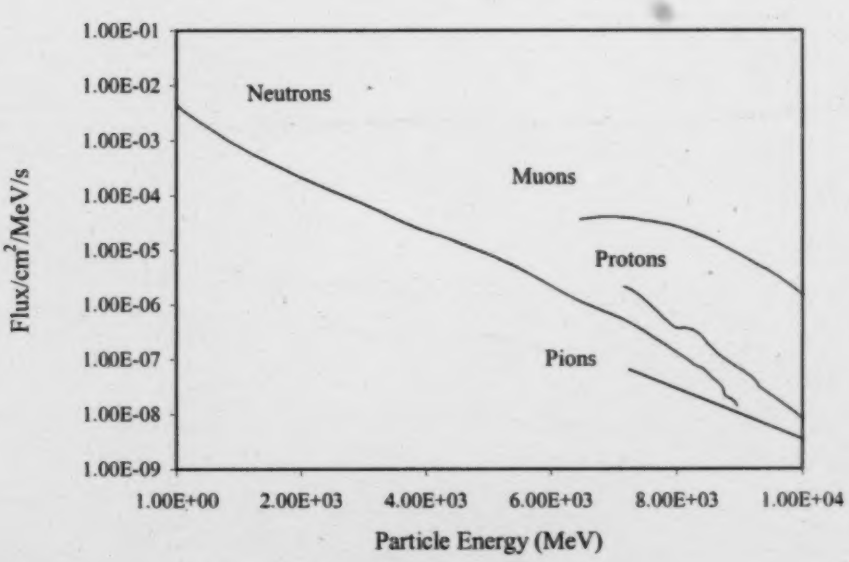

Figure 2-9. Experimental sea level spectra for cosmic shower components[6].

The flux of cosmic rays that reach the earth is not constant, but instead varies inversely with the sun's eleven-year solar cycle. The solar wind's magnetic field shields the earth from charged cosmic rays. The solar-cosmic radiation relationship for neutron fluxes can be seen below in figure 2-10.

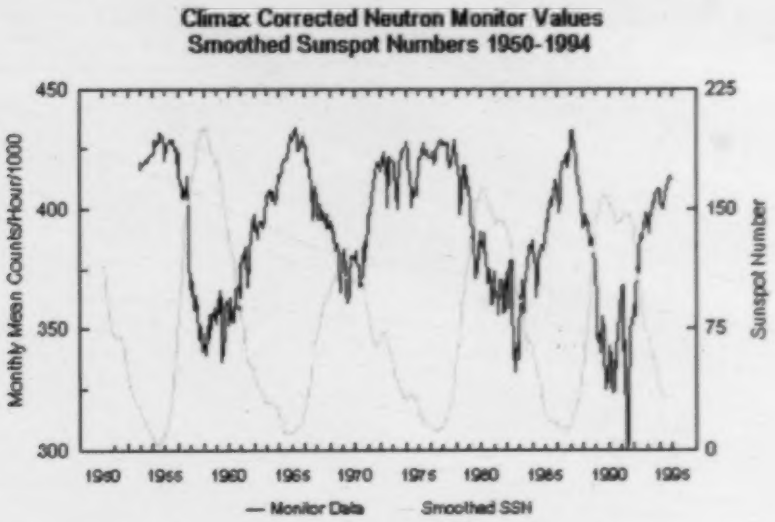

Figure 2-10. Neutron-flux / solar-wind eleven year cycle[5].

Airborne

Radiation emitted from radioactive gas or particulates can be found in air, and contributes to the overall background radiation levels. Radon (Rn-222) and Thoron (Rn-220) are short-lived radioactive gasses formed during the decay of U-238 and Th-232 respectively, commonly found in soil and construction materials. These gasses are primarily alpha emitters, and when they decay their daughter products (Po-218, Po-210, Po-216) attach themselves to particles in the air, forming radioactive dust. These dust particles decay emitting alpha, beta, and gamma radiation. The contribution of these airborne radionucludes can be quite significant, resulting in a beta emission rate of 32 emissions/100cm^3 per hour[7] for regular air from a room.

Terrestrial

Billions of years ago during the formation of the Earth radioactive isotopes were much more abundant, and today some of the original long-lived isotopes still remain. The four most prevalent remaining isotopes are K-40, Th-232, U-238, and U-235, the last three of which have their own family of radioactive daughter products that form the source for modern-day terrestrial radiation.

The daughter products from uranium and thorium emit alpha, beta, and gamma radiation, which are observable in the background radiation spectrum. The principal gamma emitting isotopes from the thorium series are Ac-228, Ra-224, Bi-212, and Tl-208, from the uranium 238 series are Ra-226, Pb-214, Bi-214, and Pb-210. Other gamma emitters include K-40, U-235, and some neutron-activated elements from cosmic ray formed neutrons.

In addition to the above radionuclides, fission products from nuclear weapons tests/use can be seen in the background spectra as well. The main radioisotope present in fallout is cesium-137, but small quantities of Zr-95, Nb-95, Ru-106, Sb-125, and Ce-144 have also been observed.

Materials

Because radionuclides are very common in the air, earth's crust, and in nature, they tend to find their way into man-made objects, and indeed are all around us. The source of material and processing methods used in forming the material will dictate the amount and type of radioactivity present. An example of this is aluminum; the skimming process used when smelting aluminum tends to create higher concentrations of Th-232 in the finished metal. As a result, aluminum has a higher activity compared with other metals. Glass is another material high in contaminants (K-40), and is the major source of PMT-detector contamination. Some other examples of gamma radioactivity present in common materials[8] can be seen in table 2-1.

Sample	Gamma C/min > 80 keV
Scotch tape regular	0.2/cm^2
60-40 soft solder	0.08/g
2 in. photomultiplier tube socket	35.4
Modern lead brick	50 – 250
Modern lead brick (sand blasted)	10 – 20
Scotch electrical tape	0.05/cm^2

Table 2-1. Experimentally measured gamma counts for common materials[8].

When designing a sensitive counting system, low-activity materials must be chosen in order to prevent unnecessary background counts. Ultra-pure materials are available which contain extremely low amounts of radiation, but a balance between sensitivity and cost must be found. This is further discussed in the next section under 'shielding'.

Human Body

Like natural and man-made objects, the human body contains radiation from the surroundings as well. Naturally occurring radionuclides in the body are discussed in the paragraphs that follow, and are summarized in table 2-2.

Potassium – 40 is the most common radioisotope in the human body, and is primarily found in muscle mass throughout the body. This long-lived isotope is a high-energy beta and gamma emitter, and is the main source of natural radiation body burden.

The next most abundant radionuclide is carbon-14, a beta emitter that is formed from neutron activated nitrogen in the upper atmosphere due to cosmic rays. C-14 finds its way into the body via ingested food.

Ra-226 and Po-210 are both gamma and alpha sources, and are also found in the body, but in smaller amounts than the previous two isotopes. These isotopes tend to collect in the bones of the body.

Trace amounts of Sr-90 in the body can also be found, and are solely attributed to radioactive fallout from nuclear weapons. This isotope is a beta emitter that concentrates in bones.

Radionuclide	Disintegrations/minute	Area deposited
^{40}K	266,000	Whole body
^{14}C	193,000	Whole body
^{226}Ra	89	Bone lining
^{210}Po	1,110	Bone/gonads
^{90}Sr (1973)	2,886	Endosteal bone/bone marrow

Table 2-2. Naturally occurring radionuclides found in the human body[9].

Experimentally Measured External Background Radiation Spectrum

To obtain an estimate of the actual background contribution from external radiation, measurements were conducted locally. The background radiation experimentally observed is made up from all of the sources discussed in this section. Figure 2-11 shows a typical background spectrum without radiation from the human body present. This spectrum was taken with a germanium (20%) detector from the SLOWPOKE reactor site in Edmonton for an acquisition time of 250000s (2.89 days).

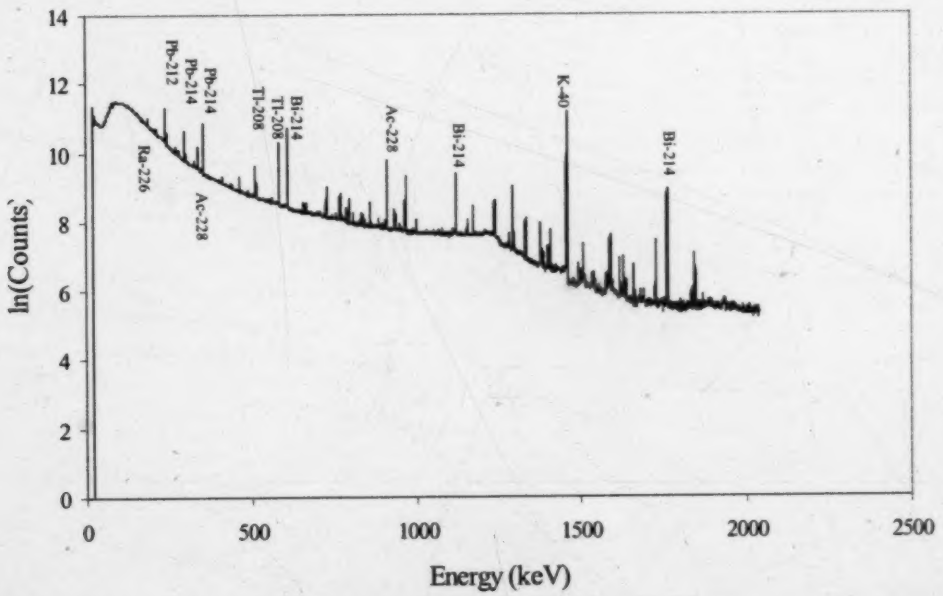

Figure 2-11. Background radiation from the SLOWPOKE reactor site.

2.3 Whole Body Counting

Basic Principles of Operation

Several components are needed in order to construct a working whole body counter, and although most counter designs are different, their underlying functionality is the same. Figure 2-12 shows the basic components found in whole body counters.

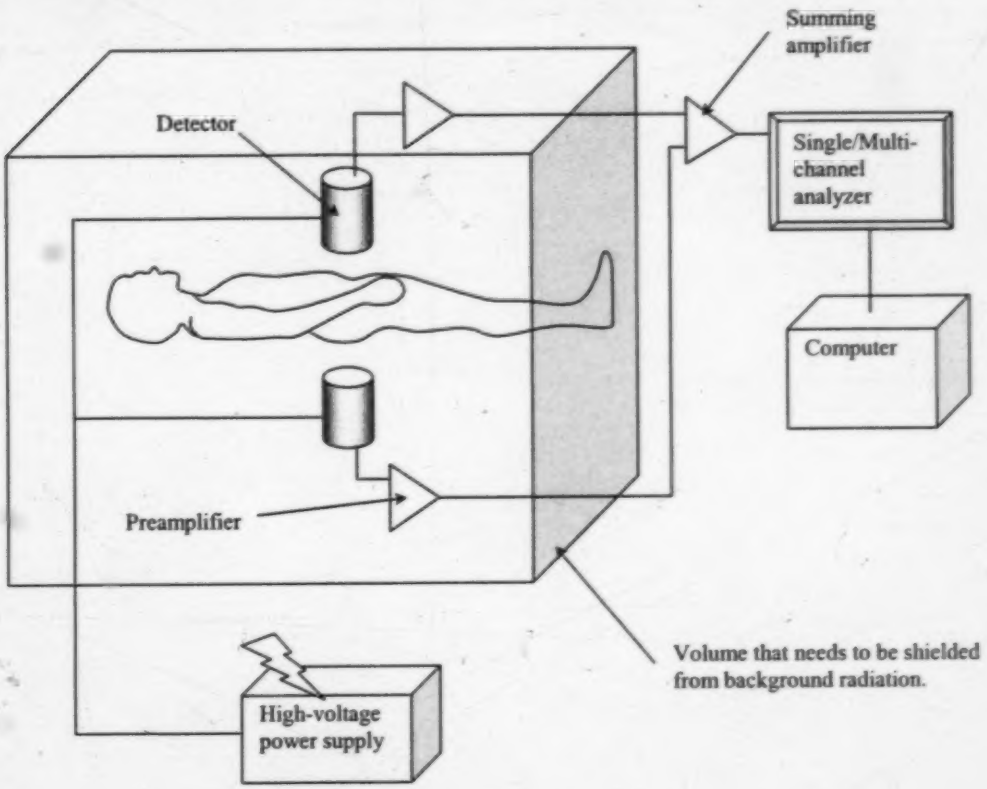

Figure 2-12. Schematic diagram of the basic components found in WBCs. In this example the two detector signals are summed.

All WBCs have a gamma detector of some sort, either a scintillation/PMT or semiconductor type used to detect radiation from the body and require a high voltage power supply in order to produce a signal. A preamplifier is then used to modify the signal from the detector, giving it the proper characteristics needed by other electronics.

This signal is then fed into a single channel or multi-channel analyzer in order to get spectroscopic information from the raw signal. When multiple detectors are used, the individual signals can be added using a summing amplifier, or individually analyzed using a multi-channel buffer placed after the preamplifiers. In order for WBCs to be effective for low-activity studies, the detectors and preamplifiers are surrounded with massive shielding.

Detector Types

There are several gamma-ray detectors available, however when dealing with photon energies above several hundred keV as is common in whole body counting, only inorganic scintillates and germanium detectors are suitable. All other detector types become extremely inefficient at these energies making them impractical for use. Only the basic operation of both detector types is discussed here, but a deeper understanding of these and other detectors can be found in other literature[10].

Germanium detectors are the preferred detectors for analyzing complex gamma spectra, and are made from semi-conducting material of either high-purity germanium (HPGe), or lithium-drifted germanium (GeLi). Signals are formed in the detector when gamma radiation interacts with the reverse biased semiconductor, where electrons deposited from gamma-ray interactions migrate to the biased ends. Much effort is spent in creating the two forms of germanium, all in an attempt to increase the active detector thickness, which increases the detector efficiency. GeLi and HPGe can be commercially made with maximum active thicknesses ranging from 1 – 2 cm; a ten-fold increase from that of regular germanium. Despite the increased detector thickness available, for the same detector size, germanium detectors are still far less efficient than NaI detectors. Germanium detectors however have a superior energy resolution (see equation 2-9) of approximately 0.15% as compared to 8% with NaI (at 662 keV), which makes them ideal for analyzing complex gamma spectra. Both types of germanium detectors require cryogens (liquid nitrogen) and a high-voltage reverse biased source (approximately 1 KV) to become operational. Only HPGe can be allowed to warm up between experiments without damage to the detector and as a result, HPGe is the most common germanium detector type.

Of the inorganic scintillating detectors, thallium-activated sodium iodide (Na(Tl)) is by far the most common, and the only one used in whole body counting. Non-activated, pure sodium iodide (NaI) detectors can be used and have slightly different properties than the activated form[11]. At room temperature, NaI(Tl) pulse times are shorter and yield more light output. For the purposes of this discussion, all references to sodium iodide (NaI) will imply the activated form. Unlike semi-conducting detectors, electrons formed from gamma-ray interactions inside the NaI detector do not form the electrical signal directly, but instead go on to lose their energy to the crystal through ionization and excitation. This in turn causes the crystal atoms to momentarily fluoresce light, which is collected by one or more photomultiplier tubes (discussed in the next section) and converted into an electrical signal. The main advantage of NaI detectors is that the NaI crystal can be made as thick as desired and in a variety of shapes, thus yielding a far superior efficiency for gamma-ray detection over HPGe detectors. Unlike HPGe detectors, sodium iodide detectors do not require cryogens to work properly, therefore flexible experimental arrangements for the detector are possible.

NaI detectors do have disadvantages, however. First there is the relatively poor energy resolution when compared to HPGe detectors. Secondly, sodium iodide crystals are very sensitive to mechanical and thermal shock, and are hygroscopic. Because of sodium iodide's affinity towards water, even slight moisture in the air can cause a breakdown of the crystal. As a result, the NaI crystal must be placed in an airtight "can", usually made of aluminum, and occasionally of brass or stainless steel. Highly reflective packing made of aluminum oxide, Mg0, or TiO_2 is placed between the can and the crystal to facilitate the light gathering to the photomultiplier tube. Figure 2-13 illustrates the typical sodium iodide detector setup.

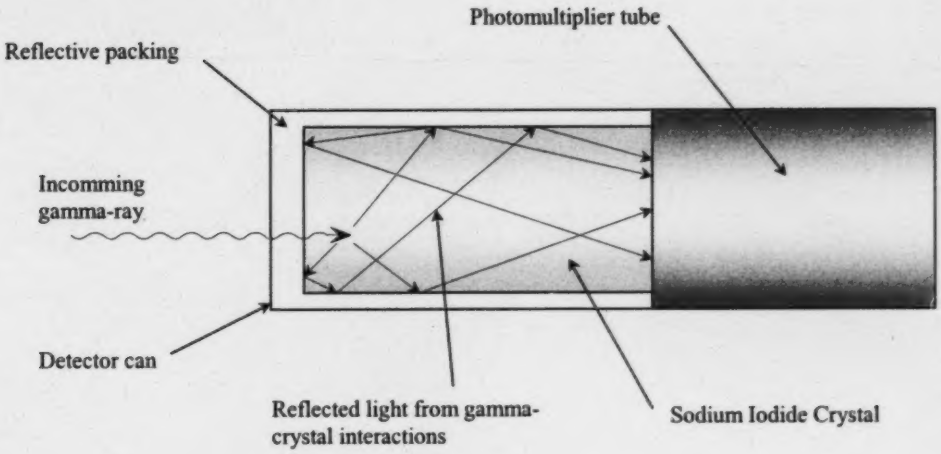

Figure 2-13. Diagram showing the sodium iodide detector arrangement and the reflective action of the packing used in detector cans.

Since the advent of GeLi detectors in 1960, and HPGe detectors in 1980, germanium detectors have become the chosen detectors for analyzing complex gamma spectra. However, sodium iodide detectors offer an energy resolution adequate for the analysis of moderately complex gamma ray spectra, and have been used in this manner since they first emerged in 1948. Good efficiency, adequate energy resolution, ease of use, and cost are the reasons why approximately 2/3 of the world's whole body counters use NaI detectors[12,13].

The background spectra from a HPGe and NaI detectors can be seen in figure 2-14. The photopeaks from gamma emitting radionuclides are clearly visible in the HPGe spectrum, however only the largest peaks are visible in the NaI spectrum. Small and similar-energy peaks from the NaI detector are either not visible, or superimposed to create one peak. Detectors with a better energy resolution also have a smaller minimum detectable activity (discussed later in Chapter 3) as compared to detectors with a larger energy resolution (for an equivalent number of net photopeak counts).

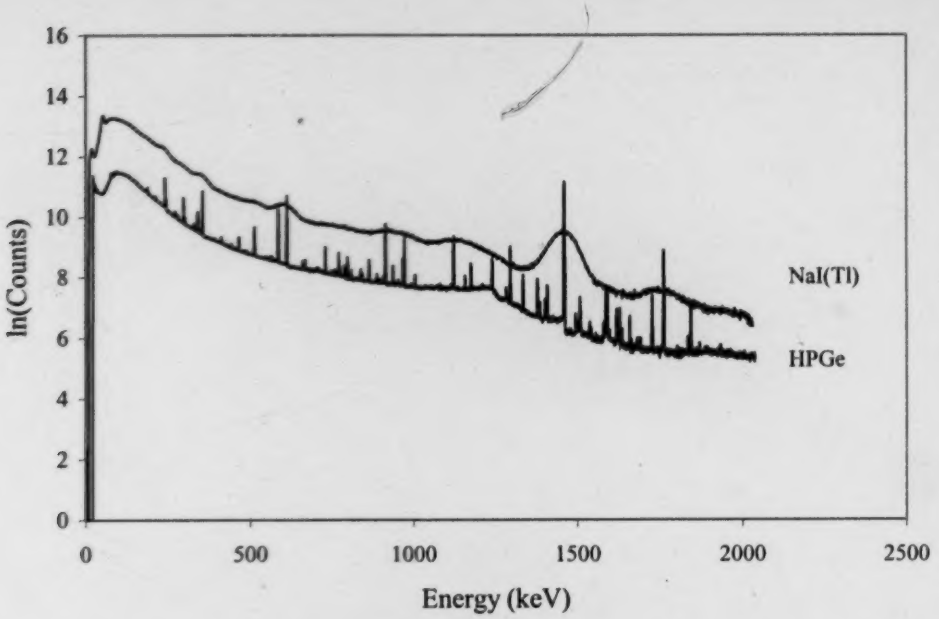

Figure 2-14. Background spectrum acquired from HPGe and NaI detectors (T=250000s).

Photomultipliers

In order to produce measurable electrical signals from light sources as small as a few hundred photons, a photomultiplier tube (PMT) is needed. Photomultipliers were first developed in 1944 by Curan and Baker, and quickly replaced the human eye in counting flashes of light, and brought about the first "modern" scintillation counter. As was seen in the previous section, PMTs are an essential component in scintillation detectors.

There are several components involved in the makeup of an efficient, reliable photomultiplier tube. The conversion of impinging light photons to electrons occurs at the first part of the PMT, the photocathode. The photocathode is made from materials whose efficiencies are tailored to fit the energy of the incoming light photon. Typical photocathodes are made from antimony plus one or more alkali metals, and are 10 – 30% efficient. The electrons generated from the photocathode are then accelerated via an electric potential (typically 100 V) towards a "dynode". Here, the electrons' kinetic energy is used to initiate the emission of even more electrons from the dynode material.

This process is repeated at each dynode stage in the PMT until the electrons are deposited at the anode, creating the final signal. Typical PMTs have 10 to 14 dynode stages which create an electron gain of roughly 10^7. A high-voltage source is needed to create the dynode potentials, and from the photocathode to the anode potentials of roughly 1000 V are needed. A schematic illustrating the components and workings of a typical PMT can be seen below.

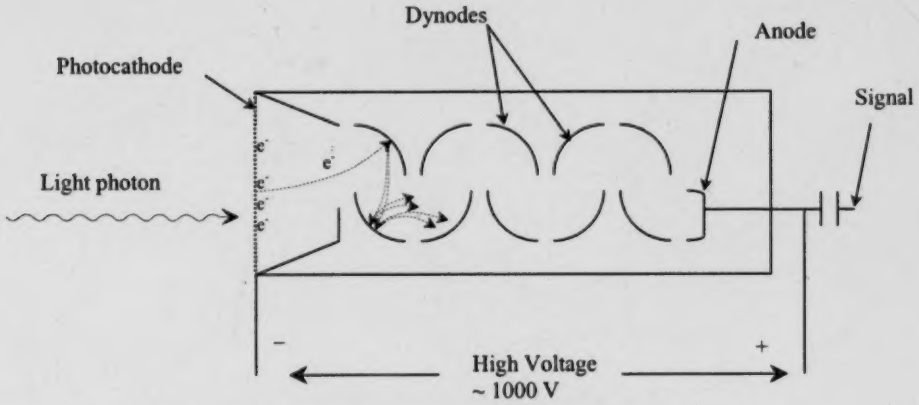

Figure 2-15. Schematic of a typical photomultiplier tube.

Detector Efficiency

The efficiency of a detector is defined as its ability to detect radiation from a given source. Therefore for a source emitting measurable, discrete quanta of energy (photons or particles), detector efficiency is defined as:

$$E = \textit{number detected} / \textit{number emitted} \qquad (2\text{-}6)$$

Efficiency as defined above is the product of geometric efficiency and intrinsic (or quantum) efficiency. Geometric efficiency is simply the number of quanta reaching the detector per number emitted, and intrinsic efficiency is the number of quanta detected per number reaching the detector. Therefore,

$$E = \frac{\textit{number reaching detector}}{\textit{number emitted}} \times \frac{\textit{number detected}}{\textit{number reaching detector}} \qquad (2\text{-}7)$$

Geometric efficiency can be easily calculated from the source-detector geometry, and the intrinsic efficiency can be calculated using:

$$Intrinsic\ efficiency = 1 - e^{-\mu t} \tag{2-8}$$

Here, μ is the linear attenuation coefficient of the detector material, and t is the thickness of the detector through which the quanta passes. This formula is similar to equation 2-4, except in this case we are interested in the proportion of quanta that interact with the material, and not the proportion that escape interaction.

Energy Resolution

The ability of a detector system to distinguish between individual energies in its spectra is expressed in terms of its energy resolution. Energy resolution is defined as:

$$Energy\ resolution = \frac{FWHM}{Peak\ energy} \times 100\% \tag{2-9}$$

In the above equation *FWHM* is the full-width-half-maximum, or simply the peak-width at half of the peak's maximum amplitude. As mentioned previously, germanium and NaI detectors have energy resolutions of roughly 0.15% and 8% (at 662 keV) respectively. The difference in peak-widths is largely attributed to the increase in shot-noise[14] found in the PMTs of NaI detectors. Generally, in order for two peaks to be distinguishable from one another, their peaks must be at least one FWHM away from each other[15].

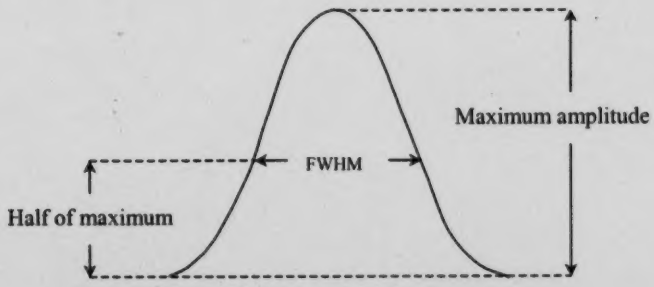

Figure 2-16. The full-width-half-maximum of a spectrum peak.

Electronics

A number of electronic devices are needed to transform raw detector signals into useful information used in whole body counting. This section describes briefly each device used, and although most WBCs are different from one-another, their associated electronics are very similar. A more detailed discussion of these and other devices applied to our whole body counter can be found in Chapter 4.

Preamplifiers are the first electronic devices encountered after the detector, and are used to amplify, impedance match, and condition the raw pulses for the electronics that follow. In order to preserve the signal-to-noise ratio of the raw signal, preamplifiers (or "preamps") are placed as close to the detector as possible so that pick-up and amplification of stray signals can be minimized. The charge-sensitive preamp is the most common for NaI and germanium detectors, and operates by creating a voltage pulse proportional in size to that of the integrated charge of the incoming signal. Preamplifiers may be used to reshape an incoming pulse into another form needed by other electronics. Common shapes include semi-Gaussian-shaped, gated-integrator-shaped in positive unipolar, positive gated integrator or positive leading bipolar forms. For whole body counters, preamps should be considered as part of the detector unit, and should be located inside the shielding to prevent radiation-induced noise.

Once the signal leaves the preamp, if more voltage amplitude is needed, an amplifier will be used. Amplifiers are more commonly used for germanium detectors since their signals are considerably smaller than those from a PMT. Additional pulse-shape modification may be performed here, and counters with multiple detectors may use a summing amplifier to combine the signals as well.

Spectroscopic information is obtained from the detector signals by using a single (SCA) or multi-channel analyzer (MCA). With a single-channel analyzer, chosen minimum and maximum allowable voltage amplitudes are preset, and any detector signal amplitude falling between these two values will be counted. SCAs are calibrated such that a given observed voltage corresponds to a known gamma energy observed by the detector. In this way, SCAs can be used for determining the number of signal counts in a given energy region. Usually the photopeak region of a spectrum is windowed, so that the number of gamma rays detected by the detector can be determined. Multi-channel

analyzers work in much the same way as SCAs, but instead of having one energy window, many are used. Here, the amplitudes of incoming analogue detector signals are digitized using an analogue-to-digital-converter (ADC). This typically divides the minimum and maximum accepted signals into 2 or 4 K, (2 K ADCs are typically used for NaI detectors, and 4 K for germanium detectors) equal-width energy windows or "bins". Each accepted signal will contribute to a count in one of the many bins, and after many signals have been acquired, the variations in signal amplitude will form a spectrum. As with the SCA, once the spectrum has been calibrated properly, information can be extracted giving energy information for various parts of the spectrum. MCAs can be used to analyze multiple, variable energy-width sections of the spectrum simultaneously, which can be used to identify nuclides.

When simultaneous acquisition of multi-detector spectra is necessary as is common in whole body counting, a multi-channel buffer (MCB) is needed. MCBs accept multiple detector inputs simultaneously, and their action is to simply acquire and store data from each detector in a spectral form. This data can then later be dumped to a MCA where the spectrum can be calibrated and analyzed. MCBs can typically accept 8 or 16 detector inputs.

An essential and integral component in modern-day whole body counting is the computer. Computers are interfaced to all components of the WBC, including the MCA, MCB, feedback sensors, and all motor controls. Control of all of these components allows the computer to optimize data acquisition automatically and dynamically. Aside from controlling the WBC, computers are also needed to process and extract important spectral information from the data, allowing for the identification, quantification, and rough spatial location of the radionuclides present.

Detector Stability

Stability of a spectroscopic system under a variety of conditions is crucial so that correct, reliable, and reproducible information can be obtained. Long acquisition times, large changes in activity levels, and high count-rates all affect the spectrum in one way or another. Attention to these effects must be given in order to reduce their effects on the

spectrum. High count-rates are not commonly observed in whole body counting, but the effects are discussed here for the purpose of completeness.

Whole body counting acquisition times can be quite long (of the order of 30 minutes or more), especially for low activities, therefore stability of the location of a spectral peak over time is vital. A measure of the amount a peak moves with time is called *drift*, which can be measured by recording the peak location for a constant activity source over a long period of time such that:

$$\text{DRIFT} = \Sigma_i \left| P_a - P_i \right| / n P_a \qquad (2\text{-}10)$$

where P_i is the *ith* measurement of the peak, n is the number of measurements, and P_a is the average of P_i over all n measurements[15]. There can be many sources of drift, but most common are PMT instabilities, temperature effects, and high-voltage instabilities. Drift affects the detector's energy resolution, and the accuracy of the data obtained from the spectral peaks. For an acceptable detector system, the drift should not be more than 1%.

Large variations in the count-rate of a detector during acquisition can have an effect on the position of the spectral peaks. At high count-rates, detector pulses can overlap with the tails of other earlier detected pulses, increasing their apparent amplitude. This will create a shift in the spectrum. At low count-rates however, this pulse overlap generally does not occur, and no shift is observed. If great enough, this difference in peak location can cause a system to become uncalibrated. It is important when calibrating the system, to use a low-activity phantom. The shift of a system can be measured by comparing a peak's position at high and low count-rates using:

$$\text{SHIFT} = \Sigma_i \left| P_i - P_n \right| / m P_n \qquad (2\text{-}11)$$

where P_n is the last measurement made for drift at a low count-rate (~1000 c/s), P_i is the *ith* measurement made at a high count-rate (~10000 c/s), and m is the number of measurements taken[15]. The shift should not exceed 1% for high-activity counting systems. Long pulse-tails from preamplifiers are the primary source of shift.

When a detector encounters a very high count-rate, a loss of counts can occur due to the time that it takes for a system to process the signal. Depending on the detector and electronics, during this time the detector may either become insensitive and reject all other incoming signals, or all signal amplitudes will be added together during this time and counted as one pulse. Either way, when multiple signals are experienced during this process time, a loss of true signal counts will result. For this reason this process time has been given the name *dead-time*. In the case where signals are added together (or *pile-up*), the resulting signal can be seen in the spectrum as a peak positioned at an integer factor above the original peak. Since the probability of two pulses occurring simultaneously is the greatest, this pile-up peak is the largest in energy and can be seen in figure 2-17.

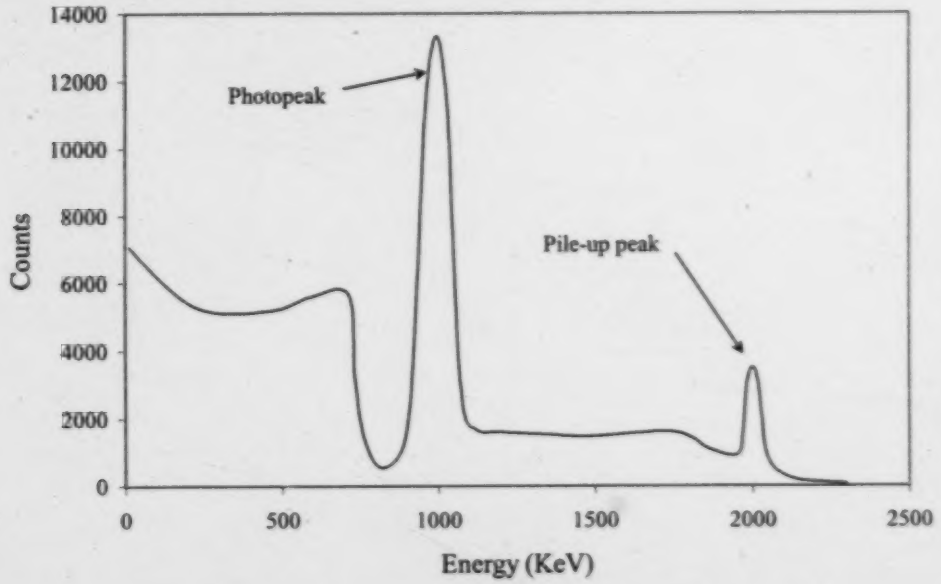

Figure 2-17. Photopeak and the first pile-up peak in a typical NaI spectrum.

If a high count-rate is observed in a detector as a result of two or more photon energies, one or more *coincidence sum peaks* will form in the spectrum. In the case of two photon energies, this peak forms when both photons are completely absorbed in the detector in coincidence with one another. Therefore, instead of contributing towards two

separate photopeaks, one resulting coincident peak will form, with an apparent energy equal to the sum of the two individual photon energies.

The dead-time τ is related to the length of the signal pulse, and if the recorded count-rate m is known, then the fraction of time that the system is dead is simply $m\tau$. The true count-rate n can then be determined to be[10]:

$$n = m / (1 - m\tau) \tag{2-12}$$

The reduced counts experienced from dead-time can seriously affect quantitative measurements made from the spectrum, and corrections must be made to minimize its effects. The most effective way to reduce dead-time however is to reduce the count-rate experienced by the detector.

Shielding

Perhaps the most important component in a whole body counter is its shielding. Shielding reduces the amount of background radiation that reaches the detector, thereby increasing the signal-to-noise-ratio (SNR). This is crucial in whole body counting, since accurate quantification of trace amounts of radiation often needs to be measured, and in a short period of time. There are several options available in the shielding design, the selection of shielding materials, the preparation of materials, and the counter location in order to optimize the effectiveness and to reduce the cost of shielding.

The selection of shielding material is mostly dictated by the type of radiation that needs to be detected. In whole body counting, the vast majority of the α and β radiation present are entirely attenuated by body tissue, making quantification of α and β emitting radionuclides extremely difficult. Gamma radiation however mostly passes through the body, making it the desired radiation to be detected. The high atomic number (Z) of germanium and iodine makes germanium and sodium iodide detectors efficient in detecting gamma radiation, making them useful in whole body counting. Whole body counter shielding therefore should be primarily designed to maximize photon attenuation[16]. Materials used to accomplish this can be divided into two classes: high-Z materials which include lead, iron, mercury, and copper, and low-Z materials including

rock, brick, sand, concrete, chalk, sugar, and water. High and low Z shielding are also referred to as *concentrated* and *bulky* shielding respectively, since much more low-Z material thickness is needed compared to high-Z materials in order to accomplish the same amount of photon attenuation. Bulky materials are relatively inexpensive, and are generally used when large volumes of space need shielding, where the use of concentrated shielding would be too costly.

Being the main component that influences the counter's performance, it is surprising that most shielding requirements of whole body counters are determined empirically. Depending on the counter's needs, more and more shielding is added until the desired background is reached. The typical primary shield thickness for lead is 10 cm[16], for steel is 23 cm[17], and for water is 150 cm[18]. A unique non-empirical method of determining WBC collimator shielding requirements is presented in Chapter 5 of this thesis.

The presence of the primary shielding used to attenuate gamma radiation creates secondary effects that can increase the apparent background count rate. Beta and gamma *build-up* radiation from meson interactions in the primary shield[19] add to the background counts in a counter. Buildup can be reduced by adding more shielding, however for lead shielding thicker than 10 cm, build-up radiation is not greatly reduced[20].

Characteristic x-rays are another radiation source generated from the shielding material. They are generated through photoelectric interactions when the inner shielding material is exposed to photons whose energy is greater than the material's k-shell binding energy. Characteristic x-rays can be substantially attenuated by placing materials of sufficient thickness and decreasing atomic mass inside the primary shield. This additional shielding is known as *graded shielding,* and results in only very low-energy characteristic x-rays being produced. In lead, characteristic x-rays have energies of ~ 72 keV, and are commonly eliminated by using cadmium-copper[21], or copper-polystyrene graded shielding. An illustration of graded shielding can be seen in figure 2-18. Buildup and graded-shielding are further discussed in Chapter 5.

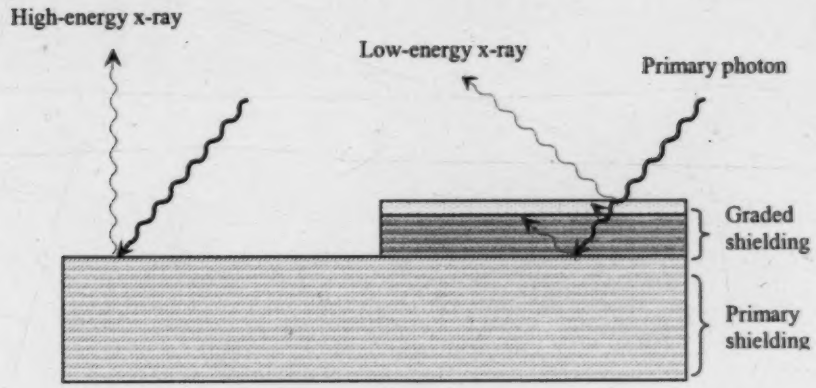

Figure 2-18. Characteristic x-rays from primary and graded shielding.

For low background levels to be obtained, careful attention must be given to the selection and preparation of shielding materials when constructing a WBC. Lead is the most common shielding material among WBCs, however lead can contain significant amounts of radioactivity. Uranium ore is commonly found near lead ore, and unavoidably some finds its way into the processing of lead. Although uranium is removed during the purification of lead, one of the uranium daughter products, Pb-210 remains. This isotope of lead has a half-life of 22 years; therefore lead several decades old is preferred over new lead. It is common in ultra-low background experiments to shield against the radionuclides found in lead by placing a second shield between the lead shielding and the detector[16]. Typically, five centimeters of distilled mercury encased in stainless steel have been used, and is effective in reducing background counts. Steel is a common shielding material that also contains radioactivity. Fall-out from nuclear weapons testing appears in steel produced after 1945, and lately cobalt – 60 which is used by the steel industry has been appearing in steel in increasing amounts as well. It is common practice to use pre-WWII steel obtained from battleships, rifles, etc to avoid radioactive contaminants in steel[16]. Although only two shielding materials have been reviewed here, all shielding materials contain contamination to some degree. Caution should be undertaken to determine a shielding material's activity level through published results[22], and by testing samples of the material during construction.

Techniques can be used to decrease the activity of materials. Although costly, pure copper can be formed from electrolysis which contains little or no contaminants. Radon and thoron gasses adsorbed by shielding materials over time can be mostly removed with nitric acid and distilled water. A simple and effective way to remove surface contamination from fallout in materials is to sandblast them prior to the assembly of the WBC. Sandblasting can reduce a material's activity by roughly ten times[22]. Painting the surface of materials with low-activity paint has also been shown to reduce the amount of surface activity, in particular beta radiation.

WBC shielding can be placed between the detector and the surroundings in one of two different ways. The most common method is by entirely surrounding a room with shielding. Because the rooms must be large enough to contain the subject, detectors, and the experimental equipment, a great deal of shielding material is necessary. In order to reduce costs therefore, bulky shields are often used. Room-shielded WBCs have the advantage that the entire inside of the room is shielded from background, therefore there are no restrictions on the detector arrangement or experimental design, which can lead to innovative WBC designs. Because of the large low-activity space however much effort must be given to ensure that room-shielded counters remain radioactive free. An alternative to shielding the entire room is to surround the detector with shielding in such a way that only the line-of-sight, or direct background radiation is shielded against. This shielding technique is called *shadow-shielding*, and if used properly, can substantially reduce the amount of shielding material that is needed. Unfortunately, the line-of-sight condition of shadow-shielding severely restricts the flexibility of counter designs. As a result, most shadow-shielded WBCs are constructed using concentrated shielding so that shield thickness does not further hamper the WBC design. Both room-shielded and shadow-shielded shielding arrangements are illustrated in figure 2-19.

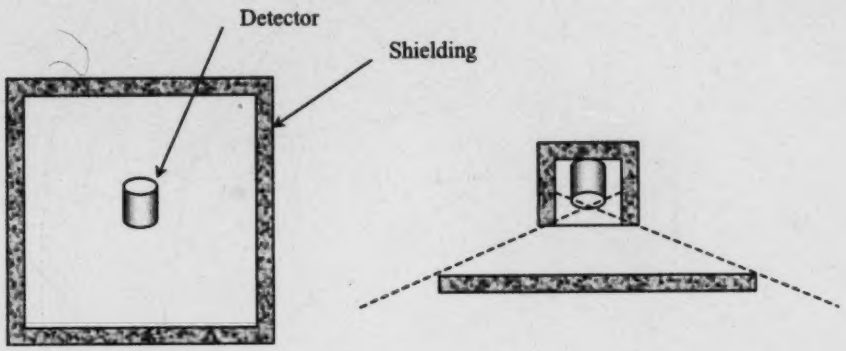

Figure 2-19. Cross-section illustration of room-shielded and shadow-shielded counter arrangements.

Attention to shield-detector angles is needed to reduce scattered radiation from being detected. In WBCs, radiation, in particular primary background radiation can scatter off of shielding towards the detector. The open-geometry of shadow-shielded WBC's makes them more subject to scattering affects, however proper shielding design can be used to minimize these affects. Photon scattering is angle-dependent, and photons of high-energy are largely forward scattered from material surfaces via Compton and Rayleigh scattering. Therefore, by shielding such that the primary radiation must scatter off of the shielding at large incident angles, or multiple times in order to reach the detector, background counts from scatter can be reduced. From the Klein-Nishina formula, an incident angle of 45 degrees or more is extremely effective in reducing scatter from photons of all energies.

The building in which a WBC sits, or ones near by are an excellent source of shielding which can be taken advantage of. Charged cosmic radiation in the Northern Hemisphere comes into the earth's atmosphere mostly from the southwest. This, combined with the fact that WBCs are usually built at ground level in or near large buildings, makes it possible to use these buildings as shadow-shields against cosmic radiation. The act of placing a WBC northeast of a building has been shown to decrease high-energy counts by roughly 30% [18]. Figure 2-20 shows this cosmic ray 'shadow' affect.

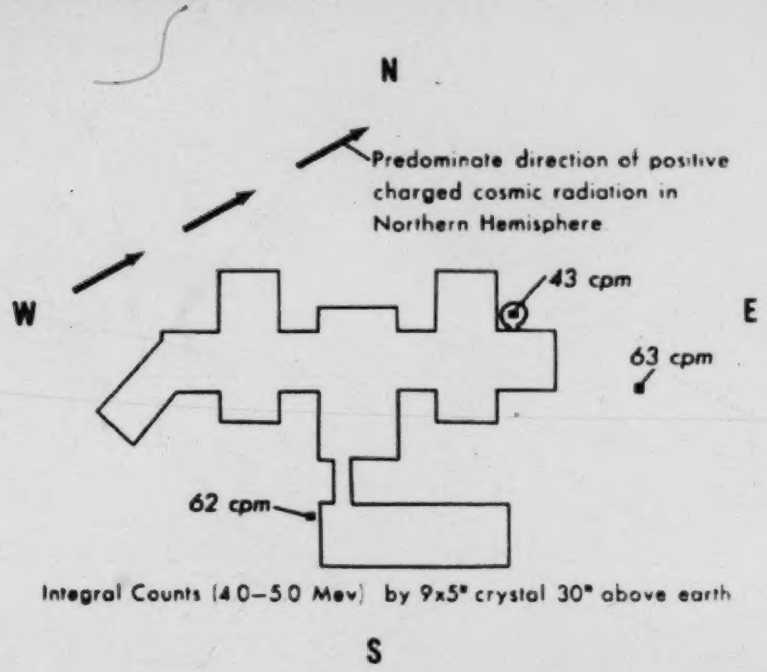

Figure 2-20. A large building used to create the cosmic ray 'shadow' affect[18].

A careful assessment of the detectors and the counter's goals must be made so that proper, financially feasible shielding can be chosen. Pre - WWII steels, old lead, and electrolytic copper are all very low in activity, but also very expensive. Depending on the counter's uses, the reduced background obtained by using these materials may not be needed. As well, if ultra low-activity detectors are not present in the detector, the benefits of using such costly materials may be too small to be cost-effective. With all WBCs a balance between cost and performance must be made so that construction of a WBC is financially feasible.

References

[1] H. Baba, T. Sekine. An Analytical Representation of the Response of the NaI(Tl) Detector for the Gamma-Ray Spectrum Analysis. *Journal of Radioanalytical Chemistry* **29**:109-119;1976.

[2] J.J. Steyn. Empirical Photofractions for NaI(Tl) Scintillation Crystals. *Nuclear Instruments and Methods* **68**:118-124;1969.

[3] Triumf Safety Group, http://www.triumf.ca/safety/rpt/rpt_4/node6.html

[4] Supernova 1987A, Image Credit: David Malin, Anglo-Australian Observatory

[5] National Geophysical Data Center - Solar and Upperatmospheric Services, http://www.ngdc.noaa.gov/stp/SOLAR/COSMIC_RAYS/cosmic.html

[6] Nasa slide show- *Components of Showers*, various teams (1954-1964). http://radhome.gsfc.nasa.gov/radhome/papers/slideshow7/sld010.htm

[7] J.A.B., J.A. Bearden, *Rev. Sci. Instrum.* **4**:271;1933.

[8] G.G. Manov, *Metrology of Radionuclides*, I.A.E.C. Conference, Vienna; 1959

[9] J. Shapiro. Radiation protection – a guide for scientists and physicists. 2nd edition:55-56;1981.

[10] G.F. Knoll. Radiation detection and measurement. *Second edition, John Wiley & Sons, Copyright 1989*

[11] S.M. Shafroth, Scintillation Spectroscopy of Gamma Radiation. pp 15-32 *Volume 1, Gordon and Breach Science Publishers, Copyright 1967*

[12] G.H. Kramer *et al*. Results of the 1993 Intercomparison/Intercalibration: Final Report. *The Canadian National Calibration Reference Center for In-Vivo Monitoring and the United States Department of Energy*. HMLTD-95-3.

[13] G. Tarroni *et al*, An intercomparison among the whole body counter centers operating in Italy. *Physica Medica* **11**(3):103-110;1995.

[14] M. Sayer, A. Mansingh. Measurement, Instrumentation and Experiment Design in Physics and Engineering. *Prentice-Hall of India, Copyright 2000*

[15] W.R. Leo. Techniques for Nuclear and Particle Physics Experiments – A How-to Approach. *Second revised edition, Springer-Verlag Press,* Copyright 1994.

[16] D.E. Watt, D. Ramsden. High sensitivity counting techniques, *Pergamon Press,* Copyright 1964.

[17] G.J. Hine *et al*, Geometrical and attentuation corrections for a two crystal whole body counter; Body scanning with an 8 by 4 in. NaI Crytal; *Radioactivity in man, 2nd symposium*, Charles C Thomas, Copyright 1965

[18] R.E. Peterson *et al*. Evaluation of a water shield whole body counter. *Radioactivity in Man, Second Symposium* (Whole body counting and effects of internal gamma ray-emitting radioisotopes). *Charles C Thomas Publisher*. Copyright 1965.

[19] J.E. Hooper, M. Scharff. The Cosmic Radiation., *Butler and Tanner Pub.*, Copyright 1958.

[20] P.P.Auger *et al.* Analyse Du Rayonnement Cosmique A L'Altitude De 3 500 Metres (Laboratoire International Du Jugfraujoch). *Journal De Physique* **2**:58-64;1935.

[21] R.L. Heath, *Scintillation Spectrometry Gamma-Ray Spectrum Catalogue,* IDO-16880, Vols. 1-2, 1964.

[22] J.R.DeVoe. Radioactive Contamination of Materials Used in Scientific Research. *National Academy of Sciences- NRC.* Pub 895, Nuclear Science Series, Report # 34, 1961

Chapter 3

Methods in Whole Body Counting

3.1 Configurations

As discussed previously, whole body counters have many diverse uses. For each use, many things must be considered and optimized. The number and position of the detectors, the shielding material, and subject-detector orientation are only a few. It is not surprising therefore that the array of different WBC designs is just as wide-varying as their potential uses. Here, only the most common whole body counter designs are presented and discussed; atypical WBCs stem from these more common ones.

Fixed versus Scanning Whole Body Counters

Whole body counters are categorized as either fixed (static) or scanning detector types. In a fixed WBC, the detector-subject orientation remains constant over time. Figure 3-1 illustrates a fixed detector setup.

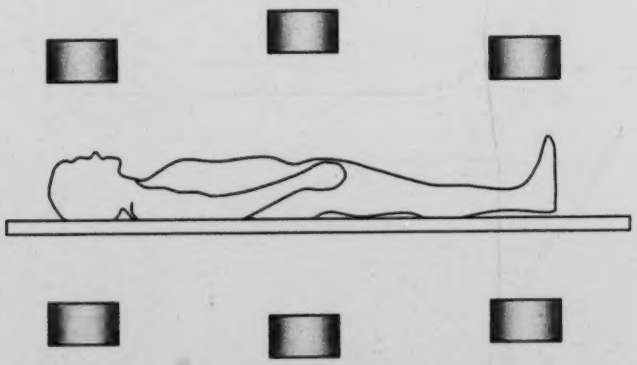

Figure 3-1. Typical fixed-detector whole body counter orientation.

These types of WBCs are mechanically very simple, however can provide at best very coarse spatial information on radionuclide distributions. With opposing detector sets,

top/bottom ratios can provide an indication of surface contamination. Much care must be taken when orientating the detectors such that they provide flat iso-response curves (good geometric response); which is especially difficult to achieve along the length of the subject.

With scanning counters, one or more detectors are slowly scanned along the length of the subject. This can be achieved by moving the detectors and keeping the subject stationary, or vice versa. Figure 3-2 illustrates this idea.

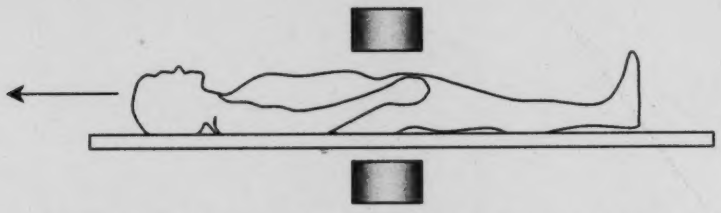

Figure 3-2. Typical scanning-detector whole body counter orientation.

Whole body counters of this type are typically much more mechanically complex than their fixed counterparts, however, they are capable of providing good spatial information on radioactive distributions in the body. In addition, because the detectors pass over the entire length of the subject, length-wise geometric responses are very good. Scanning WBCs often have detectors positioned above and below the subject (as in figure 3-2) so that activity located anywhere between the detectors (either anterior or posterior in the subject) will give a fairly constant total detector response. The detectors in scanning WBCs detect radiation from a smaller portion of the body for a given time than fixed WBCs do. Therefore, shadow-shielding is much better suited to these small field-of-view (FOV) counters. Because of the above advantages, plus comparable counting times (~ 30 min), scanning WBCc have been considered to be better than fixed WBCs[1,2], in spite of being more complex to design and construct.

Chair

One of the most common whole body counter designs is the chair-WBC seen in figure 3-3. The subject is positioned in a tilted, stationary chair usually in front of a single large detector. These WBCs can be room or shadow-shielded, and are fairly

inexpensive to construct; the disadvantage of these counters is that they do not have a very flat geometric response, and this can lead to inaccurate results.

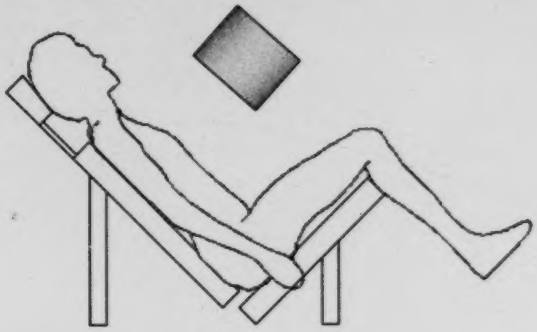

Figure 3-3. Chair-type whole body counter configuration

Large-Volume

Large-volume whole body counters make use of detectors placed around the entire subject, such that almost a 4π FOV is accomplished. Liquid or plastic scintillators are used in these counters (see figure 3-4). As can be expected, these counters are very expensive, and are electronically complex. Liquid or plastic scintillants have poor energy resolution and produce high background counts. Large-volume WBCs do give good geometric responses, however, and are very sensitive counters. These whole body counters must be room-shielded.

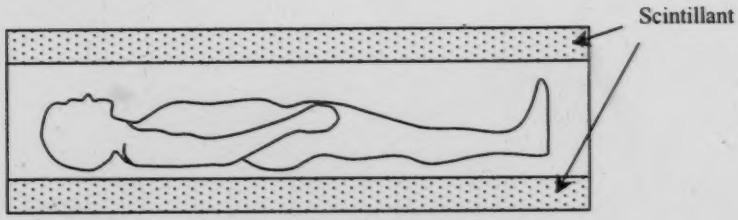

Figure 3-4. Large-volume whole body counter configuration

Arc

Another low-cost whole body counter is the arc-counter. Here, the subject lays stationary on a curved bed, such that the distance from all parts of the subject to the

detector is roughly equal (approximately 1 m, see figure 3-5). Because of the distance required to accommodate this, arc counters have a good geometric response, but are not very sensitive and usually require long counting times. Arc counters can be shadow or room shielded.

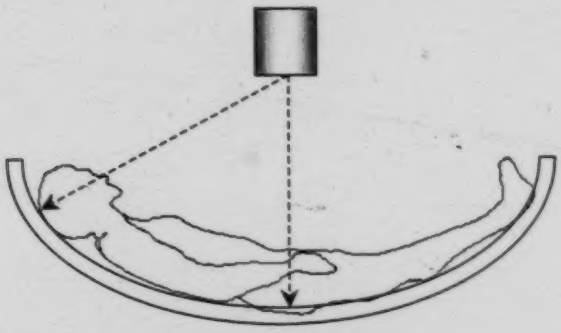

Figure 3-5. Arc whole body counter configuration

Multi-Detector

Multi-detector whole body counters make use of two or more detectors placed around the subject. When several detectors are used, they are placed in a static configuration around the subject as in figure 3-1. If the detectors are positioned properly, these WBCs have a good geometric response and are quite sensitive. When several detectors are used, multi-detector whole body counters require room shielding and tend to be quite costly. Multi-detector WBCs that make use of fewer detectors can be scanning WBCs, and can make use of shadow shielding. A typical scanning whole body counter can be seen in figure 3-2. The merits of both scanning and fixed WBCs were discussed in the previous section.

An excellent paper comparing the performance of existing counters (incorporating all of the types discussed in this section) has been published, and is highly recommended for more detailed discussion on their intercomparisons[27].

3.2 Calibration

Whole body counter calibration is the single-most important factor in acquiring accurate, relevant data for radionuclide quantification. The raw data from a counter is not

very useful on its own, and cannot be used for quantification unless the WBC is first calibrated to a standard, where phantom and detector geometry is carefully matched. Detector-subject-shielding orientation, detector type, the nuclide of interest, subject size, and subject activity will all affect the raw counts, and the calibration of a WBC. For each subject size, subject-detector orientation, and nuclide of interest, a separate calibration factor must be determined for a particular WBC. This factor, once incorporated into the raw data, can deliver very accurate quantitative information on the radionuclide activities in the subject[3]. The different methods of whole body counter calibration are briefly outlined below.

Phantom Calibration Method

By far the most common method of calibrating whole body counters is to use anthropomorphic models[4,5] or "phantoms" to determine calibration factors. Phantoms are constructed to simulate human shape, size, mass, gamma and beta attenuation/scatter, and occasionally organ size and location. Their dimensions are determined from data taken from a specific population, therefore calibration factors generated from phantoms are population specific.

F. Bush developed the first anthropomorphic phantom in 1949[6], and since that time many different phantoms have been developed. The "Bush" phantom consists of ten circular and elliptical cylinders (see fig 3-6a) which are used to emulate the human body. Other phantom designs include store-bought mannequins filled with gel packs[7], gel pads in plastic forms[8], one liter water bottles placed together to emulate a Bush phantom[9] (see fig 3-6b), and even phantoms made of hamburger[10]. The majority of phantoms use water, wax, lucite / plastic, gel, or Spiers' mixture (60% rice powder, 40% Na_2CO_3) as a body tissue equivalent. Although several phantoms have been made throughout the years, the standard for whole body counting are the Bush, the water filled BOMAB[11] (Bottle Mannequin Absorber), and Reference Man[12] phantoms. Unlike the Bush and BOMAB phantoms, the Reference Man phantom contains a skeleton and internal organs as well, and therefore is not homogeneous. These phantoms are quite costly to purchase, and therefore purpose-built, inexpensive phantoms are often constructed by individual facilities.

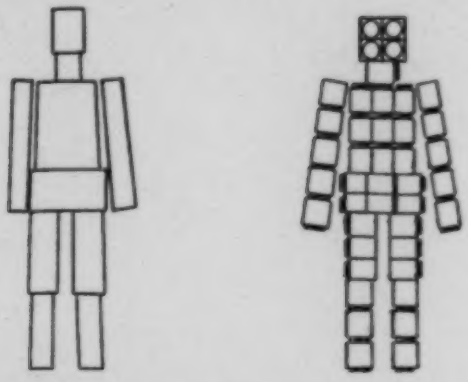

(a) (b)

Figure 3-6. Bush phantom (a) and a bottle-type Bush emulating phantom (b).

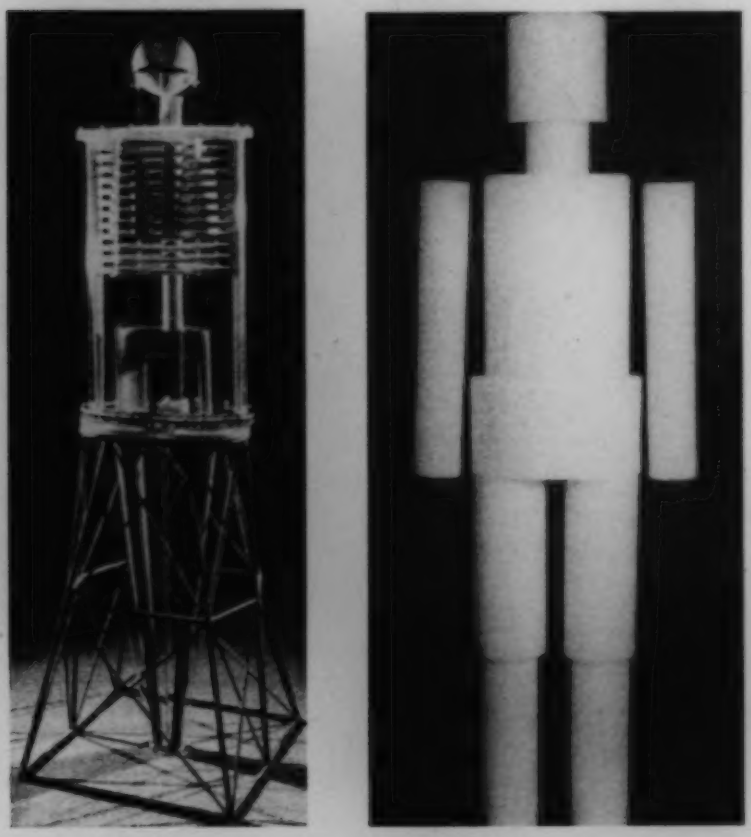

(a) (b)

Figure 3-7. Reference Man phantom (a) and BOMAB phantom (b).

In order to calibrate a whole body counter using a phantom, part or all of the phantom needs to be filled with a known type and amount of radionuclide. The relative distribution in the phantom should resemble the distribution of the real-life subject (whose radionuclide quantity is in question) as closely as possible. The phantom is then placed into the WBC, and a mock, phantom whole body count is obtained. This is repeated using a range of phantom sizes. The number of phantoms and their size will depend on the range of subject sizes that the WBC needs to be calibrated for. The detector-phantom arrangement during the acquisition should be identical to that of the desired detector-subject geometry, and with a time such that there is little error in the acquired counts (see section 3.3). Once all the phantom data is acquired for each phantom size, the net photopeak counts per second per amount of radionuclide in each phantom can be determined. This number is the "calibration factor" for that phantom. All of the calibration factors are then plotted versus their appropriate phantom dimensions (typically weight and height) and/or photon energy, and a calibration curve is obtained. Recent unpublished work at the Human Monitoring Laboratory (Bureau of Radiation and Medical Devices, Health Canada, Ottawa) has developed a function that fits counting efficiency to photon energy and Body Mass Index. Once obtained, the calibration curve is then used to determine the calibration factor, and thus the quantity of a given isotope based upon the subject's physical dimensions and their net counts obtained during a whole body scan. For homogeneously distributed radionuclides such as K-40, the calibration curve for a WBC is commonly linearly dependent on $\sqrt{weight / height}$ [13].

Same - Element Calibration Method

The same-element method uses a technique that does not require the use of phantom data to obtain real-subject calibration factors. With this method, a subject is first scanned in a whole body counter, and counts from the radioisotope of interest are recorded. After the first scan, the subject is then injected with a different radioactive isotope of the same element. The injected isotope's half-life must be long enough so that it can perfuse throughout the entire body, but short enough so that it is eliminated soon thereafter to reduce subject dose. As well, the isotope must have a gamma emission energy very close to that of the original radionuclide, so that their attenuation and

detection characteristics are virtually identical. Because the two radionuclides are isotopes of the same element, they are identical chemically and will travel to the exact same areas in the body. Once the injected isotope has sufficiently perfused throughout the body, the subject is placed into a whole body counter and scanned. By measuring the counts from the injected subject, and by knowing the amount injected, a calibration factor can be obtained. This calibration factor can then be used to quantify the amount of the original radionuclide of interest in the body. As an example of this, orally administered K-42 is typically used to obtain calibration factors for K-40 studies.

This method generates very accurate results[14] that are better than the phantom calibration method. Because the subject is literally used as their own calibration phantom, aside from positioning in the WBC, there are very few errors in the process. Larger calibration errors are inherent with the phantom calibration method since real-life subject calibration factors are derived by interpolating phantom data.

Once a large variety of subjects have been scanned in the WBC using the same-element method, a nuclide specific calibration curve can be generated in the same way as with phantoms (see previous section). The downside to the same-element method is that the whole-body studies take longer to perform, and the subject receives a small radiation dose. Also, this method is very limited to only a few isotopes.

Cadaver Calibration Method

Another method of creating calibration curves for quantification is to use cadavers. Radionuclides can be placed inside of cadavers to simulate the distribution found in living subjects. Because the cadaver's anatomy, gamma attenuation, and other properties are identical to living subjects, calibration curves can be generated in much the same way as in the phantom calibration method. Cadaver calibration methods are generally used when radioactive uptake in an organ[15] or a specific tissue needs quantification.

Although very useful, both the same-element and the cadaver method are not commonly used today. Because of the ethical issues surrounding these two methods, they are no longer considered acceptable.

Computer Methods of Calibration

Recently, thanks to the speed and memory of today's computers, virtual phantoms have been used to calibrate whole body counters[16]. This method models the entire WBC and simulates its response using a virtual phantom. As with the phantom calibration method, the response from different phantom sizes is used to create a calibration curve for a given radionuclide and distribution. The advantage of computer calibration is that there are no phantom costs, and an endless variety of phantoms can be created containing any type of radioactive distribution. Up to this point in time, only Monte Carlo simulations have been used to computer calibrate WBCs, however a modeling method described later in this thesis can also be used.

3.3 Data Analysis

Whole body counters typically have extremely small signal to noise ratios, and therefore are particularly sensitive to any error contributions. There are several methods used in nuclear spectroscopy that aid in photopeak quantification, radionuclide identification and localization, and determination of the limits of radionuclide detection. These techniques are used in whole body counting so that all possible information can be gathered, interpreted, and processed in such a way that a minimum amount of error is added to the signal.

Photopeak quantification

The statistics that govern radioactive decay and hence photopeak detection follow the Binomial probability distribution, therefore the detection curve follows a gaussian distribution. In the ideal case where there are a large number of counts defining the photopeak and its curve is well defined, the net counts can be obtained by recognizing that the peak is superimposed on a background spectrum (Chapter 2). In figure 3-8a the photopeak is lying on a flat background (B), and the photopeak counts (S) can be calculated by simply counting only the counts that contribute to the gaussian curve. Figure 3-8b shows a photopeak on a sloped background and the net counts are obtained in a similar manner.

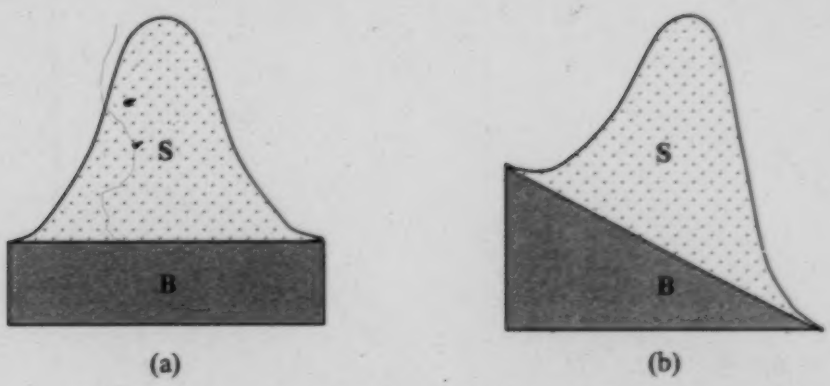

Figure 3-8. Photopeak on a flat background (a) and on a sloped background (b).

Unfortunately in whole body counting, there are often not enough counts in a photopeak to create a well-defined Gaussian curve. The photopeak curve appears "noisy", and its bounds are not well defined. Quantification of net photopeak counts, even in a simple background can be difficult.

To aid in determining the bounds of a photopeak, data smoothing is employed. This method convolves the original spectral data with a kernal to create a smoother, less random-looking photopeak curve. Each new smoothed point in the spectrum is calculated by the kernal, which assigns a weighting factor to neighboring spectral data points from the original data. The kernal is of the form:

$$S_i = (O_{i-2} + 4O_{i-1} + 6O_i + 4O_{i+1} + O_{i+2})/16 \qquad (3\text{-}1)$$

Where S_i is the smoothed data in channel i, and O_i is the original data in channel i.

Filtering in the frequency domain can also be used to smooth noisy data. The raw spectrum is comprised of high and low frequencies, all of which can be extracted using the discrete Fourier (DFT), or discrete cosine (DCT) transforms. The equations defining the DFT and inverse DFT are shown in equations 3-1a and 3-1b respectively.

$$F(u) = \frac{1}{N}\sum_{x=0}^{N-1} f(x)\exp[-j2\pi ux/N] \qquad (3\text{-}1a)$$

$$f(x) = \sum_{u=0}^{N-1} F(u) \exp[j2\pi ux / N] \tag{3-1b}$$

where x has discrete values 0,1,2,.....N-1 in the spatial domain, and u has values of 0,1,2,.....N-1 in the frequency domain. $f(x)$ are the sample values of the continuous function f. Formulas for the DCT and inverse DCT are shown below

$$C(u) = \alpha(u) \sum_{x=0}^{N-1} f(x) \cos\left[\frac{(2x+1)u\pi}{2N}\right] \tag{3-1c}$$

$$f(x) = \sum_{u=0}^{N-1} \alpha(u) C(u) \cos\left[\frac{(2x+1)u\pi}{2N}\right] \tag{3-1d}$$

where $\alpha(u) = \sqrt{1/N}$ for $u = 0$, and $\sqrt{2/N}$ for $u = 1,2,.....N-1$.

Once all the frequencies have been extracted, then in the frequency domain, select frequencies can be filtered out. The noisy component of the spectrum is primarily made up of high frequencies, and if filtered out, the data can be smoothed considerably as is seen in figures 3-9a, and 3-9b.

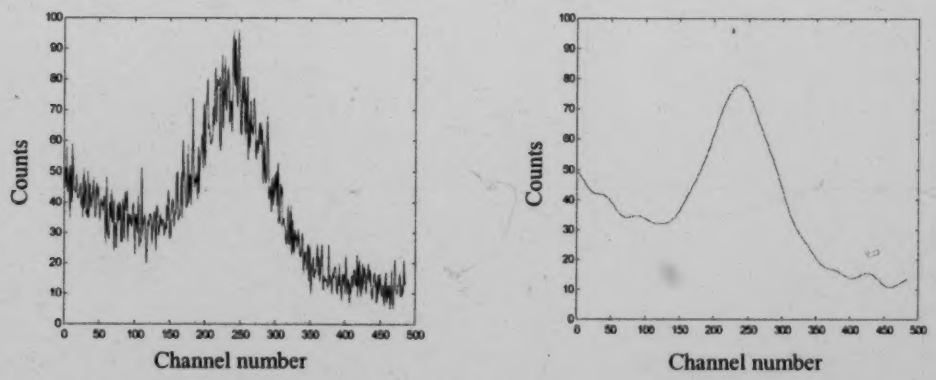

(a) (b)

Figure 3-9. Photopeak before smoothing (a) and after smoothing using DCT (b).

There are advantages and disadvantages to this method. A smoothed spectrum can be analyzed readily, however, there will be some loss of information as the original data has been replaced by an approximation.

Another method of peak quantification is to fit a Gaussian curve to the photopeak. The photopeak is known to follow a Gaussian curve, therefore once fit, its net area can be easily calculated. This method is particularly useful when two or more photopeaks are superimposed in a spectrum. These peaks can all be fitted with Guassian curves, and then be quantified. Most commercially available software such as Ortec's *GAMMA-VISION*, or *SCINTI-VISION* can perform this task. An example of a spectrum consisting of three Gaussian peaks and their individually fit curves is shown below. This kind of software can also fit the background to some polynomial instead of using a linear fit (as seen in figure 3-8), so that a more accurate background can be defined.

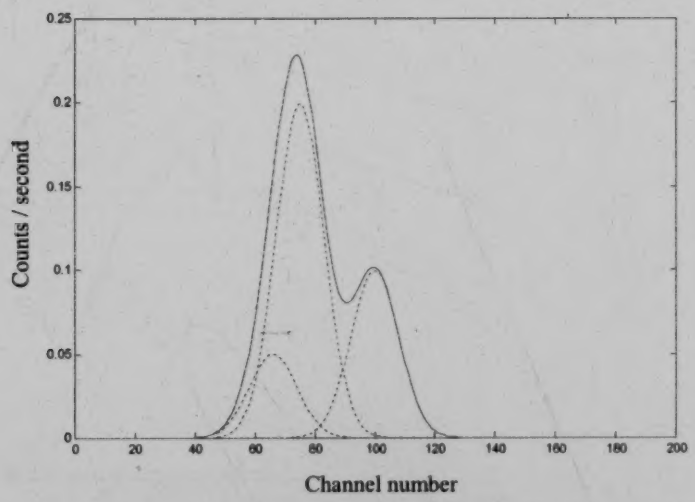

Figure 3-10. The superimposed and fitted Gaussian curves in a spectrum.

As discussed, photopeak quantification involves the subtraction of the background present in a spectrum, which is made up of signal (S) plus background (B). This introduces errors. In general for a binomial distribution, the error for total acquired counts N is $\pm\sqrt{N}$. In a spectrum, the counts appearing in an energy window E to $E+\Delta E$ is also binary, therefore the error in the counts is also $\pm\sqrt{N}$ where N is the counts in the

window E to $E+\Delta E$. When the background is subtracted from the spectrum as in figures 3-8a and 3-8b, through simple error propagation, the error in the signal is:

$$\delta\{S\} = \delta\{(S+B)-B\} = \pm((S+B)+B)^{1/2} \tag{3-2}$$

As discussed, common practice in whole body counting is to subtract the background counts from an energy region after the source-plus-background counts have been acquired. To obtain the proper background counts, a phantom must be scanned in the counter. The phantom used should have similar dimensions to that of the subject, and therefore will attenuate and scatter background radiation in the same way that the subject does[17]. Accurate background spectral information is obtained by continually acquiring background counts from the counter (when not used for subject scanning). Although not commonly done, background counts can also be taken by scanning the phantom just before or after the subject scan ensures that the effects of slight background spectrum variations are minimized. Once acquired, the background spectrum can be used to calculate the background counts in any energy window. This background count can then be subtracted from the signal-plus-background counts from the same energy window, leaving only the desired signal counts. The subject can be used in place of a phantom to do background subtraction, however because the background scan times are very long and the subject must be radionuclide-free, this is seldom done.

Radionuclide identification

Often in whole body counting, identification as well as quantification of radionuclides is needed. Subjects contaminated with one or more unknown radionuclides must have these radionuclides identified before dose assessment, and thus risk to the subject can be determined.

A common method of identifying radionuclides in a mixture is by using the 'stripping method'[18]. This method makes use of an isotope library, where all radioisotopes of interest along with their photopeak energies and spectra are recorded. The first step in the stripping method is to strip (subtract) away the background from the multinuclide spectrum. Then, the highest-energy photopeak is used in conjunction with

lower-energy peaks to identify one of the isotopes present. The net counts from the high-energy peak is then calculated, and used to quantify the isotope. It is also used to determine the proportion of the isotope's library spectrum that needs to be stripped from the multinuclide spectrum. Once stripped, the identified isotope's complete spectrum is removed, with the remaining spectrum now containing one less isotope. This method is repeated until all isotopes have been identified and quantified. The stripping method is very useful, but problems can occur if there are several photopeaks from multiple radionuclides present at the same time. Sum-peaks, formed when two different gamma energies are coincident in the detector, and pile-up peaks (Chapter 2) can become superimposed on the highest-energy photopeak used for stripping. This causes improper stripping and nuclide quantification. Methods like the matrix method[19] can be used in place of the stripping method to overcome this problem. This currently most common method uses least-squares fitting and a calibration matrix to resolve the components of a complex spectrum.

Photopeak searching / imaging

Automated photopeak searching and whole body counter imaging are both large topics on their own, and are only briefly mentioned here for the sake of completion.

There can be circumstances where several unknown photopeaks exist in a spectrum. As discussed, these peaks often need to be identified as being 'true' peaks and their individual energies determined. This task can be done by hand, however the results may be subjective, and if vast number if spectra need to be analyzed, this can become painstaking.

To avoid the downside of analyzing spectra manually, automated photopeak searching algorithms have been developed. Today, Ge spectroscopy, coupled with commercial software provides a straightforward analysis. Similar software for NaI detectors also performs well when library-driven searches are implemented. The most common method of detecting photopeaks is to calculate the second derivative of a spectrum on a channel-per-channel basis. Where suspected peaks are present, the second derivative will become negative. When the expected peak width and sensitivity criterion are included in the algorithm, accurate reproducible results can be obtained. Smooth

spectral data is essential when using this approach to avoid false positives. Other accurate methods have also been developed, some which do not require data smoothing. One such method uses a quantum mechanical model[20] to obtain probabilities for the photopeak location in a spectrum.

Although not the primary focus in whole body counting, 'images' from counters can be generated which give quantitative regional information. As with all nuclear images, the image contrast and resolution is dependent on the amount of counts acquired by the detector, and the detector / collimator size and geometry. Whole body counters generally do not collect a large number of counts, and the detectors are very large, with little or no collimation. This gives rise to very poor images, nonetheless, several whole body counters have been developed that do provide a sort of subject 'image'. The most common method of obtaining images is to use a scanning counter with a collimator positioned such that axial information can be collected. This information can then be processed to yield a longitudinal image[21]. For very high-activities and very tight collimation, a resolution of 1cm has been achieved using this method[22], and very good results can be achieved using an iterative method with little collimation[23]. Whole body counters that do give some regional information are of great use where limited FOVs are needed[24]; especially useful in retention / uptake studies[25].

Minimum Detectable Activity (MDA)

Lloyd A. Currie set the standard for determining the minimum detectable activity achievable by a detector system in 1968[26]. Prior to this time, many rules of thumb were employed, but very few had any real statistical validity. Using detection limits based on false-positives, true-negatives, and the Poisson distribution, Currie defined the minimum detectable activity (MDA) as:

$$MDA = \frac{\left\{2.71 + 4.65\sqrt{background}\right\}}{\varepsilon t} \qquad (3\text{-}3)$$

where *background* is the background counts obtained over an acquisition time t of the system, which has an absolute efficiency of ϵ. For a detector in a well-known

background, which is often the case in whole body counting, the limit for satisfactory quantitative determination is:

$$MDA_q = \frac{50\left\{1 + \left[1 + background / 25\right]^{1/2}\right\}}{\varepsilon t} \qquad (3\text{-}4)$$

The relationship between MDA_q and MDA is a complex one, and not easily derived. The reader's attention is directed to L. A. Currie's work[26].

The MDA is the gold standard for measuring a whole body counter's ability to detect and quantify minute amounts of radiation. It is very dependent on gamma energy, and is always quoted at a particular energy. MDA values for whole body counters range between 22 and 300 (averaging 91) bequerels for Cs-137 at 662 KeV. This value is for a 4 year old child phantom, scanned for approximately half an hour[27].

References

[1] G.H. Kramer. The Canadian whole body counting intercomparison program: a summary report for 1989 - 1993. *Health Physics*. **69**(4):560-565;1995.

[2] R.A. Dudley, A. Ben Haim. Comparison of techniques for whole body counting of γ-ray emitting nuclides with NaI(Tl) detectors. I: Point sources in phantoms. II: Distributed sources in phantoms and humans. *Phys. Med. Biol.* **13**(2):181-193;1968.

[3] R. Novario, L. Conte. A new method for calculating the distribution of radioactivity in man measured with a whole-body counter. *Health Physics*. **58**(5):597-607;1990.

[4] D.K. Bewley. Anthropological models for checking the calibration of whole-body counters and activation analysis systems. *Phys. Med. Biol.* **33**(7):805-813;1988.

[5] J.D. Fenwick *et al.* Intercomparison of whole body counters using a multinuclide calibration phantom. *Phys. Med. Biol.* **36**(2):191-198;1991.

[6] F. Bush. The internal dose received from a uniformly distributed radioactive isotope. *British Journal of Radiology*. **22**:96;1949.

[7] F. Steinhauseler *et al.* Low cost - and sex - specific calibration phantom for in-vivo measurements. *Health Physics*. **61**(6):916-917;1991.

[8] M.L. Maiello *et al.* An inexpensive and multipurpose calibration phantom for in-vivo measurements of internal contaminants. *Health Physics*. **51**(6):809-811;1986.

[9] N.K. Grupta *et al.* Utility of bottle phantom in calibration of whole - body counting systems. *J. of Nuclear Biology and Medicine*. **20**(3):132-134;1976.

[10] K.J. Ellis, R.J. Shypailo. Whole body potassium measurements independent of body size. *Basic Life Sciences*. **60**:371-375;1993.

[11] L.Burns *et al.* Construction and characterization of the elliptical (BOMAB) phantoms. *Human Monitoring Laboratory Technical Document.* HMLTD-90-1;1998

[12] W Snyder *et al.* Estimates of absorbed fractions for monoenergetic photon sources uniformly distributed in various organs of a heterogeneous phantom. *MIRD Pamphlet No. 5. Journal of Nuclear Medicine,* supplement 3;1969.

[13] T. Smith *et al.* Total body potassium calibrations for naormal and obese subjects in two types of whole body counter. *Phys. Med. Biol.* **24**(1):171-175;1979.

[14] L. Burkinshaw. Measurement of body potassium. Calibration and intercomparison of two whole body counters. *Phys. Med. Biol.* **12**(4):477-488;1967.

[15] N. Cohen *et al.* Body burden estimation of P-32 by measurement and calibration of bremsstrahlung radiation produced in the skull. *Health Physics*. **44**(6):668-671;1983.

[16] S. Kinase. Evaluation of response of whole-body counter using the EGS4 code. *J. Nuc. Sci. Tech.* **35**(12):958-962;1998.

[17] J.J. Estrada, G.R. Laurer. A method to obtain subject background for low-level in-vivo measurements of the head. *Health Physics*. **65**(3):306-312;1993.

[18] S.C. Choy, R.A. Schmitt. Gamma-ray spectra analyzed by computer program using the peak area method. *Nature*. **205**:758-760;1965.

[19] J.A. Blackburn. Computer program for multicomponent spectrum analysis using least-squares method. *Analytical Chemistry*. **37**(8):1000-1003;1965.

[20] Z.K. Silagadze. A new algorithm for automatic photopeak searches. *Nuclear Inst. Meth. Phys. Res.* A376:451-454;1996.

[21] S.Molloi *et al.* Whole body and regional retention of Tc-99m-labeled diphosphates with a whole body counter: a study of normal males. *Calcified tissue international*. **44**(5):322-329;1989.

[22] C.Pivich *et al.* Monitoring of the biodistribution and biokinetics of dysprosium-165 ferric hydroxide with a shadow-shield whole body counter. *European J. of Nuc. Med.* **24**(4):398-402;1997.

[23] R.Novario, L. Conte. A new method for calculating the distribution of radioactivity in man measured with a whole-body counter. *Health Physics*. **24**(4):398-402;1997.

[24] S.M.Morsay *et al.* Optimization studies of a whole-body counter to cope with possible dynamic transfer between neighboring compartments. *Health Physics*. **35**(2):325-332;1978.

[25] C.J. Edmonds *et al.* Follow-up of thyroid carcinoma by whole-body counting. *Br. J. of Radiol.* **43**:868;1970.

[26] L.A. Currie. Limits for qualitative detection and quantitative determination. *Analytical Chemistry.* **44**(3):586-593;1968.

[27] G.H. Kramer. The Canadian National Calibration Reference Center for In-Vivo Monitoring and the United States Department of Energy: Results of the 1993 Intercomparison / intercalibration: Final repart. *Human Monitoring Laboratory Technical Document*. HMLTD-95-3;1993.

Chapter 4

Hardware Considerations in Designing the WBC

4.1 History of an Old PET Scanner

Development of the high-adaptability whole body counter began with the decommissioning of an old PET scanner. The twenty-year-old PET scanner seen in figure 4-1 was originally owned by a hospital in Wisconsin, and was later sold to an agriculture equipment salesman. Being a 'PET' scanner, the salesman thought that it would be something that his clients would be interested in. He was grossly mistaken. The PET scanner was then purchased by the Cross Cancer Institute (CCI) in Edmonton, Alberta, for a very cheap price. At the CCI, the EG&G ECAT PET scanner was never

Figure 4-1. The decommissioned PET scanner with and without its cover on.

commissioned. Ultimately, components of the PET scanner were salvaged and used to develop a unique whole body gamma counter.

These components included stepper motors, gear boxes, lead, large amounts of coaxial cable, high-volt power supplies, and most importantly of all, sixty six sodium iodide detectors (NaI(Tl)).

The sodium iodide detectors taken from the PET scanner were originally arranged into six detector banks, themselves arranged in a hexagonal fashion to form a circle through which subjects could be scanned. As seen in figure 4-2b, each detector bank consisted of eleven detectors. Each detector is comprised of a NaI crystal measuring 1.5" (3.81 cm) in diameter, and 3" (7.62 cm) in length, permanently coupled to its own photomultiplier tube.

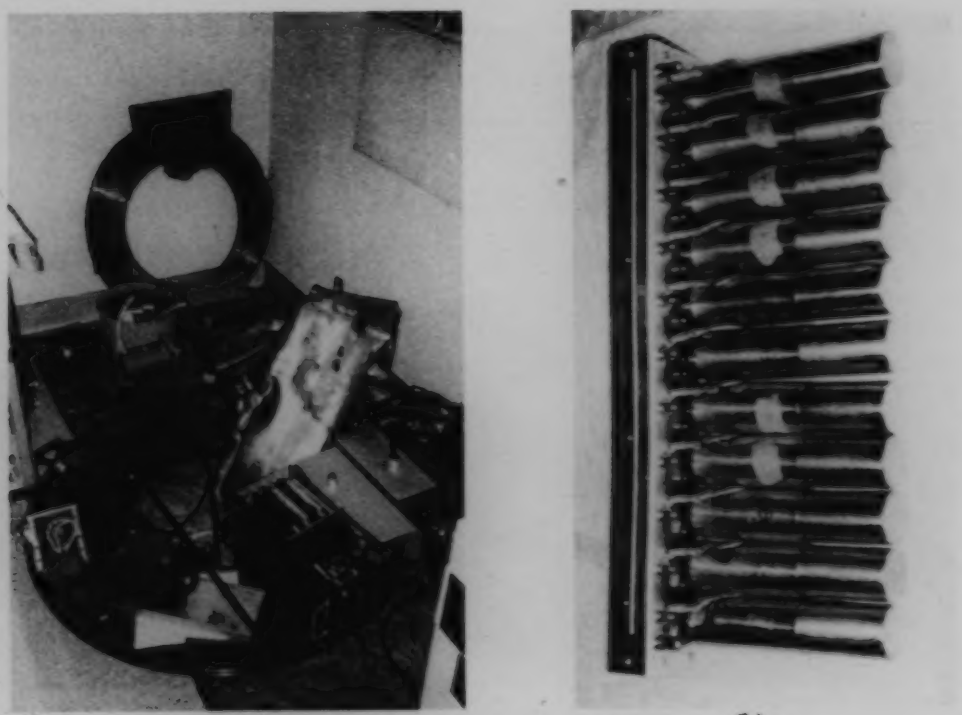

(a) (b)

Figure 4-2. The salvaged components from the PET scanner (a), and one of six detector banks (b).

4.2 Detector Characteristics

The first task that needed to be addressed was to determine the characteristics of the old PET detectors. Often with old NaI detectors, moisture from the air leaks into the hygroscopic crystal, making it less efficient. Since the crystals were approximately twenty years old, this was a primary concern. The number of detectors available, and their characteristics have a huge impact on a whole body counter's final design and performance, therefore much time was taken to assess all sixty six detectors available.

All measurements were conducted using a small point source of Cs-137 placed on the detector face, and centered. While not an ideal geometry, placing the source on the face provided source-detector geometry consistency. The 662 KeV photopeak was used to quantify efficiency, energy resolution, and photopeak position.

Detector efficiencies

The most important and crucial detector characteristic in a whole body counter is the detector efficiency. As discussed in section 3.3, the factor that most affects the percent quantification uncertainty and MDA is the absolute detector efficiency, and therefore the detector's intrinsic efficiency. A large efficiency is desired to reduce errors

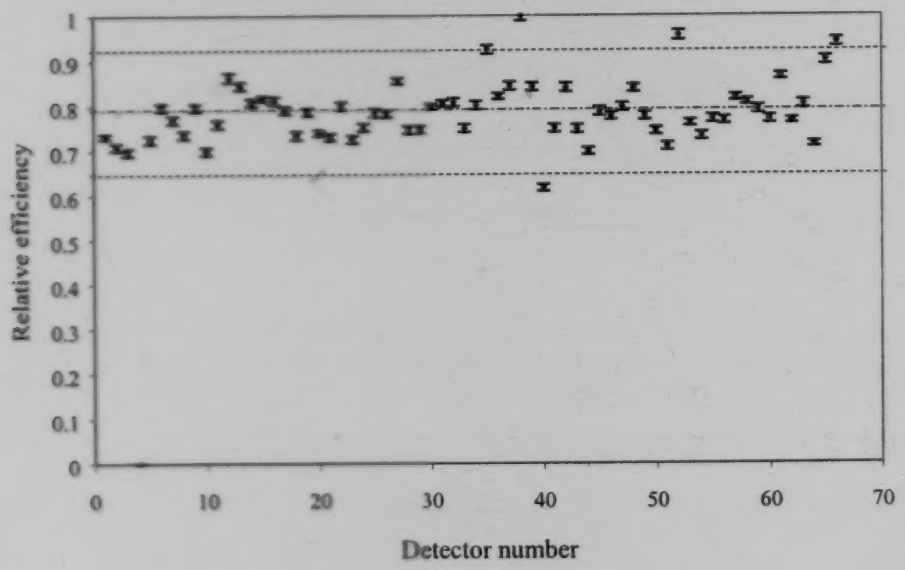

Figure 4-3. The relative efficiencies of the sixty six PET detectors

and the MDA in a WBC. The relative intrinsic efficiencies for all sixty-six detectors are shown on the previous page in figure 4-3. Dotted lines have been added to the figure to indicate the mean value of the data, and values that are two standard deviations larger or smaller than the mean. Similar labels have been added to figures 4-4 and 4-5.

As can be seen from the previous graph, almost all of the detectors have similar efficiencies. The average relative efficiency is 0.79, with a standard deviation of 0.066. Therefore, no detectors tested were suspected of being damaged, except for possibly detector number forty which is more than two standard deviations below the mean. Detector four was destroyed prior to testing. Monte Carlo simulations and experimental data were used to verify the detector efficiencies as well, and confirmed a relative efficiency of approximately 85%. The slight variations in efficiency are most likely due to slight optical decoupling from the PMTs, experimental variations, water damage in the crystal, or aging of the PMTs or dynode chain. From the efficiency data obtained from the detectors, sixty-four appear to be satisfactory for use in the whole body counter.

Energy Resolution

As discussed in Chapter 2, the energy resolution of a detector is a measure of its ability to distinguish between neighboring photopeaks.

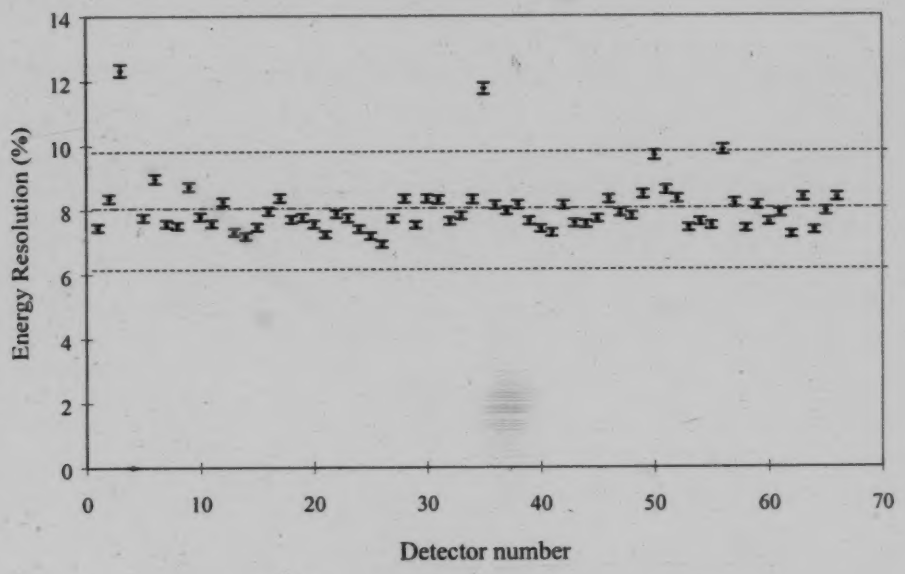

Figure 4-4. The energy resolution of the sixty six PET detectors

In multi-nuclide whole body counting, it is desired to have a good energy resolution. Figure 4-4 summarizes the measured energy resolution for the PET detectors. The average value for energy resolution is 8.0%, with a standard deviation of 0.9%. All of the detectors appear to have good and similar resolutions except for detectors 3 and 35. It is suspected that the loss of resolution is caused by an increase in noise possibly from the PMTs or dynode chain. These two detectors may still be incorporated into the WBC.

Photopeak Position

The positions of the 662 keV photopeak for the PET detectors are shown below. The average photopeak location is 198, with a huge standard deviation of 82. This huge fluctuation is most likely due to the aging PMTs and dynode chains, and can easily be adjusted by adjusting the high-voltage source, or the preamp/amp gain. Depending on how a counter is wired, when multiple detectors are used the relative location of a photopeak has a huge effect on photopeak quantification and identification. Therefore, photopeak positions often must be matched as close as possible. This will be discussed in detail later in this chapter.

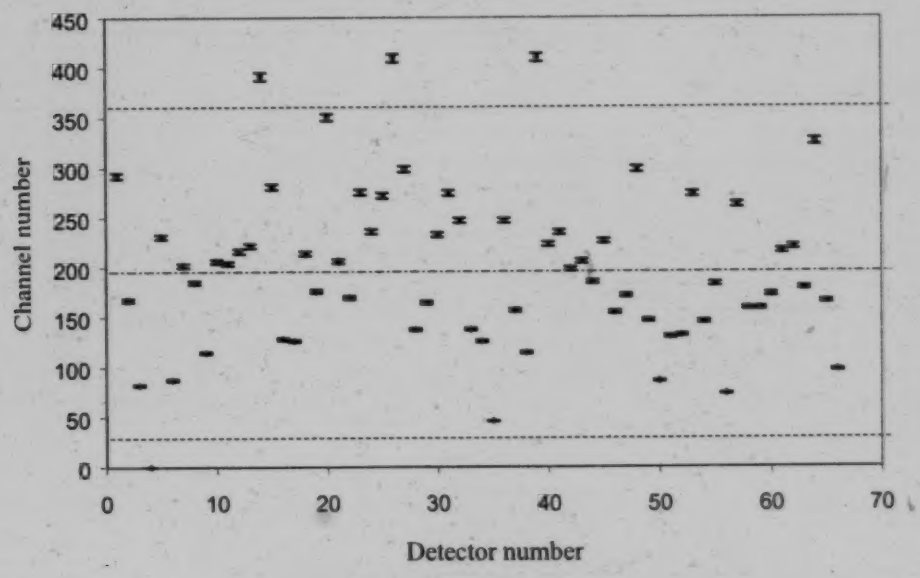

Figure 4-5. The photopeak position of the sixty six PET detectors

In conclusion, after carefully examining all sixty-six PET detectors, it was decided that sixty four detectors were suitable for use in the whole body counter. Aside from dead detector number 4, detector 40 had an efficiency 8.1% lower than any other detector and was rejected.

Electronics

Several electronic components are necessary for the whole body counter to operate properly. Chapter 2 provided a general overview of the electronics needed in whole body counting, however the following sections deal specifically with electronics developed for our counter. Particular detail is given to the components that were actually designed and build for the WBC.

4.3 Preamplifier Design

A key component in any nuclear detector system is the preamplifier. As discussed in Chapter 2, the preamplifier conditions the raw signal that comes from the detector. The raw signal from a photomultiplier tube for a Cs-137 photopeak pulse is seen below.

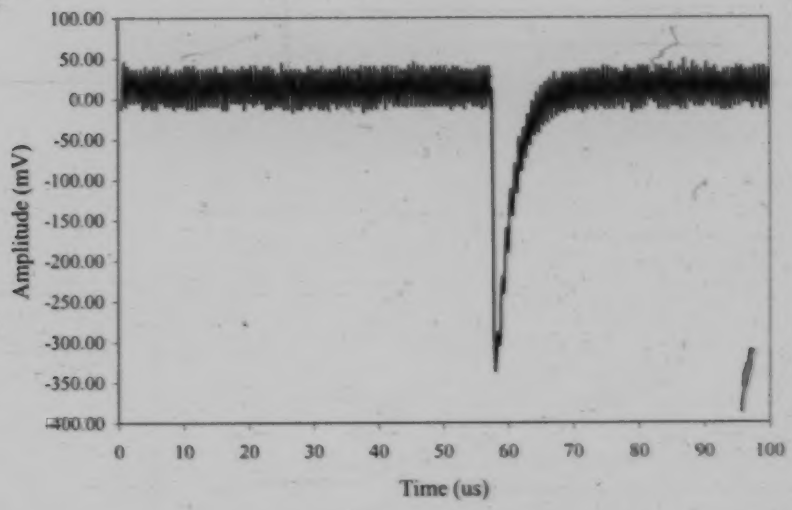

Figure 4-6. The raw signal coming from a photomultiplier tube.

The raw signal pulse shown in figure 4-6 has an amplitude of -325 mV and a pulse width of 8 μs. These characteristics are not well suited to the electronics that follow, since the detector signals must be fed into a multichannel buffer (MCB) at some point. Two Ortec 920-16e MCB's will be used for the WBC, which accept inputs that are either positive unipolar, positive gated integrator, or positive-leading bipolar. The pulses can also be as large as +10 V, and may be semi-Gaussian-shaped or gated-integrator-shaped with time constants of 0.50 to 30 μs, Z_{in}=1000 Ω, and dc-coupled. The signal in figure 4-6 has an amplitude and shape that is not accepted by the MCBs, therefore the signal must be conditioned using a preamplifier.

A charge-sensitive preamplifier, amplifier, and semi-Gaussian signal shaper were designed and constructed for use in the WBC. Mr. Chris Ediss from the Faculty of Pharmacy & Pharmaceutical Sciences did a large part of the on-paper circuit design, and a simplified schematic of the circuitry used can be seen below. In this thesis, the entire circuitry shown below is referred to as the WBC's 'preamplifier'.

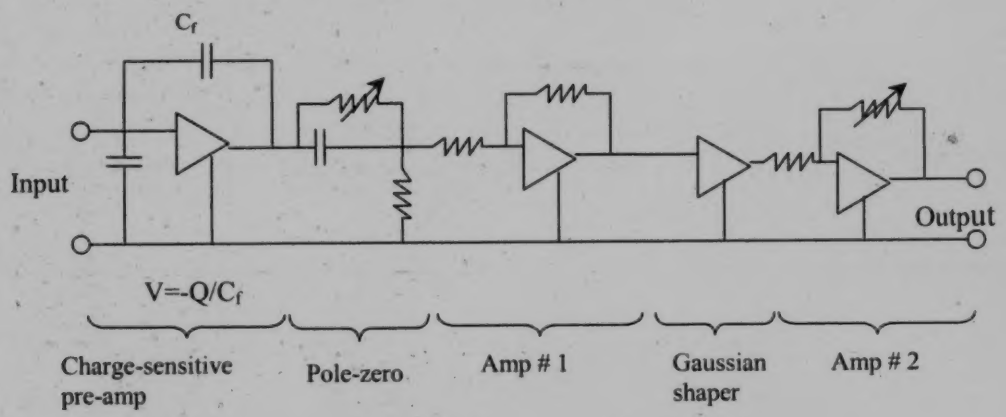

Figure 4-7. Schematic of the basic preamp designed for the whole body counter.

The preamplifier in figure 4-7 contains several components. The first stage consists of a charge-sensitive preamplifier, which generates a voltage proportional to the charge collected by the capacitor C_f. Aside from the charge collected, the voltage is also dependant on the capacitance of C_f, therefore a very stable 1% silver mica capacitor was used to ensure a stable capacitance. An adjustable pole-zero circuit was added so that the

undershoot commonly found in RC circuits[1] could be minimized. A diagram of the undershoot found in a typical RC circuit before and after pole-zero correction is shown below. Pole-zero cancellation effectively cancels most of the undershoot, which, if left uncorrected, can cause a base-line drift and therefore spectral shift under high count rates.

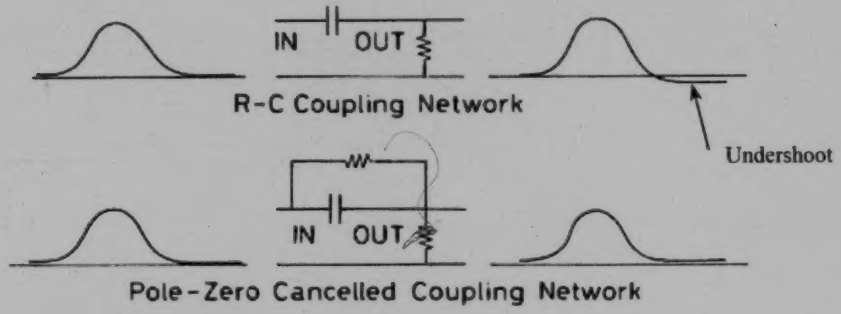

Figure 4-8. With and without pole-zero cancellation in an RC circuit.

The next section in the preamplifier is the first-stage amplifier (amp #1). This amplifier uses an LM 318N op-amp to deliver an absolute signal gain of 28. The design of the first-stage amplifier is most critical in reducing the overall noise of the system[2], therefore careful attention was paid to its design and construction. This first-stage amplifier's circuitry was intentionally isolated from components carrying large signals by maximizing the distance, and by placing large grounding wires between it and large-signal components. These measures were used to reduce induced noise in the first-stage amplifier.

The last two sections of the preamplifier contain an active filter, and a second-stage amplifier. An LM 310N op-amp is used in the active filter to change the shape of the pulse seen in figure 4-6, into a semi-Gaussian shaped pulse[3]. The second-stage amplifier (amp #2) is identical to the first-stage amplifier, but in addition, has an adjustable gain. Its absolute gain ranges from 4.7 to 28, providing the preamplifier with an overall combined signal gain between 132 and 784.

Once constructed, the preamplifier has dimensions of 7.1 cm x 4.5 cm, approximately 70 % the size of a credit card. A small PC board size was designed so that

the preamplifiers could be placed side-by-side, one behind each detector in the detector bank. The raw signal enters one end of the preamplifier through a small coaxial cable, and exits at the other end through a nine-pin plug. This plug also contains +12 V, -12 V, and -24 V power supply pins, however ground connections are placed between these and the output signal pin to reduce possible induced noise. All plug contacts are gold plated to provide the best connection possible. In order to reduce noise in the power supply lines of the PC board, capacitors were used to connect the active components' voltage pins to a ground line. This acts as a low-pass filter, and removes possible high-frequency noise in the power supply lines. The PC board was also designed so that if a preamplifier fails, a new preamplifier can be installed by unplugging only two plugs. A picture of the constructed preamplifier can be seen below, and full schematics and PC board layout are provided in Appendix B.

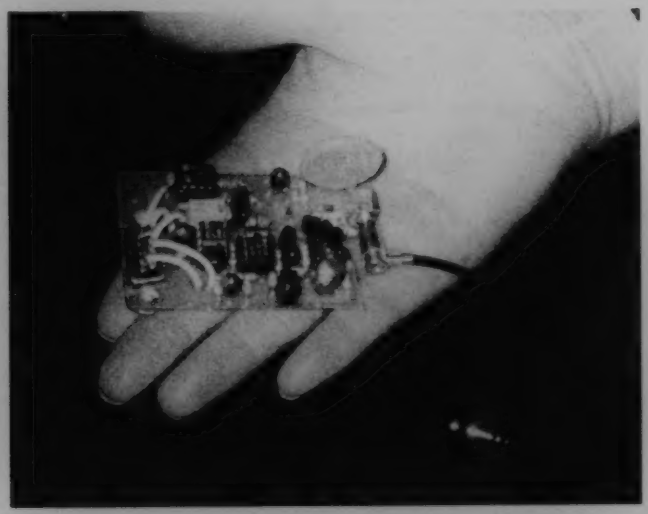

Figure 4-9. The preamplifier designed for use in the WBC.

The final processed and amplified signal from the preamplifier can be seen in figure 4-10. The pulse is positive-unipolar, and semi-Gaussian shaped. The pulse width is approximately 4 μs, and has an amplitude of 1.9 V. The pulse coming from the preamplifier is ideal for use with the Ortec 920-16e multichannel buffer.

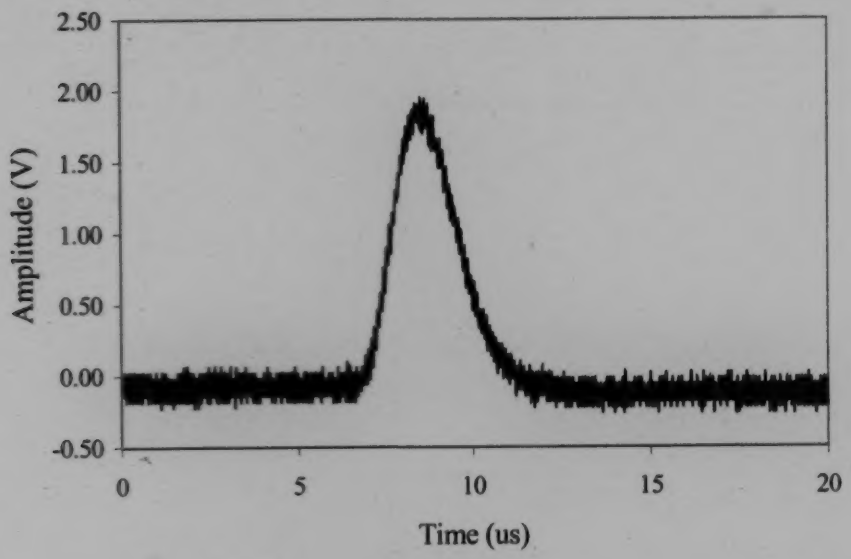

Figure 4-10. The signal coming from the preamplifier.

4.4 Testing the Preamplifier

The preamplifier that was discussed in the previous section was tested to determine whether it was satisfactory for use in the whole body counter. Several specifications are required before a preamplifier can be used in a whole body counter. Above all else, spectral stability is a must. Whole body counters typically have long counting times, therefore the photopeak position in a spectrum over time should remain as constant as possible. Whole body counters are often also used in premature or infant studies, which make use of heating lamps to keep the child warm. Therefore, it is desirable for the electronics contained within the WBC to be fairly resistant to changes in temperature. For high-activity studies, spectral stability is also desired.

Heat Tests

The preamplifier's resistance to heat was tested, by heating the PC board with a heat lamp. A thermometer was placed next to the preamplifier, and by placing the heat lamp at various distances from the preamp/thermometer, the preamplifier's performance for a range of temperatures was tested. The centroidal position of the 662 keV photopeak

from a Cs-137 source was measured after an acquisition time of 1500 seconds. The photopeak's position was measured at various temperatures, and figure 4-11 shows the results from the experiment. The FWHM of the peak was approximately 110 channels.

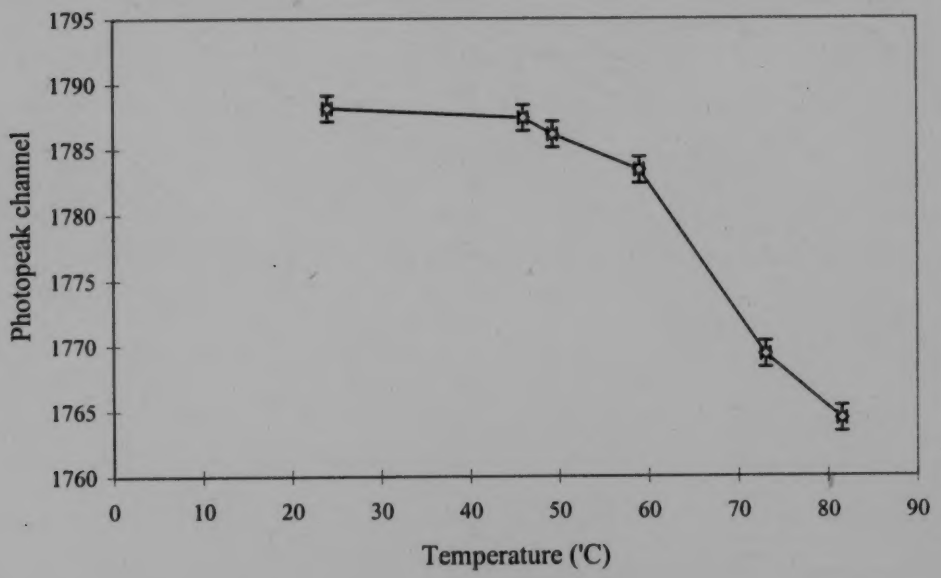

Figure 4-11. Photopeak position for a range of temperatures.

As can be seen in the figure, the position of the photopeak is very stable up until approximately 50 degrees Celsius. After that temperature, the pulse amplitude coming from the preamplifier slowly decreases. If the temperature is changed from 24 to 82 degrees Celsius, the photopeak moves a total of 24 channels, or 22% of one FWHM. For pediatric studies, temperatures in the gantries would never exceed 35 degrees Celsius, therefore the preamplifier designed for the WBC is sufficient for these types of studies.

Drift & Shift

As discussed in Chapter 2, 'drift' is a measure of the detector system's photopeak stability over time. Whole body counting generally requires long acquisition times, therefore spectral stability is a must. The detector system that was tested was comprised of one NaI detector, the preamplifier described in section 4.3, a HV power supply, and a computer-based MCA. The photopeak position from a Co-57 source was measured every

hour over a 17 hour time period, and after the data was collected, equation 2-10 was used to determine the drift of the system. The drift was measured to be (0.0906 ± 0.0017) %. An acceptable amount of drift is considered to be less than 1%, therefore our detector system is considered to be extremely stable and very well suited for whole body counting.

'Shift' is a measure of a detector system's ability to maintain a stable photopeak position while in the presence of high or low activities. Although not commonly a concern in whole body counting because of the low count-rates involved, for the sake of completion, the shift of our detector system was tested. Following the drift measurements described above, the count rate was increased by a factor of ten (to 10000 c/s). Five, separate 10 minute acquisitions were taken and the photopeak positions measured. Equation 2-11 was used to calculate the shift, which was measured to be (1.78 ± 0.01) %. The shift should be less than 1% for a detector system, and it is suspected that higher-order undershoots in the detector pulse tail are the cause of this larger shift.

Although the WBC described in this thesis is designed for high subject activities, shift should not be a problem. 'Shutters' described later in section 6.3 will be adjustable, and will be able to limit how much activity reaches the detectors. By keeping the count rate of the detectors low, the shift seen in these experiments will be eliminated.

The preamplifier and detector system experiments confirmed that they are indeed suitable for use in a whole body counter. All NaI spectra shown in this thesis were obtained using the preamplifier described in section 4.3.

4.5 Summing NIM

Each of the 64 detectors/preamplifiers in the WBC could be connected directly to the MCB/MCA, however there are advantages of placing a certain amount of electronic hardware just prior to the MCB. Cost can be reduced, the whole body counter can have a larger spectral energy range, and certain quality control and WBC calibration can be more easily achieved. For these reasons, 'summing NIM' (Nuclear Instrument Module) electronics were designed for the WBC.

Summing Electronics

The signal responses from the WBC's detectors must be summed at some point, either electronically or digitally to obtain a collective 'whole body count' from a subject. By summing the signals from two opposing detectors in a WBC, very flat detector responses can be obtained[4,5]. Sources positioned between the detectors will produce a very flat summed response, regardless of their positioning in the Y-direction. An illustration showing the two summed opposing detectors, and a source placed at two different locations can be seen below.

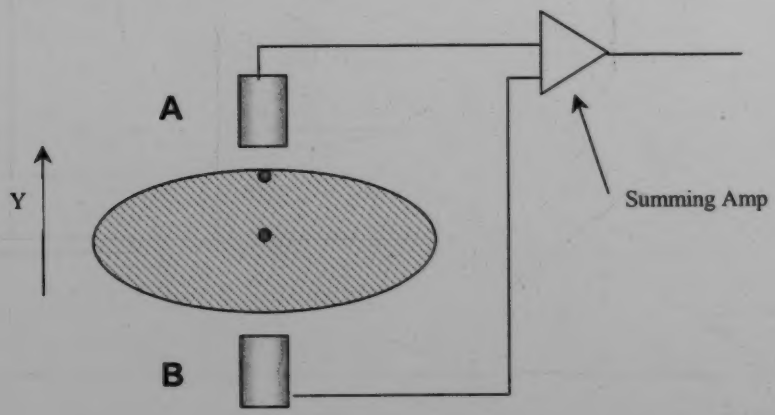

Figure 4-12. Opposing detectors in a WBC summed through a summing amp.

By electronically summing the opposing detector signals from the whole body counter, electronic costs can be reduced. The number of inputs needed for the WBC is reduced from 64 to 32, therefore only two Ortec 920-16e MCB's are required instead of four. Each multichannel buffer costs approximately $9,200, therefore summing electronics just prior to the MCB will reduce electronic costs by $18,400. Four detectors could be summed together so that only one MBC would be needed, but this would have an impact on the maximum count-rate and 'imaging' properties of the counter (see sections 8.5 and 8.6). Because of the restrictions on the number of MCB inputs, it is not cost-effective to use more than 64 detectors total, and using 64 detectors is optimal.

Unfortunately, by summing opposing pairs of detectors, information on the activity distribution between the detectors will be lost (e.g. detection of surface

contamination). Also, if only an individual detector pair is used, it will demonstrate a higher MDA than a 'composite' detector of all crystals combined.

High-Low Gain

When 16 signal inputs are connected into each of the Ortec 920-16e Multichannel Buffers, the stored spectrum contains a maximum of 1024 channels. For NaI spectroscopy, this is enough channels to resolve even low energy peaks. Each channel in the spectrum would have an energy width of 2 keV, therefore the FWHM of a 100 keV peak would span roughly 4 channels. However, looking at the energy of natural-body[6] and clinically used[7] isotopes, it can be seen that low-energy channel resolution can be increased substantially. As can be seen in figure 4-13, there is a huge energy spread between the highest energy isotope (K-40 at 1.46 MeV), and the lowest energy isotopes. Most of the interesting gamma energies are located below 400 KeV. If only these lower energy isotopes need to be quantified, then good channel resolution can be obtained by using a larger signal gain. If the maximum energy in the spectrum is set at 400 keV, then the FWHM of a 100 keV peak will span 20 channels. Therefore, electronics that produce a both fixed high and low-range signal gain before the signal reaches the MCB are very useful for isotope quantification and identification.

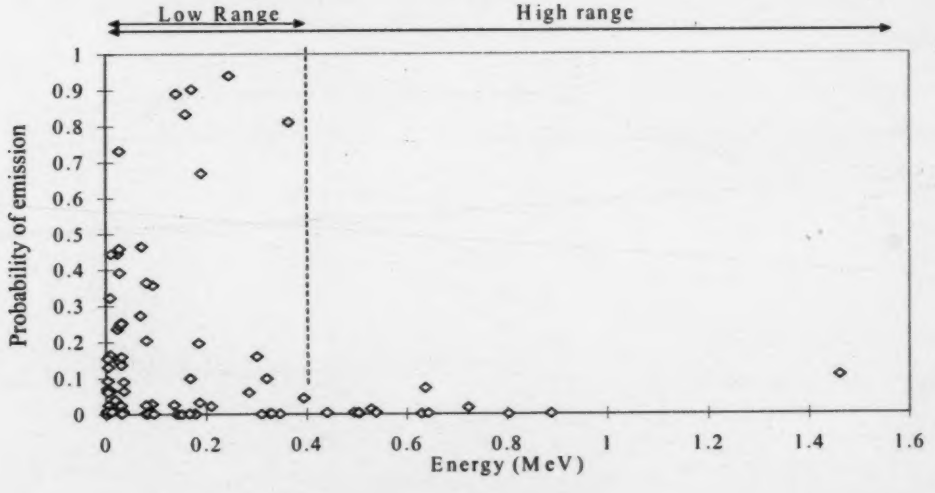

Figure 4-13. The probability of photon emission of various energies from natural body and clinically used radionuclides.

Summing NIM Schematic

All of the electronics containing the high-low gain, and the summing amps for the WBC can be placed into two, two-wide 'summing NIM' modules. Two of the old two-wide coincidence NIM modules from the PET scanner were salvaged so that they could be transformed into summing NIMs. These modules were stripped of their electronics, and new PC boards were designed so that they could be placed inside the old cases. Each PC board contains 8 summing sections, and two PC boards can fit into each NIM module. Therefore, the two NIM modules together contain 64 inputs from the 64 detectors in the WBC. Below is a schematic of one of the summing sections in the NIM PC board, where the two inputs labeled A and B come from opposing detectors' preamplifiers, as was shown previously in figure 4-12.

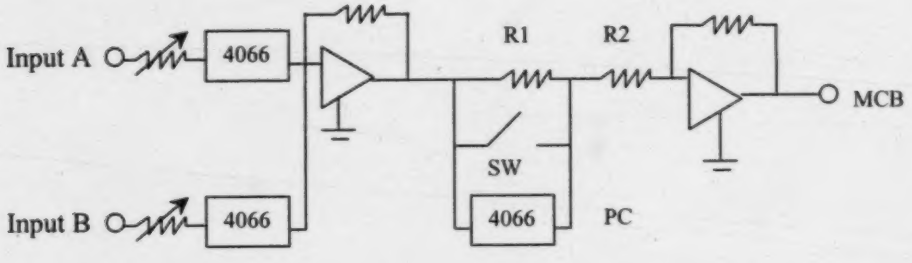

Figure 4-14. Circuit schematic for one of the summing sections in the summing NIM.

Before the signals are summed, their amplitudes must be matched to each other as closely as possible. This is done using variable resistors, and is a crucial step to ensure that good energy resolution is maintained once the two signals are combined. Recall from figure 4-5, that the photopeak signal amplitudes between the detectors vary tremendously. The variable gain in the preamplifier can serve as a rough means to match the two signals, and the summing NIM can be used to fine-tune this process.

Once the signal amplitudes are matched, they pass through a manually controlled quad bilateral 4066 switch. This switch allows one or both of the detector signals to be switched off, preventing it from reaching the MCB. This is needed, so that the individual detectors (A and B) can be adjusted and tested without physically disconnecting them.

Immediately following the 4066 switches, the signals are summed in an LM 318N op-amp.

After the two signals are summed, high-low range control is done through a computer controlled quad bilateral 4066 switch. With the physical switch (SW) open, the 4066 switch can be used to control the gain of the LM 318N op-amp that follows in the circuit. With both the physical and the computer controlled switches open, the amplifier has a unity gain. With the 4066 is closed, the op-amp has a gain of 4. With the 4066 switch open, the physical switch (SW) can be used for quality control purposes, where manual control of the gain may be more convenient.

The summing NIM module described above was completely designed, however only one of the summing sections was actually built. Complete PC board layouts for the summing NIM were made using an electronic CAD package, and are shown in Appendix B. The proposed NIM face is shown below.

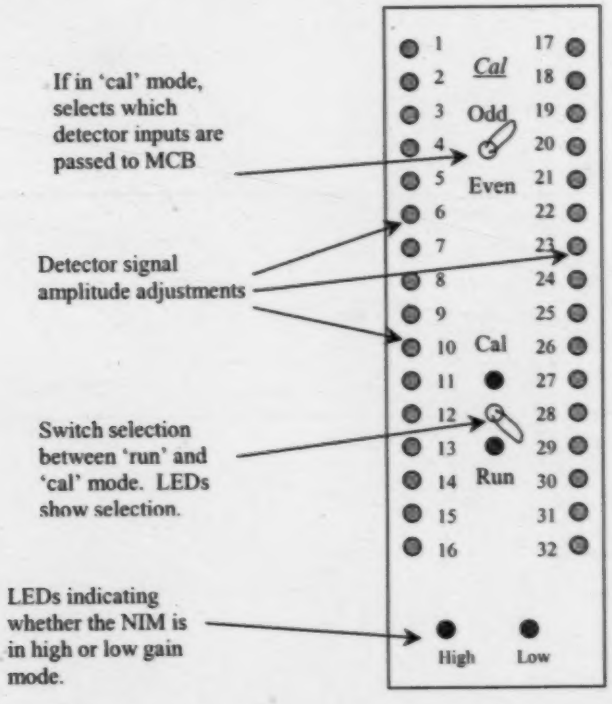

Figure 4-15. Proposed face for the two-wide summing NIM module.

The NIM module shown in figure 4-15 has two modes: 'run' and 'cal'. In run mode, the opposing detector signals are summed, and then fed into the MCB. This is the normal mode in which the WBC will be operated. For quality control purposes, where only one of the two opposing detectors needs to be examined at a time, cal mode can be used. Once in cal mode, the cal switch can be used to select whether all of the even or all of the odd numbered detector signals are passed through to the MCB. For this to properly work, the opposing detectors must be wired to the NIM module such that one is even, numbered the other odd numbered. The opposing detector pairs are grouped as [1,2], [3,4], [5,6], etc. LEDs showing high-low gain selection, and whether the NIM is in run or cal mode are added to the NIM design. Each detector input has its own tuning-pot hole at the front of the NIM, so that fine tuning of each detector signal amplitude can easily be done.

4.6 Peripheral Electronics and WBC Software

The high-adaptability counter relies on a number of different electronic devices and software to make it work. The detectors, preamplifiers, summing NIM, and the MCBs were already discussed earlier, however other peripheral electronic devices and software are needed. These additional components were not developed as part of this thesis, but are briefly mentioned in this section so that they may be referred to later.

Stepper motors and electronics

It is intended that all moving components within the whole body counter be moved using stepper motors[8]. The detectors, shutters, top gantry, and the table movement all have been designed to move with stepper motors. The advantage of using stepper motors over servos and other motors, is that they can be easily computer-controlled, and precise movement without any feedback can be achieved.

Each stepper requires a 'stepper motor driver' to make it work. Drivers can be purchased or built, and contain a power supply, computer-interface card, and software.

Top Gantry Movement Sensor

The top gantry is designed to move up and down with the contours of the subject (discussed later in section 6.2), therefore a sensor must be developed that will detect changes in subject's shape. One simple method of accomplishing this would be to mount mirrors and two small pen-lasers to the bottom of the top gantry, such that the sensor apparatus would be positioned between the subject and the top gantry. A top view (looking down at the subject – AP view) of the layout using one laser can be seen below.

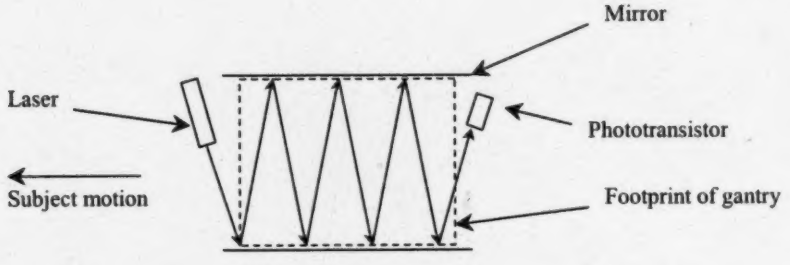

Figure 4-16. Top-view of proposed subject profile sensor.

The laser and mirrors can be positioned such that the laser's ray will be reflected back and forth between the two mirrors. By placing a phototransistor at the end of the reflected ray, it can easily be determined if there is anything blocking the ray's path. Therefore, a sensor 'plane' can be created under the entire gantry, and anything entering the plane will be detected.

By using two lasers, one placed just above the other, two sensor planes can be created. These two sensor planes, and simple Boolean electronics can be designed to move the gantry with the contours of the subject. The gantry can be programmed to move down towards the subject until the plane closest to the subject is broken. If while being scanned, the subject breaks the second plane, then the gantry can be programmed to move up a certain amount until only one plane is broken. Spacing between the two lasers would determine how accurately the top gantry will follow the subject's contours.

Other Electronics

A kill switch is included in the whole body counter design as well. This kill switch is wired such that upon activation, the top gantry will immediately lift, and the table move towards the nearest possible WBC exit. Both the subject and the WBC operator will have access to this switch during the scan in case of an emergency.

To prevent accidentally exceeding the maximum range-of-movement of the detectors, shutters, table, and gantry, small physical switches shall be strategically placed throughout the counter. In the case of the table, a small switch can be placed at both extreme table positions (entrance and exit). If the normal table position is exceeded, this would activate the switch. Once activated, the switch can prevent further table movement in that direction. By using small physical switches, damage to the WBC caused by exceeding the maximum range-of-movement can be prevented. These switches can be interfaced to the computer using an interface card, and will act as a back-up system to the stepper motor controller.

Software

Software is needed to control the movement of the WBC's various components and to analyze the data after it is acquired. Some of the software can be purchased, however most of it is very specific to the whole body counter and must be developed.

The two MCB's are controllable / programmable from a computer, and have a unique high-level language of their own. The MCB responds to several commands, which can be executed from other programs in order to start / stop acquisition, save acquired spectra, etc. Several different functions containing many commands need to be programmed, so that they can be executed at certain times during the scan.

In order to acquire data from the WBC, a windows interface must be created. Much like the front-end of any complicated device, a simple and intuitive interface must be programmed so that an operator can easily control the WBC. *Visual C++* or *Visual Basic* both could be used to develop this interface. The stepper motor drivers, subject-gantry sensor input, high-low summing NIM control, maximum-movement switches, MCB control, and the kill switch must all be incorporated into the program. Pre-

programmed scanning procedures need to be constructed and implemented into the software for regular subject, calibration, background, and QC scans.

The software required to analyze the acquired spectra can be purchased. Ortec's *Maestro / Scinti-vision* software can be used to peak-search, de-convolve superimposed photopeaks, smooth / strip spectra, and quantify photopeak counts over any background. Analyzing all 32 channels individually using this software would be extremely tedious, however 'job' files can be created, that will instruct the system to do the analysis automatically.

4.7 Electronic Configuration of the Counter

The high-adaptability WBC's electronic configuration, with all components, can be seen in the figure 4-17. There are two options to interface the stepper motor drivers to the computer. If the drivers are home-built, then they can easily be controlled through an 8255 I/O card. The other option available (see the dotted arrows) is to purchase already-built stepper drivers, in which case the drivers can be connected directly to the computer through their own interface card. NIM modules in the schematic include three HV power supply NIMs for the photomultiplier tubes (salvaged from the old PET scanner), two summing amp NIMs (to be built), and two 920-16e NIMs (to be purchased). If purchased, the stepper motor drivers can come in a NIM module as well. Low-voltage power supplies for the pen-lasers, preamplifiers, Boolean circuits, and stepper-motor drivers also need to be purchased.

The 8255 I/O interface card plays a major role in interfacing the WBC to the computer. Very inexpensive PC cards containing two 8255 I/O integrated circuits on one card can be purchased. Each card contains 48 I/O ports, which can easily be controlled through a computer. Drivers for *DOS*, *Visual C++*, *Visual Basic*, and other programs come with these interface cards. The computer's parallel port can also be used for I/O purposes.

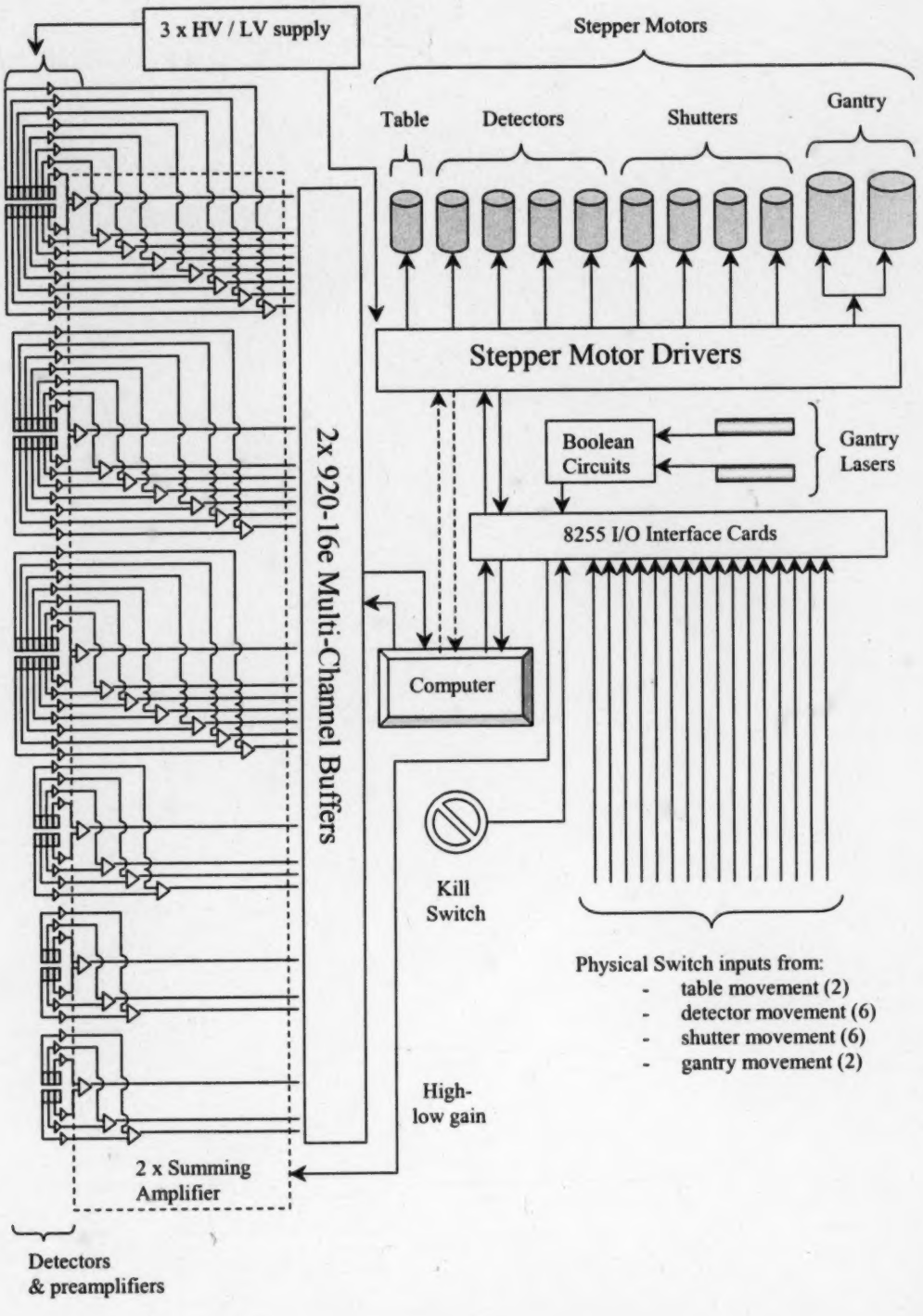

Figure 4-17. The electronic configuration of the high-adaptability WBC.

References

[1] W.R. Leo. Techniques for Nuclear and Particle Physics Experiments – A How-to Approach. pp 281-282, *Second revised edition, Springer-Verlag Press,* Copyright 1994.

[2] M. Sayer, A Mansingh. Measurement, Instrumentation and Experiment Design in Physics and Engineering. pp 106-107, *Prentice-Hall India,* Copyright 2000.

[3] E. Fairstein, J. Hahn. Nuclear Pulse Amplifiers – Fundamentals and Design Practice (Part 3). *Nucleonics.***23**(11):50-55;1965.

[4] P. Fothill, J.M. Galt. Quantitative profile scanning for the measurement of organ radioactivity. *Physics in Medicine and Biology.***16**(4):625-634;1971.

[5] R.S. Budd. Whole body counting using a twin-detector scanner. *Australasian Radiology.***17**(4):464-469;1973.

[6] J. Shapiro. Radiation protection – a guide for scientists and physicists. 2nd edition:55-56;1981.

[7] J.T. Bushberg *et al.* The essential physics of medical imaging. pp 479-483, *Williams & Wilkins,* Copyright 1994.

[8] P.P. Acarnley. Stepping Motors: a guide to modern theory and practice. *Short Run Press Ltd,* Copyright 1982.

Chapter 5

Theoretical Considerations in Designing the WBC

5.1 Ray-Tracing Computer Simulation

There are sixty-four working detectors available for use in the WBC, however without computer modeling, there is no way to accurately predict whether their responses in the counter will be satisfactory for clinical use or not. For a given scan time, a WBC's MDA will depend on the number of detectors, their size, and on the whole body counter design. Not all MDAs will be sufficient to quantify natural body background. A quantification error of less than 10% (as defined by equation 3-2) for naturally occurring isotopes was considered satisfactory for our needs. To determine whether our detectors could indeed be used in a satisfactory way, a unique ray-tracing computer simulation was developed to evaluate the optimized counter.

Overview of Simulators and their Shortcomings

There are several techniques for modeling photopeak responses in detectors, however none of them are well suited for modeling a multi-detector whole body counter. Several authors have used Monte Carlo[1,2], ray tracing[3,4,5], and analytical[6,7,8] modeling methods to obtain accurate photopeak responses in detectors. Ray-tracing methods make use of experimentally determined weighting factors, which correct for geometry-dependant peak-to-total ratios. Obtaining these weighting factors is time consuming, and once calibrated, only specific detector-source geometries can be used. Papers published on this topic only deal with the simplest case: fixed, symmetric, and like-coordinate geometry for the source and detector. Analytical modeling methods have similar restrictions. For the more complex case where no symmetry is present, a Monte Carlo simulation is usually performed. Monte Carlo programs can be very costly, or free programs such as EGS4[9] can be very tedious to set up and to run. To obtain statistically

valid spectral information from Monte Carlo, considerable CPU time is required, unless the geometry is straight forward, and a single detector is modeled. In the case of multiple, heavily shielded detectors as found in our whole body counter, the task of detector modeling by means of Monte Carlo becomes vast and very time consuming.

The Semi-Empirical-Regression Method

Because of the drawbacks of using conventional modeling techniques to model WBCs, a new 'Semi-Empirical-Regression' method was developed. Similar to other ray-tracing algorithms, the Semi-Empirical-Regression Method calculates the absolute efficiency of the detector, and uses peak-to-total ratios to obtain the detector's absolute peak efficiency at a certain gamma-ray energy. This method has been shown to be insensitive to variations in scattering and energy resolution[10].

In general, the absolute peak efficiency for an on-axis point source is given by:

$$\varepsilon_p(E) = T(E)P(E) \tag{5-1}$$

where $T(E)$ is the absolute efficiency of the detector, and $P(E)$ is the peak-to-total ratio (PTTR) at gamma energy E. For a point source, the absolute efficiency $T(E)$ of a detector is given by the following:

$$T(E) = \frac{1}{4\pi}\int_0^{2\pi} d\varphi \int_0^{\pi} [1 - \exp\{-\tau(E)t_d\}] \exp\left(\sum_{i=1}^{n} -\mu_i(E)t_i\right) \sin\theta d\theta \tag{5-2}$$

where $(1/4\pi)\sin\theta\, d\theta\, d\phi$ is the probability that an emission from the point source will fall in the solid angle element $\sin\theta\, d\theta\, d\phi$, $\tau(E)$ is the total linear attenuation coefficient (not including coherent) for the detector at energy E, t_d is the thickness of detector that the ray passes through, $\mu_i(E)$ is the total linear attenuation coefficient at energy E for material i that the ray passes through (thickness t_i) before it reaches the detector for n different materials.

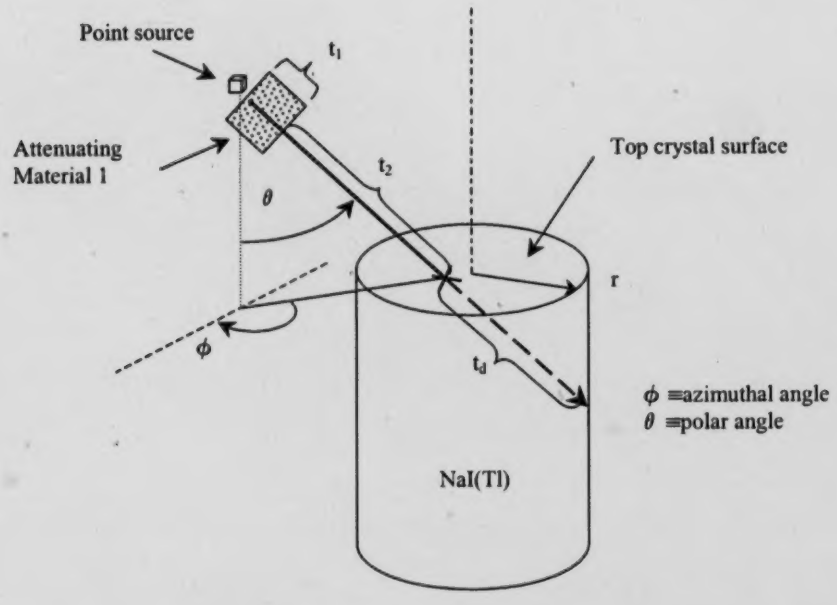

Figure 5-1. Geometry for a point-source ray entering a square cylindrical detector.

For ray-tracing analysis, the crystal surface needs to be segmented into finite element sizes. The absolute efficiency of a point source located above the crystal and whose distance from the crystal axis is $\leq r$ is therefore:

$$T(E) = \frac{1}{4\pi} \sum_{\substack{crystal \\ surface}} \frac{A_e \cos\theta}{\left(\sum_{i=1}^{n} t_i\right)^2} \left[1 - \exp\{-\tau(E) t_d\}\right] \exp\left(\sum_{i=1}^{n} - \mu_i(E) t_i\right) \qquad (5\text{-}3)$$

where A_e is the surface area of an element on the crystal surface.

Once the absolute efficiency is calculated for a point source, equation 5-1 can be applied in order to get the absolute peak efficiency. However, the PTTR (and therefore equation 5-1) is *only* valid for point sources on the axis of the detector. On the axis, the PTTR remains invariant to source-crystal distance[11], and can be used. However, off-axis, the PTTR is not constant[12], and changes as a function of the polar angle theta (θ); a minimum can be observed at roughly 45° for square-cylindrical detectors. In order to use

equation 5-1 for off-axis point sources, a weighting factor would need to be implemented such that:

$$\varepsilon_p(E,\theta) = T(E)P(E)W_{pttr}(E,\theta) \qquad (5\text{-}4)$$

where $W_{pttr}(E,\theta)$ is a weighting factor with a theta (θ) dependence. This weighting factor can be determined experimentally for each crystal size.

Equation 5-4 not only corrects for PTTR variations, but can also take any other variations or asymmetries into account as well. Many detector arrangements contain shielding, neighboring crystals, inhomogeneous detector responses, the presence of a magnetic field, and a host of other factors, all of which can contribute to create an asymmetrical detector response. To model these different situations through analytical, Monte Carlo, or conventional ray-tracing methods would be extremely difficult, if not impossible.

The semi-empirical-regression method assigns all variations, both symmetric and asymmetric, to one weighting factor that has a theta (θ) and phi (ϕ) dependence such that:

$$\varepsilon_p(E,\theta,\varphi) = T(E)P(E)W_{tot}(E,\theta,\varphi) \qquad (5\text{-}5)$$

where $W_{tot}(E,\theta,\phi)$ is a polynomial defining a weighting factor for the *complete* detector setup over the desired range of theta and phi. Multiplying equation 5-5 by the activity of the point source will yield the number of photopeak counts expected per time interval in the detector from that point source.

Determining $W_{tot}(E,\theta,\phi)$

$W_{tot}(E,\theta,\phi)$ is the ratio of the experimentally determined photopeak efficiency to the calculated efficiency. The detector needs to be modeled therefore, but since off-angle corrections are taken care of by the weighting factor, only accurate on-axis modeling is necessary. It is, however, crucial for the model to accurately determine *relative* changes in the detector's efficiency for all source-detector distances and for all angles. Equation 5-3 can be used in this case, where only the surface area of the detector face needs to be

incorporated in the model. This simplification is a first-order approximation of the actual detector response, which is described in section 5.2 of this thesis.

In general, to determine $W_{tot}(E,\theta,\phi)$, the absolute photopeak efficiency must be experimentally measured (ε_{px}) at a known theta, phi, and distance from the detector face, and divided by the expected value from the first-order approximation.

$$W_{tot}(E,\theta,\varphi) = \frac{\varepsilon_{px}}{T(E)P(E)} \tag{5-6}$$

To 'map' out all of the weighting factors for a detector arrangement, a maximum field-of-view (FOV) in terms of theta and phi of the detector system must be chosen, and a point source emitting gamma radiation at energy (E) of known activity must be obtained. Once all of the data is collected at regular theta and phi intervals over the entire FOV, it can be fit to a 3D-regression curve. The polynomial defining the curve can then be used to calculate $W_{tot}(E,\theta,\phi)$ at any point in space, and the photopeak counts (at energy E) for any activity distribution can be accurately simulated. By using equation 5-5 in conjunction with the $W_{tot}(E,\theta,\phi)$ polynomial, and by summing up the activities from several point sources, any volume or activity distribution can be modeled. As well, any elemental size can be given to the activity distribution. Should another isotope with a different energy be used, a new map must first be generated.

Direct application of the Semi-Empirical regression method and examples of the $W_{tot}(E,\theta,\phi)$ polynomial will be discussed in section 5.3.

5.2 Ray-Tracing Simulation: A First-Order Approximation

A first-order ray-tracing simulator was developed so that the $W_{tot}(E,\theta,\phi)$ weighting factors and relative detector responses could be determined. As seen in the last section, a first-order approximation is required in order to calculate $W_{tot}(E,\theta,\phi)$ as defined by equation 5-6. An approximation for relative detector responses for different detector positions in relation to one or more point sources is also required, and was used to optimize various aspects of the counter.

Development and Experimental Verification

Equation 5-3 was implemented to calculate a first-order approximation, where only the surface area of the detector face was incorporated in the model. For our purposes, we were interested in the detector's response at a distance of approximately 5cm or more, therefore the detector face was only segmented into 25 square elements as shown in figure 5-2b. The detector face was modeled as a square face with the same surface area and volume as the original detector. This was done to speed up the simulation, however more segments and a circular face will provide more accurate results at small source- detector distances.

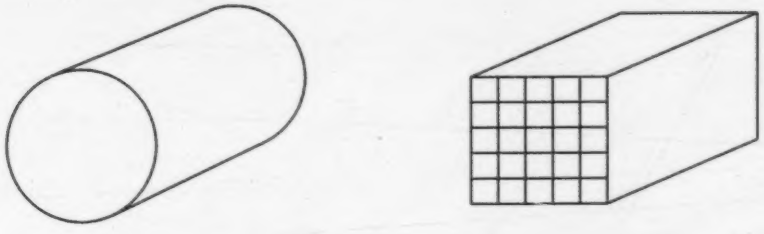

(a) (b)

Figure 5-2. The original cylindrical crystal (a), and its rectangular modeled equivalent (b).

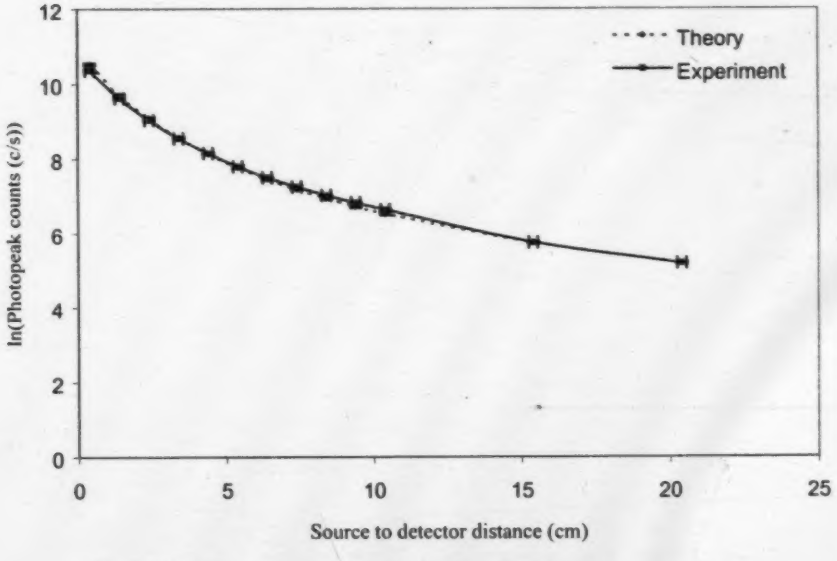

Figure 5-3. Theory versus experiment for a Co-60 point source on-axis.

Figure 5-3 shows excellent agreement between experiment and the calculated photopeak counts for a large range of source-detector on-axis distances. The photopeak counts were derived from equation 5-3 using the segmented detector described in figure 5-2b, and PTTR's which were obtained experimentally and verified via Monte Carlo simulations. Accurate photopeak quantification for source-detector distances as close as 3.5 cm were obtained on-axis using the segmented crystal face.

Photopeak responses through different attenuating materials were verified using EGS4-Nova Monte Carlo simulations. As can be seen below, for parallel beams of 1.46 MeV photons through different materials, the first-order approximation agrees well with theory. Note that a different photon flux for each material arrangement was used to generate the data seen in figure 5-4.

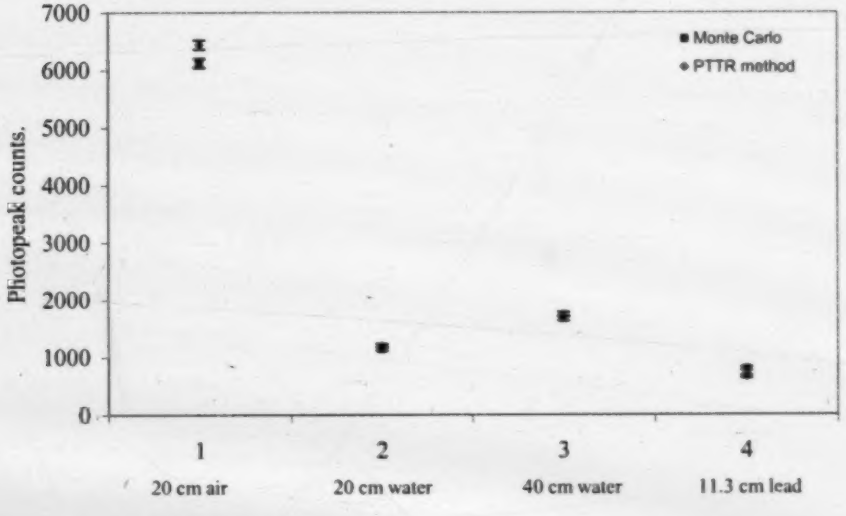

Figure 5-4. Monte Carlo and first-order approximation detector responses.

Relative detector responses from homogeneous distributions were obtained using a first-order approximation. The semi-empirical regression method that was described in section 5.1 can deliver accurate detector response for homogeneous sources, however, a particular detector arrangement has to physically exist so that $W_{tot}(E,\theta,\phi)$ can be mapped out experimentally. This can be impractical to do when several slightly different detector geometries need to be compared with one another, as was done later on to optimize the

WBC. Where absolute quantification is NOT required, but instead, just a relative approximation is needed, the first-order approximation described in this section can be used.

'Collimators' were added to the simulator such that only a predefined FOV from a homogenous source would be accepted as part of the detector response. The Reference Man thorax (40 cm wide, 20 cm thick, and 70 cm long) was modeled as our homogeneous source by using an 11x11 matrix of point sources for each axial slice, and fifteen equally spaced slices to model the thorax length. Path-lengths for body, air, and crystal were calculated for all rays emitted from the ensemble of point sources (see fig 5-5).

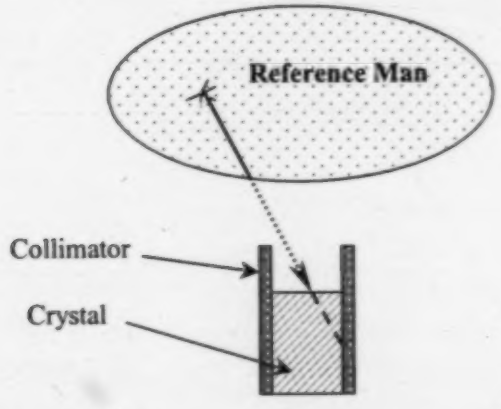

Figure 5-5. The detector-collimator-source geometry for the first-order approximation.

The path-lengths were used to determine the extent of attenuation as rays passed through material, and to calculate each ray's intrinsic efficiency in the crystal. Circular and elliptical path-lengths were verified for the various source and detector positions in and around the Reference Man thorax as seen in Figure 5-6.

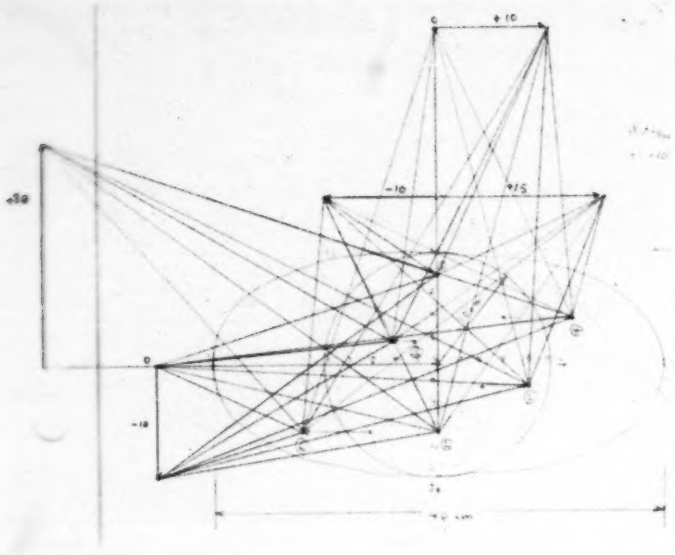

Figure 5-6. Path-lengths verified on paper for different source-detector positions.

Figure 5-7 shows the first-order detector response from a homogeneous source (Reference Man thorax) with and without simulated collimators. The detector was placed at the mid-height of the Reference Man thorax, and at several different source-detector distances.

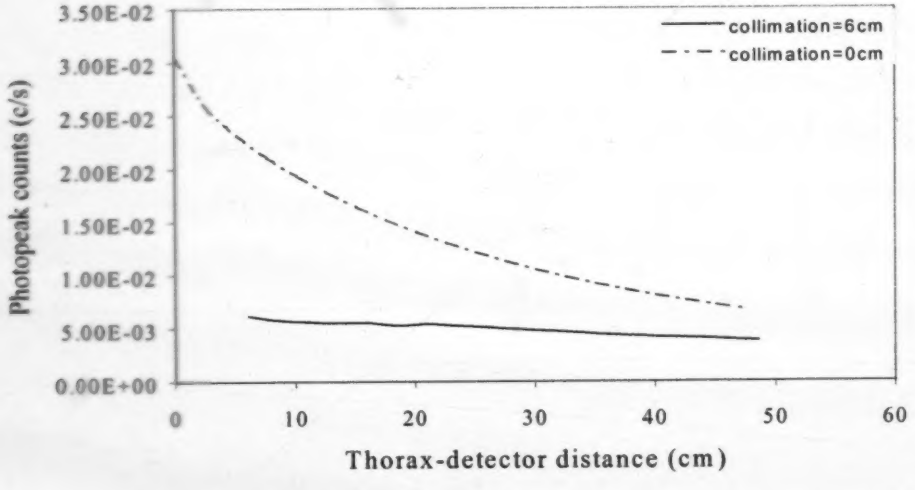

Figure 5-7. Collimated and uncollimated detector responses from a homogenous source.

Detector responses calculated from the first-order approximation method using homogeneous activities and slight collimation were verified experimentally. An 18 liter water bottle was used as a phantom to test the theory in the setup seen below in figure 5-8. The water bottle was filled with 11.7 liters of water, and 4 Kg of KCl salt was added to create a saturated KCl solution. Naturally occurring K-40 in the solution gave it an activity of 6941 Bequerels for 1.46 MeV photons. The water bottle measured 25.7 cm in diameter, and 34.3 cm in height; dimensions similar to a human thorax. The experimental and theoretical results can be seen below as the detector is placed 19 cm away from the phantom, and moved laterally.

Figure 5-8. Experimental setup for measuring the homogeneous source.

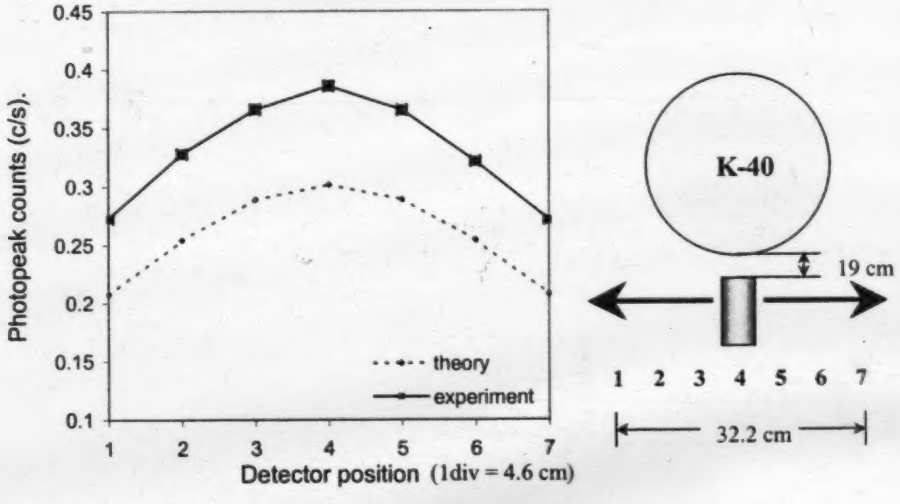

Figure 5-9. Theory and experimental detector responses for lateral detector movement.

As seen in figure 5-9, the simulated relative detector response from a collimated, homogeneous distribution is excellent. The phantom contained K-40 radioactivity, had similar dimensions to a human thorax, and was placed at a reasonable distance from the detector. The lateral movement was performed in steps of 4.6 cm, which was the distance separating the detectors in their original PET detector bank. The relative detector activity (represented as a sim/exp ratio) for each position is summarized below in table 5-1.

Detector Position	Response - sim (c/s)	Response - exp (c/s)	Sim /exp ratio
1	0.208	0.273	0.762
2	0.254	0.328	0.774
3	0.289	0.366	0.790
4	0.302	0.386	0.782
5	0.289	0.365	0.792
6	0.254	0.321	0.791
7	0.208	0.271	0.768

Table 5-1. Ratio of simulated to experimental detector responses.

It is obvious that there is an absolute offset, but this will be dealt with later in this Chapter. The purpose of this test was simply to model lateral offset and shape.

Experiments were also conducted using point sources located at different distances but at the same θ, ϕ angles from the detector face. These values were compared with experimental values, and also showed excellent relative activities.

The first-order approximation method, verified for its relative detector response for point as well as homogeneous radioactive distributions, with the addition of collimators was considered suitable for optimization of certain aspects of the WBC.

Concerns About Build-Up and Quantification

The only hesitation in using the first-order approximation simulator to optimize parts of the WBC, was the unknown effect of build-up on the expected detector responses. The ray-tracing computer simulations discussed in this thesis depend on peak-to-total-ratios in air. However, all rays pass through some amount of attenuation other than air. This creates 'build-up' in the photopeak, which may or may not affect photopeak

quantification. If the effects of build-up on quantification are the same, regardless of the amount and type of material that a ray passes through, then the effects of build-up can be removed in the WBC calibration. Therefore, the predicted and actual detector responses can be directly correlated, and the first-order approximation can be used to optimize parts of the WBC.

'Build-up' counts come from forward-scattered Compton events that have an energy very close to that of the full-energy photon. The primary photons are scattered by the air, subject tissue, WBC shielding, or any other attenuating material, and appear as a continuum next to the true photopeak. Build-up photons typically must have energies within one FWHM of the photopeak, and occur when the primary photon is scattered by approximately 15 degrees or less (for 1.46 MeV photons).

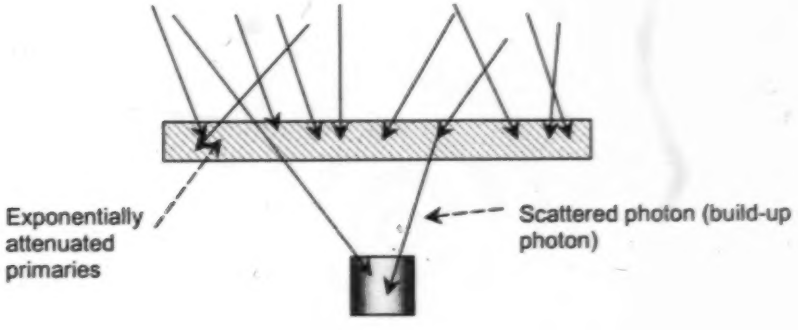

Figure 5-10. Build-up in a detector from forward-scattered photons in a material.

When a NaI crystal detects build-up photons, they appear in the same observed photopeak as the full energy photons. This happens because the two energies are too close for NaI crystals (~ 8% energy resolution) to resolve, and the result is a slightly skewed photopeak (see figure 5-15). Also, in the presence of build-up, using a simple linear fit may not be satisfactory for net photopeak quantification.

Figure 5-11 shows a Monte Carlo generated energy spectrum for 1.46 MeV photons passing through 20 cm of air. There is very little attenuation and scatter of the photons through air, therefore, excluding the photopeak, the build-up in the 8% ROI is very minimal. In contrast, when the same photons pass though 11.3 cm of lead (figure 5-

12) there is substantial attenuation and scattering, therefore a lot of build-up. In this case, in a NaI crystal, it is uncertain whether true photopeak quantification can be achieved.

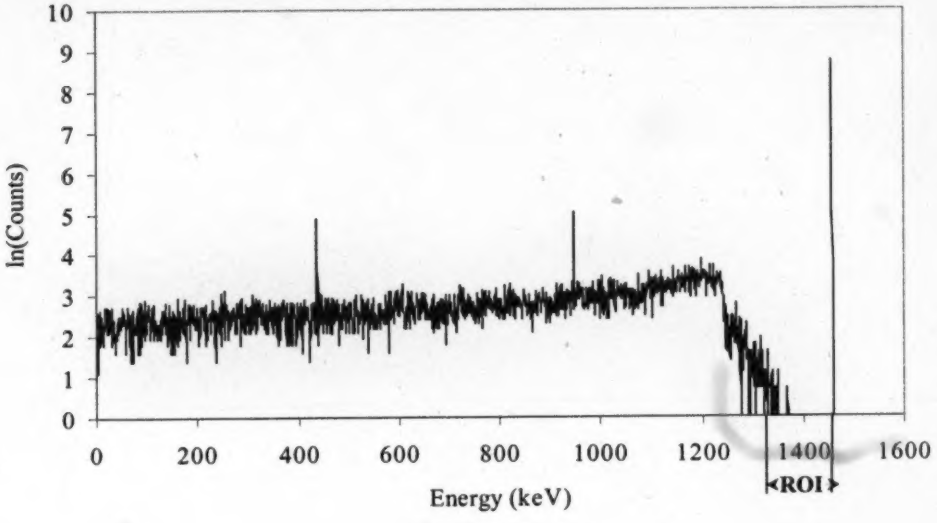

Figure 5-11. Build-up in ROI from 1.46 MeV photons passing through 20 cm of air.

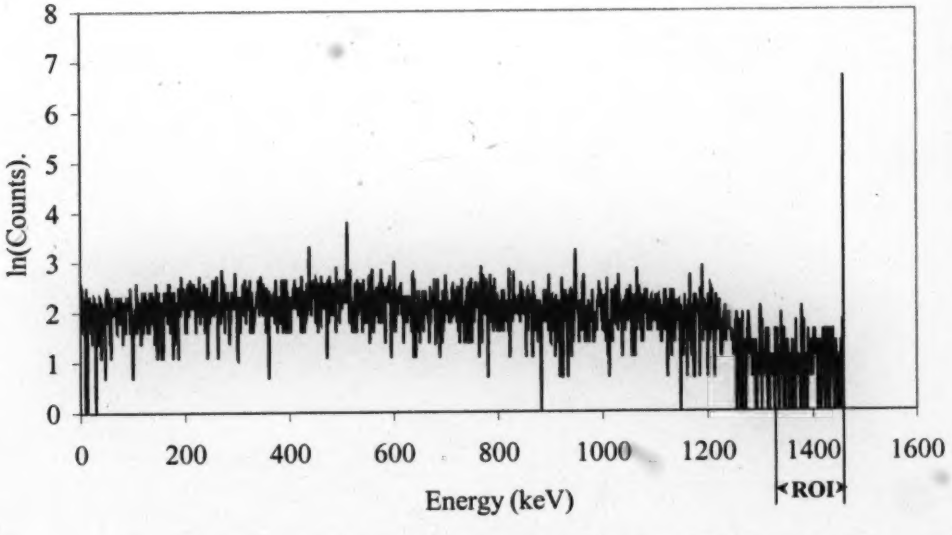

Figure 5-12. Build-up from 1.46 MeV photons passing through 11.3 cm of lead.

To determine the extent of build-up from lead, water, and air attenuation, the fraction of counts from build-up in the ROI as compared to the photopeak were graphed. As can be seen in the figure below, as much as a third of the total ROI counts in lead are from build-up.

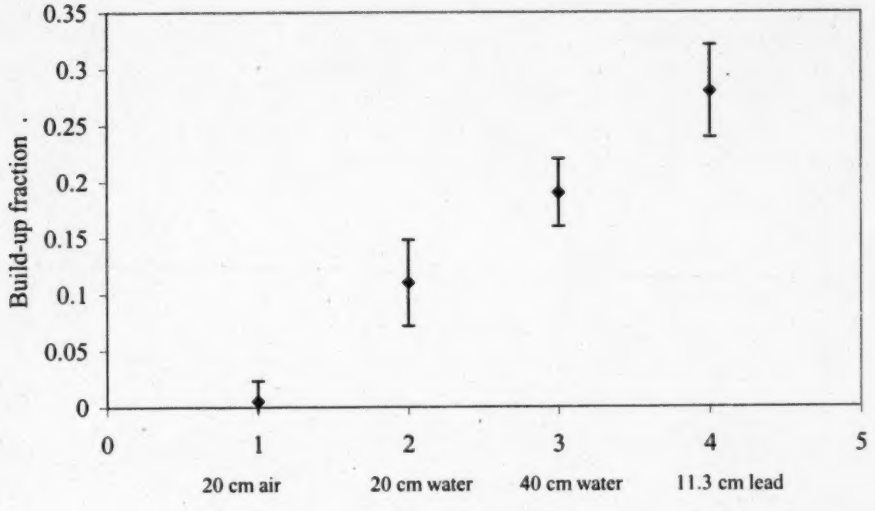

Figure 5-13. Fraction of ROI counts attributed to build-up from different materials.

Quantification of photopeak counts was discussed in section 3.3, however it is difficult to determine whether a simple linear fit (as seen in figure 3-8b) is adequate to quantify the photopeak in the presence of build-up. Subtraction of the buildup by this simple means may not be sufficient to obtain accurate photopeak information, especially when a large amount of build-up is present. To simulate the spectral response from our NaI detectors, the Monte Carlo spectra were convoled with a gaussian kernel that emulated an energy resolution of 8%. The transformed Monte Carlo spectra from figures 5-11 and 5-12 are seen in figures 5-14 and 5-15 using this method. The net photopeak counts were determined using a linear fit method, and the effects of build-up on the spectra were obvious. The counts from build-up created a much larger, highly sloped background, from which the net photopeak counts needed to be determined.

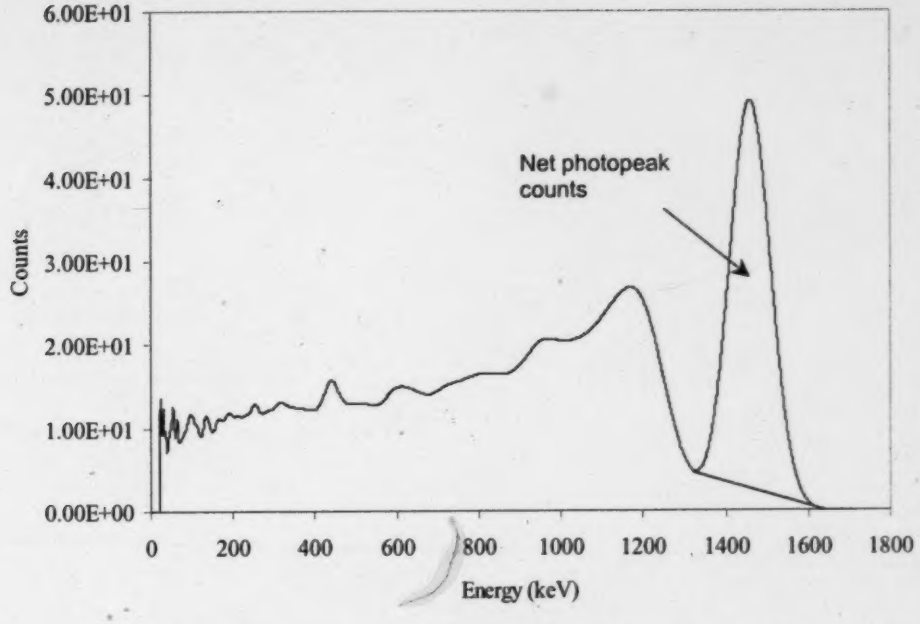

Figure 5-14. Monte Carlo NaI spectrum for 1.46 MeV photons through 20 cm of air.

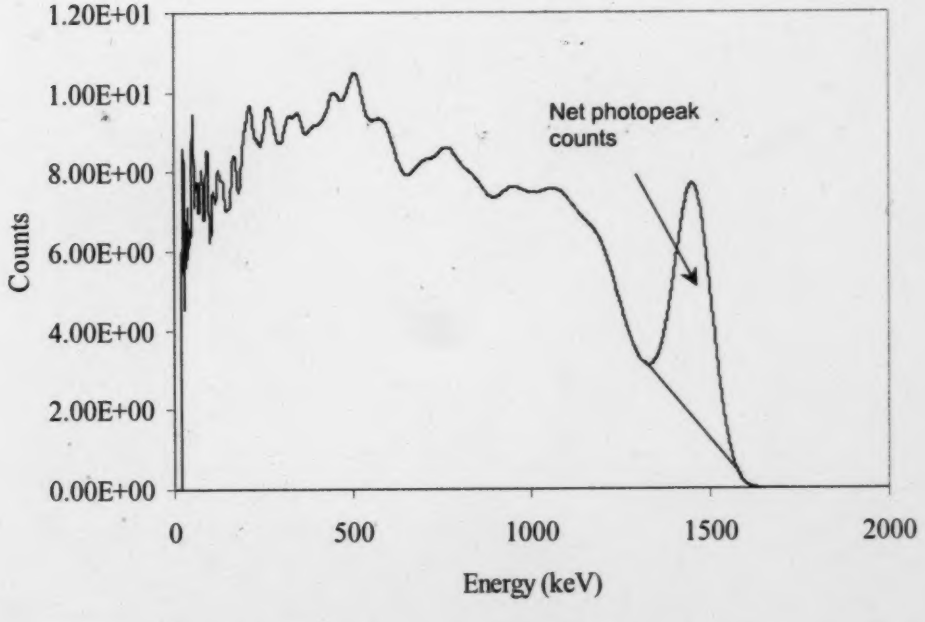

Figure 5-15. Monte Carlo NaI spectrum for 1.46 MeV photons through 11.3 cm of lead.

Using the generated NaI spectra and the linear fit model, the net photopeak counts were calculated for each material and thickness shown in figure 5-13. The fraction of the measured net photo-counts from the NaI spectra, and the true photopeak counts from Monte Carlo simulations were then plotted.

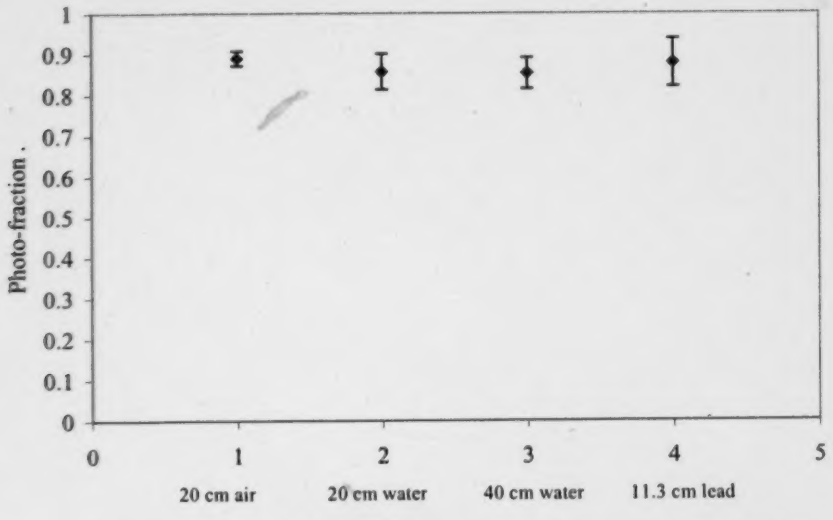

Figure 5-16. The fraction of calculated to actual photopeak counts for air, water, and lead.

Within error, all materials and thicknesses have the same relative net photopeak response when calculated using the linear fit model, despite the amount of build-up present. Therefore, the linear fit model for background was effective in eliminating the affects of build-up on photopeak quantification. The first-order approximation method therefore will indeed deliver fairly accurate relative detector responses when compared with the photo-counts from actual (experimental) spectra. The consistent offset between measured and calculated values seen in figure 5-16 will be corrected for by applying the calibration factor for the WBC.

5.3 WBC Optimization: Theoretical & Experimental Methods

Optimization and design of the high-adaptability WBC was made possible by implementing experimental data with theoretical modeling. Many aspects of the counter's design, including collimator-shielding thickness, counter length, and detector

positioning would have been extremely difficult to do with experiment or theory alone. The Semi-Empirical-Regression method described in the previous section, and the first-order approximation simulator are applied here to various aspects of WBC design, optimization, and absolute quantification determination.

Primary Shielding Thickness

As discussed in Chapter 2, whole body counters are surrounded by massive amounts of shielding in order to reduce detected background radiation levels. This increases the signal-to-noise ratio, thereby helping reduce quantification errors and the MDA.

There are various types of shielding used in whole body counting as seen in Chapter 2, however most common for gamma sensitive detectors is the use of lead or steel as the primary shielding material. Lead shielding was chosen for our whole body counter because it is the most concentrated (high atomic number) common shielding material available. Concentrated shielding delivers the largest attenuation properties per unit volume, therefore imposes the least number of constraints on WBC design. All counter types, including shadow and room shielded counters can be made using lead as a shielding material. New lead does contain some Pb-210 contamination, however there are methods (see Chapter 7) which can be employed to minimize its affect on the acquired WBC spectra.

In general, the more shielding that is added around a detector, the lower the detected background counts, but how much shielding is "enough"? Chapter 2 reviewed the sources of background radiation, and among all sources, cosmic radiation is the most difficult to shield against. Cosmic radiation partly contains an electromagnetic or 'soft' component, which is made up of photons and electrons/positrons which are easy to attenuate. There is also a 'hard' or meson component to cosmic radiation as well, which is extremely difficult to shield against. Pi-mesons go on to produce mu-leptons, which have the same charge as an electron or positron, but are approximately two hundred times heavier. As a result, muons do not lose much of their kinetic energy through Bremsstrahlung radiation, but instead almost entirely though excitation and ionization. Muons have a low cross-section for nuclear interactions, but when they do react or decay,

they create more radiation in the shielding called 'build-up' radiation. Much work has been done in determining the extent of cosmic ray buildup[13,14], and ways to shield from cosmic rays[15,16].

Par Pierre Auger examined the attenuation of cosmic rays through various thicknesses of materials[17], and his results using lead and aluminum as attenuating materials can be seen in figure 5-17 below.

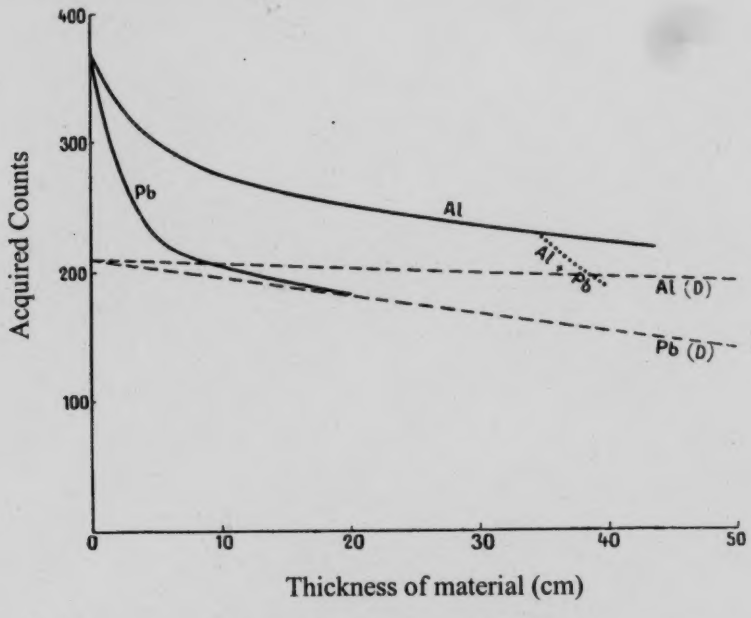

Figure 5-17. Cosmic ray attenuation through various thicknesses of Al and Pb.

The above figure clearly shows the different attenuating characteristics of the hard and soft cosmic ray components. The dotted curves show the hard-component contribution, and the solid line shows the total detected counts. The soft component is for the most part completely attenuated using approximately 10-11 cm of lead, however the hard component is still largely present after even 50 cm of shielding due to build-up effects in the material. Using more than 10 or 11 cm of lead shielding has little effect in shielding against cosmic radiation.

Eleven centimeters of lead is sufficient for shielding soft cosmic rays, however the *appropriate* shielding thickness will also depend on the WBC's uses. Using 11 cm of

lead may be excessive if a counter is not used for very low level studies, or if low-energy isotopes need quantification. On the other hand, if extremely low-level studies need to be performed, and high-energy isotopes need to be quantified, more shielding may be necessary.

For our purposes, we are interested in quantifying activity levels as low as natural body background. High-energy isotopes are more difficult to quantify than low-energy ones. Therefore, the most difficult to measure naturally occurring isotope commonly found in the body is potassium-40. K-40 quantification gives information on body composition, therefore is of interest in whole body counting. Potassium-40 decays primarily by beta-minus decay, however 11% of the time will emit a 1.46 MeV gamma following electron capture.

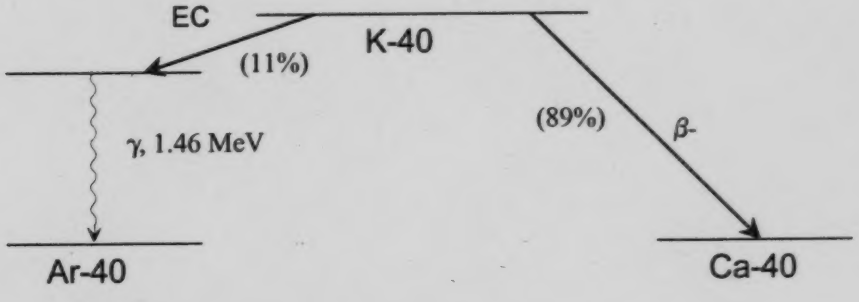

Figure 5-18. Decay scheme for Potassium - 40.

In order to quantify low levels of K-40, background levels around the 1.46 MeV photopeak must be low in a WBC. This is difficult to do however, because potassium-40 is *the* largest terrestrial contributor to the background spectrum. Potassium-40's 1.46 MeV peak is very prevalent in the background spectrum, as seen in figure 5-19, first seen in Chapter 2. Enough shielding therefore must be used to virtually eliminate the 1.46 MeV background peak. This can be achieved by using 11 cm of lead, which was shown to be satisfactory for attenuating soft cosmic radiation, and is the $1/760^{th}$-value layer for 1.46 MeV photons. The one thousandth-value layer thickness was considered to be enough to 'virtually eliminate' the K-40 peak, however in addition to the primary shielding, graded shielding was also to be used, which will help in attenuating the K-40

photons. Therefore, a lead thickness of 11 cm was considered satisfactory as the primary shielding in the whole body counter.

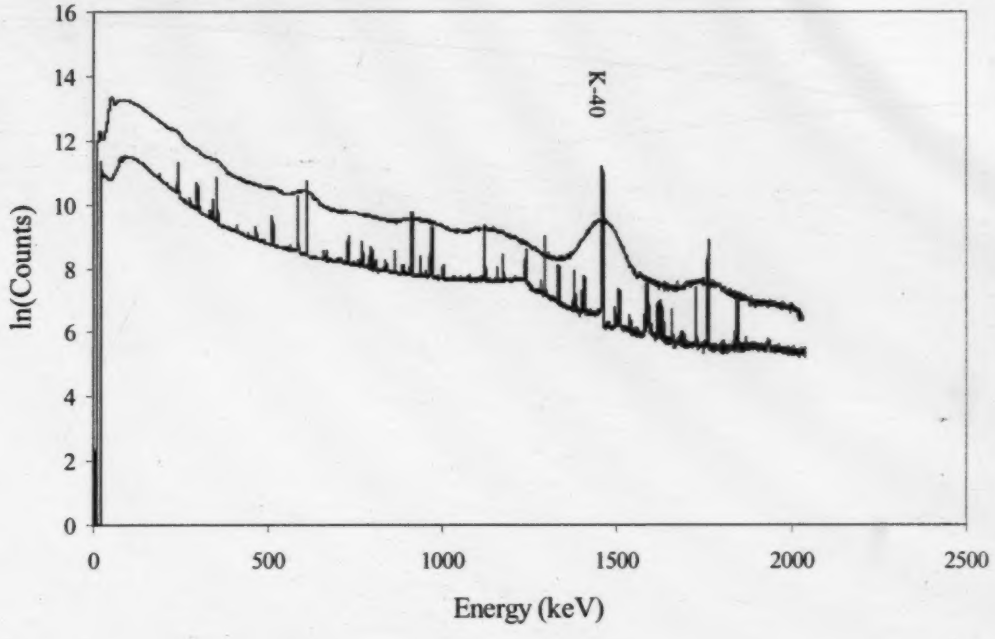

Figure 5-19. Background radiation spectrum for the Edmonton region.

Graded Shielding

As already discussed in Chapter 2, graded shielding is used to attenuate characteristic x-rays that are produced in materials. If unshielded, these characteristic x-rays can appear in a detector's spectrum, can increase the background counts, and can interfere with isotope quantification. A common method of attenuating these x-rays is by placing one or more lower Z materials between the detector and the source of x-rays. Since lead is used as the primary shielding material in our WBC, lead x-rays of ~ 72 keV need to be attenuated. If left unshielded, the quantification of Xe-133 (81 keV), Ga-67 (93 keV), and Tl-201 (71 keV) would be compromised. Copper is commonly used to shield lead x-rays, and was chosen in our counter because it can be made relatively free of radioactive impurities[18]. The one thousandth-value layer for 72 keV x-rays in copper (0.7 cm) was chosen to attenuate the lead x-rays. Copper's characteristic x-rays have an energy of ~ 8 keV, and although not necessary to remove these x-rays for whole body

counting, it does no harm to eliminate these as well via graded shielding. Perspex is commonly used to attenuate copper x-rays because of its very low isotope contamination, however in our counter we chose to use aluminum. Aluminum tends to be higher in activity, however only 0.04 cm is required to reach the one thousandth-value layer for copper x-rays (as opposed to 0.4 cm of perspex). The NaI crystals are housed in aluminum cans, therefore the detectors are already susceptible to Al impurities. Aluminum was also chosen so that the inside surface of the WBC would be easy to clean, and aesthetically pleasing. Aluminum characteristic x-rays (1.5 keV) will not penetrate the detector can, therefore do not need to be shielded.

When both the primary (11 cm Pb) and graded shielding (0.7 cm Cu, 0.04 cm Al) are taken into account, the $1/910^{th}$ value layer for 1.46 MeV photons is reached. This is very close to the $1/1000^{th}$ value layer originally sought. Only perpendicular rays were used in the attenuation calculations. Practically however, the $1/1000^{th}$ value layer will be exceeded since many gamma rays will strike the shielding on an angle, adding to the actual ray-length through the shielding material.

Shadow versus Room Shielding

Room and shadow shielding techniques were discussed in Chapters 1 and 2 of this thesis, however in this section experimental spectra from each shielding method are compared with one another to determine which method is more effective.

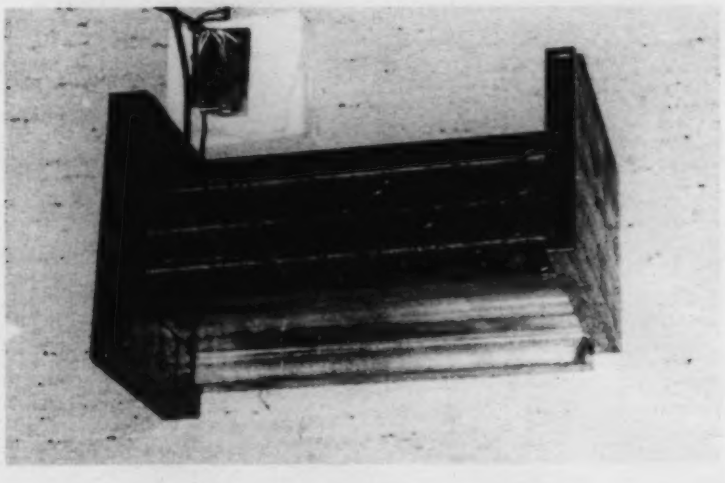

Figure 5-20. Lead shielding configured in a room-shielded arrangement.

Lead shielding was constructed in a room-shielded configuration, and one of the NaI detectors was placed inside. The shielding was made 3 cm thick, with a 2 cm thick face. A picture of the room-shielded setup can be seen in figure 5-20. A similar setup was also constructed for the shadow-shielded case, where the face of the room-shielded setup was replaced by a shadow-shield. This arrangement, with some of the shielding removed, can be seen in figure 5-21. The arrows show one possible path for background radiation to scatter into the detector.

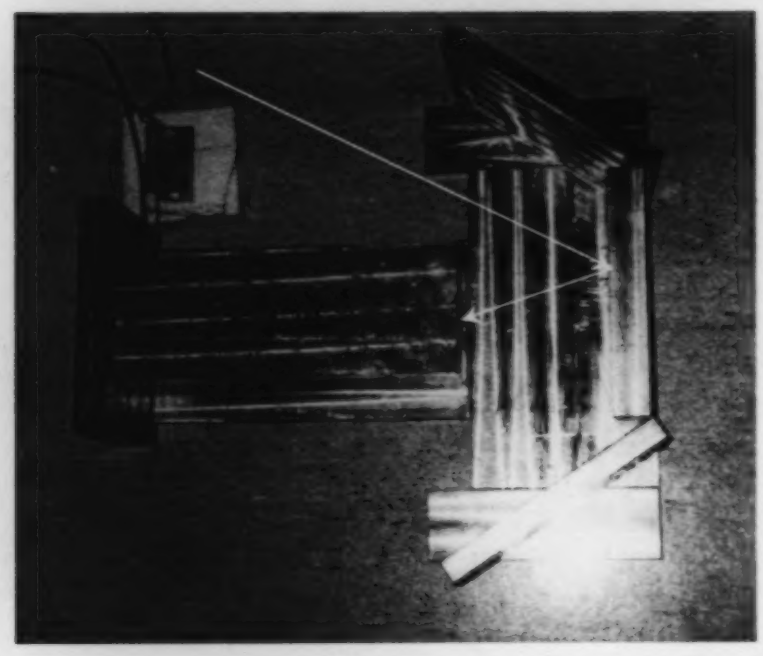

Figure 5-21. Lead shielding configured in a shadow-shielded arrangement.

With the shadow-shielding configuration, it was expected that there would be more background counts towards the lower end of the energy spectrum as compared with the room-shielded spectra. Part of the counter is open to the outside background radiation, and although there is no direct line-of-site, some scattered radiation should find its way to the detector. Compton scattered photons, and bremsstrahlung from charged particles in the shielding will contribute to the low end of the energy spectrum. The

impact of this extra scatter on the spectrum is difficult to quantify, and is the reason behind these experiments. The smoothed spectra for both shielding configurations (for a two-day background acquisition) can be seen below.

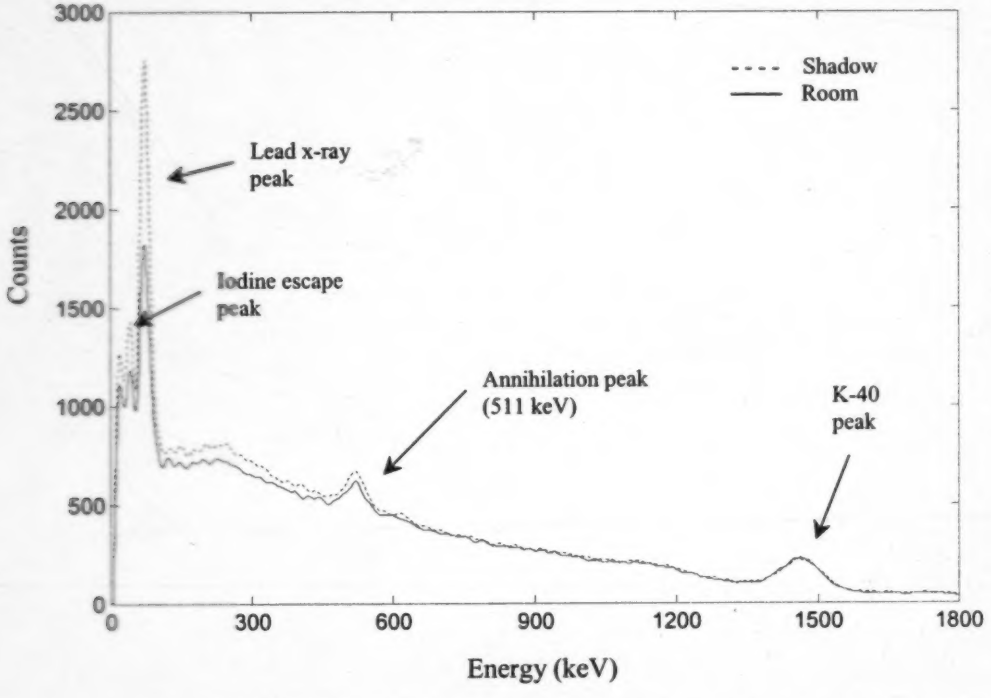

Figure 5-22. Shadow and room shielded background spectra for ~2 cm of lead shielding.

As expected, the lower end of the energy spectrum in the shadow-shielded case does contain more counts. The overall shadow-shielded spectrum, excluding energies less than 100 keV contains approximately 5.8% more counts than in the room-shielded case. For energies less than 100 keV, there was a 25.9 % increase in counts. This region of the spectrum contains a lead x-ray peak at 72 keV, and an iodine escape peak at 47 keV. There is a dramatic increase in the amount of lead x-rays produced for the shadow-shielded setup due to the higher radiation flux striking the inside lead surface. Approximately 61.4 % more lead x-rays were produced in the experiment, which in turn produce the iodine escape peak. The iodine escape peak increased by 31.9%.

The increased low-energy background counts observed in the previous experiment will be present in a shadow-shielded WBC, but to a much lesser degree. Graded shielding will eliminate the lead and iodine escape peaks, which make up a large fraction of the increased background. Because the emission of bremsstrahlung radiation is dependant on Z^2 of the shielding material, the low-Z graded-shielding will reduce the production of bremsstrahlung radiation. The shadow-shielded surfaces in the experiment ranged from 0 – 10 cm away from the detector, however in a WBC they would be much further away. This would reduce the probability that scattered, back-scattered, and bremsstrahlung radiation would strike the detector, thereby reducing the background radiation. The presence of a human body or phantom in a whole body counter will act as a scattering medium for radiation, and will contribute to the background counts. However, it will also attenuate primary, scattered, and bremsstrahlung radiation, therefore reducing the overall low-energy background counts[19]. All of these factors reduce the low-energy background counts in a shadow-shielded WBC, making its spectrum approach that of the room-shielded spectrum.

Based on the shielding experiments, there is little difference between shadow and room-shielded background spectra. Therefore, shadow shielding was chosen for our whole body counter. The advantages and disadvantages of both shielding types was discussed in Chapter 2, however because shadow-shielded counters require less shielding material to construct, and the entire room does not have to be altered, this shielding method was chosen. Shadow-shielded counters are difficult to construct to be both efficient and stationary, therefore a scanning, shadow-shielded WBC design was chosen. As mentioned earlier, scanning WBCs are considered to be preferable to static counters.

WBC Length Optimization

The length of a whole body counter will have a direct impact on the counter's efficiency and therefore its MDA. As can be seen in figure 5-7 for both the collimated and uncollimated case, the closer that a detector can be placed to a subject, the greater its efficiency. For a scanning WBC therefore, given that a detector has a flat response across the width of the subject, it should ideally be placed as close to the subject as possible (shown in figure 5-23).

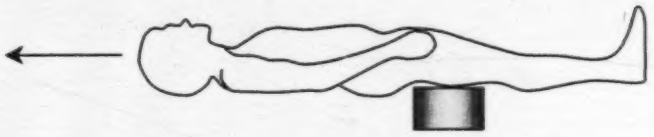

Figure 5-23. Ideal subject-detector configuration for a scanning WBC.

With a shadow-shielded WBC, this 'ideal' subject-detector setup can not be practically accomplished. Shadow-shielded whole body counters have a finite length, and this restricts how close a detector can be placed to the subject while still remaining well shielded. Figure 5-24 illustrates this point.

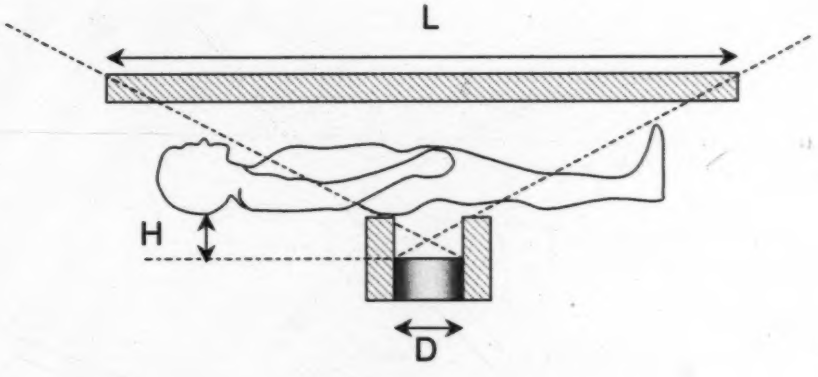

Figure 5-24. The critical distances in shadow-shielded WBCs.

The length *L* of the WBC and the diameter *D* of the detector will determine the minimum subject-detector distance *H*. The shortest subject-detector distance is achieved using a long WBC. The length of the WBC is dependent on the diameter of the detectors.

Since we have chosen to use a shadow-shield configuration in our WBC, and the detector diameter is known, the length of the counter can be optimized. The Reference Man thorax and the first-order approximation were used to determine the relative detector response for varying lengths of a WBC. Figure 5-25 shows the results of varying the counter length from 100 cm to 375 cm.

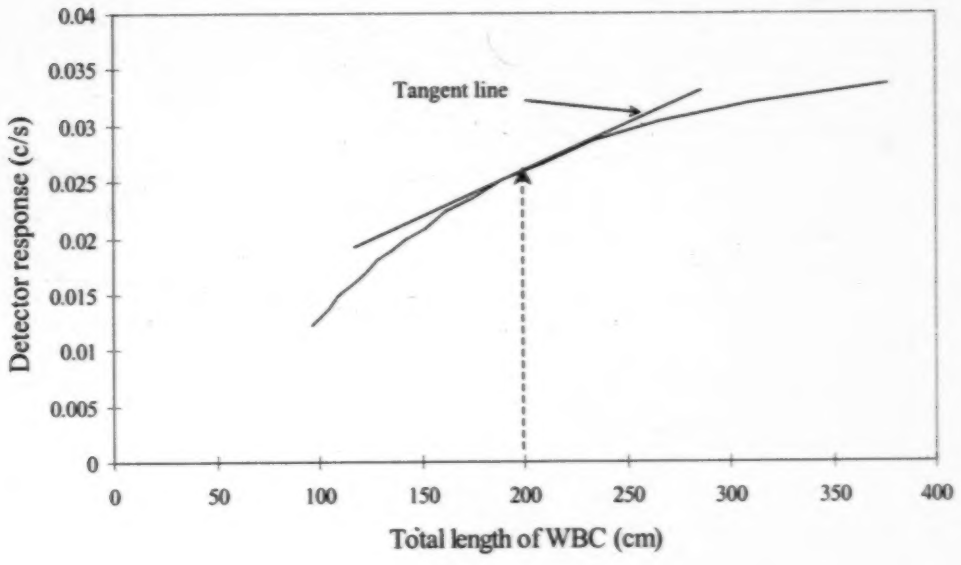

Figure 5-25. The relative detector response from a varying-length WBC.

As expected, for longer counter lengths, there is an increase in the detector response. The curve seen in figure 5-25 will continue to increase, until it reaches its asymptote at L = infinity (or subject-detector distance = 0 cm). It can be seen from the graph, that the detector response increases more drastically with a slight increase in length if the WBC is shorter to begin with. For longer WBCs, lengthening the device does not produce as drastic a gain in response. This gain becomes smaller and smaller, until a constant rate of gain is achieved at approximately 300 cm. Practically, the thickness of the lead has to be added to the length, as well as the superstructure thickness. A counter with 300 cm of shielding can practically become 350 cm long. This length can be hard to fit into a room if a scanning bed is to be added. This will add another 200 - 400 cm to the length, making the overall length of the counter quite long. For these reasons, a counter shielded length of 200 cm was chosen for our counter. At this length, 82% of the detector response obtained at 300 cm is achieved, while keeping the counter at a reasonable length. A tangent line at the 200 cm point on the curve has been drawn in figure 5-25, and shows an acceptably flat slope at this point.

The NaI detectors that will be used for our WBC have a small diameter, therefore are well suited to a shadow-shielded arrangement. The small detector diameter allows the detectors to be placed very close to the subject while remaining fully shielded.

Detector Bank Configurations

The large number of detectors available, and their small size allows for a large combination of possible shadow-shielded detector arrangements. All viable configurations were investigated using the first-order approximation and the Reference Man thorax. A summary of the findings and the methods are discussed here.

For a scanning WBC, the detector response across the width of the subject should be as flat as possible. This means that a point source placed in the left or rightmost section of the thorax would give the same response as if it were placed in the center. Our small NaI detectors on their own would definitely not deliver a flat response, since their efficiency is highly spatially dependent on the lateral position of the source. The geometric efficiency for a single detector face can be seen in figure 5-26.

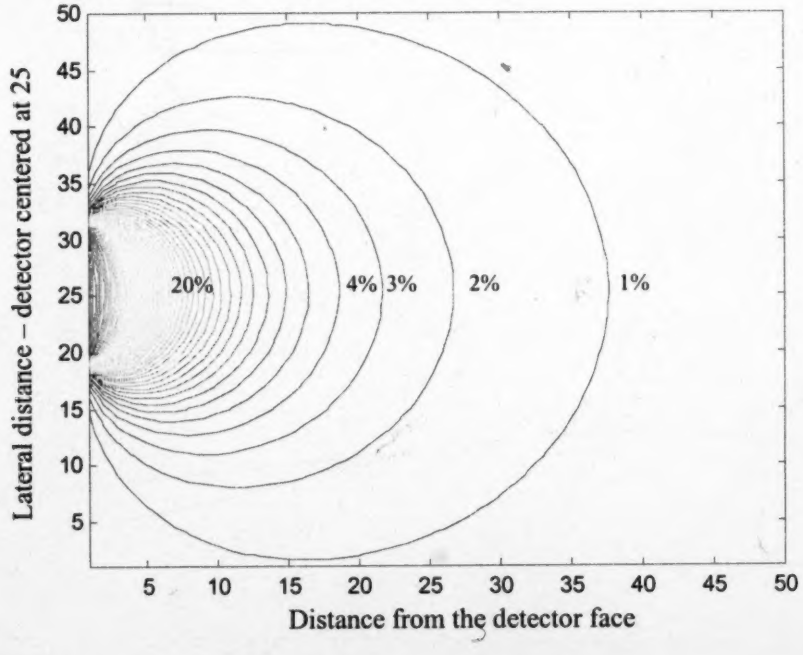

Figure 5-26. Geometric efficiency iso-response curves for a single detector (1div=3mm).

When several of these detectors are placed side by side however, as is the case with one of the detector banks (figure 4-2b), and placed perpendicular to the subject, the lateral response is very good.

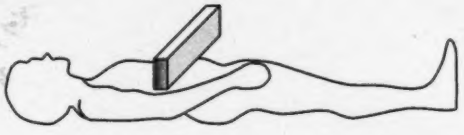

Figure 5-27. A detector bank placed perpendicular to the subject.

The individual responses from each of the detectors in the bank can be summed to create an overall flat response. This summing affect is seen below in figure 5-28, where the iso-response curves for the geometric efficiency of the entire detector bank is shown.

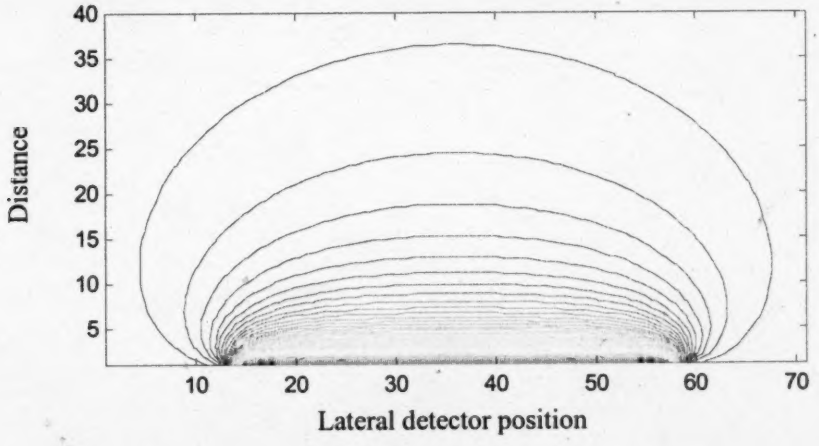

Figure 5-28. Geometric efficiency iso-response curves for a detector bank (1div=12mm).

The iso-response curves are very flat for all distances, deviating only by approximately one percent over the width of the bank. Detectors placed side-by-side in a linear fashion perpendicular to the subject proved to deliver excellent detector responses, therefore this detector bank orientation was chosen for our scanning WBC. Because of the small size of our detectors, other orientations do not deliver flat responses. Longitudinal responses in scanning counters are always flat since all subject sources are always scanned past the detector in exactly the same way, regardless of their longitudinal position. Large

rectangular crystals would provide better detection efficiency, however this project was constrained to work with the available detectors.

Up to this point, it has been decided that a shadow-shielded, scanning WBC, with its detector banks placed perpendicular to the subject is the optimal configuration for our counter. There are two further arrangements that need to be investigated: side-by-side detector bank positioning, and shielding-separated banks. These two configurations are illustrated below.

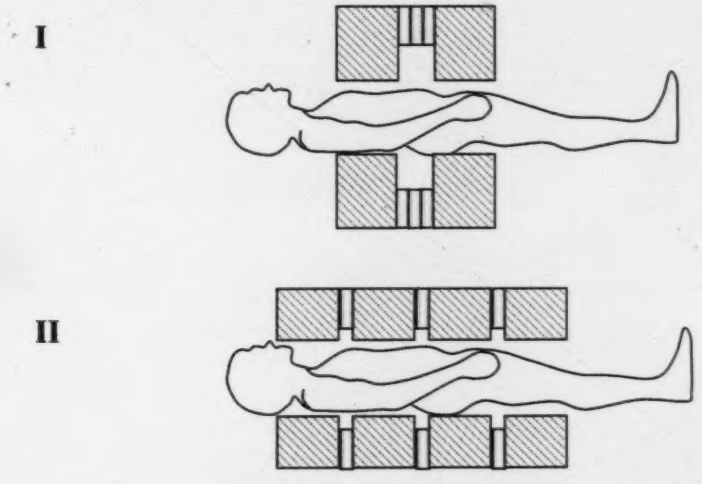

Figure 5-29. Side-by-side (I), and shielding-separated (II) bank configurations.

The side-by-side configuration has the six detector banks stacked side-by-side, three above the subject, and three below the subject. Collectively, the three detector banks and their detectors act as one large detector. Conversely, the shielding-separated configuration has shielding placed between each detector bank. With this setup, because only one detector bank needs to be shadow-shielded by its adjacent shielding (or 'collimators'), the detectors can be placed approximately two times closer than with the 3-bank side-by-side configuration. Recall from figure 5-24 that the subject-detector distance is related to the detector's diameter.

The two configurations were compared using the first-order approximation and the Reference Man thorax. Eight detectors were placed in each detector bank, and the cumulative relative detector response for homogeneous and point-source (located at the

center of the thorax) activities was modeled. Point source responses were calculated for the cases where the point source was always inline with the detector bank, when it was inline with the central detector bank only, and when it was scanned past the banks. The results can be seen in table 5-2.

Activity distribution	Side-by-side activity	Shielding-separated activity
Homogeneous	0.425	0.521
Point, inline with banks	2.07	2.34
Point, inline with middle bank	1.76	0.849
Point source, scanned	0.409	0.476

Table 5-2. Relative activities for side-by-side and shielding-separated WBCs.

Because the detectors in the shield-separated configuration are twice as close to the subject as in the side-by-side case, there is generally a better detector response. For homogeneous distributions, it is 23% better, for inline point sources it is 13 % better, and for a point source scanned past the banks, it was 16% better. For a point source located inline with the middle detector bank only however, the side-by-side arrangement is 107% better than the shield-separated configuration. This is because the off-center banks in the side-by-side arrangement are very close to the middle detector, and almost inline with the point source. The off-center banks with the other configuration are much farther away from the middle bank.

For whole body counting, homogeneous or somewhat distributed sources need to be quantified rather than a single point source, and with our counter this will be done in a scanning fashion. Therefore, the shield-separated configuration is best suited for our WBC. The only advantage in using the side-by-side arrangement would be if a point source needed to be quantified, and the counter was held in a static manner with the detectors held directly above the source. A four-bank shield-separated arrangement was also investigated, however its detector responses were lower than the three-bank system described here.

Collimator Thickness Optimization

In the last section, the shield-separated configuration used a collimator-shielding thickness of 11.3 cm of lead to separate the detector banks, however this may not be the optimized amount. If very little collimator shielding thickness is used, then the amount of background radiation reaching the detector will increase, and the detector's signal-to-noise-ratio (SNR) will *decrease*. However, because the detector can be positioned closer to the subject (see figure 5-30b), it is more efficient at detecting radiation from the subject, and this will *increase* the SNR. Using a massive thickness of collimator shielding (figure 5-30a) will have the opposite affect on the SNR. An optimal collimator shielding thickness exists, where there is a perfect balance between the extent of background shielding, and detector efficiency. This optimal collimator thickness needs to be determined.

In a WBC, the collimators should allow for proper shielding of the detectors, while delivering a maximum detector field-of-view. For the central bank, the shielding method for collimation is fairly straightforward. All primary rays from background pass through a minimum amount of shielding material before reaching the detector, and a wedge-shaped section allows for a large detector field of view. The middle bank collimators are shown below for the two extreme cases. Collimator design for the entire counter is discussed in the next section.

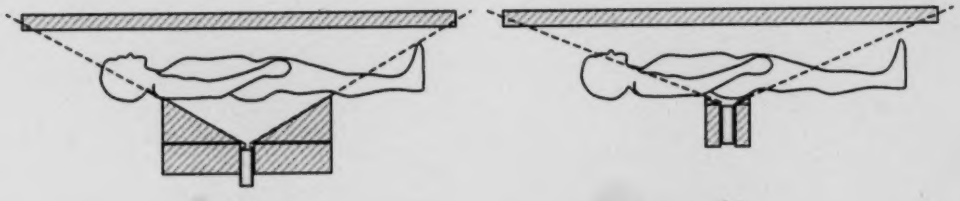

Figure 5-30. Thick and thin collimator arrangements for the middle bank.

To determine the proper collimator thickness, an optimization curve needed to be generated. A WBC's performance can be measured by its MDA, therefore the MDA was optimized, and not the SNR. The MDA incorporates both background counts, and the detector efficiency, therefore it will change as the collimator's thickness varies. At the

point where the MDA reaches a minimum, the collimator thickness will be optimal. Recall from equation 3-3 that the MDA is dependent on the background radiation counts, the detector efficiency, and the acquisition time. If acquisition time is held fixed at 30 minutes (as is common for K-40 whole body counting), then an optimization curve can be generated relating the MDA to the shielding thickness. Because efficiency is inversely proportional to the MDA, the first-order approximation can be used to calculate the detector efficiencies for different collimator thicknesses. With background count information, these relative efficiencies can then be used to obtain relative MDAs, from which an optimization curve can be generated. This curve will have the same shape as if absolute efficiencies were used. The relative efficiencies calculated were for a detector placed in the center of the bottom middle detector bank, with a Reference Man thorax placed above it, containing a homogeneous activity of K-40. Efficiencies were calculated for a variety of collimator thicknesses. The background radiation counts must be determined experimentally, and related to the lead shielding thickness.

To determine how background radiation drops off with shielding thickness, several different thicknesses of lead were placed around one of the NaI detectors. The detector was four-pi shielded, and special attention was taken to ensure that no direct-path background radiation could strike the detector. Lead shielding with a thickness of 2, 3, 5, 6, 8, and 11 cm was constructed, and the gross background counts in the K-40 photopeak were measured. An end view of the shielding used can be seen in figure 5-31.

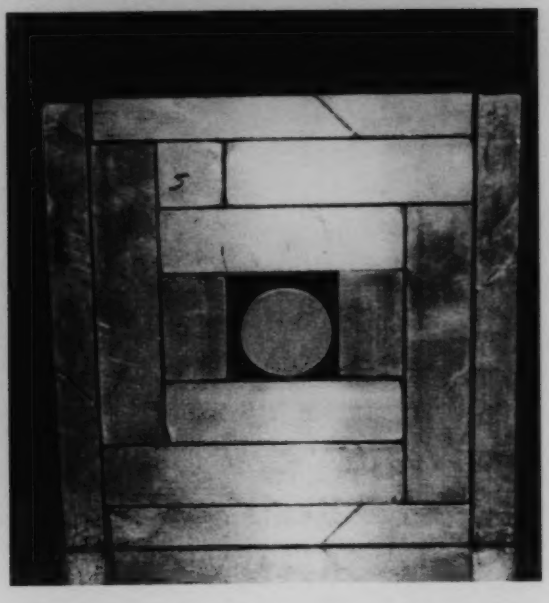

Figure 5-31. End-view of the shielding used to determine background attenuation.

For each shielding thickness, a different background count was measured (figure 5-32), and a different relative efficiency was calculated from that thickness of collimator.

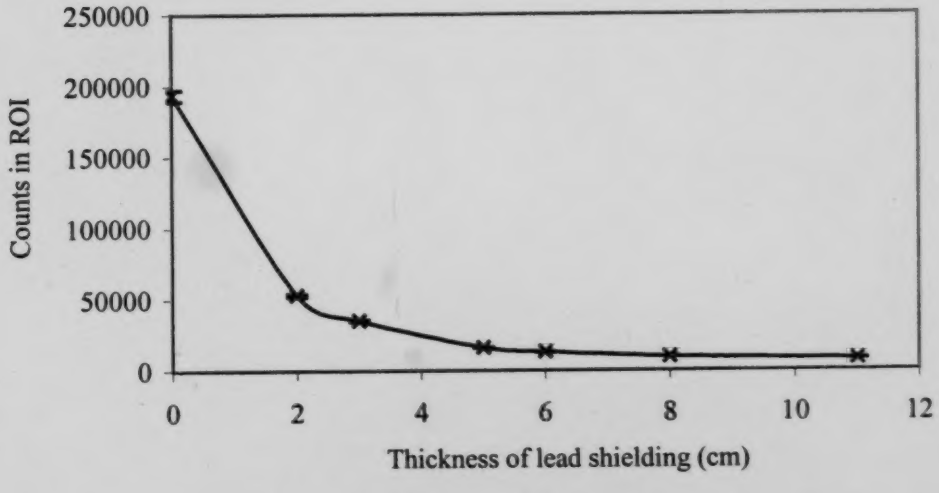

Figure 5-32. Attenuation of background through different thicknesses of lead.

The MDA for each collimator thickness could then be calculated, and an optimization curve plotted. This curve can be seen below in figure 5-33.

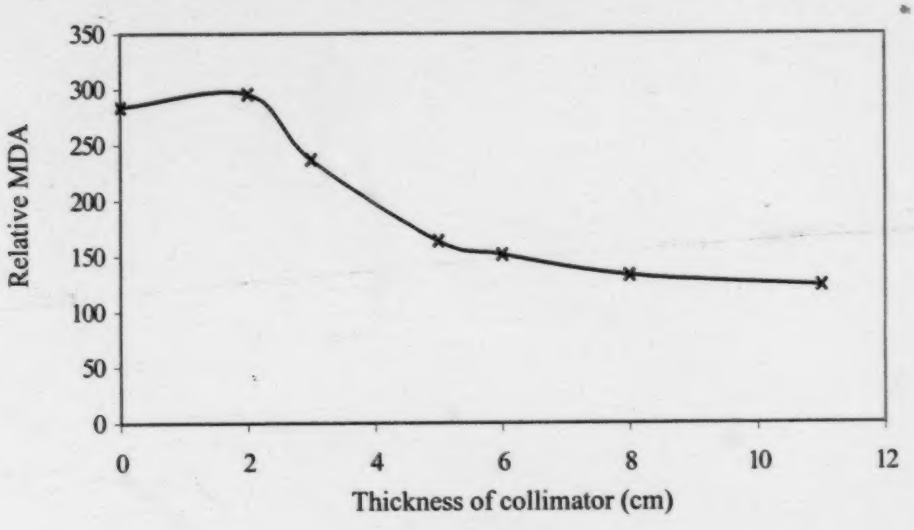

Figure 5-33. Optimization curve for lead collimator thickness.

The collimator optimization curve flattens off at approximately 8 cm, and continues to decrease slowly up until 11 cm. By extrapolating the experimental data, it was shown that with more lead shielding, the MDA does increase from this minimum. This curve confirms that using 11.3 cm of lead as the collimator thickness is indeed the proper thickness. Less shielding should not be used, and adding more shielding would only decrease the MDA by very little if any. A lead collimator shielding thickness of 11.3 cm, the same as the primary shielding thickness, was chosen for the WBC's collimators.

The MDA's in figure 5-33 are quite high, however it is expected that the actual MDAs will be lower. This is because the first-order approximation used to generate the MDAs underestimates the detector's efficiency, as was shown in figure 5-9.

Collimator Design

The basic collimator design for the middle detector banks was discussed in the last section, however when the neighboring detector banks are added to the whole body

counter, this complicates the design somewhat. The collimators must accommodate both detector banks, and still have a good shielding design.

Ideally in a shadow-shielded whole body counter, there are several criterion that need to be satisfied: 4-pi shielding for all detectors, largest FOV possible, detectors placed as close to the subject as possible, shielding inside the counter allowing primary radiation to strike only at large incident angles, and lead x-rays properly attenuated. These factors have all been incorporated into the final collimator design, seen below.

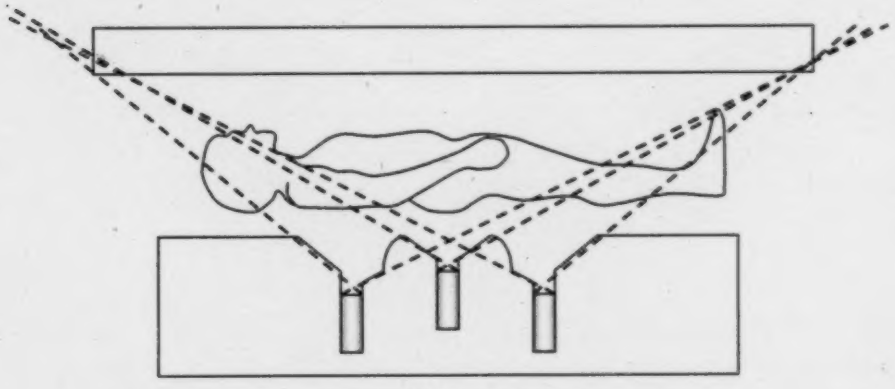

Figure 5-34. Final collimator design for the whole body counter.

The central detector banks are shielded such that the detectors have the maximum FOV, while remaining shielded at all angles. For all angles, primary background radiation must pass through 10.7 cm of lead, and two layers of graded shielding, totaling 11.3 cm lead shielding equivalent. A minimum amount of material was used so that the detectors could be placed as close to the subject as possible. A diagram of the central bank shielding and its graded shielding is seen in figure 5-35.

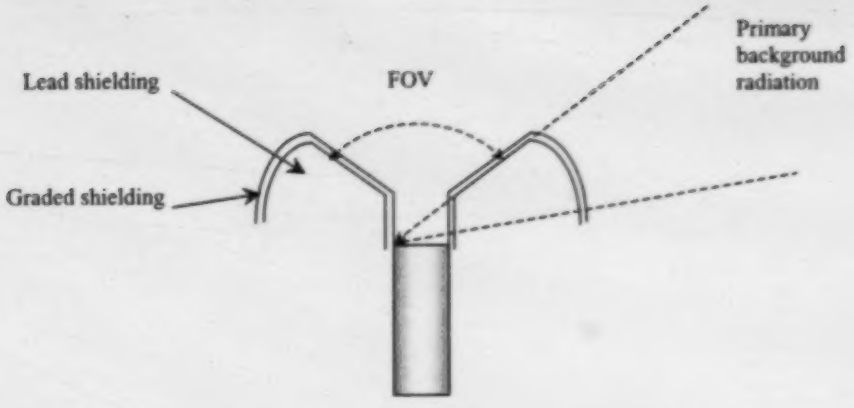

Figure 5-35. The central-collimator shielding design.

The neighboring detector banks need to be shielded in a different manner, since their collimator shielding is partly made up of the central bank's shielding. Because of the geometric constraints of shadow-shielding, in order to place the neighboring banks as close to the subject as possible, they must be located as close as possible to the center of the WBC. The neighboring banks must be adequately shielded however, which limits how close they can be placed to the center of the WBC. Optimal positioning can be achieved by using the central bank's collimators as part of the primary shielding necessary for the neighboring banks. More shielding can be added, such that the combined thickness of the added shielding and the center bank's collimator thickness is equal to the lead equivalent of 11.3 cm. This thickness is denoted by 't', defined by the ray 'A' as seen in the illustration on the next page (figure 5-36), which describes the neighboring bank collimator shielding.

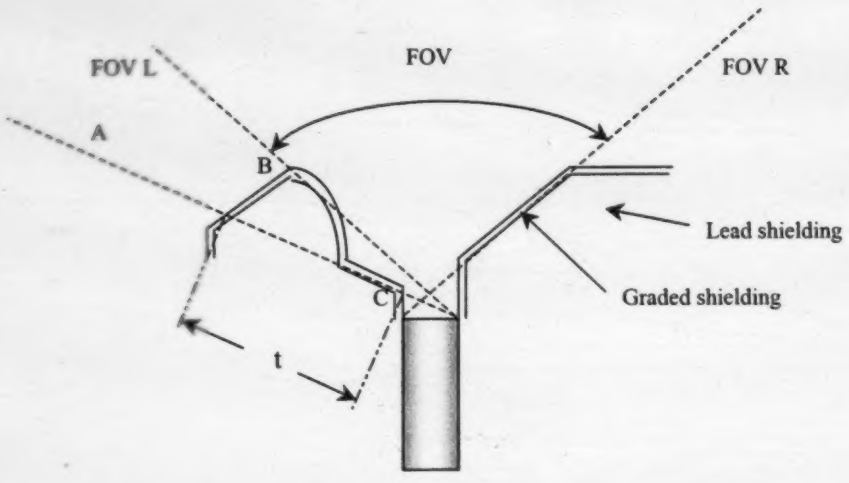

Figure 5-36. The neighboring-bank collimator shielding design (right side).

The collimator shielding design described here will also minimize the amount of scattered radiation that appears in the detector's spectra. From the Klein-Nishina formula (equation 2-2), Compton scattered photons of high-energy are forward scattered off surfaces, and the probability for low-energy photon scattering reaches a minimum at a scattering angle of 90 degrees. With the collimator shielding design in place, primary background radiation will have to scatter off of the graded shielding at an angle of roughly 80-150 degrees in order to reach the detector. Photon scattering closest to the detector occurs at approximately 80 degrees. Rayleigh scattering is highly forward scattering for keV and MeV photons, and will be reduced by this collimator design as well.

The discussion and results in these last two sections were based on detector banks placed below the subject, however by symmetry, the exact same argument can be used to place three banks above the subject as well. Therefore, the same collimator design and thickness used for the bottom banks were also used for the top banks.

To make construction of the WBC's collimators an easier task, the curved surface in the collimators was replaced by a flat surface which spanned the corners labeled 'B' and 'C' in figure 5-36.

Number and Location of the WBC's Detectors

In order to optimize the number and location of the detectors in the WBC, a combination must be found that will deliver the most efficient and flattest combined detector response possible.

Optimum placement of the detector banks has been achieved, however whether or not to use the original eleven detectors in each bank is yet to be determined. With six detector banks available, three banks could be placed above the subject, and three below. The geometric efficiency from a point source for the detector faces from two opposing banks containing eleven detectors each can be seen in figure 5-37. Neighboring iso-response lines correspond to a one percent change in the overall geometric efficiency.

The area contained within the dashed box defines the physical limits that a subject would be confined to inside the WBC. A fixed subject width of 57 cm was used for the WBC so that most of the Canadian population could fit inside it; the shoulder width of the 95th percentile Canadian (BOMAB) man is 57 cm. The height of the subject area in the figure was set at 20 cm, the thickness of the Reference Man thorax. This distance will vary with the subject thickness, and is discussed in detail in Chapter 6. The distance between the dashed box and the detectors is the distance needed to properly shadow-shield the detectors in a 200 cm long WBC.

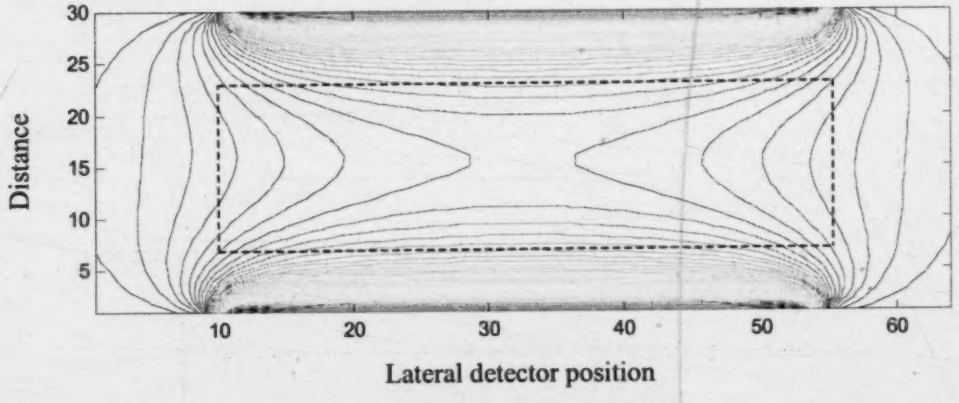

Figure 5-37. The geometric efficiency from two opposing detector banks (1div=12mm).

When only looking at the area inside the dashed box, the response is fairly uniform, but could be better. When close to one bank or the other, the responses are fairly

flat when moving laterally, however at the mid-point between the banks, the lateral response is not very flat. In the vertical direction, the central and end sections of the banks deliver a fairly uniform response, while the response from the other sections is not quite uniform.

To create a flatter overall response, some of the detectors from the original banks were used to create side detector banks. Various combinations were investigated, however the best overall response was found when the length of the banks was similar to the height and width of the Reference Man. Detector banks containing 7 and 8 detectors for the end and middle banks respectively, and with 3 and 4 detectors for the side banks were chosen. A diagram showing the detector arrangement around the WBC's graded shielding is shown below.

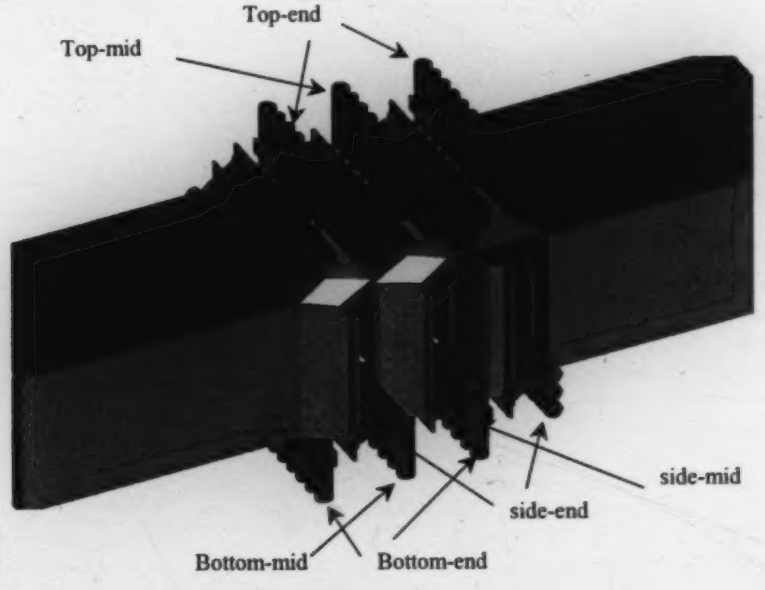

Figure 5-38. The optimized detector arrangement and the WBC's graded shielding

The presence of the side detectors has a two-fold effect on the whole body counter's response. Firstly, the side detectors will contribute towards the detection of laterally placed activity in the subject. This is obvious, since the side banks will be closest to the activity found in the lateral parts of the subject. Finally, placing the side banks opposite each other will create a slight increased response in the center of the

WBC, thus creating a larger flat-response section in the center of the counter. Both of these factors contribute to make a more flat response than was found by using just two opposing banks. The response-flattening effects of the side banks can be seen below. Responses from the end-banks also show a flatter response when side banks are used.

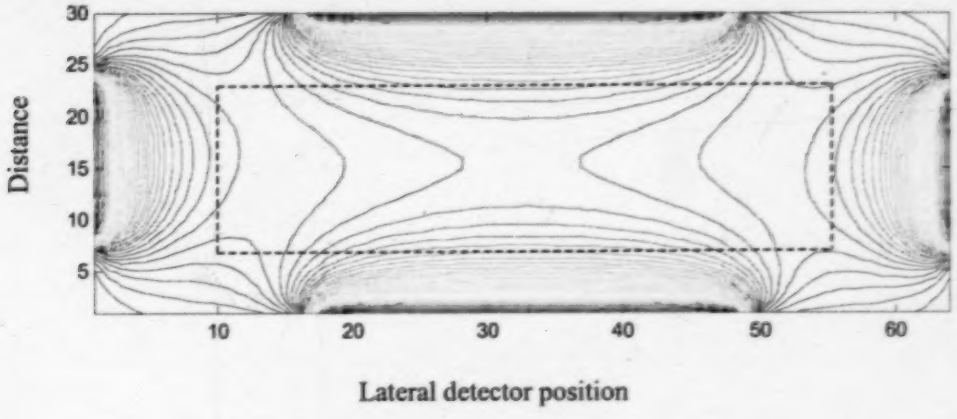

Figure 5-39. The geometric efficiency from all four detector banks (1div=12mm).

Individual detector responses for each possible detector and detector-bank configuration were also determined to ensure that the final WBC would have the highest possible efficiency. Figure 5-40 summarizes the findings.

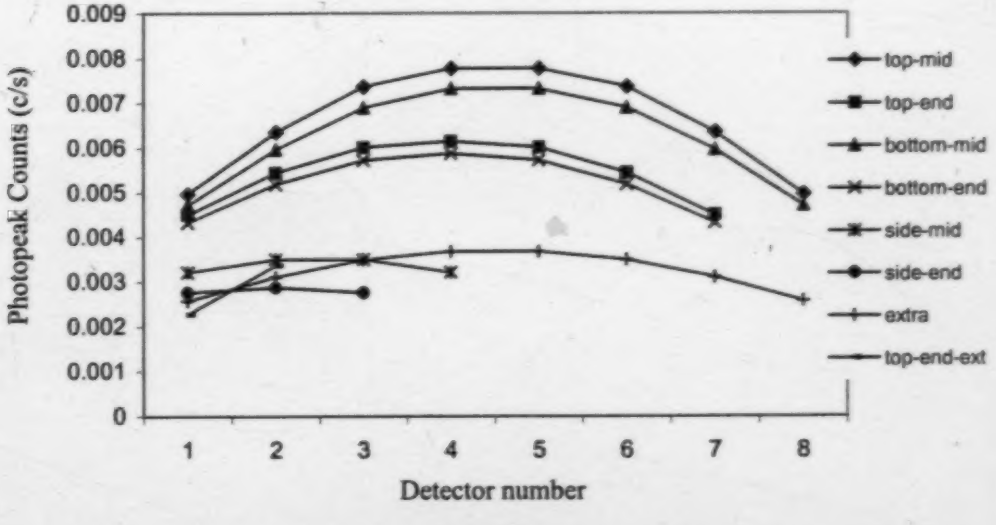

Figure 5-40. Individual detector responses from several detector bank arrangements.

The responses in figure 5-40 were generated using the first-order approximation method for the detectors placed around the mid-section of a K-40 filled Reference Man thorax.

As can be seen from the detector responses in figure 5-40, the detector number and bank configuration illustrated in figure 5-38 is optimal. The side detector responses labeled "side-mid" and "side-end" have a higher response compared to the end-detector responses from a bank containing eleven detectors. The two end-responses for the top-middle detector bank are labeled "top-end-ext" in the figure. If the side detectors were instead used to make up another end-bank for the WBC such that there would be five banks above and below the subject, then the extra bank's response would follow the curve labeled "extra". This response curve is approximately equal to those from the side banks, however the advantage of using side detectors would be lost if this extra bank was implemented. In addition, a five-bank top gantry would be very long, and would have negative implications on efficiency. Top gantry length and its implications are discussed in Chapter 6 of this thesis.

The addition of the side detector banks not only flattens the WBC's response, but is also needed for optimal counter efficiency, therefore was incorporated into the final WBC design.

5.4 Determining and Implementing $W_{tot}(E,\theta,\phi)$

Up to this point in the Chapter, the first-order approximation simulation was used exclusively to investigate several aspects of the WBC. This was necessary since a vast range of WBC length-detector-collimator combinations needed to be examined. As was mentioned earlier, the semi-empirical-regression-method could have been used, however for each different configuration, ideally, a different experimental setup would have had to be constructed so that $W_{tot}(E,\theta,\phi)$ could be determined. This would have been incredibly time consuming, and not of great value.

Up to this point in the project, the whole body counter has been optimized, and its precise dimensions are known. What is not known however, is its absolute quantification ability. Only approximate, relative efficiencies were capable with the first-order approximation simulation, therefore only relative values were obtained for the counter's efficiency. To obtain absolute values, $W_{tot}(E,\theta,\phi)$ needs to be determined for each

detector bank. This is not a daunting task at this point, since there are a small number of bank configurations in the counter. This section discusses the method used to acquire $W_{tot}(E,\theta,\phi)$, and how it was implemented in the whole body counter.

Mapping out $W_{tot}(E,\theta,\phi)$ for the WBC

To map out $W_{tot}(E,\theta,\phi)$ for the whole body counter's detector banks, the bottom-middle bank was constructed, complete with accurate detector spacing, graded shielding, and neighboring NaI detectors. Only five detectors were needed for the map however, due to symmetry. The bottom-middle bank used to map out $W_{tot}(E,\theta,\phi)$ is seen below.

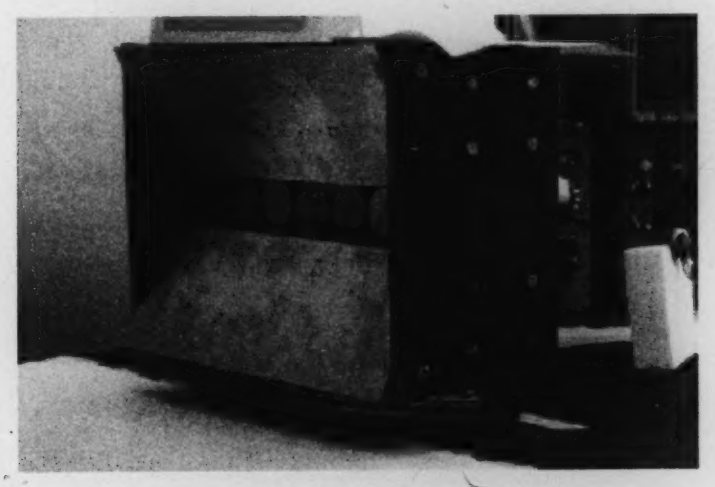

Figure 5-41. The bottom-middle detector bank used to map $W_{tot}(E,\theta,\phi)$.

Because of the rectangular nature of the shielding, a Cartesian coordinate system was adopted in order to map the weighting factors. To map out the weighting factors, a square grid large enough to cover the FOV of interest was constructed and placed perpendicular to the detector face, at a known distance *d*. The distance *d* was chosen to be 20 cm, which is the approximate distance from the detector face to the middle of the Reference Man thorax. The angular position of the source was defined by β_x (the angle between the detector face and the position of the source on the *x* axis), and β_y (the angle between the detector face and the position of the source on the *y* axis). A photograph of the actual matrix setup and an illustration of it are seen in figures 5-42, and 5-43.

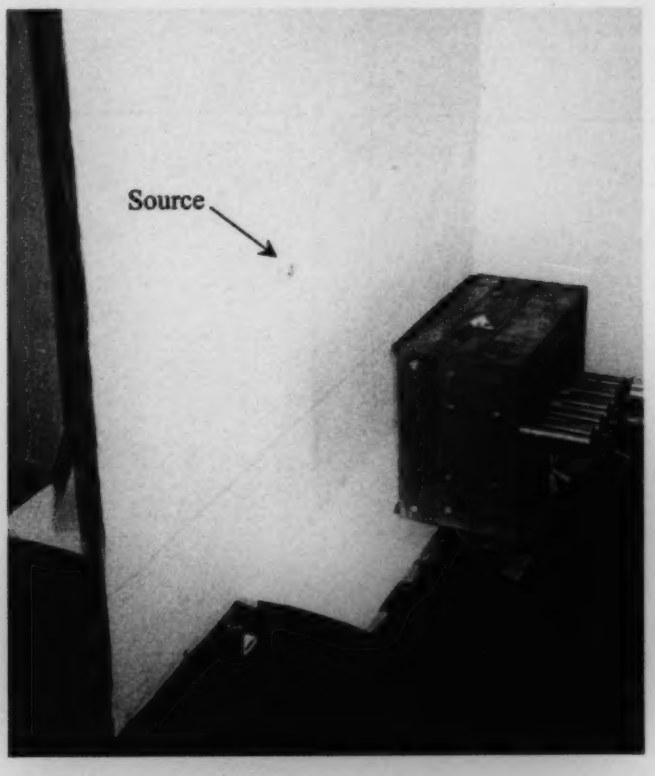

Figure 5-42. The experimental setup used to map $W_{tot}(E,\beta_x,\beta_y)$.

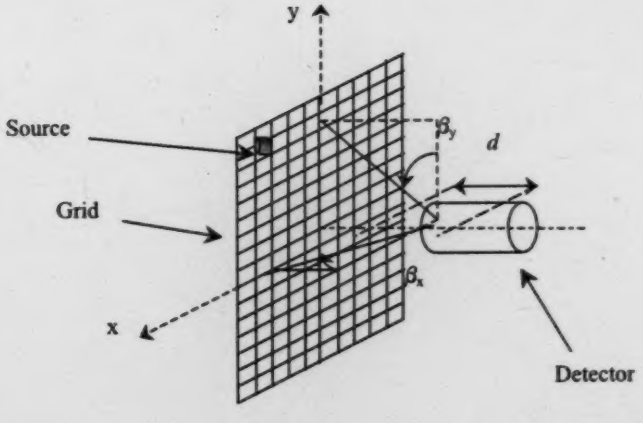

Figure 5-43. The grid-detector orientation used to measure $W_{tot}(E,\beta_x,\beta_y)$.

$W_{tot}(E,\beta_x,\beta_y)$ was mapped out by placing a small radioactive source at periodic locations on the grid, such that the entire FOV of interest was covered. The source was taped to a thumbtack, which was placed at different points on the grid. The WBC's response to naturally occuring K-40 needed to be determined, therefore a source emitting photons with an energy of 1.46 MeV was desired. No K-40 source was available however, therefore the closest energy isotope available, Na-22, was used. Na-22 emits a 1.27 MeV photon with no other gamma emissions above 0.511 MeV, therefore its high energy photopeak is easy to quantify. Na-22's high energy photons will penetrate through the shielding to virtually the same extent as K-40's 1.46 MeV photons, therefore the $W_{tot}(1.46\ MeV,\beta_x,\beta_y)$ and $W_{tot}(1.27\ MeV,\beta_x,\beta_y)$ maps will be virtually identical. The linear attenuation coefficients for lead are 5.62×10^{-2} cm^2/g, and 5.16×10^{-2} cm^2/g for 1.27 MeV and 1.46 MeV photons respectively. The activity of the Na-22 source was measured in a calibrated well counter, and was determined to have an activity of 100209.84 Bq. Ideally, a point source should be used, however the smallest source available was 2 cm in diameter. This larger source size was incorporated into the error calculations.

The entire FOV needed to be mapped, however to save time in acquiring $W_{tot}(E,\beta_x,\beta_y)$, a minimum number of points on the grid were selected by making use of regression analysis via *Excel*. By implementing equation 5-6, several weighting factors were calculated at points on the x and y grid axis, and plotted. One by one in a trial-and-error method, points were removed from the regression analysis, and the integrity of the curve was observed. A minimum number of points were kept, while keeping the regression curve virtually unchanged. Figures 5-44 and 5-45 show the results of this method. To be more thorough, a mathematically rigorous method[20] to determine the minimum number of data points needed to properly define a regression curve could have also been used.

The 'chosen data' regression curve in figure 5-44 is a second-order polynomial defined by only four data points, and the curve in figure 5-45 is a fifth-order polynomial defined by only seven points. Therefore, only a 4x7 $W_{tot}(E,\beta_x,\beta_y)$ matrix, whose β_x and β_y points were defined by the two regression curves was needed. The drastic change in detector response seen in figure 5-45 is due to the shielding in the y direction (see figure

5-41). It is not surprising therefore that a higher-order polynomial is needed to define this curve. It should be noted that at beta angles of 90 degrees (directly inline with the detector's axis), the weighting factor is equal to one. By observing symmetry in the positive and negative directions of the x and y axis, only one quadrant was mapped.

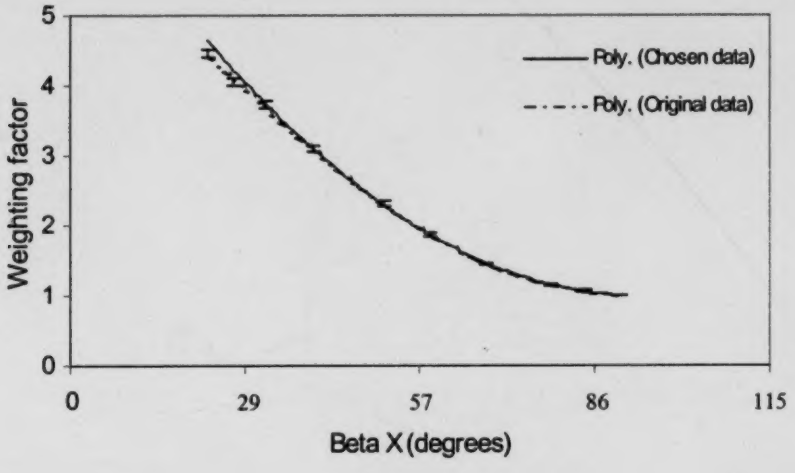

Figure 5-44. The original versus the chosen data set and their regression curves.

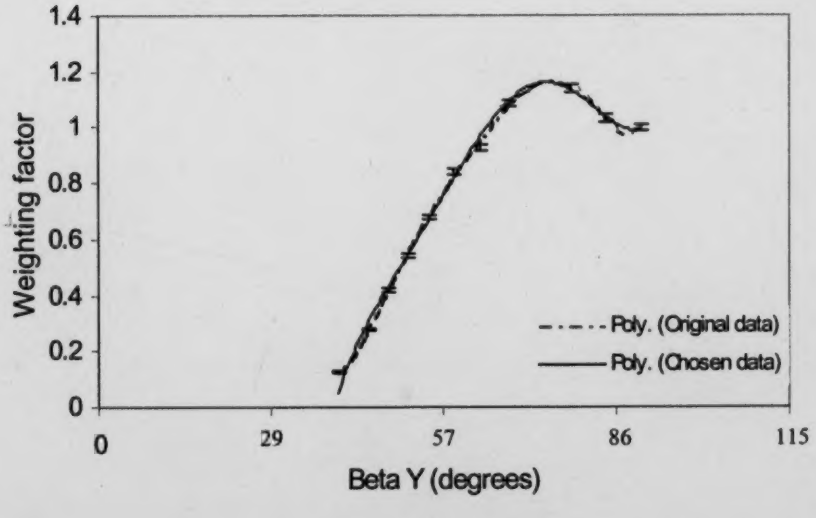

Figure 5-45. The original versus the chosen data set and their regression curves.

The physical setup that was constructed in figure 5-41 was of the bottom-middle bank, however it was used to map $W_{tot}(E,\beta_x,\beta_y)$ for all detector bank configurations. This could be done, since the FOV's for the different banks were similar. The range of detector bank FOVs were accommodated experimentally, by changing the detector distance *d* from the grid. Several maps needed to be obtained since most end-bank's had two different FOVs, as was illustrated in figure 5-36 by 'FOV L' and 'FOV R'. In all, eleven different FOVs were mapped.

Once the 4x7 matrix of data, plus three maximum-FOV points were taken, *Mathematica* was used to fit a 3D-regression curve to each detector bank $W_{tot}(E,\beta_x,\beta_y)$ map. An eighteen-term, second and fifth-order polynomial of the form seen below defined each $W_{tot}(E,\beta_x,\beta_y)$ map.

$$W_{tot}(\beta_x, \beta_y) = a_0+a_1\beta_x+a_2\beta_x^2+a_3\beta_y+a_4\beta_x\beta_y+a_5\beta_x^2\beta_y+a_6\beta_y^2+a_7\beta_x\beta_y^2+a_8\beta_x^2\beta_y^2+a_9\beta_y^3+ a_{10}\beta_x\beta_y^3+a_{11}\beta_x^2\beta_y^3+a_{12}\beta_y^4+a_{13}\beta_x\beta_y^4+a_{14}\beta_x^2\beta_y^4+a_{15}\beta_y^5+a_{16}\beta_x\beta_y^5+a_{17}\beta_x^2\beta_y^5$$

The eleven regression curves and their polynomials are shown in figures 5-46 through 5-56 in the pages that follow. The curves are arranged such that the map from the largest field-of-view detector bank is presented first, and the smallest FOV last. The relative detector face orientations were based on the bottom-middle bank. Therefore, a bank whose detectors were 1 cm closer to the grid that the bottom-middle detectors, were labeled '+1 cm'. This convention is used in labeling the regression curves.

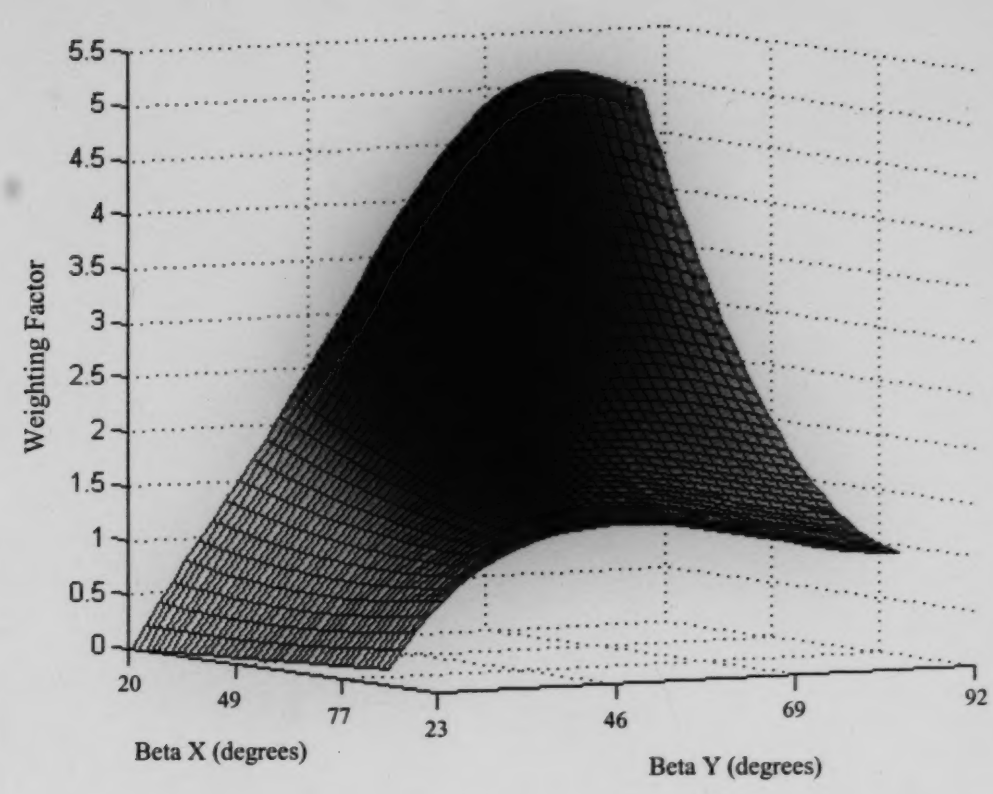

Figure 5-46. The regression surface for one quadrant defining $W_{tot}(\beta_x,\beta_y)$, for – 2.17 cm

$W_{tot}(\beta_x,\beta_y)$= -20.44 + 39.60 βx - 19.11 βx^2 + 123.42 βy - 253.32 βx βy + 121.14 βx^2 βy - 288.73 βy^2 + 610.56 βx βy^2 - 286.24 βx^2 βy^2 + 334.85 βy^3 - 693.51 βx βy^3 + 317.30 βx^2 βy^3 -179.44 βy^4 + 363.54 βx βy^4 - 163.76 βx^2 βy^4 + 35.67 βy^5 - 71.28 βx βy^5 + 31.88 βx^2 βy^5

Error in fit = 1.35%, R^2 = 99.99%

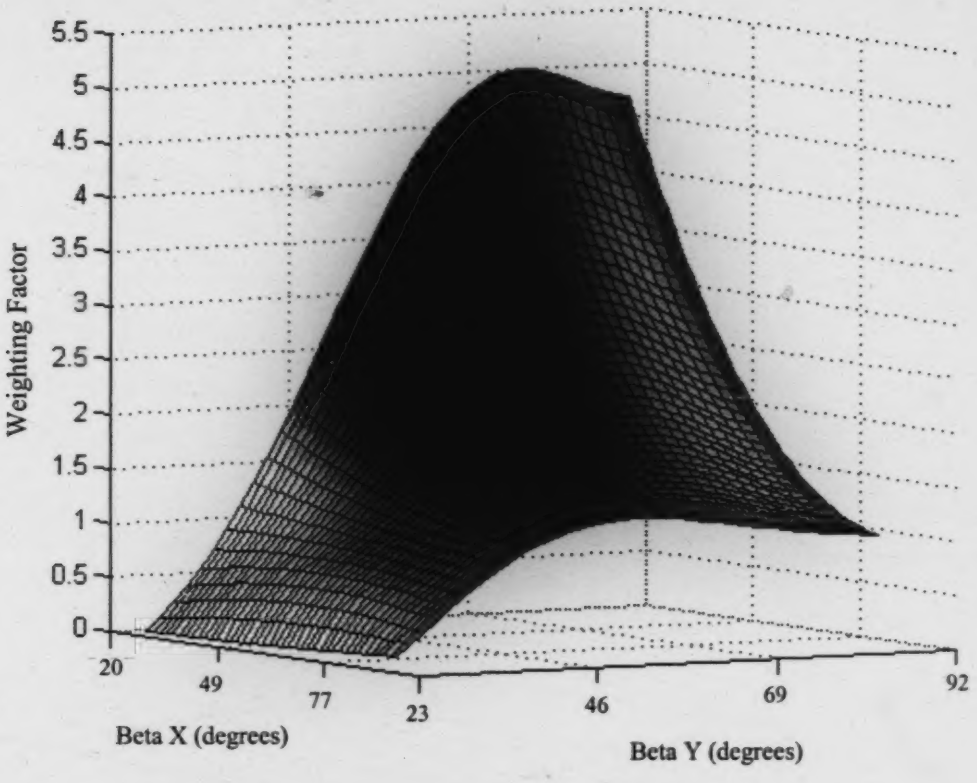

Figure 5-47. The regression surface for one quadrant defining $W_{tot}(\beta_x,\beta_y)$, for – 1.73 cm

$W_{tot}(\beta_x,\beta_y)$= 19.39 - 89.90 βx + 51.00 βx^2 - 97.09 βy +491.44 βx βy - 286.31 βx^2 βy + 158.50 βy^2 - 995.60 βx βy^2 + 603.22 βx^2 βy^2 - 91.77 βy^3 + 947.33 βx βy^3 - 602.69 βx^2 βy^3 + 14.60 βy^4 - 437.05 βx βy^4 + 290.52 βx^2 βy^4 + 1.68 βy^5 + 79.04 βx βy^5 - 54.39 βx^2 βy^5

Error in fit = 3.36%, R^2 = 99.91%

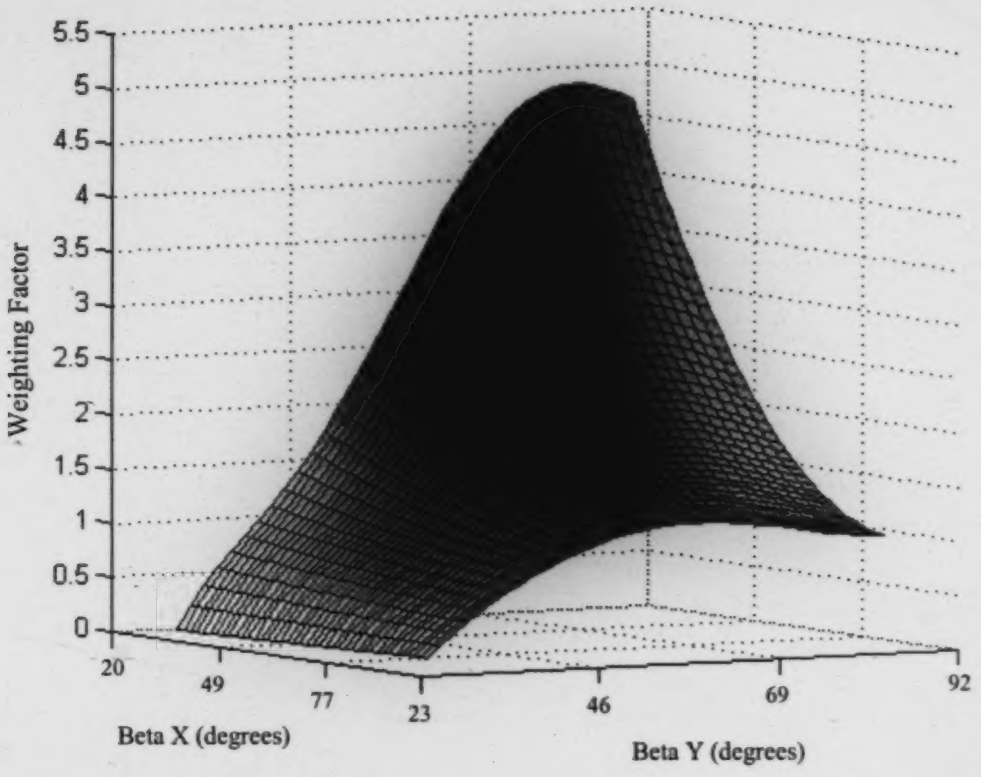

Figure 5-48. The regression surface for one quadrant defining $W_{tot}(\beta_x,\beta_y)$, for – 1.23 cm

$W_{tot}(\beta_x,\beta_y)$= -44.74 + 29.96 βx - 1.88 βx^2 + 243.95 βy - 171.92 βx βy + 12.73 βx^2 βy - 519.83 βy^2 + 379.83 βx βy^2 - 31.88 βx^2 βy^2 + 537.58 βy^3 - 396.22 βx βy^3 + 35.10 βx^2 βy^3 - 260.99 βy^4 + 188.90 βx βy^4 - 15.64 βx^2 βy^4 + 47.77 βy^5 - 33.39 βx βy^5 + 2.31 βx^2 βy^5

Error in fit = 1.27%, R^2 = 99.99%

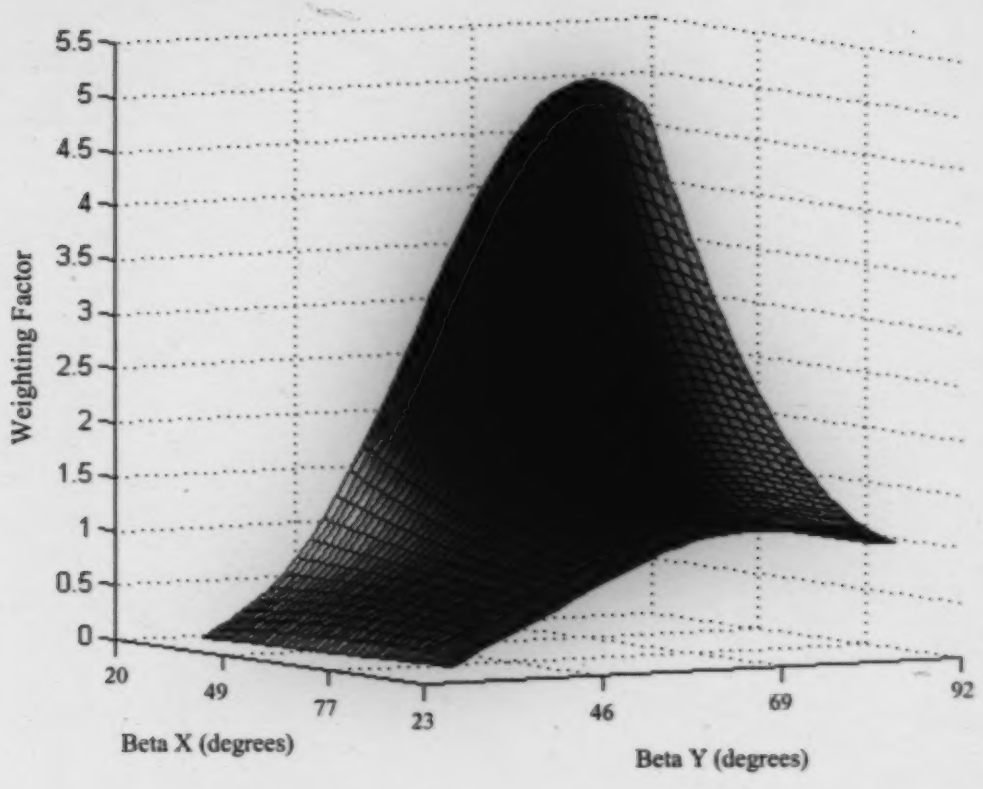

Figure 5-49. The regression surface for one quadrant defining $W_{tot}(\beta_x,\beta_y)$, for – 0.57 cm

$W_{tot}(\beta_x,\beta_y)$= -12.29 - 35.90 βx + 24.92 βx^2 + 92.18 βy + 140.91 βx βy - 111.57 βx^2 βy - 248.46 βy^2 - 188.15 βx βy^2 + 186.51 βx^2 βy^2 + 296.36 βy^3 + 105.71 βx βy^3 - 149.30 βx^2 βy^3 - 152.74 βy^4 - 29.65 βx βy^4 + 60.25 βx^2 βy^4 + 28.15 βy^5 + 4.36 βx βy^5 - 9.99 βx^2 βy^5

Error in fit = 0.96%, R^2 = 99.99%

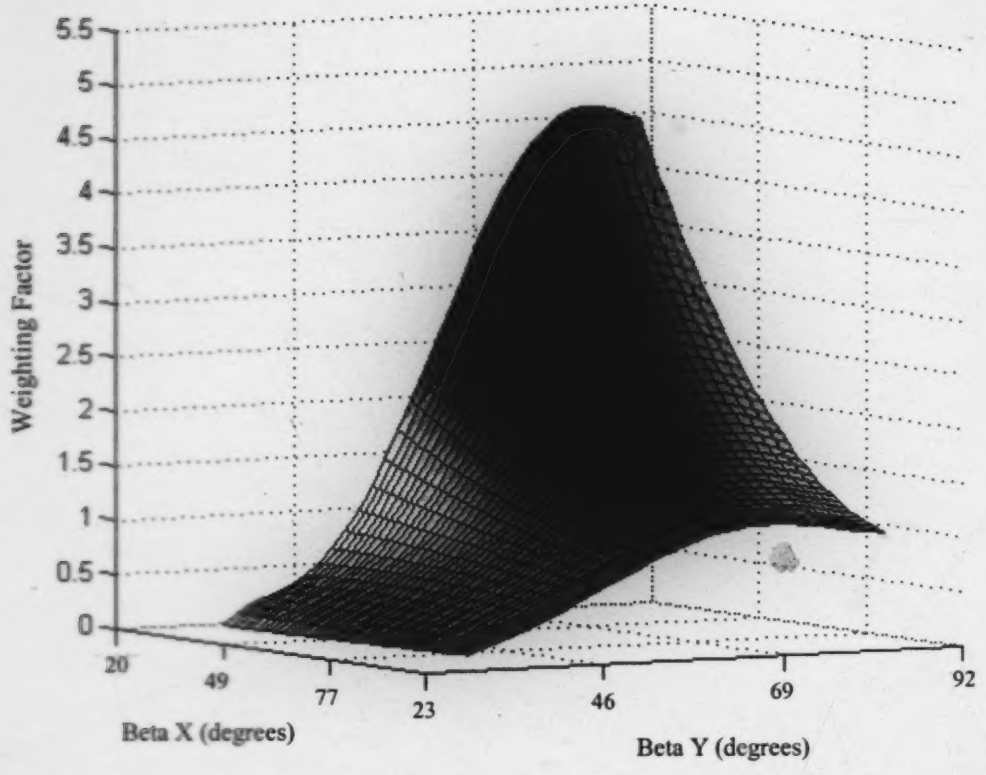

Figure 5-50. The regression surface for one quadrant defining $W_{tot}(\beta_x,\beta_y)$, for – 0.13 cm

$W_{tot}(\beta_x,\beta_y)$= -156.92 + 225.45 βx - 83.12 βx^2 + 834.71 βy - 1205.41 βx βy + 447.12 βx^2 βy - 1715.16 βy^2 + 2480.12 βx βy^2 - 924.82 βx^2 βy^2 + 1690.99 βy^3 - 2443.07 βx βy^3 + 916.07 βx^2 βy^3 - 794.55 βy^4 + 1149.41 βx βy^4 - 434.20 βx^2 βy^4 + 143.06 βy^5 - 207.86 βx βy^5 + 79.25 βx^2 βy^5

Error in fit = 1.72%, R^2 = 99.98%

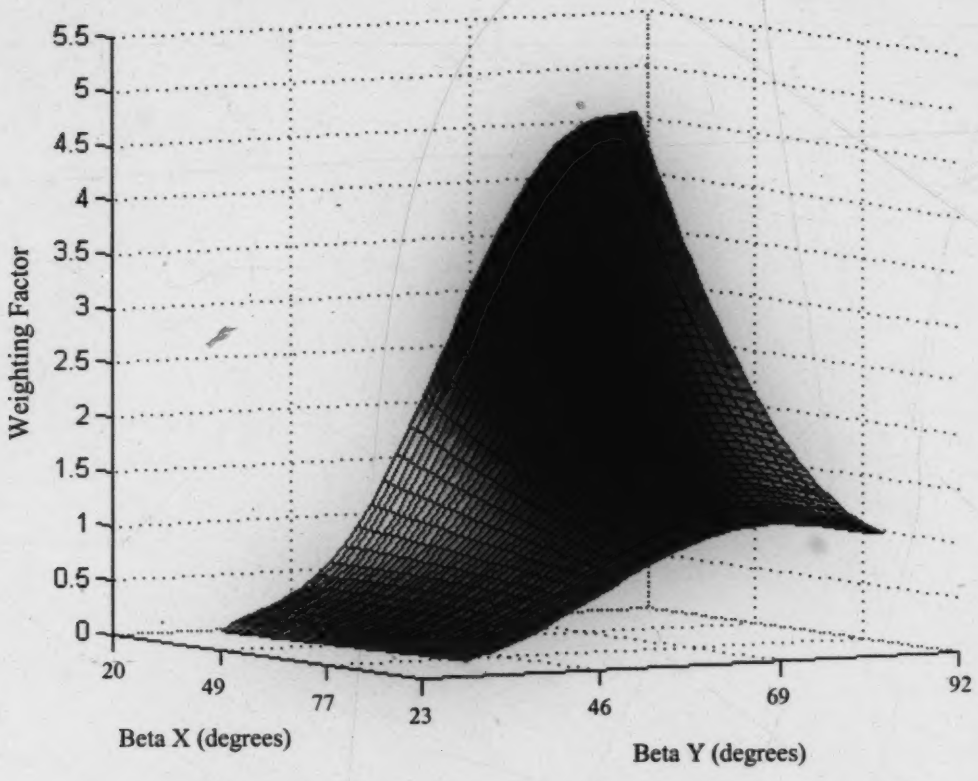

Figure 5-51. The regression surface for one quadrant defining $W_{tot}(\beta_x,\beta_y)$, for 0 cm

$W_{tot}(\beta_x,\beta_y)$= -105.85 + 121.38 βx - 35.45 βx^2 + 559.25 βy - 639.62 βx βy + 188.20 βx^2 βy - 1139.68 βy^2 + 1291.42 βx βy^2 - 381.64 βx^2 βy^2 + 1111.04 βy^3 - 1240.68 βx βy^3 + 367.41 βx^2 βy^3 - 513.77 βy^4 + 565.34 βx βy^4 - 167.84 βx^2 βy^4 + 90.82 βy^5 - 98.72 βx βy^5 + 29.45 βx^2 βy^5

Error in fit = 1.20%, R^2 = 99.99%

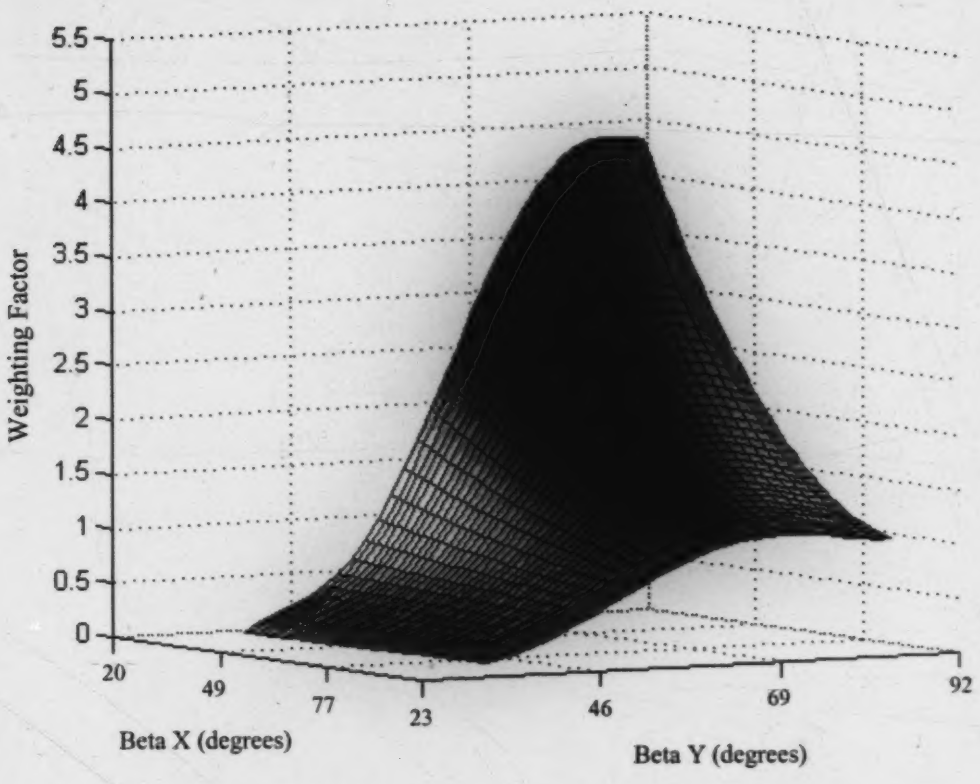

Figure 5-52. The regression surface for one quadrant defining $W_{tot}(\beta_x,\beta_y)$, for +0.37 cm

$W_{tot}(\beta_x,\beta_y)$= -146.41 + 135.55 βx - 28.80 βx^2 + 739.92 βy - 673.94 βx βy + 141.24 βx^2 βy - 1448.02 βy^2 + 1287.07 βx βy^2 - 263.33 βx^2 βy^2 + 1361.97 βy^3 - 1171.23 βx βy^3 + 230.70 βx^2 βy^3 - 611.02 βy^4 + 504.55 βx βy^4 - 93.94 βx^2 βy^4 + 105.10 βy^5 - 82.83 βx βy^5 + 14.28 βx^2 βy^5

Error in fit = 1.32%, R^2 = 99.99%

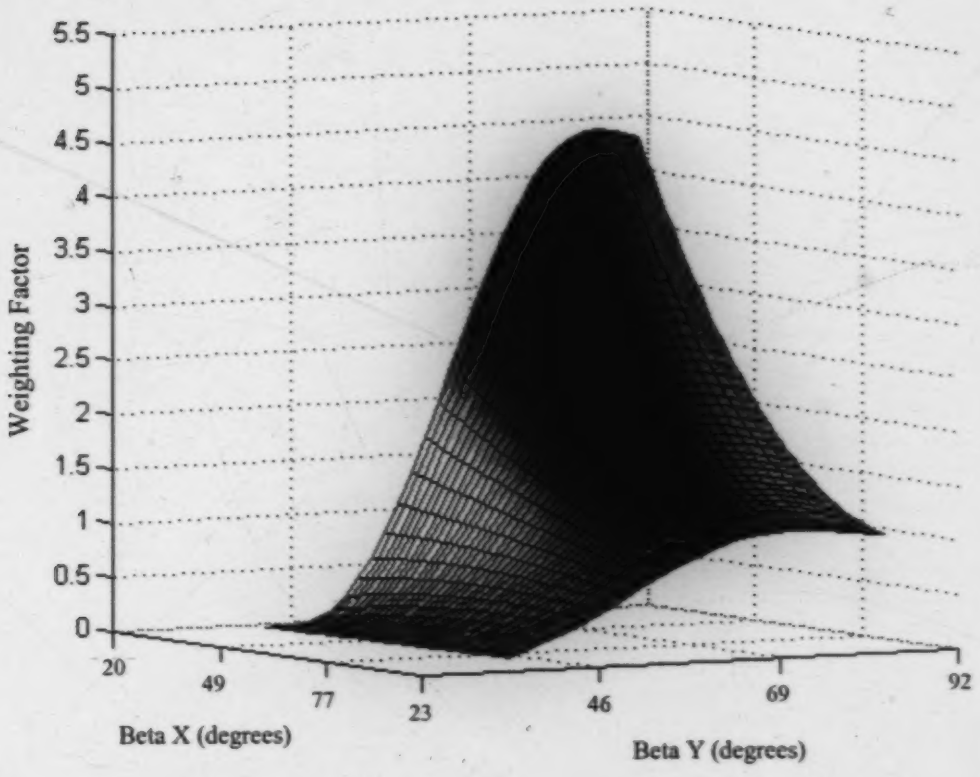

Figure 5-53. The regression surface for one quadrant defining $W_{tot}(\beta_x,\beta_y)$, for +0.57 cm

$W_{tot}(\beta_x,\beta_y)$= -229.83 + 324.02 βx - 117.16 βx^2 + 1180.58 βy - 1632.72 βx βy + 583.48 βx^2 βy - 2340.90 βy^2 + 3169.49 βx βy^2 - 1119.37 βx^2 βy^2 + 2227.45 βy^3 - 2951.11 βx βy^3 + 1030.60 βx^2 βy^3 - 1013.64 βy^4 + 1316.63 βx βy^4 - 455.36 βx^2 βy^4 + 177.37 βy^5 - 226.37 βx βy^5 + 77.65 βx^2 βy^5

Error in fit = 0.66%, R^2 = 100.00%

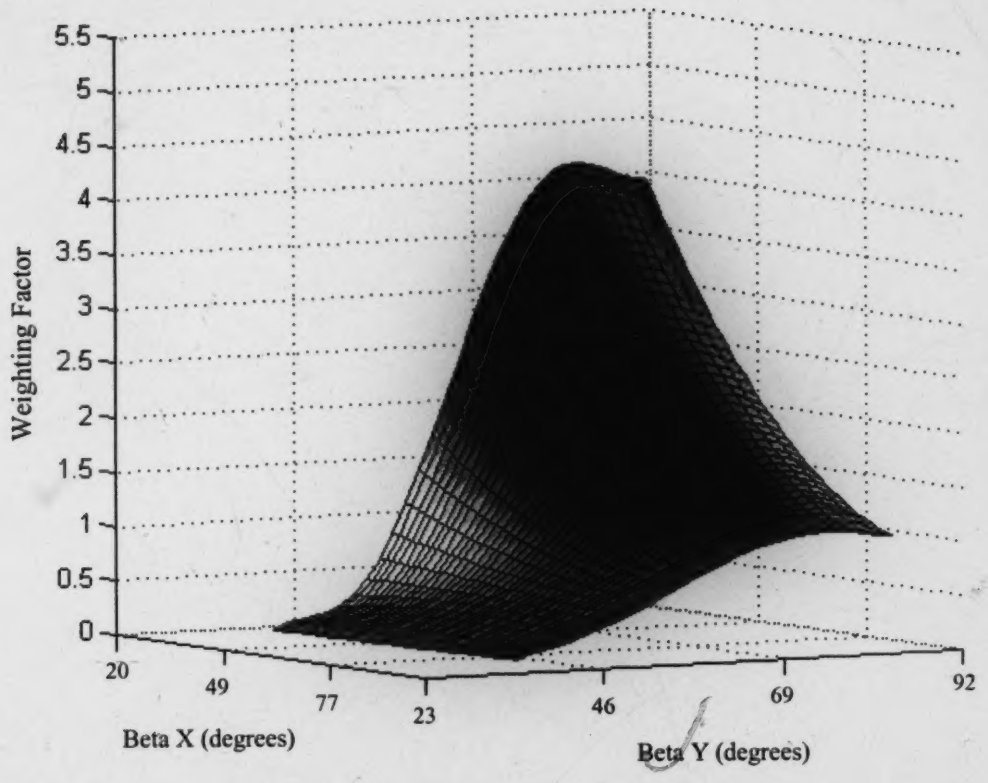

Figure 5-54. The regression surface for one quadrant defining $W_{tot}(\beta_x,\beta_y)$, for +0.87 cm

$W_{tot}(\beta_x,\beta_y)$= -440.57 + 603.19 βx - 213.64 βx^2 + 2236.52 βy - 3099.73 βx βy + 1108.20 βx^2 βy - 4419.03 βy^2 + 6190.65 βx βy^2 -2232.17 βx^2 βy^2 + 4232.34 βy^3 - 5989.35 βx βy^3 + 2177.20 βx^2 βy^3 -1959.96 βy^4 + 2803.74 βx βy^4 - 1027.62 βx^2 βy^4 + 351.98 βy^5 - 509.35 βx βy^5 + 188.24 βx^2 βy^5

Error in fit = 3.13%, R^2 = 99.94%

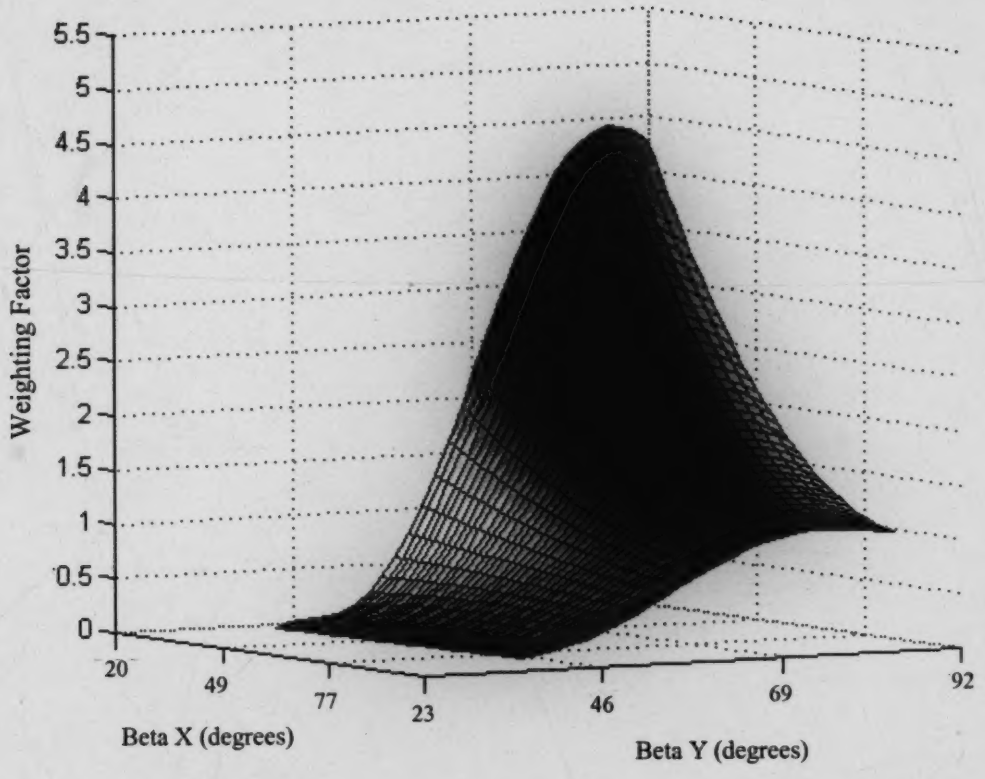

Figure 5-55. The regression surface for one quadrant defining $W_{tot}(\beta_x,\beta_y)$, for +1.14 cm

$W_{tot}(\beta_x,\beta_y)$= -307.05 + 418.21 βx - 147.19 βx^2 + 1489.31 βy - 2023.21 βx βy + 714.75 βx^2 βy - 2799.68 βy^2 + 3793.44 βx βy^2 - 1345.96 βx^2 βy^2 + 2537.79 βy^3 - 3434.70 βx βy^3 + 1225.85 βx^2 βy^3 - 1105.54 βy^4 + 1500.09 βx βy^4 - 539.90 βx^2 βy^4 + 185.84 βy^5 - 253.88 βx βy^5 + 92.39 βx^2 βy^5

Error in fit = 1.35%, R^2 = 99.99%

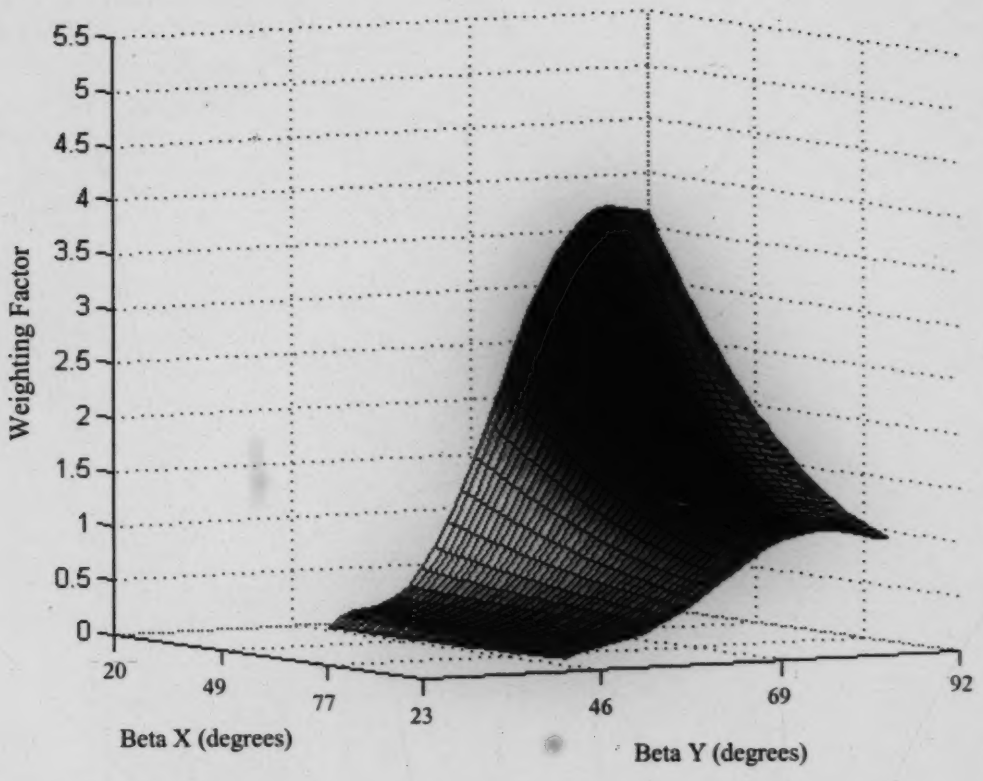

Figure 5-56. The regression surface for one quadrant defining $W_{tot}(\beta_x,\beta_y)$, for +2.12 cm

$W_{tot}(\beta_x,\beta_y)$= -931.52 + 907.41 βx - 281.00 βx^2 + 4143.65 βy - 4021.09 βx βy + 1242.49 βx^2 βy - 7235.16 βy^2 + 6985.07 βx βy^2 -2153.08 βx^2 βy^2 + 6185.86 βy^3 - 5934.49 βx βy^3 + 1824.80 βx^2 βy^3 - 2585.84 βy^4 + 2463.21 βx βy^4 - 755.76 βx^2 βy^4 + 423.32 βy^5 - 400.19 βx βy^5 + 122.55 βx^2 βy^5

Error in fit = 1.30%, R^2 = 98.83%

All of the $W_{tot}(\beta_x,\beta_y)$ polynomials presented showed excellent agreement with their experimental data points (ranging from 0.66% to 3.36% error in the regression fits), and were used in the semi-empirical regression method. By using the $W_{tot}(E,\beta_x,\beta_y)$ polynomial in conjunction with equation 5-5, accurate, absolute WBC responses for K-40 were expected.

Verification of the Semi-Empirical-Regression Method

Prior to use in the WBC, the Semi-Empirical-Regression Method and the bottom-middle bank's $W_{tot}(\beta_x,\beta_y)$ map were verified experimentally. A large 18 liter water bottle was filled with saturated KCl solution, and was modeled using 11x11x15 elements. The water bottle had a diameter of 25.7 cm and was filled to a height of 34.3 cm, chosen to approximate a human thorax. Four kilograms of KCl salt was needed to saturate the solution. The 1.46 MeV photon activity from the naturally occurring K-40 in the solution was 6941 Bq. The water bottle was positioned on end, and placed 8.91 and 19.01 cm away from the detector face for the detector configuration shown in figure 5-57.

Figure 5-57. Water bottle with KCl solution placed in front of the detector arrangement.

The water bottle was moved laterally 4.6 cm (in the *x* direction) after each measurement was taken, such that the axis of the water bottle and the axis of the detector crossed at the midpoint.

As can be seen in figure 5-58, experimental and theoretical values for the K-40 photopeak detector response are in excellent agreement with one another.

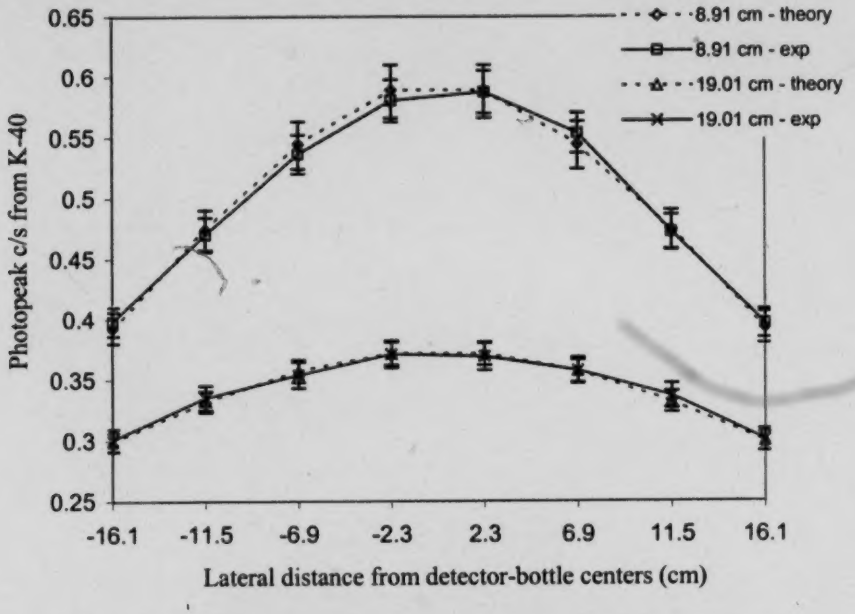

Figure 5-58. Experimental versus theoretical photopeak detector responses.

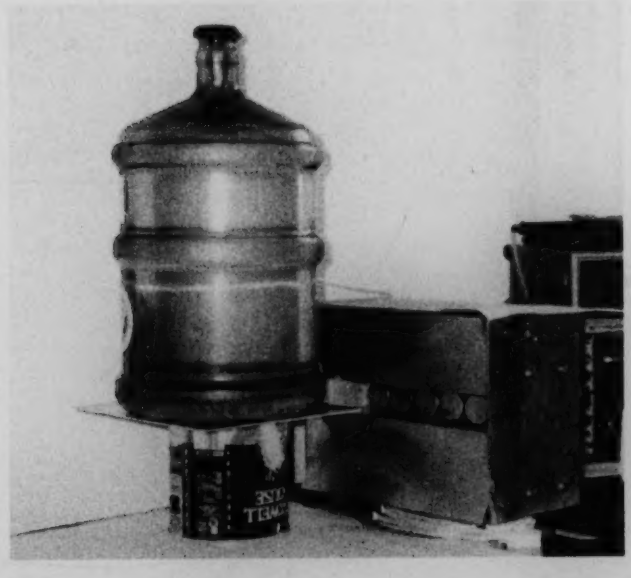

Figure 5-59. Water bottle elevated and placed in front of the detector arrangement.

The robustness of the semi-empirical-regression method for when the water bottle is moved in the vertical direction was also tested. The water bottle was elevated so that the bottom of the bottle was level with the center of the detector, then moved laterally as before. The experimental setup is seen in figure 5-59. The graph in figure 5-60 shows the result from experiment and theory, and once again, excellent agreement is seen between experiment and the semi-empirical-regression method.

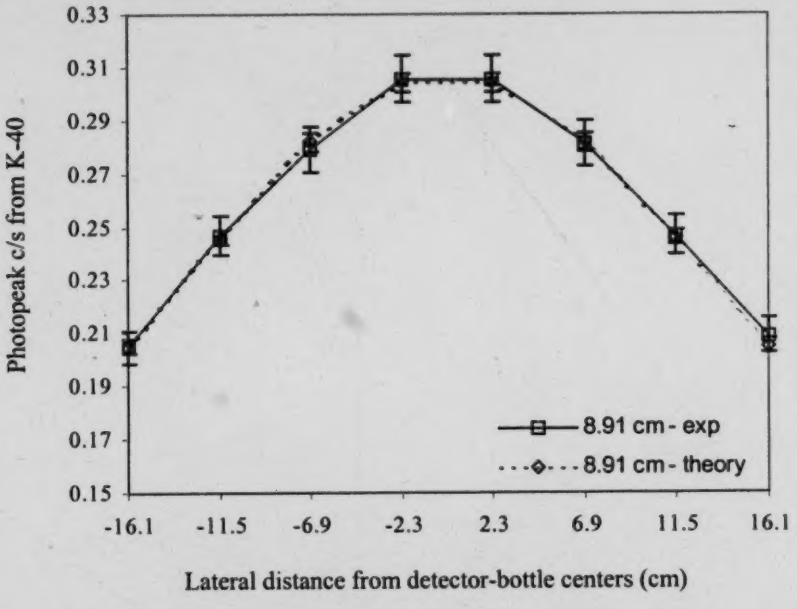

Figure 5-60. Experimental versus theoretical responses for an elevated water bottle.

To properly model the WBC's response from naturally occurring K-40 found in the human body, the semi-empirical-regression method must deliver accurate detector responses for a range of modeled phantom sizes. The large water bottle seen in previous figures approximately resembles a human thorax, however human arms, head, and legs have a very different size. Therefore, the semi-empirical-regression method was also tested using a very small bottle, to see whether it could properly accommodate for variable source sizes. The bottle used was 7.7 cm in diameter, and was filled with KCl salt to a height of 10 cm. The total amount of KCl in the bottle was 498 g, which gave a 1.46 MeV activity of 864 Bq. The detector bank was placed on end, and the bottle was

positioned length-wise (as in figure 5-61) and placed at different heights. Experimental and theoretical results for this bottle and its movement are graphed in figure 5-62.

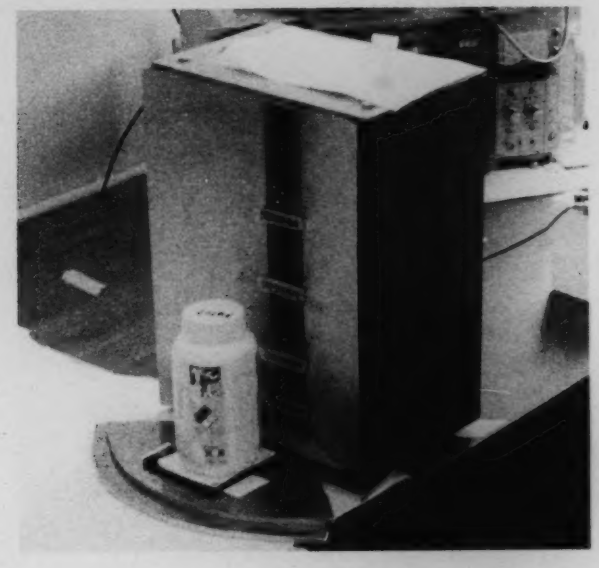

Figure 5-61. Water bottle placed length-wise in front of the detector arrangement.

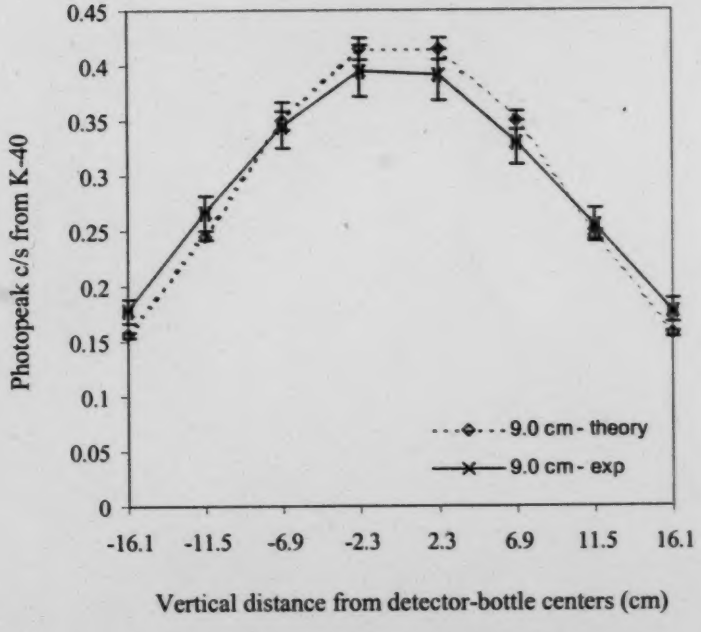

Figure 5-62. Experimental versus theoretical responses for the small bottle.

The experimental detector response from the small bottle being placed 9 cm from the detector face, and positioned at various heights, agrees well with theory. To within error, the theoretical and experimental detector responses are the same. These results however are not as good as the ones seen previously for the large bottle. This is because the weighting factor curves were not constructed using a point source, but instead a distributed source with a 1 cm diameter. There is uncertainty in the position of the Na-22 source, and therefore in the angle-dependant weighting factors. These uncertainties become larger at small source-detector distances, therefore when the entire source is located close to the detector (as with the small bottle), the integrated source activity will have a large uncertainty as well. Because theory and experiment agree well with theory, the semi-empirical-regression method is indeed flexible for all activity sizes ranging from a large 17 liter, to a small 0.5 liter phantom.

The semi-empirical-regression method was shown to model very accurate K-40 photopeak responses in large and small phantoms. All possible detector-source positions were investigated, and in all cases, excellent theoretical and experimental correlation was shown. The semi-empirical-regression method therefore was chosen to obtain accurate, absolute detector responses for the entire WBC. The results from this thorough investigation are presented in Chapter 8.

References

[1] R. Rieppo. Calculated Photopeak Efficiencies of NaI-Crystals for a 4π-Detecting Geometry. *Nuclear Instruments and Methods* **115**:541-543;1974.

[2] N.A. Vartanov, P.S. Samoilov. Total Efficiencies, Photofractions, and Photoefficiencies of NaI(Tl) and CsI(Tl) Crystals. *Instruments and Experimental Techniques* **2**:310-313;1965.

[3] R. Rieppo. Calculated Photopeak Efficiencies of NaI(Tl)-Scintillation Detectors with Self-Absorption in the Source. *Nuclear Instruments and Methods* **107**:209-212;1973.

[4] M.L. Verheijke. Calculated Efficiencies of NaI(Tl) Scintillation Crystals for Marinelli Beakers with Aqueous Sources. *International Journal of Applied Radiation and Isotopes* **21**:119-126;1970.

[5] F. Cejnar, I. Kovar. Experimental and Calculated Photopeak Efficiency Values for Well-type NaI(Tl) Detectors. *International Journal of Applied Radiation and Isotopes* **31**:79-84;1980.

[6] J.J. Steyn. Empirical Photofractions for NaI(Tl) Scintillation Crystals. *Nuclear Instruments and Methods* **68**:118-124;1969.

[7] P. Holmberg *et al.* Calculated Efficiency Values for Well-Type NaI(Tl)-Detectors. *International Journal of Applied Radiation and Isotopes* **23**:115-120;1972.

[8] H. Baba, T. Sekine. An Analytical Representation of the Response of the NaI(Tl) Detector for the Gamma-Ray Spectrum Analysis. *Journal of Radioanalytical Chemistry* **29**:109-119;1976.

[9] W.R. Nelson *et al*, SLAC-265, 1985

[10] N.H. Lazar *et al.* Peak Efficiency of NaI. *Nucleonics* April:52:52;1956.

[11] R.L. Heath. Scintillation Spectrometry - Gamma-ray spectrum catalogue. Report No. IDO-16880-1;1964

[12] T. Doke *et al.* Angular Dependencies of Efficiencies for Sodium-Iodide Crystals. *J. Phys. Coc. Japan* **15**:737-738;1960.

[13] K. Greisen. Range of Cascade Showers in Lead. *Physical Review*. **75**(7):1071-1074;1949.

[14] G. Cocconi. Some Properties of Cosmic-Ray Ionizing Particles That Generate Penetrating Showers. *Physical Review*. **75**(7):1074-1078;1949.

[15] J.H. Kaye *et al.* Background Reductions Obtained with Gamma Detectors by use of Massive Cosmic-Ray Shielding. *Nuclear Instruments and Methods*. **100**:333-348;1972.

[16] B.Grinberg, Y. Le Gallic. Caracteristiques Fondamentales d'un Laboratoire de Mesure de Tres Faibles Activites. *Int. J. Appl. Rad Isotopes*. **12**:104-117;1961.

[17] P.P.Auger *et al.* Analyse Du Rayonnement Cosmique A L'Altitude De 3 500 Metres (Laboratoire International Du Jugfraujoch). *Journal De Physique* **2**:58-64;1935.

[18] J.R.DeVoe. Radioactive Contamination of Materials Used in Scientific Research. *National Academy of Sciences- NRC*. Pub 895, Nuclear Science Series, Report # 34, 1961

[19] T. Hawkins, A.W. Goode. The determination of Total-body Potassium using a Whole-body Monitor. *Physics in Medicine and Biology*. **21**(21):293-297;1976.

[20] G. Heo. Restricted Minimax Robust Designs for Misspecified Regression Models. *The Canadian Journal of Statistics, to appear.*

Chapter 6

High-Adaptability WBC Design and Function

6.1 The Physical Layout of the WBC

The whole body counter that was developed in this thesis is a shadow-shielded, scanning counter, which contains sixty-four NaI detectors. An illustration of the counter can be seen below, and an assembly drawing (drawing 1000000) can be seen in Appendix A. All of the illustrations that are shown in this chapter are only a representation of the actual WBC, and some details of the counter's shielding, etc, may not be shown.

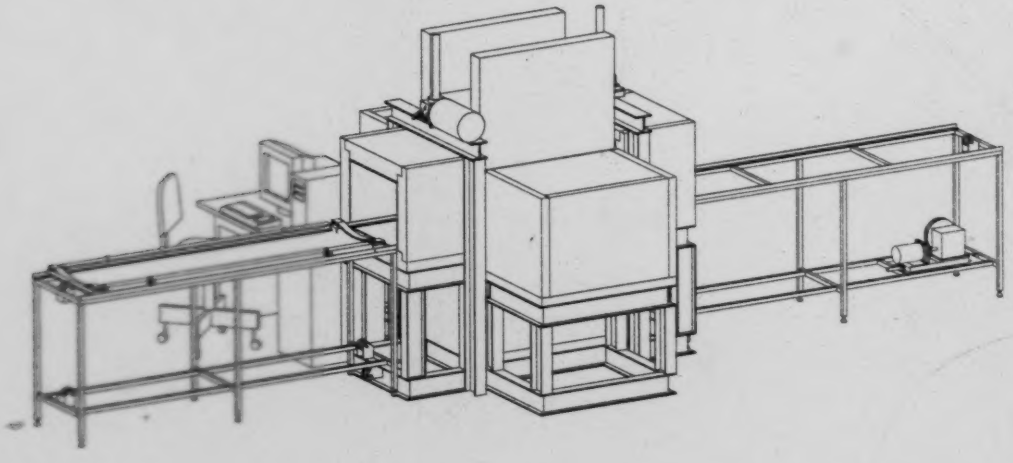

Figure 6-1. Illustration of the shadow-shielded scanning whole body counter.

The whole body counter has two table extensions attached to it, one located at its entrance, and the other at its exit. Initially, subjects will lie with their back on the table at the counter's entrance, and will be passed through the counter. As the subject is passed through the WBC, the detectors inside will collect information on the radionuclides

present in the subject. This data collection will continue until the subject passes through to the exit side of the WBC. A proposed method for data collection is discussed in detail in the next chapter. A cut-away view of the counter is seen below.

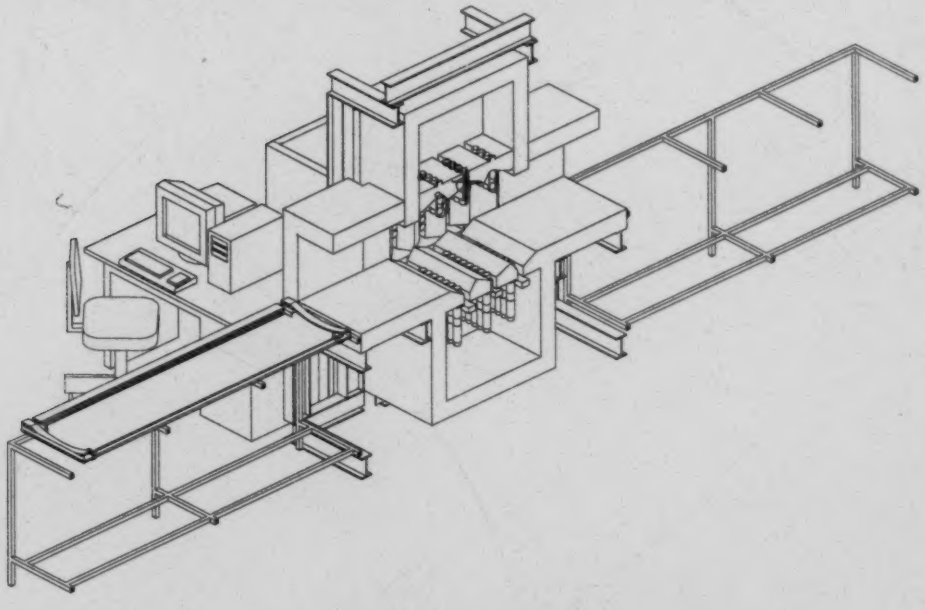

Figure 6-2. Cut-away view of the shadow-shielded scanning whole body counter.

In the cut-away view of the whole body counter, the detector-collimator orientation can be clearly seen. The three banks for the top, bottom, and side of the WBC are seen here, as well as the collimator design and its orientation to the detectors.

Figure 6-3 shows an end-view of the whole body counter. The positioning of the sixty four detectors can be seen in the figure, showing their relative position around the subject. The lengths of the banks have roughly the same dimensions as the height and width of the subject.

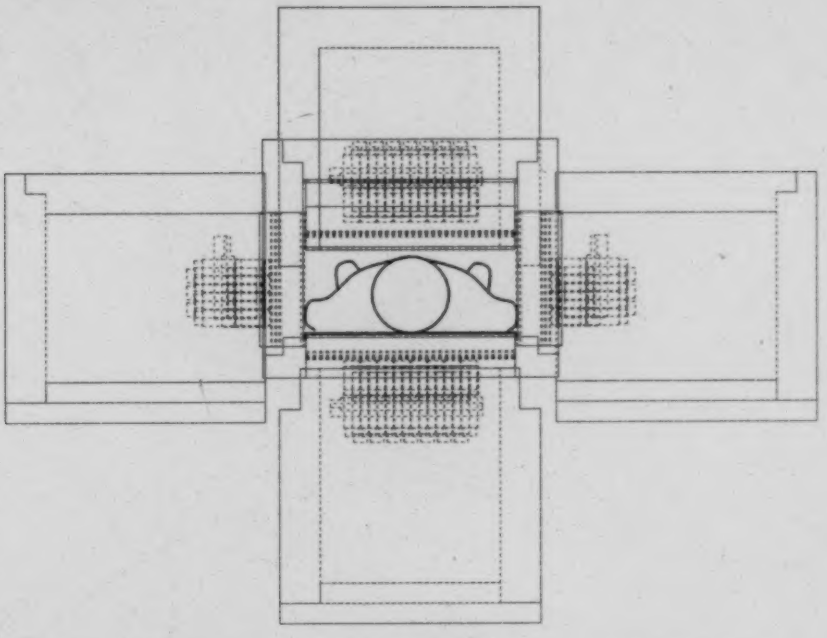

Figure 6-3. End view of the whole body counter, with an adult subject inside.

6.2 High-Sensitivity Mode

For the usual case where extremely small amounts of radionuclides within the subject need to be quantified, the counter will be able to accommodate all subject sizes in order to provide the highest degree of sensitivity.

Top Gantry Movement

Detector responses are very sensitive to source-detector distances, therefore a movable top detector gantry was implemented into the WBC design (seen in drawing 1080000, Appendix A). This will enable the top detectors to be placed as close to the subject as possible, and to move along the subject's contours throughout the entire scan. The top gantry was optimized to a minimum length of ~ 64.5 cm so that it could better follow the subject's contours, and provide the highest WBC detector response possible. The WBC has been designed to accommodate a maximum subject thickness of 35-40 cm. The varying height of the top gantry is seen in figures 6-4 and 6-5, where two different gantry heights are shown for an adult and child scan.

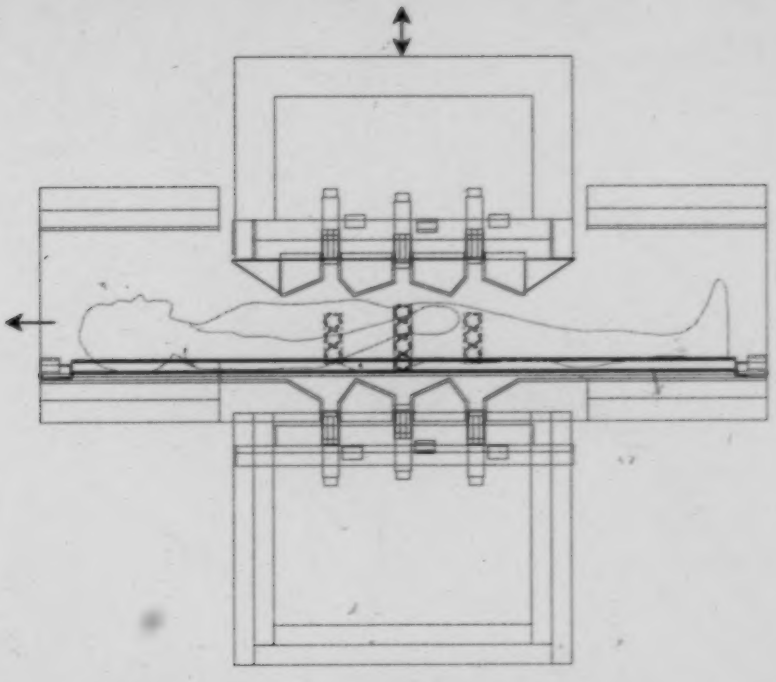

Figure 6-4. Side view of the counter, with the top gantry positioned for an adult.

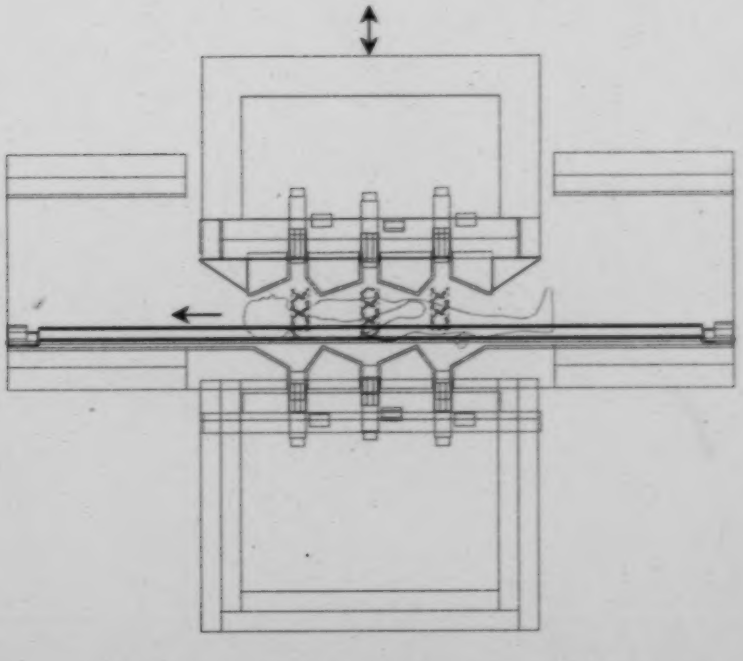

Figure 6-5. Side view of the counter, with the top gantry positioned for a child.

Because of the small number of side detectors and the complexity of moving them, it was decided that the side detectors should be held at a fixed position. The side detectors were fixed so that a 57 cm wide 95th percentile Canadian man could fit inside the WBC.

Top-Detector Movement

Moving the top gantry towards the bottom of the counter has the same effect as adding length to a shadow-shielded counter. The top detectors do not need to be positioned as deep in the collimator shielding to remaining fully shielded, and can be moved outward. By doing this, the detector's FOV will increase, and smaller subject-detector distances can be accomplished. These two factors will increase the top detectors' response, therefore top-detector movement was incorporated into the WBC design. The effect of the top-detector movement can be seen in the illustration below.

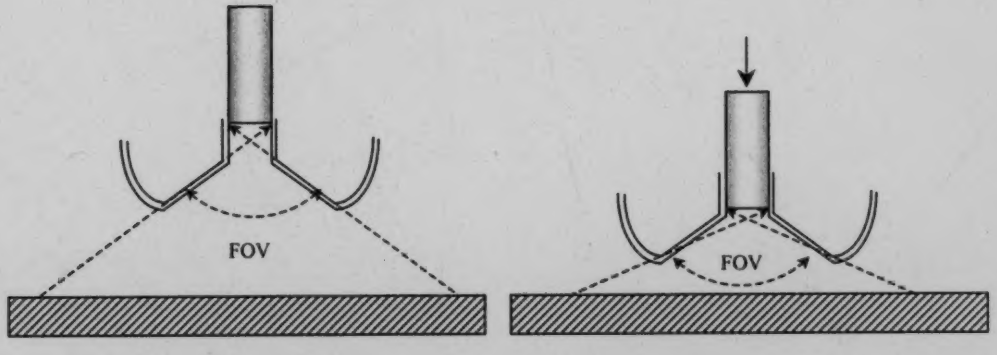

Figure 6-6. The top gantry positioned far away and close to the bottom shielding.

Because the top gantry has a variable height but its collimators are not adjustable, a specific gantry height must be chosen to optimize the collimators. The collimators were optimized for a gantry height of 25 cm, which is the height of the Reference Man thorax plus 5 cm between the gantry and the subject. For gantry heights larger or smaller than this height, the top detectors should move towards or away from the subject to reach their most optimal detector-collimator position.

Infant Positioning in the WBC

Infants and subjects shorter than approximately 50 cm long are best suited lying stationary, in a length-wise position along the bottom middle bank. A lucite table, molded to the shape of the bottom-middle collimators can be used to bring the subject closer to the detectors. This will increase the bottom middle detectors' efficiency greatly. By placing the top gantry just above the subject, the top-middle detectors can also be placed very close to the subject, thereby essentially forming a stationary infant WBC with the two middle banks. A top view of an infant laying over the bottom middle detectors is seen below.

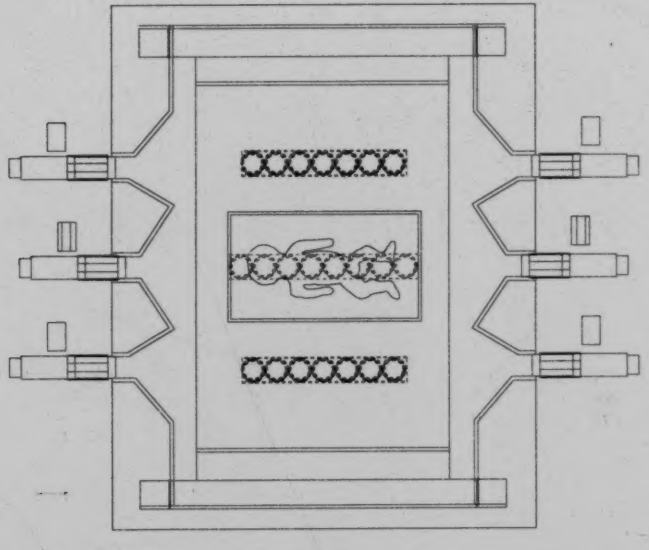

Figure 6-7. Placement of a very small subject in the whole body counter.

By utilizing the top gantry movement, and static length-wise positioning for small subjects, the high-adaptability WBC can accommodate all subject sizes.

6.3 Low-Sensitivity Mode

For cases where high-activity subjects need to be quantified, the whole body counter described in this thesis will be able to adapt to high-activities. The WBC will

accommodate for high activities without the adverse effects on quantification from summing peaks in the spectrum, and dead time.

Detector Retraction & Shutters

High-activity accommodation is achieved by reducing the amount of activity that reaches the detectors. This is accomplished in two ways. First, the detectors are retracted away from their original positions so that their responses are significantly reduced. The amount of retraction is variable, depending on the activity of the subject. For subjects with very high activity, retraction of the detectors may not be enough to prevent the detectors from becoming saturated, and the second method of reducing the detectors' response is employed. For these cases a variable 'shutter' is used to physically block radiation, in whole or in part, from reaching the detector. Each shutter contains a 2 cm thick lead core, with graded shielding placed on all detector-exposed sides. This amount of shielding will attenuate the highest-energy therapy radionuclide (I-131 at 364 keV) by a factor 1/2700. A cross-sectional view of the detector retraction and the shutter movement is seen in the illustration below.

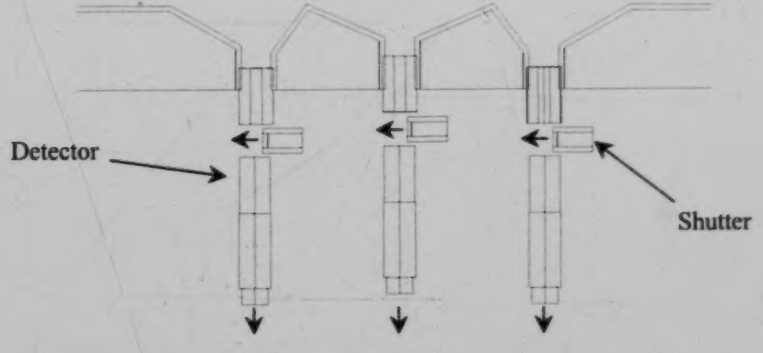

Figure 6-8. The detector and shutter movement during low-sensitivity mode.

The two methods of reducing detector responses were incorporated into the WBC's design. Detector retraction and shuttering mechanisms were designed for all sixty-four detectors in the WBC. The retraction and shutter motions in each of the four

gantries in the whole body counter are independent from each other. The assembly drawing for the side shutters can be seen in drawing 2021000, in Appendix A.

With the entire WBC equipped to deal with high-activity subjects, it will be able to accommodate all subject activities, ranging from natural body background (21 Bq) to therapeutic doses (7400 MBq) of I-131. For each of these situations, with the shutters and detectors repositioned, different iso-response curves will exist, and new calibration factors will have to be determined. A diagram showing a cross section of the WBC with its detectors fully retracted and shutters partially closed, can be seen below.

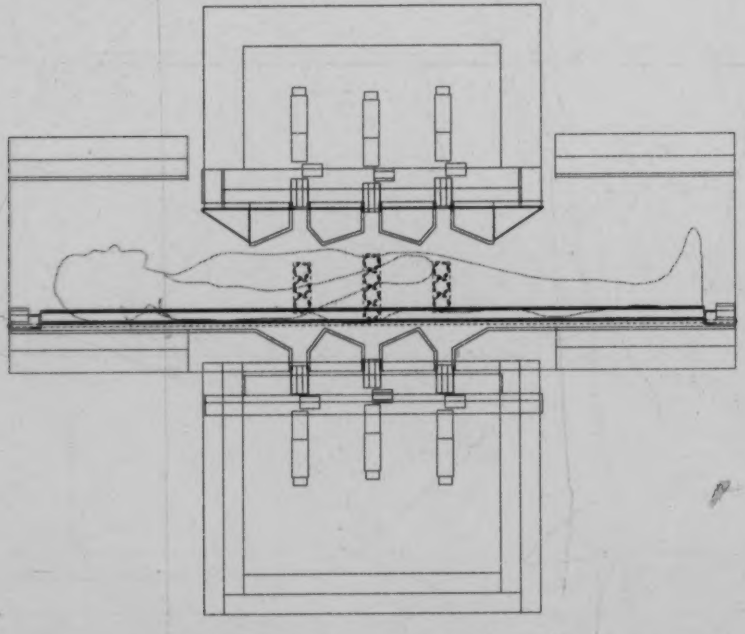

Figure 6-9. Side view of the counter in low-sensitivity mode for an adult subject.

6.4 WBC Drawings

Detailed engineering drawings for the construction of the WBC have been completed. A mechanical engineer[1] was hired to do the design / drafting of the WBC. The WBC's superstructure was reviewed and approved by a certified civil engineer[2].

Appendix A contains a select number of WBC drawings, and all drawing numbers in this section refer to drawings from that appendix. The complete set of drawings are not included in this thesis, since they number 450 pages! Should the reader wish to view these, the author will be most happy to provide the 3 volume set for perusal.

A large amount of effort was made to ensure that the WBC was properly shadow-shielded but made up of sections small enough for two people to handle (~ 100lbs). Considering that the WBC is expected to weigh approximately 46,000 lbs, this was not an easy task. To accomplish this, several small sections of lead were placed in a stacked fashion in order to provide a satisfactory shielding thickness. Drawings 106000, and 4060000 show how this method was used for the entrance / exit openings, and for the detector bank (drawing 4000000) shielding respectively.

Drawings 8030000, and 8050001 show the WBC's superstructure and table assembly. The table seen diagramed has already been acquired, but needs slight modification so that it can be used in the counter.

References

[1] Mr. Barton Pawluski, P.Eng, IDEAS DDM (Design Drafting & Manufacturing)

[2] Dr. P. Dozzi, P.Eng, Professor Emeritus, Faculty of Engineering, University of Alberta

Chapter 7

Selecting Low-Background Conditions

As seen in equation 3-3, the minimum detectable activity of a WBC is sensitive to the amount of background radiation present in the acquired spectra. Therefore, it is important to remove as much background counts as possible, not only by using primary and graded shielding, but also by reducing other factors that contribute to the background count as well. The materials present in the WBC, and its proximity to natural and man-made radiation sources must be considered and reduced as much as possible, so that a low MDA can be achieved.

For ultra low-level, non whole-body counting, extreme measures[1] can be taken to minimize the amount of background counts. In whole body counting however, this ultra-low background environment becomes too costly, and a compromise between background level and manufacturing costs must be reached.

7.1 WBC Manufacturing Considerations

As mentioned in Chapter 2, almost all materials contain radioactive impurities of some sort. Therefore, careful consideration to the selection and preparation of all WBC materials must be given to ensure that low background conditions exist.

Materials

When building a WBC, awareness of the materials that are being used in its construction is a must. Table 2-1 in Chapter 2 showed a brief list of select materials and their associated activities, however much larger tables exist[2] that list the radioactive impurities found in a large variety of substances. Tables such as these should be consulted to determine which materials should be avoided, and which ones are relatively free from impurities, and therefore appropriate for use in a WBC. The extent of

radioactive contamination in a given material can vary a great deal from one sample to the next, and depends mostly on the material's original supply source. The only way of being certain if a material has a low activity is by taking on-the-spot samples, and testing them in a well counter. This method should be used when constructing the WBC.

The primary shielding for the whole body counter is made up of lead, therefore there will be some Pb-210 impurities in the shielding. The amount of Pb-210 can be significantly reduced if 70 year old lead is used, however this type of lead is several times more expensive than modern day lead. The cost of constructing the WBC entirely from old lead would be enormous. Instead, 'semi-old' lead can be used to reduce the amount of Pb-210. Semi-old 'Defense Logistics Agency' (or DLA) lead that is at least 30 years old, has been stockpiled in the USA for use in bomb shelters in the case of nuclear war. This lead is being sold off now, and in large quantities, it can be purchased at the same cost as new lead. After 30 years, Pb-210 undergoes approximately 1.4 half-lives, therefore much less (approximately 64% less) Pb-210 is present in the lead. Therefore, DLA lead should be used in place of modern day lead. Another option would be to use old lead only for the lead shielding immediately adjacent to the detectors, and semi-old lead for the rest of the shielding. Pb-210 emits beta and gamma radiation below 60 keV, therefore only a small thickness of old lead would be needed to substantially attenuate new-lead radiation.

Even though Pb-210 impurities will be present in the primary shielding, the graded shielding implemented into the WBC design will virtually eliminate their effects in the acquired spectrum. The graded shielding was designed to eliminate lead x-rays, therefore the less penetrating 60 keV radiation from Pb-210 should be virtually eliminated as well. Only a small part of the detectors' FOV is directly exposed to lead, however the high-adaptability WBC was designed so that this lead could be easily removed, and replaced with old lead. If need be, it could even be replaced with graded shielding if Pb x-rays are present. These lead items (labeled 1-4) are shown in drawing 4040200 found in Appendix A.

The Pb-210 quantity in the lead bricks used for shielding (see figure 7-1) was measured using an HPGe detector in a lead cave for a 2 day acquisition, and no quantifiable amount of Pb-210 was measured.

Before the chosen materials are placed inside a WBC, they should be prepared such that they contain/emit the least amount of impurities/radiation as possible. Table 2-1 showed a ten-fold decrease in activity present in sandblasted lead bricks as compared to non-sandblasted bricks. This is because adsorbed gasses and radioactive fall-out impurities lie mostly on the surface of materials, and are removed during sandblasting. Therefore, all WBC parts, or at least ones closest to the detectors should be sandblasted with K-40 free blasting material. In addition to sandblasting, all WBC parts close to the detector should be painted with radionuclide-free spray paint. Plastic-based paint attenuates beta radiation emitted from materials, thereby reducing background counts. Painting WBC parts will also reduce the adsorption of radioactive gases, as well as corrosion between dissimilar metals due to voltage potential differences.

Aside from the primary and graded shielding materials, all other materials within the counter are made of either brass or mild steel. Structural components of the WBC were designed using mild steel, and parts of the copper shielding are fastened using brass bolts. Brass is made from zinc and copper, therefore its characteristic x-rays are almost identical to those from the copper shielding. Both mild steel and brass were selected, since they typically are fairly free from radioactive impurities.

K-40 PMT Contamination

In section 5-3, varying amounts of lead shielding were used to determine the attenuation characteristics of background radiation. When larger amounts of shielding were used, it was noticed that the K-40 photopeak did not diminish as much as expected. The net K-40 photopeak count rate from a detector placed in 11 cm of lead shielding, was measured to be 0.02520 ± 0.00059 c/s, where it should have been approximately 0.0007 c/s. Figure 7-1 shows the 11 cm shielding used in the experiments, and the detector position inside the shielding.

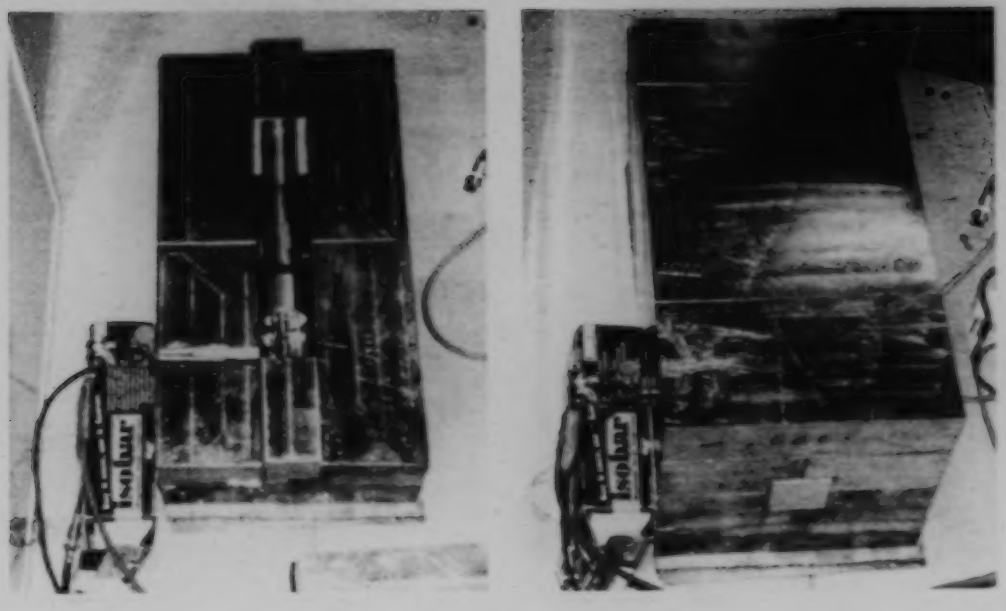

Figure 7-1. The 11 cm thick lead shielding arrangement, half and fully shielded.

K-40 detector contamination was therefore suspected, and was confirmed by using a HPGe detector at the University of Alberta's SLOWPOKE reactor site. Hamamatsu, the company that made the detectors was contacted, and they supplied K-40 contamination specifications for their detectors, which are summarized in table 7-1 below.

Part	K-40 Content	K-40 Counts
Window	3.89 Bq/Kg	0.016 Bq
Side Bulb	1340 Bq/Kg	31.2 Bq
Stem	402 Bq/Kg	2.09 Bq
Chip Tube	1340 Bq/Kg	0.67 Bq
	Total:	**34.0 Bq**

→ 0.02 c/s in detector

Table 7-1. K-40 activities from various parts of Hamamatsu PMTs.

Hamamatsu reported that approximately 0.02 c/s in the K-40 photopeak should be expected from the K-40 contaminants in the PMT. This value corresponds well with the measurements taken in the 11 cm lead shielding. Although this is not a large count rate, each of the 64 detectors will contain this amount of contamination, and the collective counts will definitely affect the WBC's performance. Particularly affected will be K-40 subject quantification, however, lower-energy isotope quantification would also be affected; the K-40's compton continuum will add to low-energy background. Chapter 8 quantifies the impact on the WBC's MDAs when this contamination is present. Figure 7-2 shows the NaI background spectrum acquired over two days, when the detector is placed inside the 11cm lead shielding. The 1.46 MeV K-40 photopeak in the spectrum is evident, and is mostly due to K-40 contamination in the PMT.

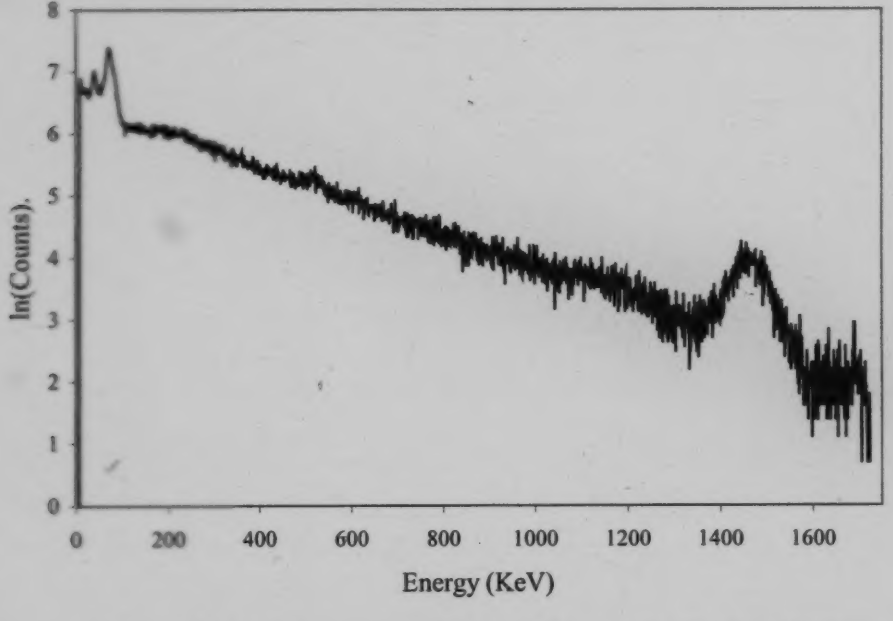

Figure 7-2. The NaI spectrum acquired over 48 hours in the 11 cm lead shielding.

Low-activity detectors especially constructed for low-activity work such as whole body counting, can also be used to decrease the background counts. These detectors use brass detector cans in place of aluminum ones, and use purified glass in the PMTs, which is free from K-40 impurities. Glass-free PMTs can also be purchased, which use very

pure quartz as the PMT window. Low activity NaI detectors are quite costly however, costing approximately twice that of standard NaI detectors.

7.2 Location

The physical location of a whole body counter can greatly affect the background counts observed in its acquired spectra. Although no location will be free from background radiation, awareness of a WBC's surroundings is necessary so that its background can be reduced as much as possible. It may even be possible to avoid some background elements altogether.

Desired Conditions

Several conditions for a WBC's location are desired to help achieve a low background count. As seen in Chapter 2, cosmic radiation can be minimized if a WBC is placed in the northeastern-most section of a building. By doing this, the building acts as a shadow-shield against the predominantly northeast directed cosmic radiation.

K-40 is a large component in background radiation, and is abundant in brickwork, cement, glass, and other building materials. New buildings made of metal, drywall and vinyl siding contain far fewer background counts from K-40 as compared to old structures made of brick and plaster. The net K-40 counts from the SLOWPOKE reactor site, which is located in the basement of an old brick building, is 2.5 times greater than that obtained from a more modern building. Therefore, a whole body counter should be placed in a building made of modern, K-40 free materials.

The last major type of background radiation that can be reduced by selecting a counter's location comes from Rn^{222} gas. Radon gas is a decay product of U-238, which is naturally found in soil and construction materials. In particular, brick rooms that are located on the ground or basement level of a building, and whose air is stagnant, are prone to high radon activity. Well-ventilated rooms made from modern materials should be used to house WBCs. Most WBCs are located on the ground or basement floor due to their mass, therefore an air-tight sealant should be used on the floor to minimize the amount of radon gas that leaches through the flooring. For ultra-high sensitivity

counting, the counter (not a whole body counter) is usually purged of air using nitrogen gas, so that any existing radon gas in the air is removed.

For a well-shielded counter, the various background contributions from K-40, Rn-222, and cosmic radiation can be seen in the figure below.

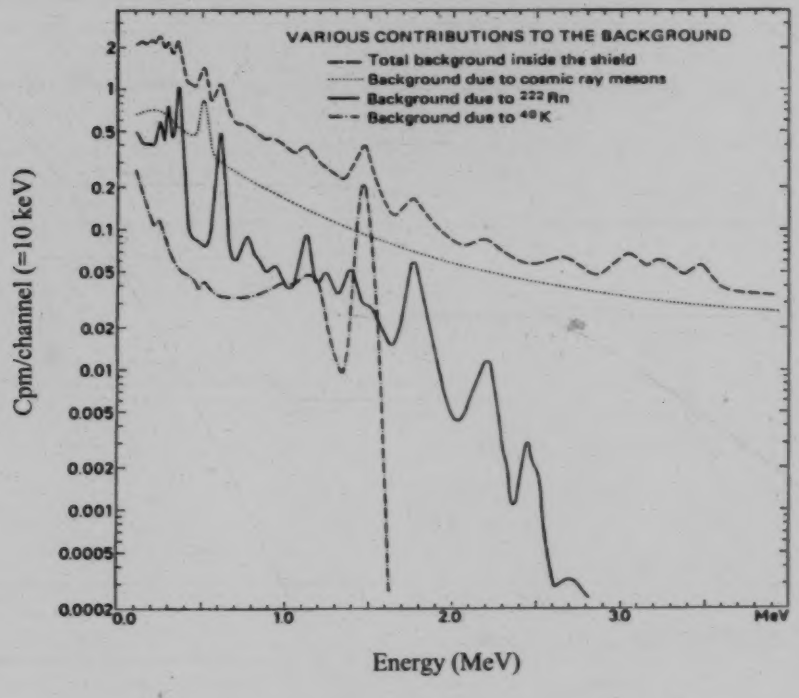

Figure 7-3. Background contributions for a shielded NaI detector[3].

As can be seen from the graph, for energies up to 1.5 MeV, the main component in the background spectrum comes from cosmic radiation. This is followed by the radon gas contribution, and then closely by the K-40 component. These relative contributions will vary greatly depending on the shielding thickness, the purity of the air (Rn-222, Rn-220 free) in the counter, and the counter's location.

Aside from the materials used to house the counter, the work conducted in nearby rooms should also be noted when selecting a location for a WBC. Adjacent rooms that use radionuclides are of particular concern, since this presents a high-background environment. Radionuclides can be physically tracked into the WBC, thereby increasing

the counter's apparent background count rate. Particular attention should be paid to potentially airborne radionuclides, and positive-pressure rooms should be used to reduce diffusion of these radionuclides into the counter. Room-shielded counters are more prone to contamination than shadow-shielded counters, because of the larger detector FOV and counter volume. However, in the presence of a high-background environment, shadow-shielded WBCs have a higher low-energy background count, since some radiation is scattered into the counter. If the direction of the external radiation flux is known, a shadow-shielded WBC should be positioned perpendicular to it, so that scattering into the counter can be minimized. Areas which contain a higher than average background should be avoided if possible.

Conditions at the CCI

The proposed location for the high-adaptability WBC is in the nuclear medicine area of the Cross Cancer Institute (CCI), in Edmonton, Alberta. Being in a nuclear medicine environment, the background counts will be very high, and this is an obvious concern for the WBC. In order to assess exactly the extent of background in the nuclear medicine department, a NaI detector was placed in the proposed WBC room 1 meter above the ground, and a one-hour acquisition was taken. The spectrum can be seen in figure 7-4, and was considered the worst-case scenario, since it was acquired while two injected patients were being scanned in adjacent rooms.

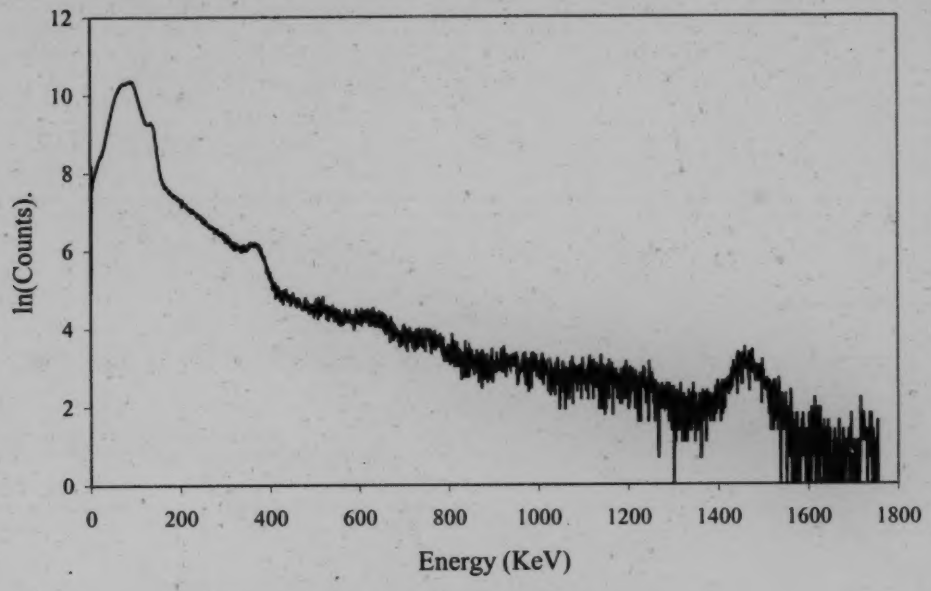

Figure 7-4. The worst-case background spectrum obtained from the CCI.

As expected, the spectrum acquired in the nuclear medicine department contains an enormous amount of low-energy background radiation. In particular, photon energies around 100 keV (from Tc^{99m}, Ga^{67}) are very abundant, and some higher energies exist as well (364 keV from I^{131}). The total number of counts in the CCI spectrum for all energies below 400 keV is approximately 3.5 times that of a normal background environment. Although the CCI tests showed very large low-energy background counts, the newer building materials used there generated a low K-40 count. Approximately 2.5 times fewer net K-40 counts were recorded in the CCI spectra as compared to the SLOWPOKE reactor site.

It was of interest to see how much the CCI background spectrum changed over time. For long WBC acquisitions, the stability of the background counts is very important, and affects the standard deviation and errors in the measured background. If a long WBC acquisition is taken in a high-background environment, but then later a low-background is subtracted, large quantification errors will result. Therefore, the NM department was monitored over a 5 day period of time. The acquired counts from 2-hour acquisitions for energies of up to 400 keV can be seen in figure 7-5.

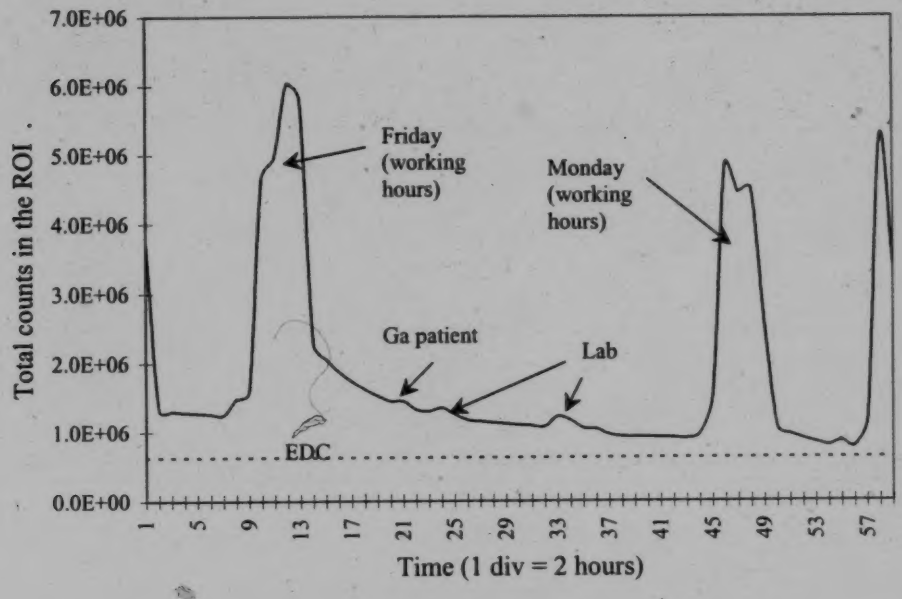

Figure 7-5. The total spectrum counts up to 400 keV acquired at the CCI over 5 days.

Figure 7-5 shows a tremendous variation in the amount of radioactivity present in the nuclear medicine department over time. The largest background measurements are observed during the regular working hours (maximum on Friday), and are 7.7 times larger than the smallest measurements, which are seen after-hours (minimum on Monday morning). This large background variation could present a problem if a shadow-shielded whole body counter is placed in the nuclear medicine area at the CCI.

Aside from observing that the CCI nuclear medicine department has very large time-varying background levels, other interesting facts can be observed from figure 7-5. Because the NM department is located near a radiopharmaceutical laboratory, its background counts are also very dependent on what happens in the lab next door. In figure 7-5, the increased activities indicated by the labels 'lab' show times when deliveries were being made to the lab. Also, figure 7-5 shows that the after-hours background appears to accumulate over the workweek (compare the after-hours background level on Monday with after-hours background level on Friday), but most of it decays over the weekend. The Sunday/Monday levels are very close to the EDC (our experimental lab), which has a low background environment. The decay time from the

curve indicates that the after-hours background is from a mix of radionuclides, most likely Tc^{99m}, Ga^{67} and I^{131}.

In order to assess the impact of the high-background environment on a shadow-shielded WBC, the arrangement in figure 5-21 was set up at the CCI. The smoothed spectra obtained at the CCI and EDC can be seen below in figure 7-6.

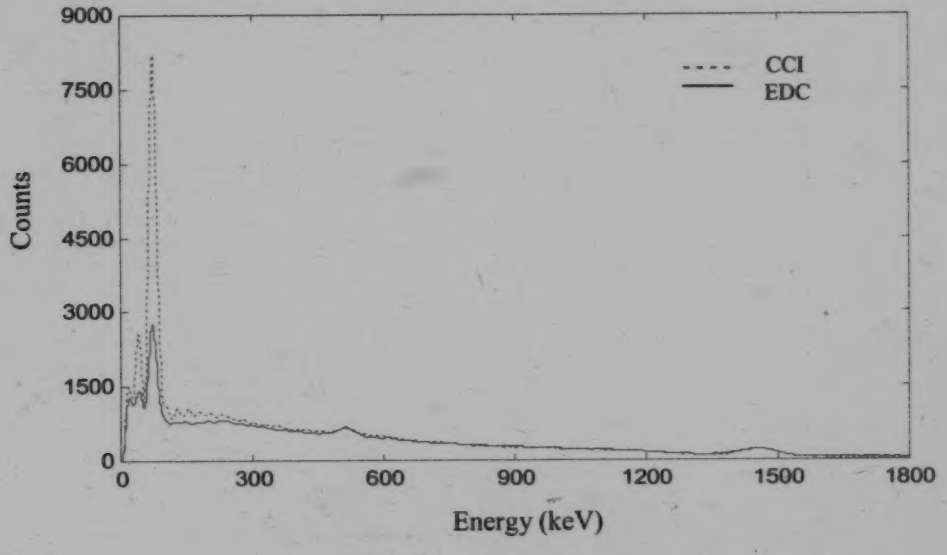

Figure 7-6. Shadow-shielded spectra from the CCI and the EDC, 2 day acquisition.

It is obvious from figure 7-6 that an increase in the background activity has an effect on the shadow-shielded spectrum. Similar to figure 5-22, a large increase in the low-energy part of the spectrum from scattered radiation is seen. Above 100 keV, only a 6.3% increase in counts is observed, however below 100 keV, the number of counts is doubled. The lead and iodine-escape x-ray peaks are also greatly increased. In the presence of a high background, the lead x-ray peak is increased by 187%, and the iodine peak is increased by 150%. As mentioned in Chapter 5, these effects will be greatly reduced in the presence of graded shielding, and larger detector-shielding distances.

The building engineer at the CCI was consulted, and confirmed that individual room ventilation within the NM department can be easily adjusted. A particular room can have a positive pressure compared to the surrounding rooms. By making the WBC room

the highest-pressure room in the area, the flow of airborne radionuclides from surrounding rooms into the WBC can be minimized. In particular, airborne radionuclides from xenon gas and iodine-injected patients can be reduced significantly.

The NM department at the CCI is not a good location for low-energy radionuclide quantification using a shadow-shielded WBC. Although graded-shielding experiments have not been done, it is expected that even with this shielding in place, some scatter radiation will be detected by the WBC. The huge background fluctuations in the department will present a larger source of error when quantifying background radiation, thus making radionuclide quantification difficult near the counter's MDA . For the quantification of radionuclides with energies of 400 keV or greater however, this high-background environment will have little effect.

References

[1] J.H. Kaye *et al.* Background reductions obtained with gamma detectors by use of massive cosmic-ray shielding. *Nuclear Instruments and Methods*. **100**:333-348;1972.

[2] J.R. DeVoe, Radioactive contamination of materials used in scientific research. *National academy of sciences-NRC*. Pub 895, nuclear science series, report #34;1961.

[3] A. Stenberg, I.U. Olsson, *Nuclear Instruments and Methods*. **61**:125;1968.

Chapter 8

Expected Performance

8.1 Proposed Operation

The process by which the WBC will operate is shown below, in flowchart form. Several points of positional feedback and data acquisition will be required so that the high-adaptability WBC can operate to its full capacity.

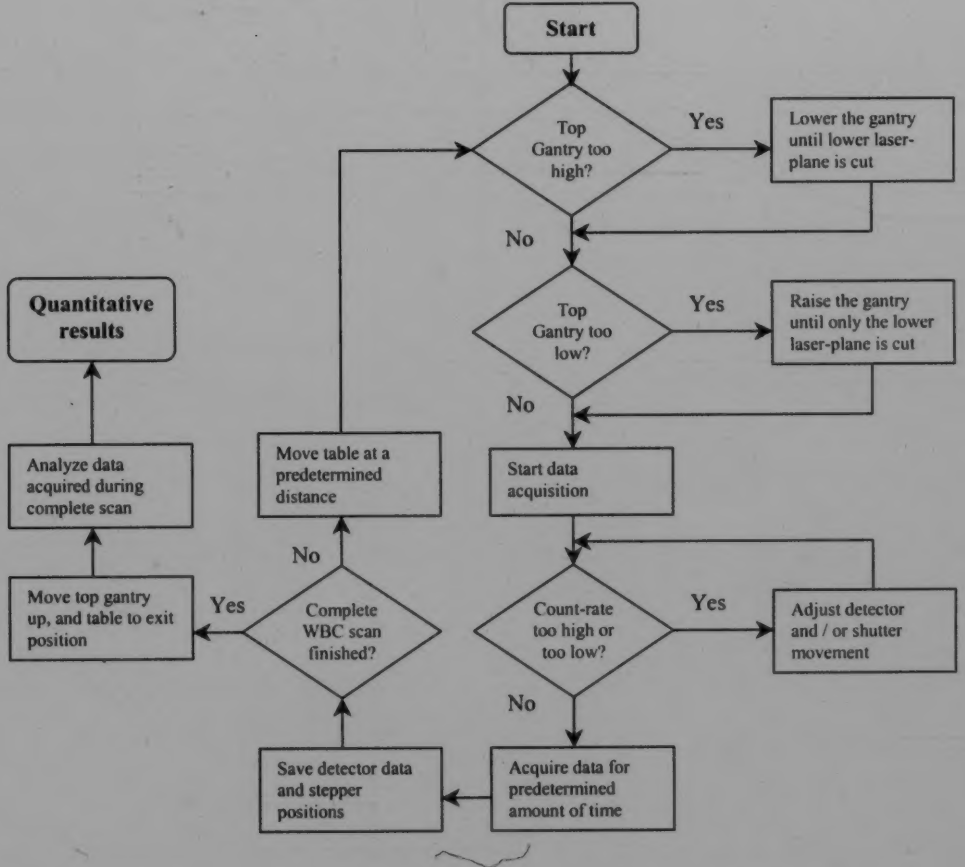
Start
Top Gantry too high?
Yes
Lower the gantry until lower laser-plane is cut
No
Top Gantry too low?
Yes
Raise the gantry until only the lower laser-plane is cut
No
Start data acquisition
Count-rate too high or too low?
Yes
Adjust detector and / or shutter movement
No
Acquire data for predetermined amount of time
Save detector data and stepper positions
Complete WBC scan finished?
No
Move table at a predetermined distance
Yes
Move top gantry up, and table to exit position
Analyze data acquired during complete scan
Quantitative results

Figure 8-1. Flow-chart describing the proposed operation of the high-adaptability WBC.

Prior to starting the WBC scan ('start' in the flow-chart), the subject needs to be positioned on the table, and guided into the counter at a pre-defined start position. One proposed start position of the scan would be to place the subject head-first into the WBC, and start the scan when the end-most detector bank is right above the subject's head. The other detector banks would therefore be positioned over the subject's neck and thorax. The end of the scan would be completed when the detector banks are all positioned over the legs, with the end-bank situated near the subject's ankles.

Once the subject is initially positioned, and the end-of-scan table position is determined, the WBC can scan the subject automatically. The top gantry can automatically adjust its height via laser feedback (discussed in Chapter 4), to accommodate for varying subject contours. Once the top gantry height is adjusted, data acquisition will proceed. A quick check on the WBC acquisition count rate will be made to determine whether the WBC's detector sensitivity should be increased or decreased. Detector and shutter movement will be adjusted accordingly, or an override used, which would enable the WBC to acquire counts even though it experiences huge count rates. This is desired, so that local hotspots like the bladder will not affect the overall sensitivity of the counter. The 'hot' data can be removed later from the data set once the full scan is complete. Once the appropriate WBC sensitivity is set, it is proposed that data from the subject be acquired in a step-and-shoot manner. This method was chosen to make data analysis simpler. The duration of the acquisition at a specific table location will depend on the total scan-time, and the number of steps taken during the scan. Collimators separate the detector banks in our WBC, therefore between the banks there is decreased sensitivity. It is proposed therefore, that the table be moved in steps of half the distance between the banks (10 cm steps). By doing this, a flatter longitudinal response will be achieved. For an adult subject scan of 30 minutes, approximately eleven, 10 cm steps will be required, each lasting approximately 3 minutes. At the end of each step, the acquired data will be saved to the computer, and the table and top gantry moved in preparation for the next scan. This process is repeated until the whole length of the subject has been scanned. The data from the subject can then be used to extract quantitative information. Computer-based whole body counter analysis[1] and control[2] of this sort has been accomplished by other facilities.

The automated procedure described can also be used to calibrate the whole body counter. By making use of a calibrated source (see Chapter 3), acquisitions at various top-gantry heights, detector / shutter positions, and table positions can be obtained. This data will then be used to generate the necessary calibration curves needed for radionuclide quantification.

8.2 Subject Count Rate

The Semi-Empirical Regression Method was used to simulate subject count rates from a variety of body sizes during a virtual scan in the high adaptability WBC. The proposed scan described in the previous section was modeled, complete with top-gantry and top-detector movement. The regression maps shown in Chapter 5, which describe the detector responses from the detector banks were used to accurately model all 64 detectors in the counter. Six different body sizes were investigated, all containing homogeneously distributed natural-body levels of K-40 (7 Bq/Kg of 1.46 MeV gamma activity). The dimensions for the six subjects were taken from the BOMAB phantoms described in Chapter 3. The six body types included:

- PM – Phantom Reference Male
- PM5 – Phantom Male Fifth Percentile
- PM95 – Phantom Male Ninety Fifth Percentile
- PW – Phantom Reference Female
- P10 – Phantom Reference 10 year old
- P4 – Phantom Reference 4 year old

A baby phantom (BB) was also simulated, however instead of a scanning-bed count, its stationary response above the bottom-middle detectors was modeled. The BB phantom was modeled using a single cylinder, with a diameter of 11 cm, a height of 31.6 cm, and a weight of 3 kg,. The phantom was placed over the bottom-middle detector bank on a virtual crib made of 3 mm thick polycarbonate plastic. The top gantry was then lowered, such that it was 10 cm above the bottom of the counter, just enough so that a baby could be kept at a comfortable temperature via heating lamps, if necessary. Only the

detector responses from the top and bottom-middle banks were measured during the whole body count.

The results from all seven simulations are summarized in table 8-1 below, along with the total number of detectors contributing towards the count rate. All count-rates and efficiencies shown below were individually simulated for each phantom type. The K-40 (c/s) uncertainty was calculated by implementing the maximum and minimum possible weighting factors to the phantom simulations to create an uncertainty, and adding to this in quadrature, the average uncertainty from the regression maps. Because the WBC's efficiency changes during a head-to-toe scan, the average WBC detector efficiency (shown below) for each phantom type was used for later calculations.

Phantom Type	K-40 (c/s)	Uncertainty (c/s)	Active detectors	WBC efficiency	Uncertainty
PM	0.509	0.009	64	0.00104	1.84×10^{-5}
PM5	0.434	0.008	64	0.00126	2.32×10^{-5}
PM95	0.535	0.009	64	0.000730	1.23×10^{-5}
PW	0.466	0.008	64	0.00119	2.04×10^{-5}
P10	0.373	0.007	64	0.00148	2.78×10^{-5}
P4	0.232	0.005	64	0.00185	3.99×10^{-5}
BB	0.117	0.005	16	0.00560	2.39×10^{-4}

Table 8-1. Summary of the detector responses simulated using seven different phantoms.

As expected, the larger-sized subjects yielded a larger count rate. The worst count-per-detector response came from the 4 year old phantom. This phantom is 92.5 cm long, which is too large to be placed length-wise along the bottom-middle detector bank, but almost too short to be scanned in the normal fashion. The WBC has the worst response for these intermediate sized subjects.

8.3 Minimum Detectable Activity

The minimum detectable activity and its uncertainty (through standard error propagation) was calculated for each of the phantom types mentioned previously, by using the generated data shown in table 8-1. As mentioned, the PMTs have K-40 contamination, therefore the WBC's MDA for K-40 quantification will be affected. Before the MDA could be calculated however, the background count rate in the energy window of interest was required. For K-40 quantification, the window of interest for our NaI detectors was 1334 – 1586 keV. The smoothed energy spectrum acquired using 11 cm of lead shielding at the Cross Cancer Institute was used to determine the background count rate. The background counts in the K-40 energy window was measured to be 0.04505 ± 0.00051 c/s. This is the gross background count rate with K-40 contamination present. Subtracting the K-40 peak from the background yields a count rate of 0.01985 ± 0.00078 c/s. Each of the 64 detectors in the WBC is expected to experience this count rate. Using equation 3-3, the MDAs for the different phantom sizes with and without K-40 contamination (digitally subtracted from the spectrum) were calculated for a 30 minute scan, and are shown below in table 8-2.

Phantom Type	Natural body K-40 activity (Bq)	MDA (Bq) - *no PMT contamination*	Uncertainty (Bq)	MDA (Bq) - *with PMT contamination*	Uncertainty (Bq)
PM	491.24	120.68	3.19	181.06	3.36
PM5	344.73	99.32	2.68	149.02	2.87
PM95	732.93	171.30	4.43	257.02	4.56
PW	391.27	104.99	2.74	157.52	2.85
P10	251.23	84.22	2.29	126.36	2.48
P4	125.27	67.51	1.97	101.30	2.26
BB	20.90	11.30	0.53	16.89	0.73

Table 8-2. The WBC's MDAs for a 30 minute scan, with and without PMT K-40 contamination.

The MDAs shown in table 8-2 are very good. Even with K-40 contamination, all of the MDAs are lower than the total amount of K-40 present in the phantoms. Therefore, natural body background levels of K-40 in all body sizes will be detectable by the WBC.

Although the Semi-Empirical Regression Method was not used to model the MDAs from different isotopes, calculations based on the first-order approximation method and BOMAB phantoms were made. Half-hour simulated scans were made, where the phantoms contained the same amount of radioactivity as shown in table 8-2. The calculated MDA for Cs-137 (662 keV) in the P4 phantom was approximately 51 Bq, with a quantification error (equation 3-2) of only 9.5%. This MDA value was based on K-40 free PMTs, and would increase to approximately 74 Bq with contamination. These values are very good, and are better than the average MDA (91 Bq) for a typical WBC[3]. Lower-energy isotopes have a smaller MDA, since the PTTR and intrinsic efficiency of the detector increases substantially compared to the increase in background observed at lower energies. For instance, an isotope emitting 122 keV photons, the PM man would only have an incredibly low quantification error of ~ 0.4 %.

Although the WBC will have a very small MDA and quantification error at low energies, these values will vary slightly with time if the counter is placed in the nuclear medicine department at the CCI. As discussed previously, below 400 keV the background counts in the NM department fluctuate, and this will add an additional uncertainty when gamma energies below 400 keV are being quantified. Without shielding, the background counts around 122 keV would vary by a factor of 10. With shielding, a fluctuation at least 2-4 times normal background would be expected. This would cause the quantification to vary from ~ 0.4 % to 0.5 %, and the MDA to vary from 2.61 to 5.21 Bq. Near the counter's MDA, these fluctuations may cause problems.

Aside from the MDA, if a well-known background is present, the MDA_q can be determined using equation 3-4. MDA_q is the minimum detectable activity that is required to statistically satisfy quantitative determination. Below this amount of activity, quantitative information can not be obtained that will be statistically useful. The background spectrum in the K-40 photopeak region (1334 – 1586 keV) is very stable, and therefore 'well-known'. This is evident from the NaI-HPGe background spectra shown

in figure 8-2, which were acquired in an open-geometry (2500000 s), using a 30% HPGe and a 1.5" x 3" detector. Here, 95% of the total counts in the NaI spectrum that make up the K-40 peak, are actually from the K-40 isotope. These K-40 counts in the background spectrum are extremely stable over time in any given environment. The rest of the counts in the photopeak come from Bi-214, which is a Rn-222 decay product, so therefore will vary slightly over time.

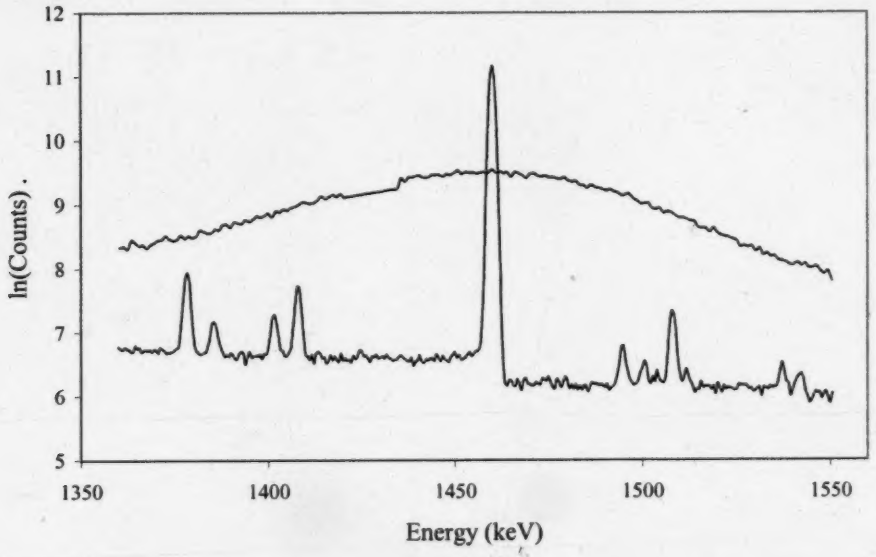

Figure 8-2. The NaI and HPGe background spectra in the K-40 photopeak region.

The MDA_q values (using equation 3-4) for naturally found K-40, and the percent errors for K-40 quantification were calculated for all 7 phantom types described in section 8.2. To decrease the errors in K-40 quantification, an 8 hour background acquisition was used to determine the background count rate. All results are summarized in tables 8-3, and 8-4. Other sources of uncertainty during scanning will include activity of the standard, size and thickness of the subject, and counting statistics.

Phantom Type	Natural body K-40 activity (Bq)	MDA_q (Bq) - *no PMT contamination*	Uncertainty (Bq)	MDA_q (Bq) - *with PMT contamination*	Uncertainty (Bq)
PM	491.24	284.60	7.52	414.00	7.69
PM5	344.73	234.23	6.31	340.73	6.57
PM95	732.93	403.99	10.45	587.66	10.43
PW	391.27	247.60	6.46	360.17	6.51
P10	251.23	198.62	5.40	288.92	5.66
P4	125.27	159.22	4.64	231.62	5.16
BB	20.90	29.20	1.37	41.05	1.77

Table 8-3. The WBC's MDA_qs for a 30 minute scan, with and without PMT K-40 contamination.

Phantom Type	Natural body K-40 activity (Bq)	% error - *no PMT contamination*	Uncertainty (%)	% error - *with PMT contamination*	Uncertainty (%)
PM	491.24	6.31	0.13	8.75	0.19
PM5	344.73	7.25	0.16	10.16	0.22
PM95	732.93	6.05	0.12	8.36	0.17
PW	391.27	6.82	0.14	9.50	0.20
P10	251.23	8.29	0.19	11.71	0.26
P4	125.27	12.78	0.32	18.44	0.46
BB	20.90	13.58	0.60	18.93	0.84

Table 8-4. Quantification errors for the WBC, with and without PMT K-40 contamination.

Originally, it was desired to have a maximum K-40 quantification error of less than approximately 10% for a half hour scan. This amount of error occurs approximately at the MDA_q. As can be seen from table 8-4 however, the two smallest phantoms (P4 and BB) fall short of this original target. It should be noted however, that a typical WBC will have an even higher quantification error for the P4 phantom. For the BB phantom, the

quantification error could be reduced from 18.93 % to 13.58 % if 16 K-40 free detectors were used to replace the current detectors. These low-activity detectors would also help to improve the counter's sensitivity for all other scans as well. If 16 of the WBC's detectors were replaced, and a 45 minute scan was done, the quantification for the P4 and BB phantoms could be reduced to 14 % and 11 % respectively. For K-40 quantification in small subjects, the 16 top / bottom middle detectors should be replaced with K-40 free detectors.

If 16 K-40 free detectors were purchased and the WBC was held in a static position at the thorax, a K-40 quantification error of only 9.55% for a 45 minute scan can be accomplished for the P4 sized subject.

In our WBC, a slight improvement in the sensitivity is expected. The above calculations were based on 11 cm thick lead shielding experiments, however the WBC will use 11.3 cm of lead equivalent material, plus an additional thickness from structural materials. Also, the actual path-lengths through the shielding will be more than 11.3 cm in most cases. These factors will give an effective lead thickness of roughly 17 cm, approximately 1.5 times the measured shielding thickness. The detector in the experimental shielding was positioned extremely close to the shielding walls, and this added to the background counts as well. A small Compton back-scatter peak located at ~ 250 keV is present in the spectra, however this should be significantly reduced if the detector-shielding distance is increased[4]. A large portion of the detectors' FOV in the actual WBC contains large detector-shielding distances, therefore lower background counts around 250 keV is expected.

8.4 Flatness in the WBC's Response

Point source iso-response curves similar to the ones first shown in Chapter 5 were constructed for the completed WBC. The semi-empirical regression method was used to generate accurate iso-response data, however unlike the geometric efficiency plots shown in Chapter 5, total absolute efficiencies were calculated. The lateral iso-response plot for one of the bottom-middle detectors can be seen in figure 8-3.

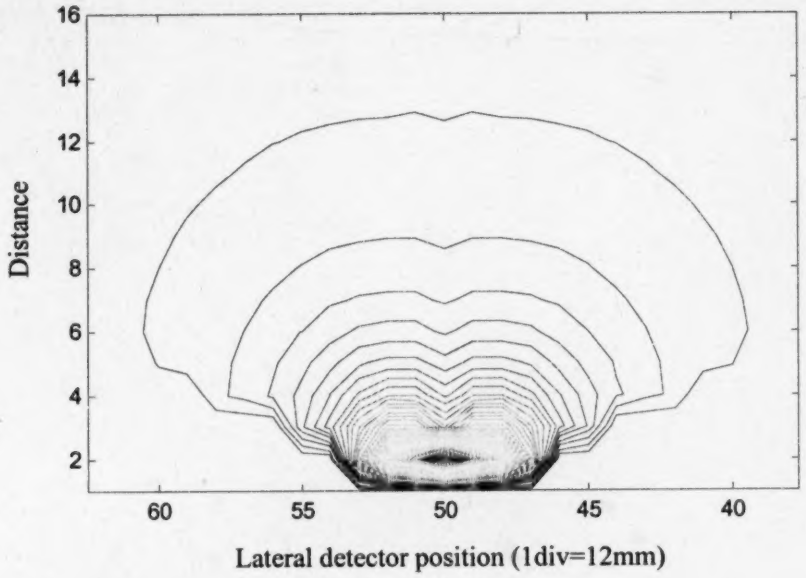

Figure 8-3. Iso-response plot for one bottom-middle detector (1div=12mm).

Iso-response plots for the middle and end detector banks are shown in figures 8-4 and 8-5. Like the previous iso-response curves, each line in the graph represents a 2% relative change in response.

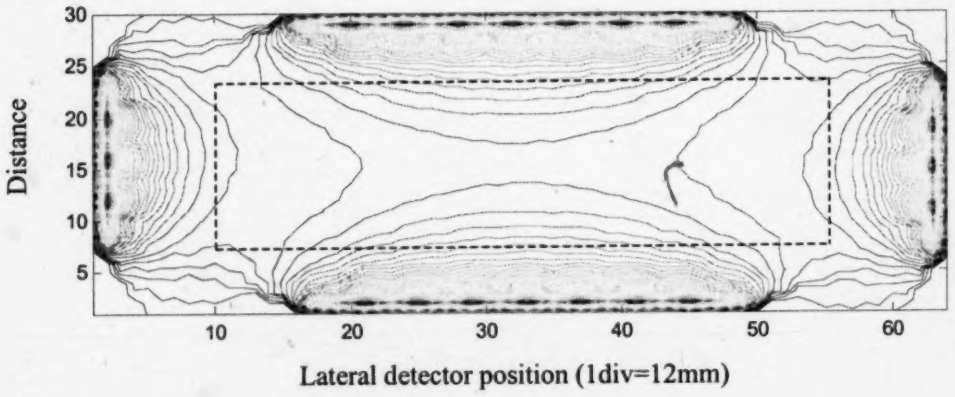

Figure 8-4. Iso-response curves for the middle detector banks of the WBC (1div=12mm).

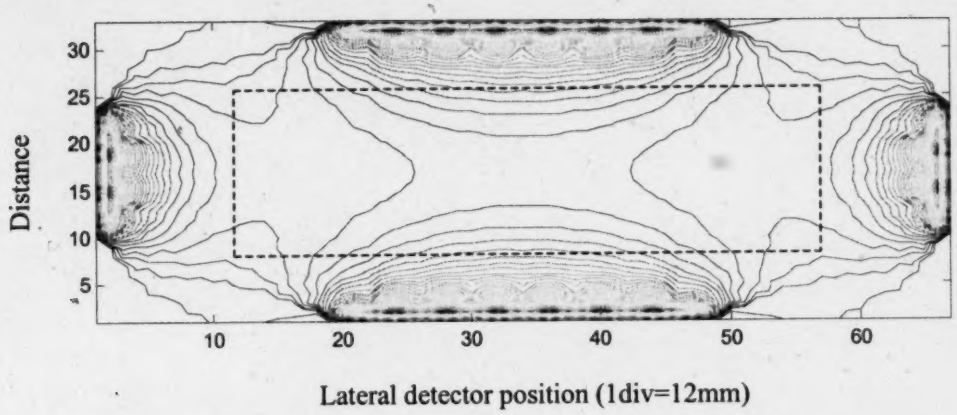

Figure 8-5. Iso-response curves for the end detector banks of the WBC (1div=12mm).

The iso-response curves show a fairly flat WBC response for both the middle and the end detector banks. In the area where a subject would lie (dotted area) within the counter, there exists only a maximum deviation of 8% in the counter's response, and most of the subject area has only a 4% deviation. Because of the top moving gantry, a greater deviation is expected for larger subjects, and less for smaller ones. These iso-response are better than the ones seen in Chapter 5, since the absolute efficiencies are less angle dependant than the geometric responses shown earlier.

The WBC design has a fairly flat response in all directions, making it suitable for whole body counting. No hot or cold spots in a subject will be undetected, and therefore accurate radionuclide quantification will be possible.

8.5 Maximum Subject Activity

As mentioned, the whole body counter will be able to adapt to high activities by detector retraction and shutter movement. The maximum amount of subject activity will depend on the amount of shift and dead-time that are considered acceptable. Shift was chosen as the limiting factor however, since the dead-time of a system can be corrected for if the count-rate is known (equation 2-12). The shift of a detector system should be less than 1%, therefore this amount of shift was used to define the maximum subject activity. From previous shift experiments (Chapter 4), it was determined that a shift of

1% corresponded to a count-rate of approximately 5600 c/s. Since opposing detectors in the WBC will have their signals summed in the summing NIM, the maximum count-rate per detector will be reduced to 2800 c/s.

In order to determine the subject activity that would create a 1% shift, the worst-case scenario was modeled for the entire WBC. When a subject is injected with a radionuclide, much of the activity ends up accumulating in the subject's bladder. The volume of the bladder is small (1 liter). Therefore, if the bladder were placed on the detector's axis ~ 20 cm away, the detector's response would be almost identical to the response from a point source with the same activity and location as the bladder. Simulations based on this point-source approach were used to generate the worst-case maximum subject activity. A point source was placed in the middle of the Reference Man thorax, and the response from a detector placed directly beneath it was modeled. The bottom-middle detector bank is the most sensitive, therefore its dimensions were used in the modeling. The PTTR for 364 keV photons, and the first-order approximation was used to model the detector's response. The generated response should be very accurate, since the source lies on the detector's axis. Remember that on-axis sources are given a weighting factor of 1.0 when the semi-empirical regression method is used. Table 8-5 summarizes the maximum subject activities for a variety of detector retraction and shuttering combinations.

Detector position (% retracted)	Shutter position (% closed)	Maximum subject activity (GBq)
0	0	0.00484
50	0	0.00812
100	0	0.01234
100	50	0.02467
100	75	0.0493
100	95	0.245
100	99	1.19
100	100	33.32

Table 8-5. The maximum subject activity for different detector and shutter positions.

By using detector retraction and shuttering, the spectral shift can be kept below 1%, even in the presence of extremely high-activity subjects. Subjects who have recently undergone iodine therapy, and have received injections in the gigabequerel range will not overwhelm the WBC.

8.6 WBC 'Imaging'

The large number of detectors used in the high-adaptability WBC makes it ideal for obtaining regional information or 'imaging' of radionuclide distributions in subjects. By using the WBC's collimators and shutters, each of the thirty two opposing-detector inputs provides information that can be used to create a rough 'image' of subject activity. The use of collimators is effective in obtaining regional subject information[5,6], and to isolate certain organs such as the thyroid and lungs for counting[7].

The full-width-half-maximum of a peak is an approximate rule of thumb in determining how close two photopeaks can be together and still be resolved[8]. This rule is based on Rayleigh's criterion, which is used to determine how close two interference peaks can be to each other and still be resolved. This criterion was used to approximate the WBC's resolution. An illustration of two peaks placed one FWHM apart from each other, and their resultant superimposed intensity profile can be seen in figure 8-6 below.

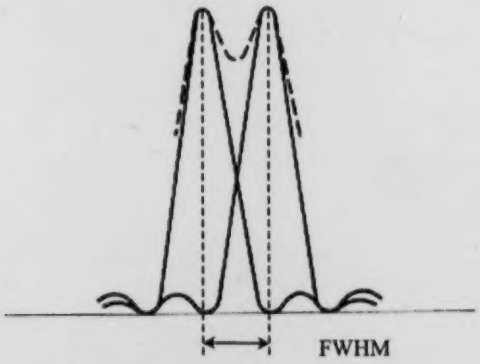

Figure 8-6. Illustration of Rayleigh's criterion for the resolution of two peaks.

The counter's approximate resolution was determined experimentally for a variety of conditions. A detector was placed inside the mock bottom-middle detector bank seen in figure 5-41, and a Na-22 point source was placed on the grid system 20 cm away from the detector (shown in figure 5-42). The source was then moved in a lateral and longitudinal direction while the detector's response to 511 keV photons was measured. The detector's response versus lateral and longitudinal distance was then graphed. From the graph, the FWHM was calculated, and therefore the spatial resolution of the setup was determined. This method of determining the WBC's resolution was used for several detector arrangements, including the detector in: high-sensitivity position, fully retracted position, and half-shuttered position. In addition to these arrangements, a 1 cm diameter hole was drilled in the 3 cm thick lead shutter, and the response with the hole centered on the detector was measured as well. This shutter design was investigated, since it was expected to deliver a better lateral resolution than the solid shutter, and can easily be incorporated into the WBC's design. The detector responses for all four arrangements are shown in figures 8-7 to 8-10.

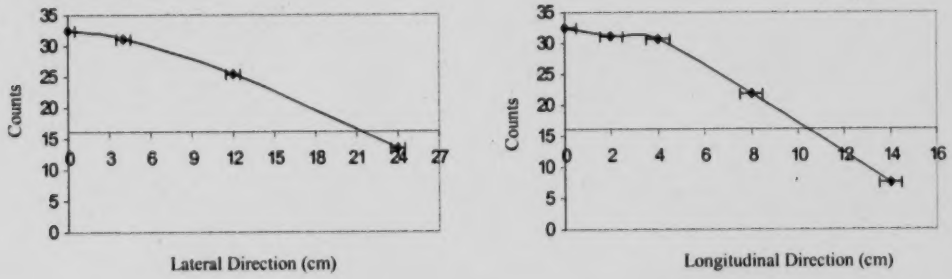

Figure 8-7. Lateral and longitudinal responses for the high-sensitivity position.

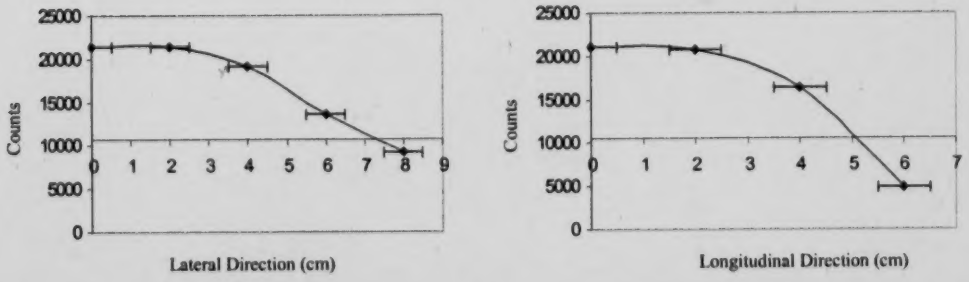

Figure 8-8. Lateral and longitudinal responses for the fully retracted detector.

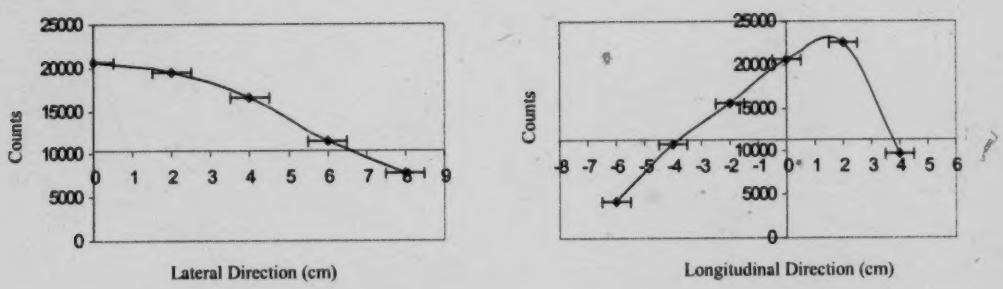

Figure 8-9. Lateral and longitudinal responses for the half-shuttered detector.

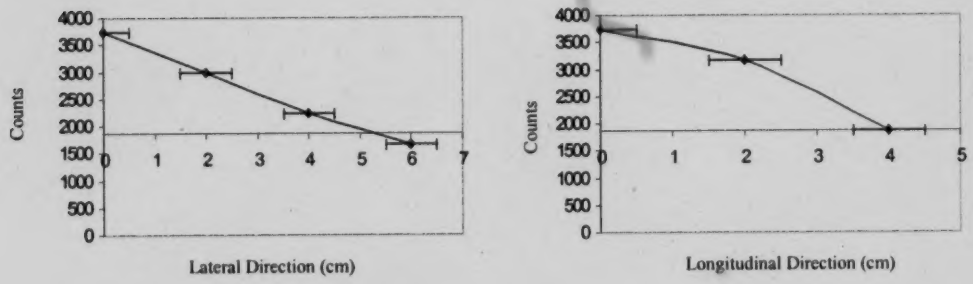

Figure 8-10. Lateral and longitudinal responses for the detector placed behind a 1cm hole.

The approximate lateral and longitudinal WBC resolutions obtained from the above graphs are summarized in table 8-6 below, where a smaller lateral or longitudinal value corresponds to a better resolution. Because the point source was placed 20 cm away from the detector, the resolutions shown below are for the bottom and top detectors within the WBC. Because they are further away from the subject, the side detectors are expected to have resolutions approximately two times the values seen below.

Arrangement	Lateral resolution (±1cm)	Longitudinal resolution (±1cm)
High-sensitivity	21	21
Fully retracted	14.5	10
Half-shuttered	13	7.5
1cm hole in shutter	10.5	8

Table 8-6. Summary of the lateral and longitudinal resolutions for various detector arrangements.

As seen in table 8-6, in general, the WBC's resolution is better in the longitudinal direction than in the lateral direction. There are two reasons for this. The more massive collimators are oriented to attenuate radiation coming from the longitudinal direction, and secondly, the collimator's physical location in the counter provides narrow collimation. In contrast, in the lateral direction, only thin sections of lead placed between the detectors for collimation purposes are used. This 'lead housing', which can be seen in Appendix A (drawing number 4040003) is only 2 mm thick, and is positioned further back from the source, making narrow collimation difficult. Higher resolution in the lateral direction is expected for lower-energy isotopes.

As is always the case with resolution in nuclear medicine, higher resolution means less detector sensitivity. In order for the resolution to increase, the detector's FOV has to decrease, which leads to poorer detector efficiency. This was seen experimentally, where the best WBC resolution was observed when the detector was, aside from a small hole, fully collimated. When the detectors were placed in the high-sensitivity position, they exhibited the worst resolution. In order to do high-resolution scans therefore, either a very active subject, or extremely long scan times will be needed. Iterative localization methods have been used to increase WBC resolution without the use of increased collimation[9], and could be used in the counter presented here.

All detector responses were symmetrical, except for the half-shuttered case. Because of the additional longitudinal collimation over only half of the detector from the shutter, a skewed detector response was observed. The amount of spatial shift in the apparent location of a point source should be taken into consideration when creating WBC 'images'.

Although experimentally the lateral resolution has an uncertainty of ± 1 cm, in the WBC, the smallest uncertainty possible will be ± 2.3 cm. This larger uncertainty occurs because the lateral spacing of the detectors in each bank is not small, being spaced 4.6 cm apart. Because the middle detector banks contain one more detector than the end banks, they are shifted one-half the width of a detector laterally with respect to the end detectors (see figure 6-7). By doing this, instead of obtaining lateral information every 4.6 cm, the sampling rate can be doubled to every 2.3 cm, thereby reducing the resolution uncertainty

from 4.6 cm to 2.3 cm as well. Because the table can move in extremely small steps, resolution in the longitudinal direction has a much smaller uncertainty.

Vertical resolution of activity distribution (i.e. surface contamination) is sacrificed by summing opposing detector pairs. As well, when more than one isotope is present, the spectrum needs to be deconvoluted before positioning information can be determined. The accuracy in position will be slightly degraded in this case.

The resolutions determined in this section were conducted using a point source, however for a distributed source in the subject these resolutions can change. For distributed sources with well-defined boundaries (such as I-131 in the thyroid), the location of the *edge* of the source distribution will be determined with the same resolution as was seen for the point source. For distributed sources whose boundaries are *not* well defined though, the location of the edge of the distribution will be more difficult to locate, since no true 'edge' exists.

References

[1] Z. Shaodong *et al.* Preliminary programmed whole-body counter. *Nuclear Science and Techniques*. **6**(3):159-163;1995.

[2] H.P. Chou *et al.* A microcomputer-based Whole-body Counter for Personnel Routine Monitoring. *Calcified tissue international*. **44**(5):815-819;1993.

[3] G.H. Kramer. The Canadian National Calibration Reference Center for In-Vivo Monitoring and the United States Department of Energy: Results of the 1993 Intercomparison / intercalibration: Final repart. *Human Monitoring Laboratory Technical Document*. HMLTD-95-3;1993.

[4] R.L. Heath. Scintillation Spectrometry - Gamma-ray spectrum catalogue. Report No. IDO-16880-1;1964

[5] S. Molloi *et al.* Whole body and regional retention of Tc-99m - labeled diphosphonates with a whole body counter: A study with normal males. *Calcified tissue international*. **44**(5):322-329;1989.

[6] C. Pirich *et al.* Monitoring the biodistribution and biokinetics of dysprosium-165 ferric hydroxide with a shadow-shield whole body counter. *European Journal of Nuclear Medicine*. **24**(4):398-402;1997.

[7] S.M. Morsey *et al.* Optimization studies of a whole-body counter to cope with possible dynamic transfer between neighboring compartments. *Health Physics*. **35**(2):325-332;1978.

[8] G.F. Knoll. Radiation detection and measurement. pp 115, *Second edition, John Wiley & Sons, Copyright 1989.*

[9] R.Novario, L. Conte. A new method for calculating the distribution of radioactivity in man measured with a whole-body counter. *Health Physics*. **58**(5):597-607;1990.

Chapter 9

Conclusions and Future Work

9.1 Conclusions

A novel mix of theoretical and experimental methods was used to develop a whole body gamma counter that encompasses all of the benefits from shadow, room-shielded, and high-activity counters into one, unique, highly adaptable counter. The final design is a shadow-shielded counter containing 64 detectors, all capable of being retracted and 'shuttered' so that high activity subjects can be scanned. For low activity subjects, the top gantry can be moved coarsely with the subject's contours, ensuring that the highest sensitivity is achieved throughout the scan.

The scanning-bed shadow-shielded configuration is sufficient for providing the flexibility needed to design a high-adaptability WBC. By using a shadow-shielded design, less material is needed to properly shield the detectors within the WBC than would be possible with a room-shielded design. The collimation required to properly shield the detectors due to the shadow-shield design, is actually a benefit when localization of radionuclide distribution is desired. For low-sensitivity counting, the collimators alone provide a longitudinal resolution of 10 cm. The large number of detectors in the counter, and the WBC's scanning movement provides lateral and longitudinal information for both the top-bottom, and side-side detector pairs. After an acquisition, this information can be used to provide rough localization of the radionuclide distribution in the subject.

Implementation of a moving top gantry into the WBC design allows the counter to be highly adaptive to all subject sizes. The top gantry moves close to the subject throughout the scan, regardless of the subject's size or shape. This enables the top detectors in the WBC to maintain maximum detector efficiency throughout the scan, which is necessary for natural body background-level quantification.

With the use of detector retraction and shutters, the WBC is able to scan high-activity subjects, and provide localization with better resolution. Pulling the detectors away from the subject limits the detector's FOV, which gives the counter a better spatial resolution. This limited FOV and larger detector-subject distance also substantially reduces the detector's efficiency and therefore its count-rate. The addition of shutters further limits the detector's FOV, making it possible for the WBC to scan very high-activity subjects, without appreciable detector saturation or spectral shift.

All 64 detectors in the WBC were modeled, and virtual scans were done, so that complete WBC specifications could be determined. This was accomplished by using the 'Semi-Empirical-Regression Method', which was developed so that NaI detector responses could be simulated in a quick and accurate manner. The high-adaptability WBC is expected to satisfactorily quantify naturally found K-40 in all subject sizes. Except for the smallest two subject sizes (P4 and BB), this will be accomplished by performing a half hour head-to-toe scan. K-40 quantification for the two smallest phantom sizes will be most easily accomplished if the 16 middle detectors in the counter are replaced with low-activity detectors, and a 45 minute stationary acquisition is taken. By using detector retraction and shuttering, high-activity subjects containing GBq amounts of activity will be accommodated as well. The WBC's design will give it a fairly flat detector response, with a maximum relative deviation of only 8% inside the WCB's usable volume. In addition to this for high-activity WBC counting, spatial radionuclide localization with a resolution of approximately 10 cm in the lateral direction and 8 cm in the longitudinal direction is expected.

This WBC's impressive and well-rounded specifications makes it very unique, and therefore well-suited to perform new and innovative studies. In particular, whole body long-term perfusion, retention, and quantitative localization studies can be performed, where subjects are injected with diagnostic or therapeutic-sized activities.

9.2 Future work

The design and optimization of the high-adaptability WBC has been completed, however an enormous amount of work still needs to be done before the WBC is able to perform its first subject scan.

All drawings for the WBC have been completed, therefore construction can commence as soon as funding and space for the WBC have been obtained. During construction, on-the-spot material samples need to be taken, and tested for contamination. Holes in the WBC still have to be planned and drilled during construction so that cables associated with the stepper motors, detectors, and switches inside the gantries can penetrate the shielding. The mechanical switch placements are not included in the drawings either, therefore they must be incorporated into the WBC as it is being built.

For the electronics, sixty-four copies of the preamplifier discussed in Chapter 4 need to be built, as well as summing amplifiers. Stepper motor drivers have to be purchased or be designed / built / tested as well. If home-built, the stepper drivers will have to be interfaced to a PC via a 8255 I/O card, and tested to make sure that they all work well together.

Once all the electronics and the WBC are assembled, a program will need to be written that will control all aspects of the counter's movement, data collection, and data analysis. The exact position of the shutters, top gantry, detectors, and table all need to be tracked and controlled, so that data from the MCB's has meaning. The front-end of the program should be very user-friendly so that a technician can operate the WBC, and built-in scans should be pre-programmed into the software. Data analysis including peak-search, photopeak quantification and deconvolution can be programmed or the software purchased, and ideally should be interactive with the front-end program for ease of use. Once a program has been developed that will compile and analyze spectral information, the WBC will be ready for calibration.

The WBC will require significant calibration. Various sized phantoms will have to be made or purchased so that calibration curves can be generated. Several calibration curves for each subject size will need to be generated, one for each shutter, detector, isotope, scan-type, and gantry position anticipated during a scan. With proper programming however, once a phantom is positioned on the table, calibration data for all of the requested combinations will be automatically obtained.

After the WBC is fully calibrated and tested, it will then be ready for its first real subject scan. Subject sizes ranging from newborn infants to full-grown adults will be accommodated, and subject activities ranging from natural body background to several

GBq will be accurately measured. The added versatility of variable subject size and detector sensitivity will make this whole body counter a unique, valuable and useful research and clinical tool.

Appendix A

Select WBC Drawings

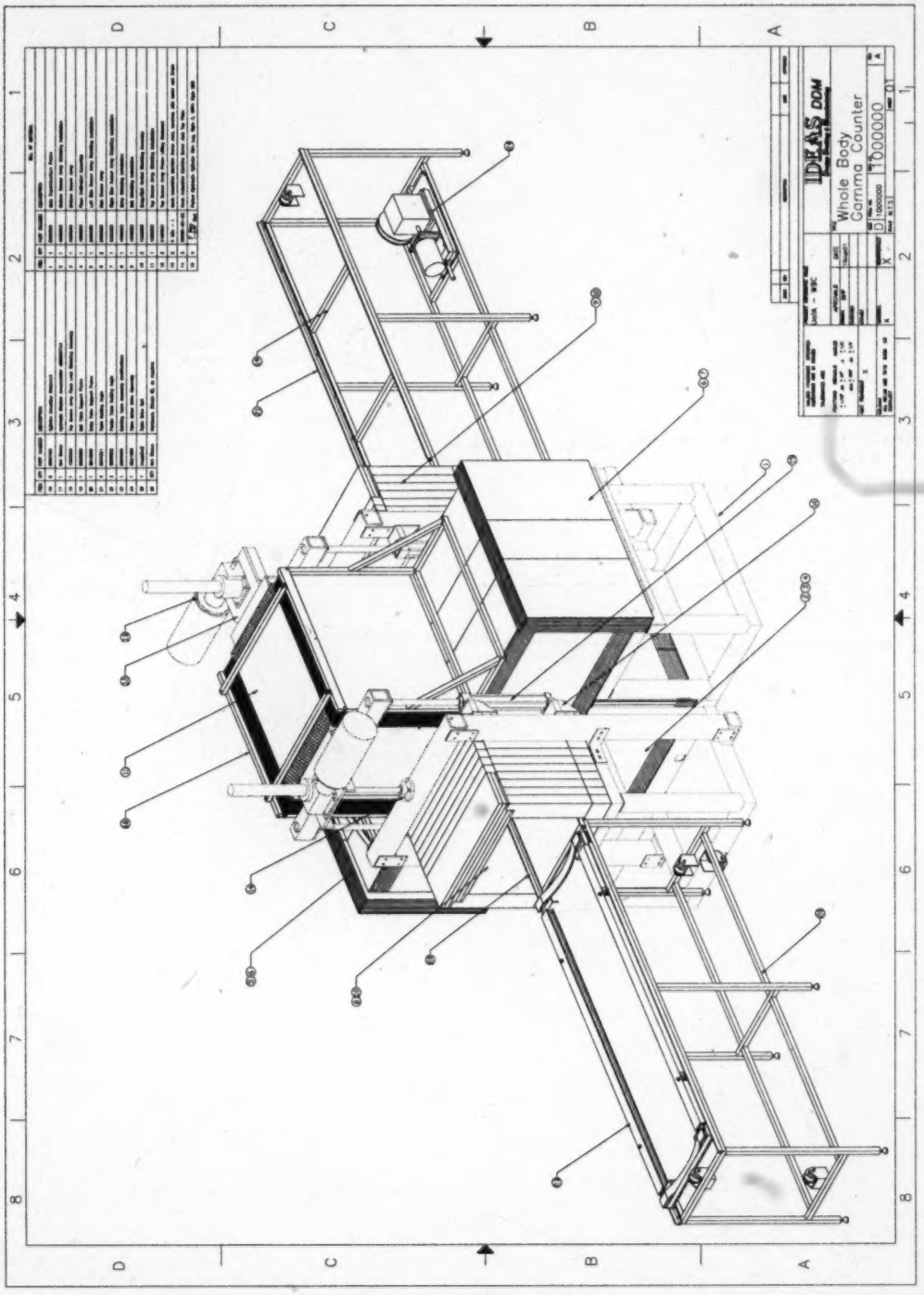
IDEAS DDM
Whole Body
Gamma Counter
1000000

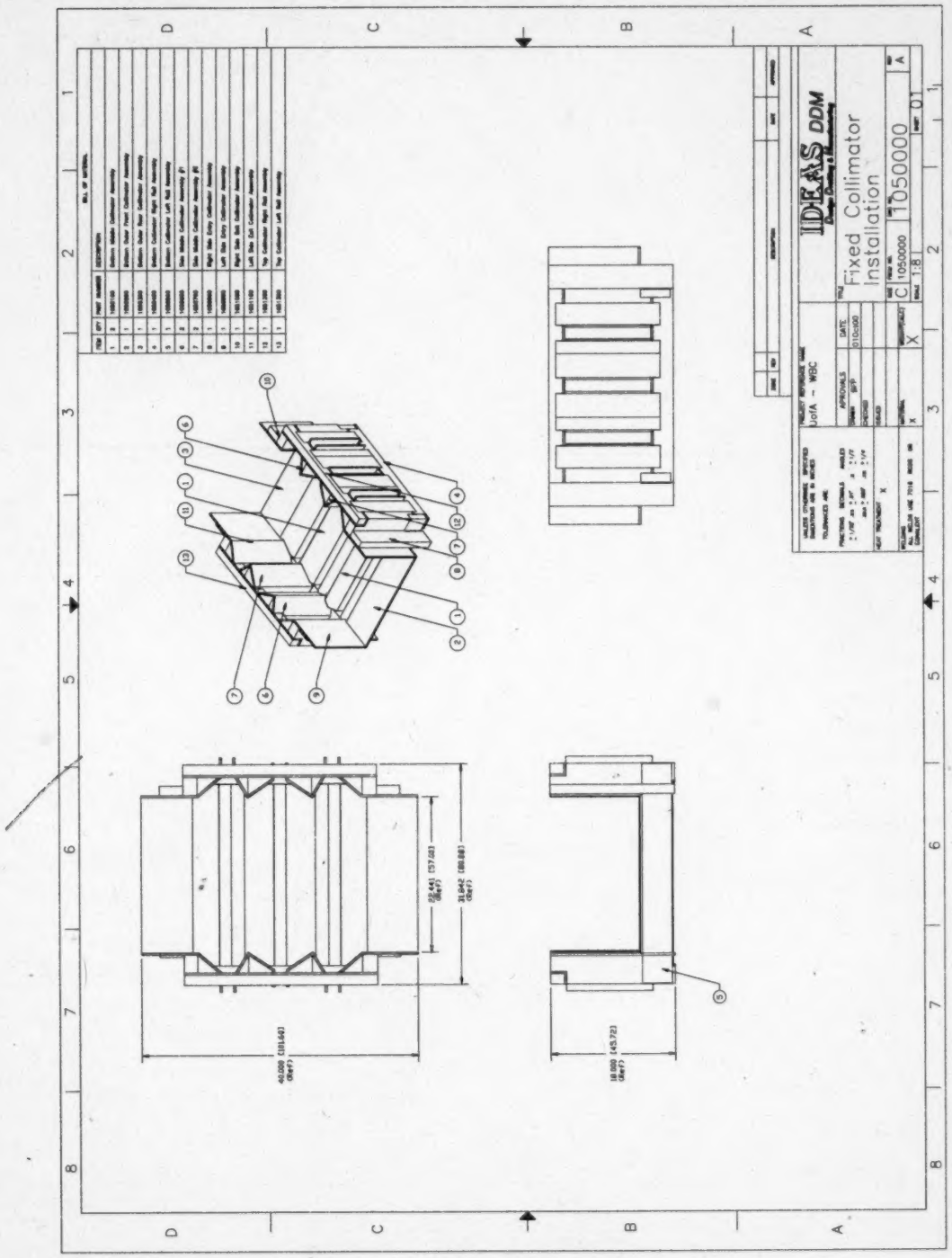
IDEAS DDM
Fixed Collimator Installation
1050000
C
SCALE 1:8
SHEET 01
A
UofA – WSC
DATE
2/10/2000
X
40.000 [101.640] (Ref)
18.000 [45.722] (Ref)

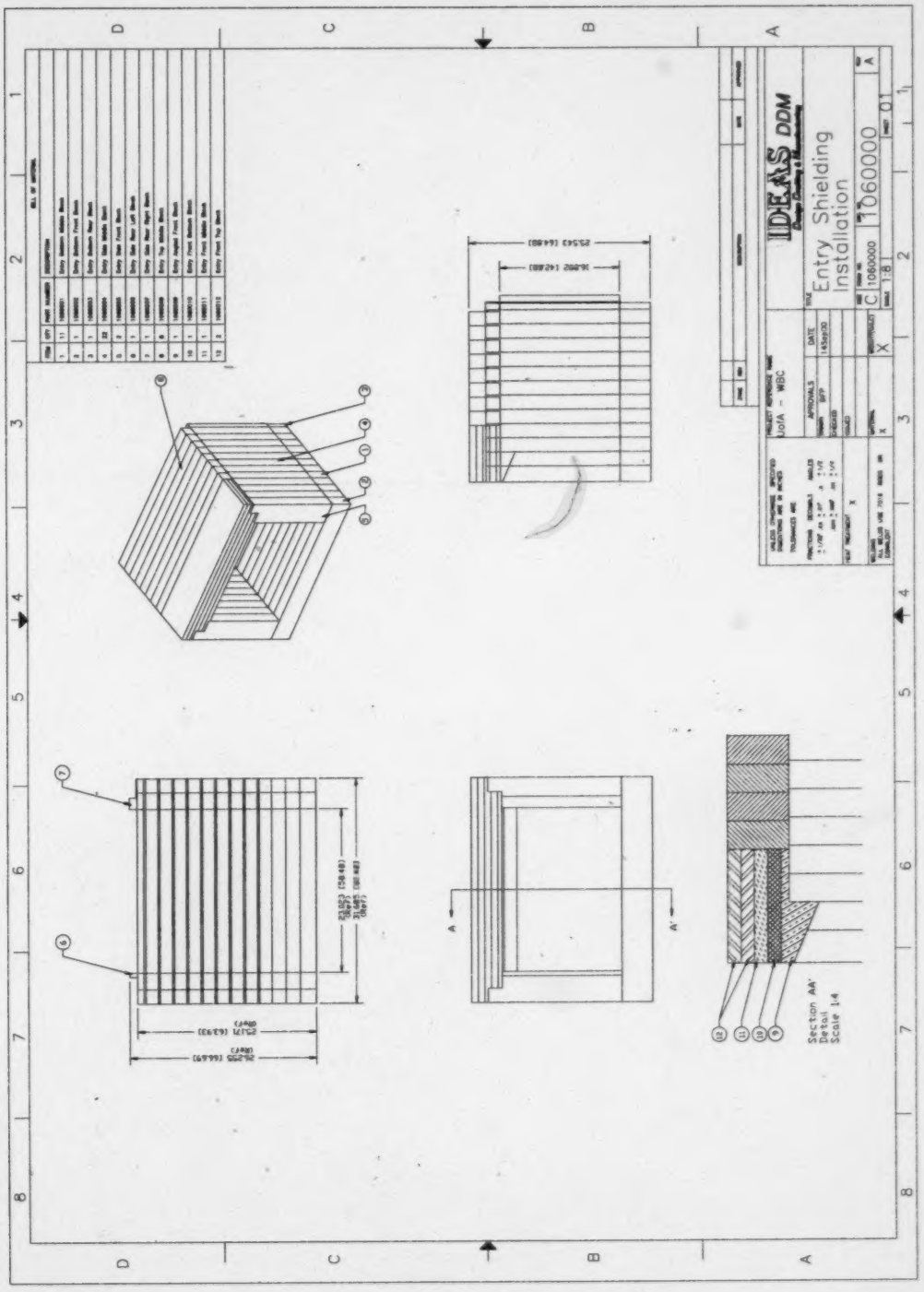
IDEAS DDM
Entry Shielding Installation
1060000
C
Section AA'
Detail
Scale 1:4

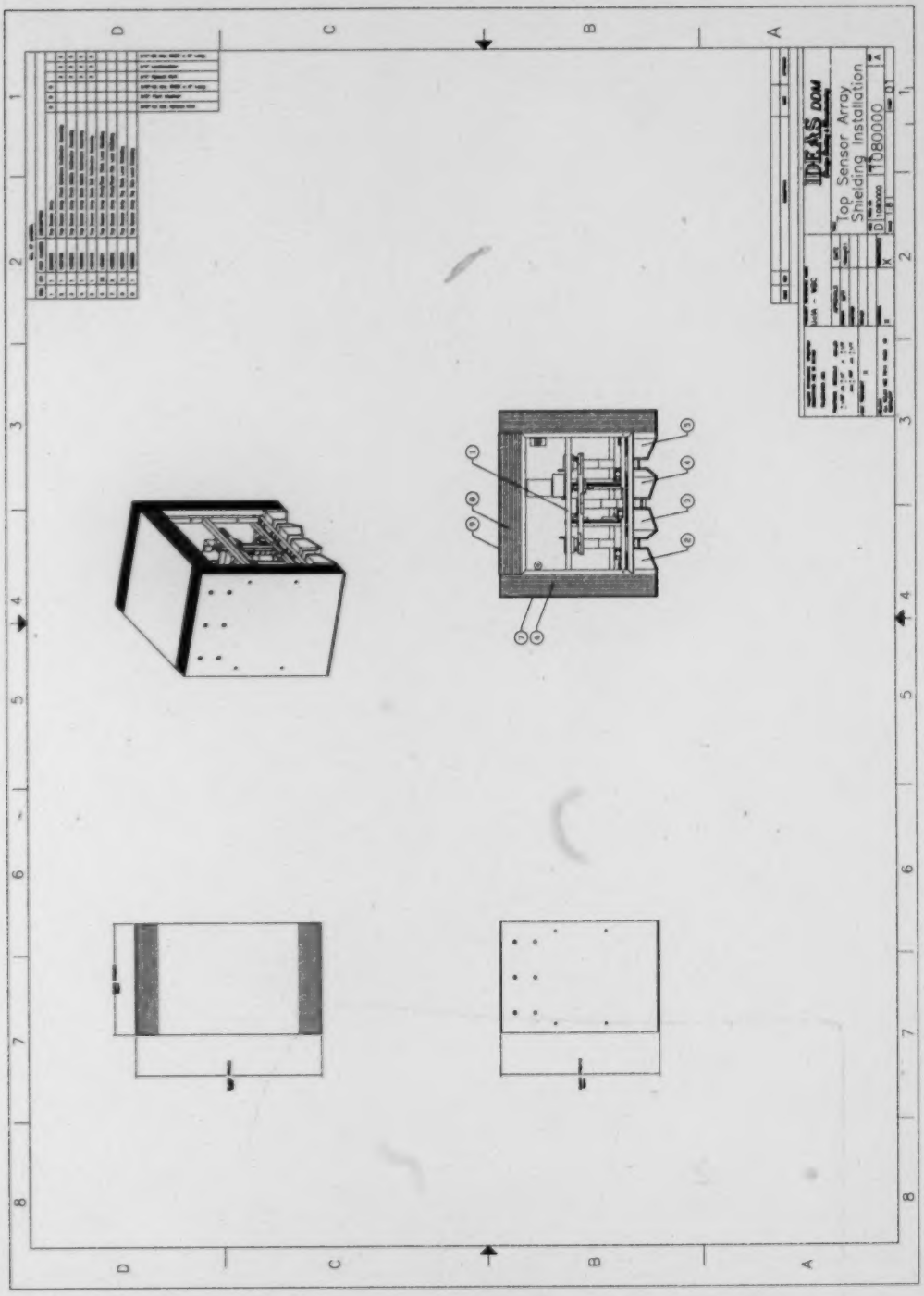
IDEAS DOW
Top Sensor Array
Shielding Installation
1080000

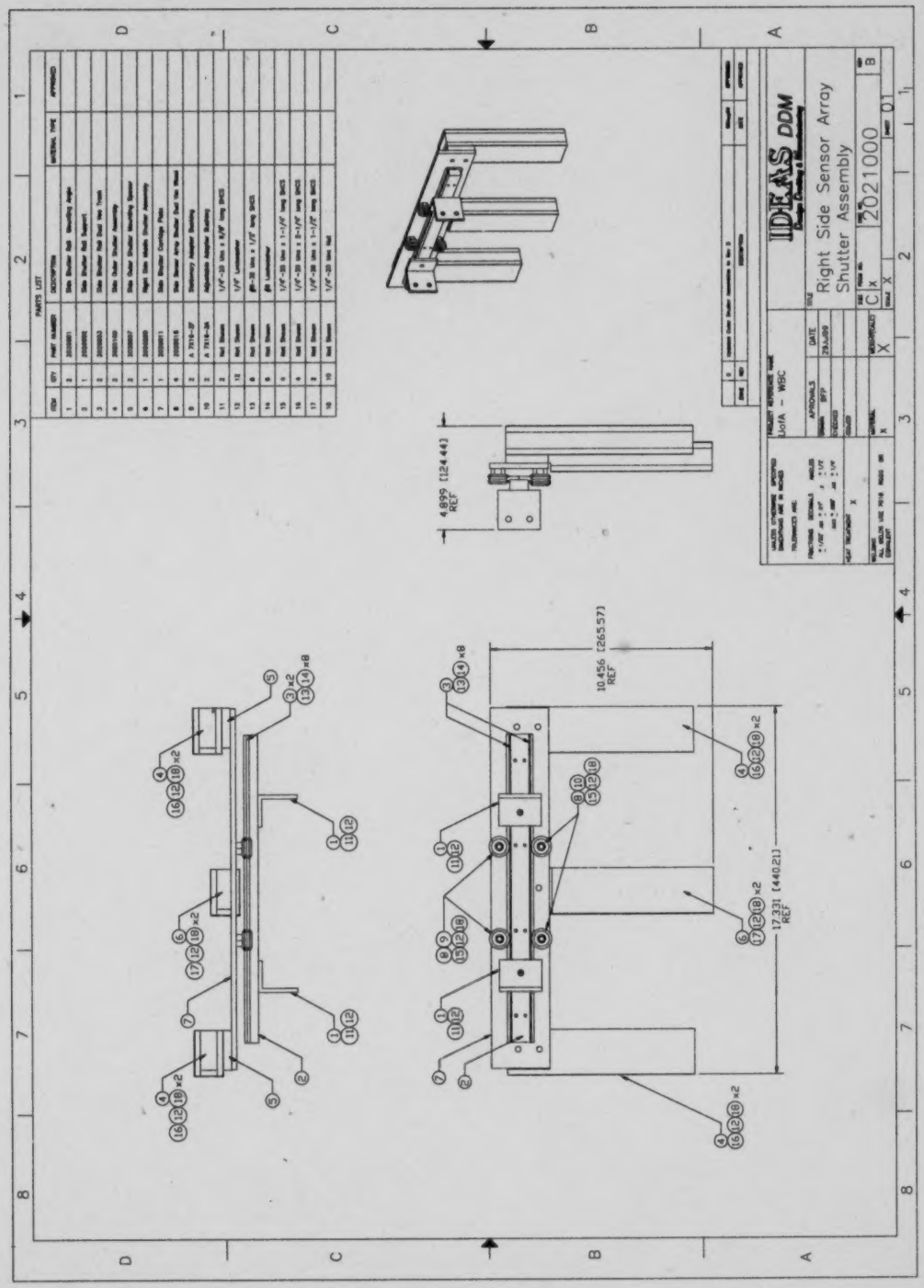
PARTS LIST
IDEAS DDM
Right Side Sensor Array
Shutter Assembly
2021000
4.899 [124.44] REF
10.456 [265.57] REF
17.331 [440.21] REF

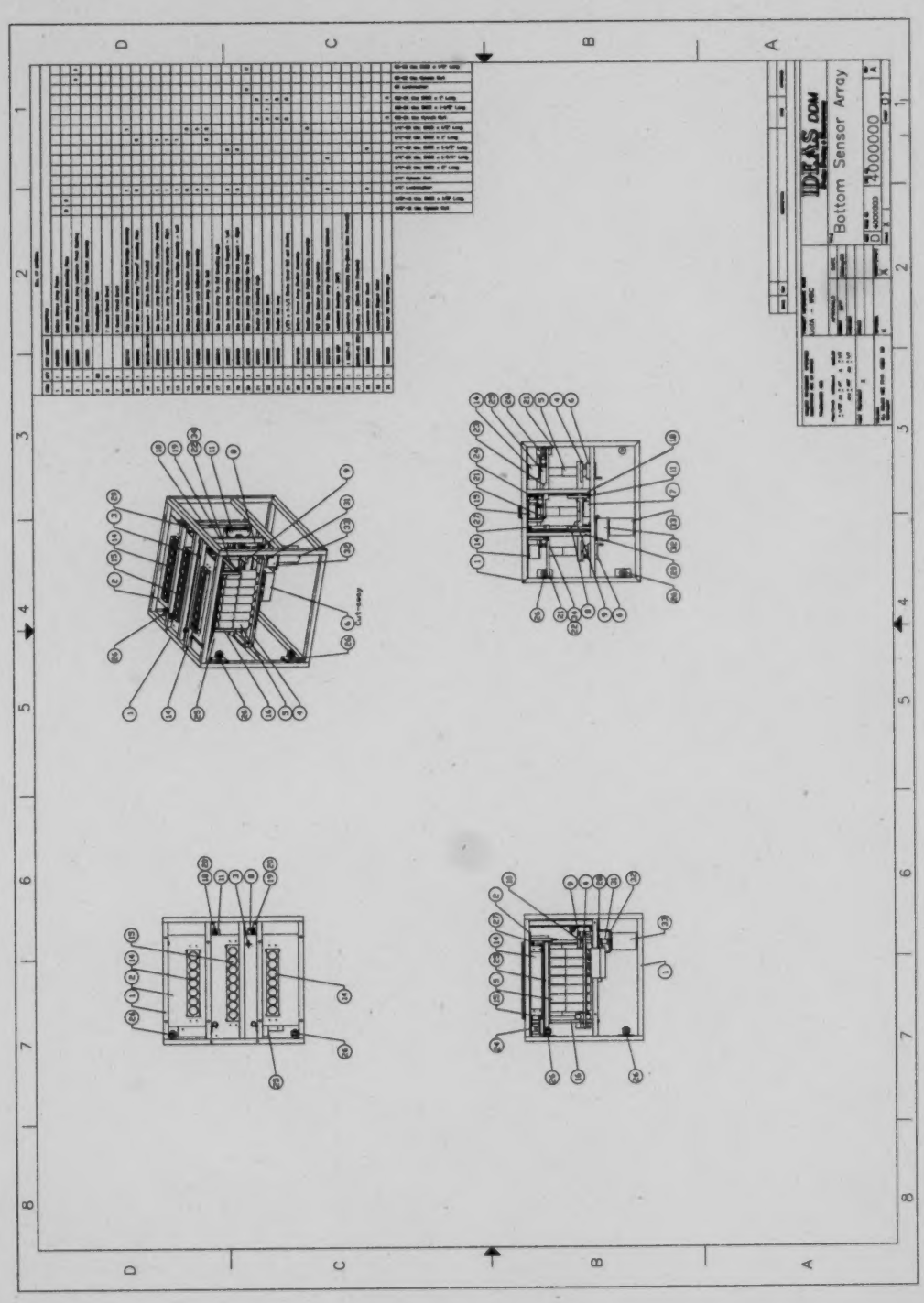
Bottom Sensor Array

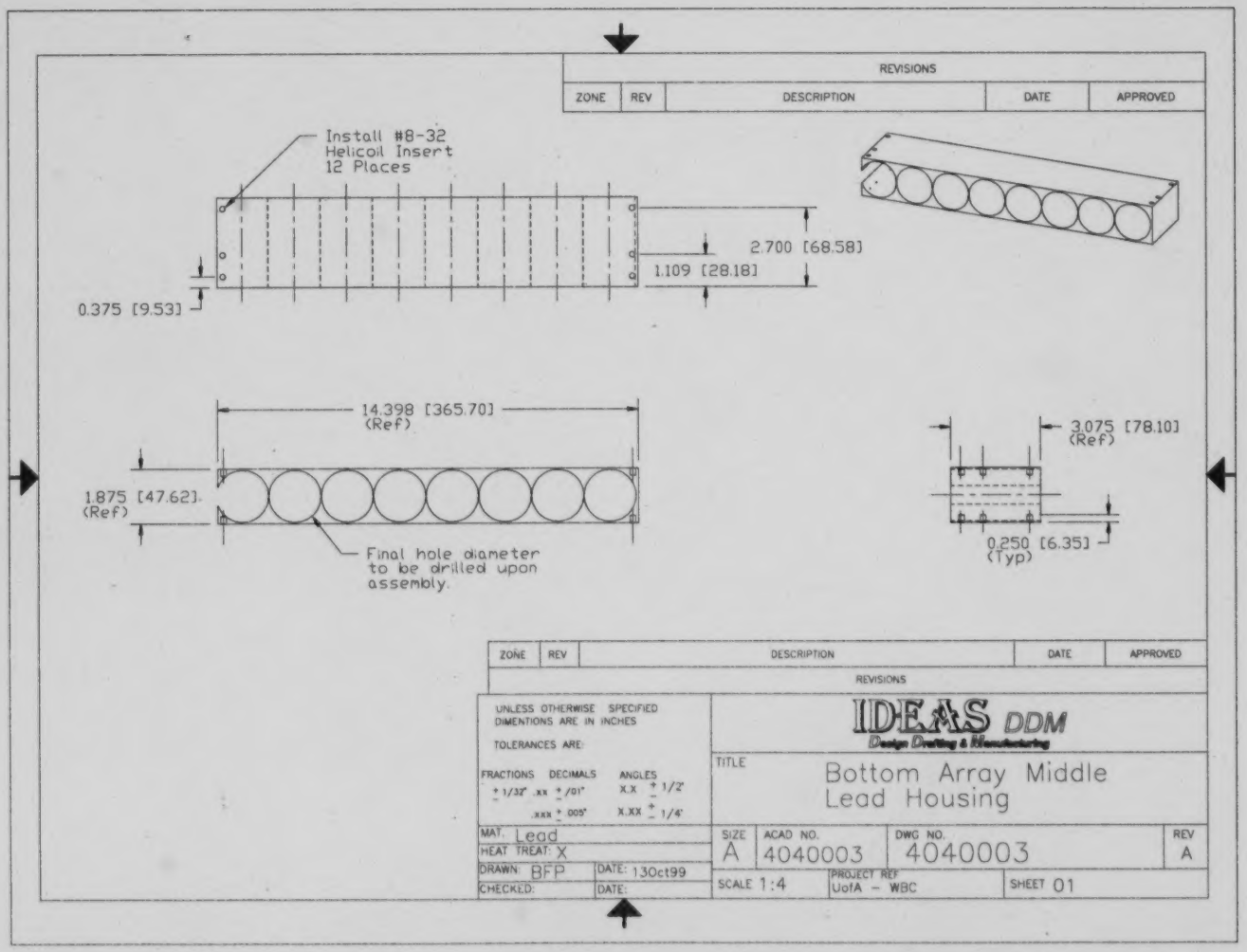
REVISIONS
ZONE
REV
DESCRIPTION
DATE
APPROVED
Install #8-32
Helicoil Insert
12 Places
2.700 [68.58]
1.109 [28.18]
0.375 [9.53]
14.398 [365.70]
(Ref)
1.875 [47.62]
(Ref)
Final hole diameter
to be drilled upon
assembly.
3.075 [78.10]
(Ref)
0.250 [6.35]
(Typ)
ZONE
REV
DESCRIPTION
DATE
APPROVED
REVISIONS
UNLESS OTHERWISE SPECIFIED
DIMENTIONS ARE IN INCHES
TOLERANCES ARE:
FRACTIONS DECIMALS ANGLES
± 1/32" .xx ± .01" X.X ± 1/2°
.xxx ± .005" X.XX ± 1/4°
IDEAS DDM
Design Drafting & Manufacturing
TITLE
Bottom Array Middle
Lead Housing
MAT. Lead
HEAT TREAT: X
DRAWN: BFP
DATE: 13Oct99
CHECKED:
DATE:
SIZE
A
ACAD NO.
4040003
DWG NO.
4040003
REV
A
SCALE 1:4
PROJECT REF
UofA – WBC
SHEET 01

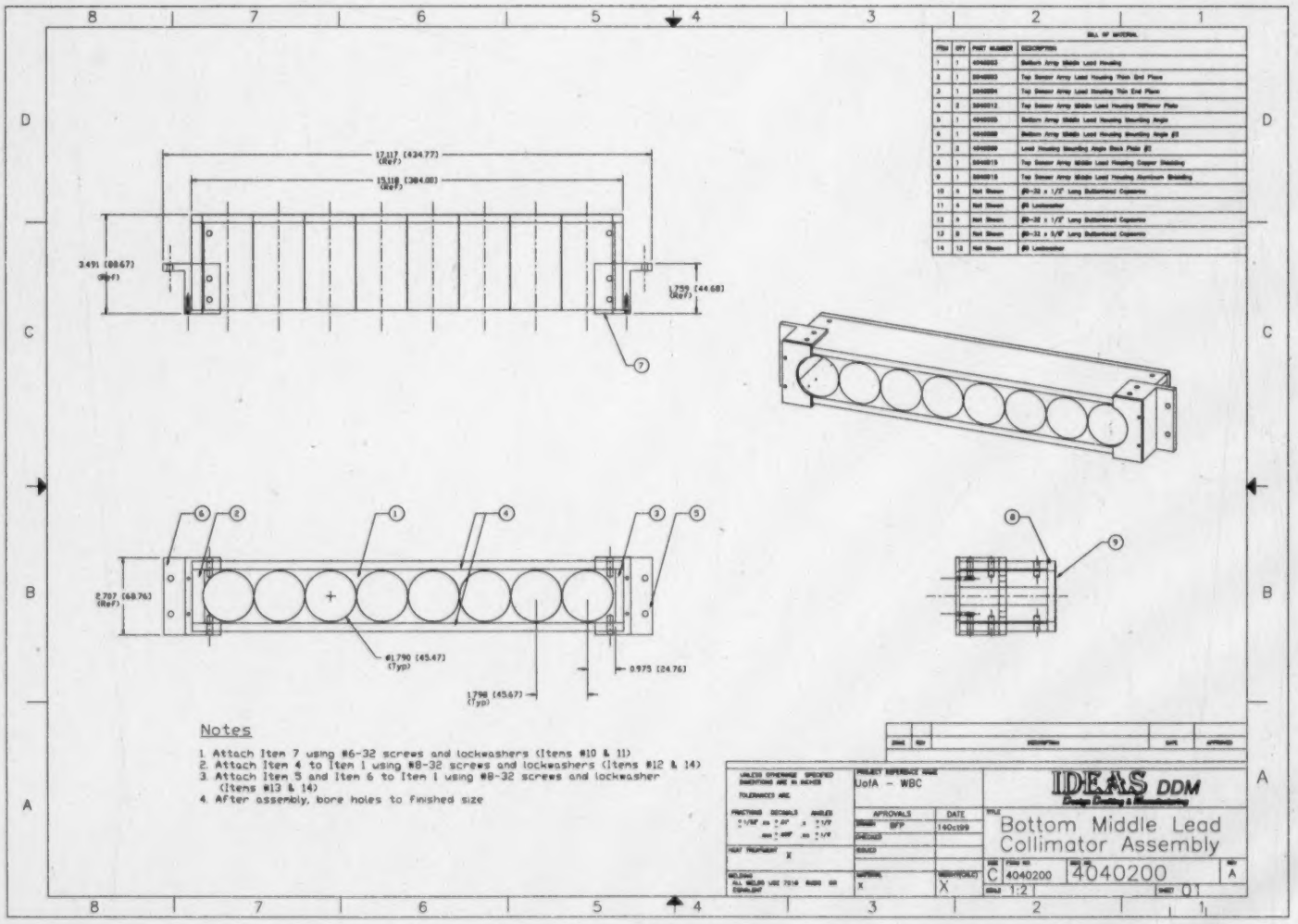

ITEM	QTY	PART NUMBER	DESCRIPTION
1	1	4040003	Bottom Array Middle Lead Housing
2	1	4040002	Top Sensor Array Lead Housing Thick End Plate
3	1	4040004	Top Sensor Array Lead Housing Thin End Plate
4	2	4040012	Top Sensor Array Middle Lead Housing Stiffener Plate
5	1	4040005	Bottom Array Middle Lead Housing Mounting Angle
6	1	4040008	Bottom Array Middle Lead Housing Mounting Angle #2
7	2	4040009	Lead Housing Mounting Angle Back Plate #2
8	1	4040015	Top Sensor Array Middle Lead Housing Copper Shielding
9	1	4040016	Top Sensor Array Middle Lead Housing Aluminum Shielding
10	6	Not Shown	#6-32 x 1/2" Long Buttonhead Capscrew
11	6	Not Shown	#6 Lockwasher
12	6	Not Shown	#8-32 x 1/2" Long Buttonhead Capscrew
13	8	Not Shown	#8-32 x 5/8" Long Buttonhead Capscrew
14	12	Not Shown	#8 Lockwasher

Notes

1. Attach Item 7 using #6-32 screws and lockwashers (Items #10 & 11)
2. Attach Item 4 to Item 1 using #8-32 screws and lockwashers (Items #12 & 14)
3. Attach Item 5 and Item 6 to Item 1 using #8-32 screws and lockwasher (Items #13 & 14)
4. After assembly, bore holes to finished size

ZONE	REV	DESCRIPTION	DATE	APPROVED

UNLESS OTHERWISE SPECIFIED DIMENSIONS ARE IN INCHES
TOLERANCES ARE:
FRACTIONS ± 1/64" DECIMALS ± .01" ANGLES ± 1/2°
.xxx ± .005" .xx ± 1/2°
HEAT TREATMENT: X
WELDING: ALL WELDS USE 7018 RODS OR EQUIVALENT

PROJECT REFERENCE NAME: UofA – WBC

APPROVALS	DATE
DRAWN BFP	14Oct99
CHECKED	
ISSUED	
MATERIAL: X	WEIGHT/WORLD: X

IDEAS DDM
Design Drafting & Manufacturing

TITLE: Bottom Middle Lead Collimator Assembly

SIZE	FSCM NO	DWG NO	REV
C	4040200	4040200	A

SCALE 1:2 SHEET 01

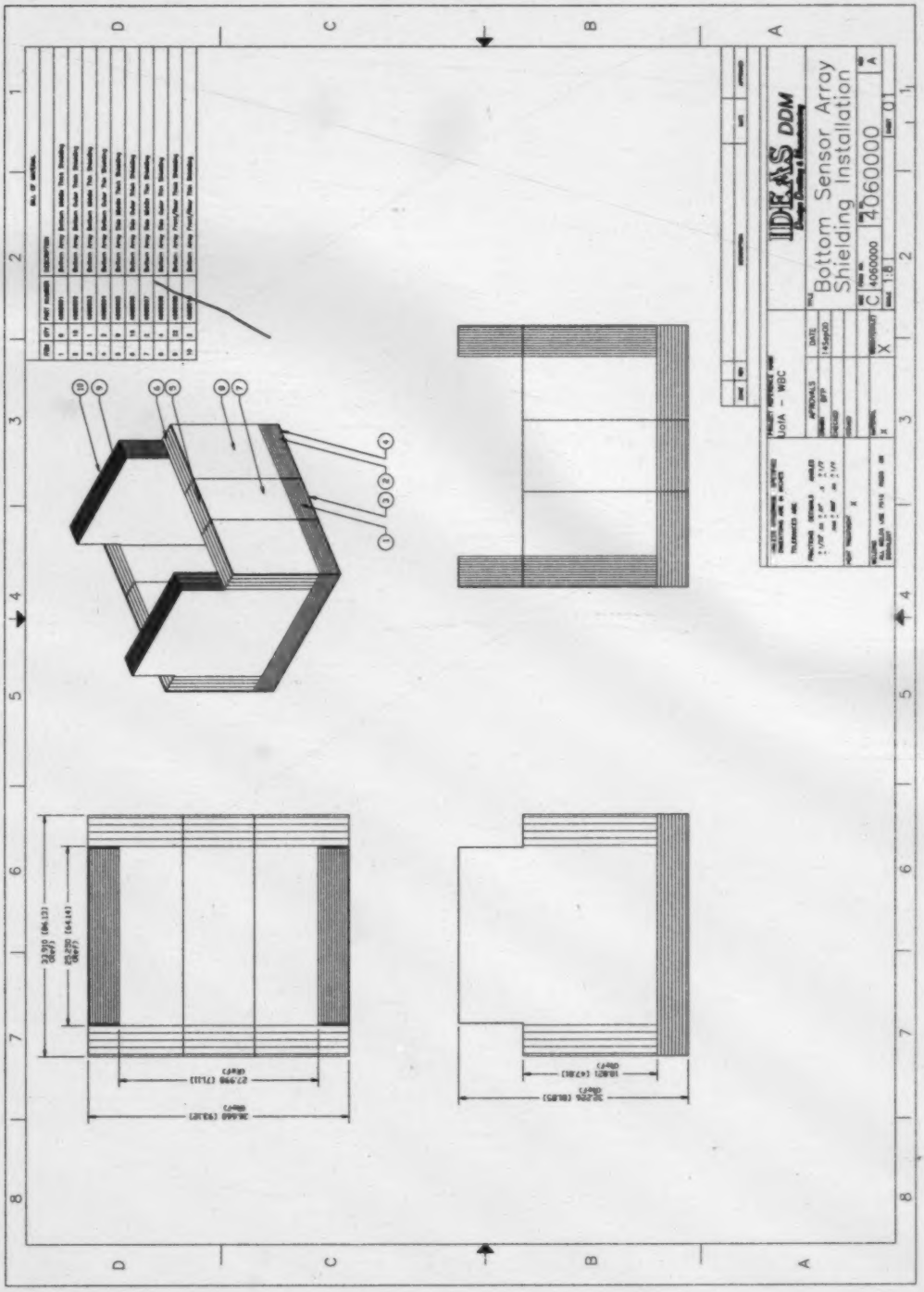
IDEAS DOM
Bottom Sensor Array
Shielding Installation
4060000
A
C
SHEET 01

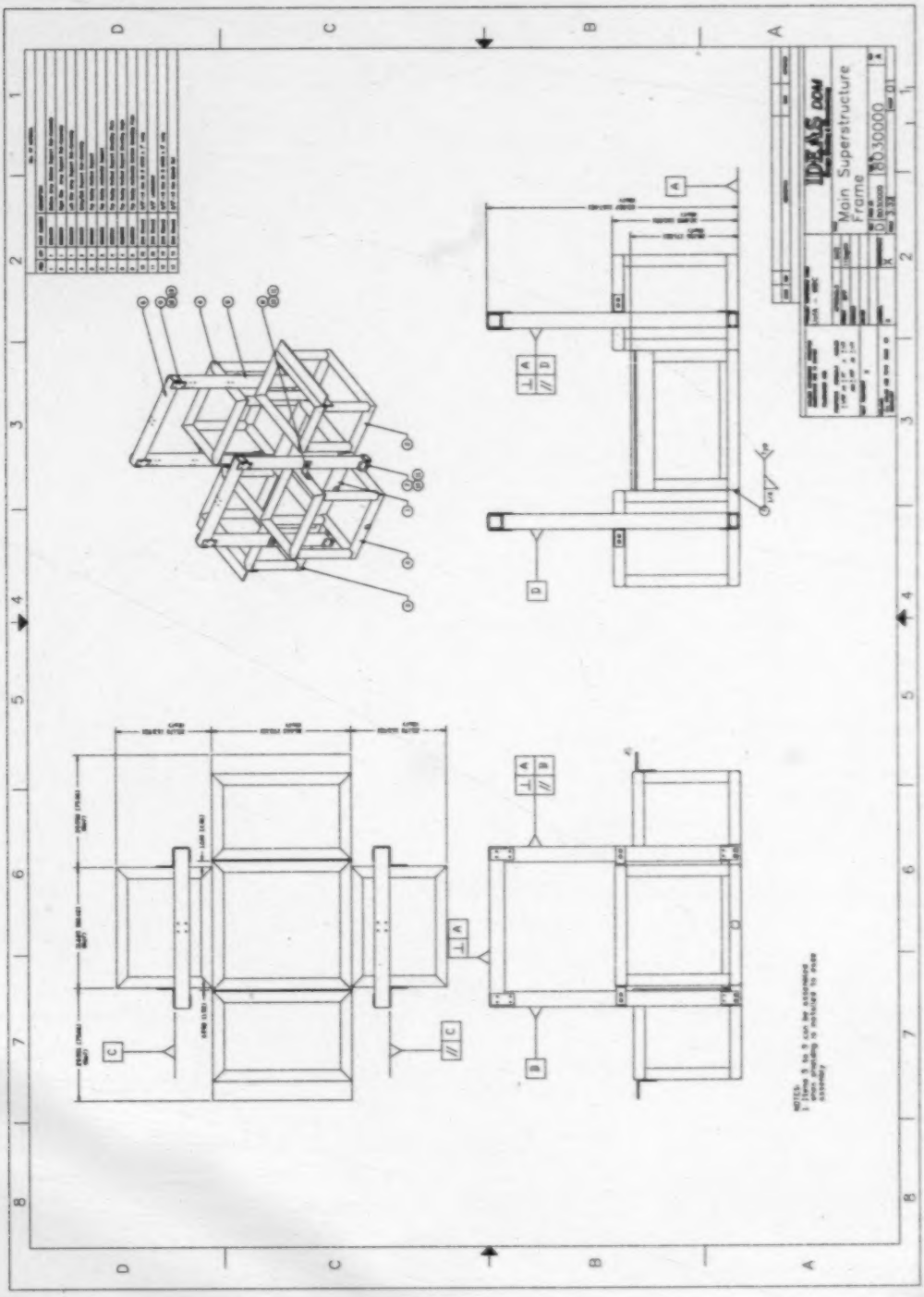
Main Superstructure
Frame
80.30000

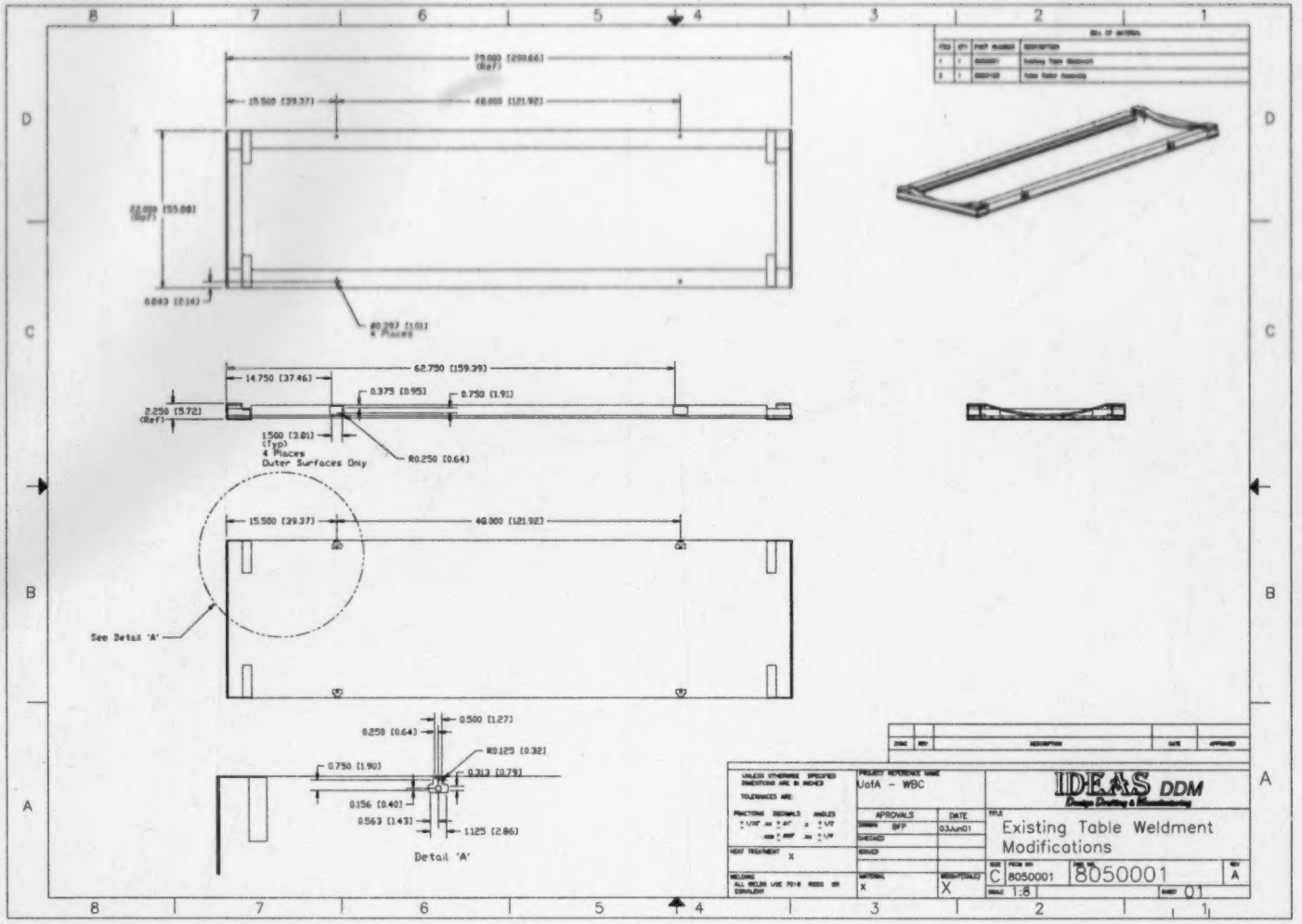
78.000 [200.66] (Ref)
15.500 [39.37]
48.000 [121.92]
55.000 [55.00] (Ref)
0.063 [2.14]
62.750 [159.39]
14.750 [37.46]
0.375 [0.95]
0.750 [1.91]
2.250 [5.72] (Ref)
1.500 [3.81] (Typ) 4 Places Outer Surfaces Only
R0.250 [0.64]
See Detail 'A'
0.500 [1.27]
0.250 [0.64]
R0.125 [0.32]
0.750 [1.90]
0.313 [0.79]
0.156 [0.40]
0.563 [1.43]
1.125 [2.86]
Detail 'A'
UofA – WBC
IDEAS DDM
Existing Table Weldment Modifications
8050001
C
A
1:8
01

Appendix B

Electronics

Preamplifier Schematics

Schematic of the Preamplifier designed for the WBC

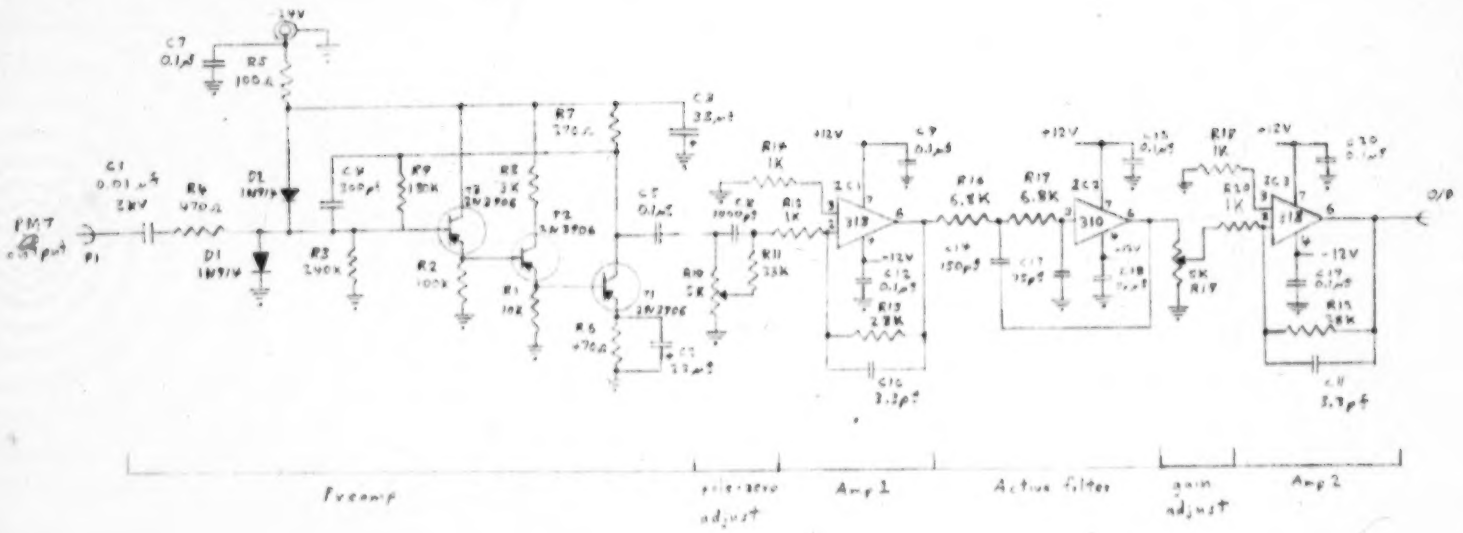

note

- all power inputs make use of a 10μF capacitor in the following manner prior to this schematic:

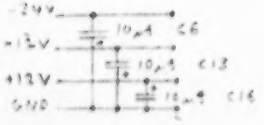

Preamplifier component list.

Plugs

P1	Gold plated PC mount sub-miniature right angle coaxial male plug.
P2	Gold plated 9 pin male plug.

Integrated Circuits

IC1	LM 318N opamp
IC2	LM 310N opamp
IC3	LM 318N opamp

Transistors

T1	2N 3906
T2	2N 3906
T3	2N 3906

Diodes

D1	1N 914
D2	1N 914

Capacitors

C1	0.01 uf, 3KV ceramic	C11	3.3 (3.6) pf ceramic
C2	22 uf, 15V tantelum	C12	0.1 uf ceramic
C3	33 uf, 35V tantelum	C13	10 uf, 35V tantelum
C4	300 pf, 100V 1% silver mica	C14	150 pf, 100V 5% silver mica
C5	0.1 uf ceramic	C15	0.1 uf ceramic
C6	10 uf, 35V tantelum	C16	10 uf, 35V tantelum
C7	0.1 uf ceramic	C17	75 pf, 100V 5% silver mica
C8	1000 pf, 100V 5% silver mica	C18	0.1 uf ceramic
C9	0.1 uf ceramic	C19	0.1 uf ceramic
C10	3.3 (3.6) pf ceramic	C20	0.1 uf ceramic

Resistors (ohms, 1/4 watt)

R1	10 K	R11	33 K
R2	100 K	R12	1 K, 1 %
R3	240 K	R13	28 K, 1%
R4	470	R14	1 K
R5	100	R15	28 K, 1%
R6	470	R16	6.8 K
R7	270	R17	6.8 K
R8	3 K	R18	1 K
R9	180 K	R19	5 K, 20 T variable
R10	5 K, 10 T variable	R20	1 K, 1%

Preamplifier PC board layout.

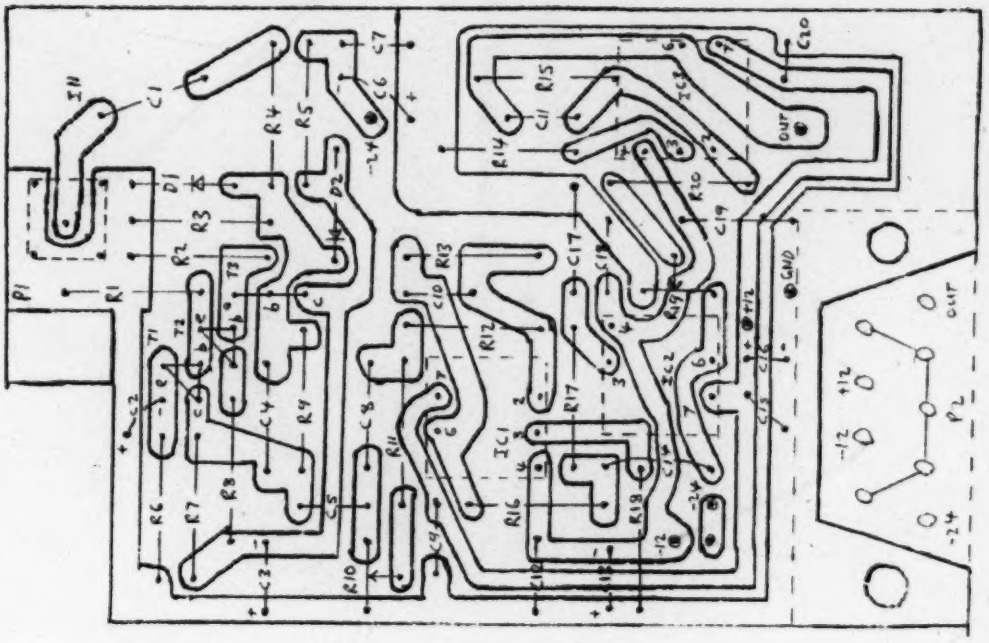

The enlarged preamplifier PC board and its component layout.

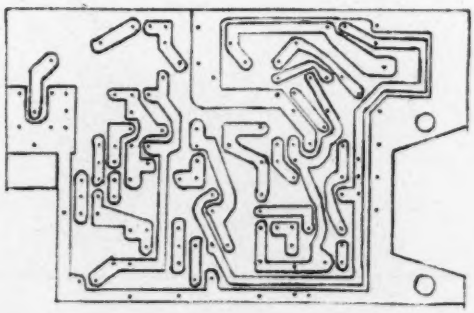

The actual size of the constructed preamplifier PC board.

Summing NIM Schematics

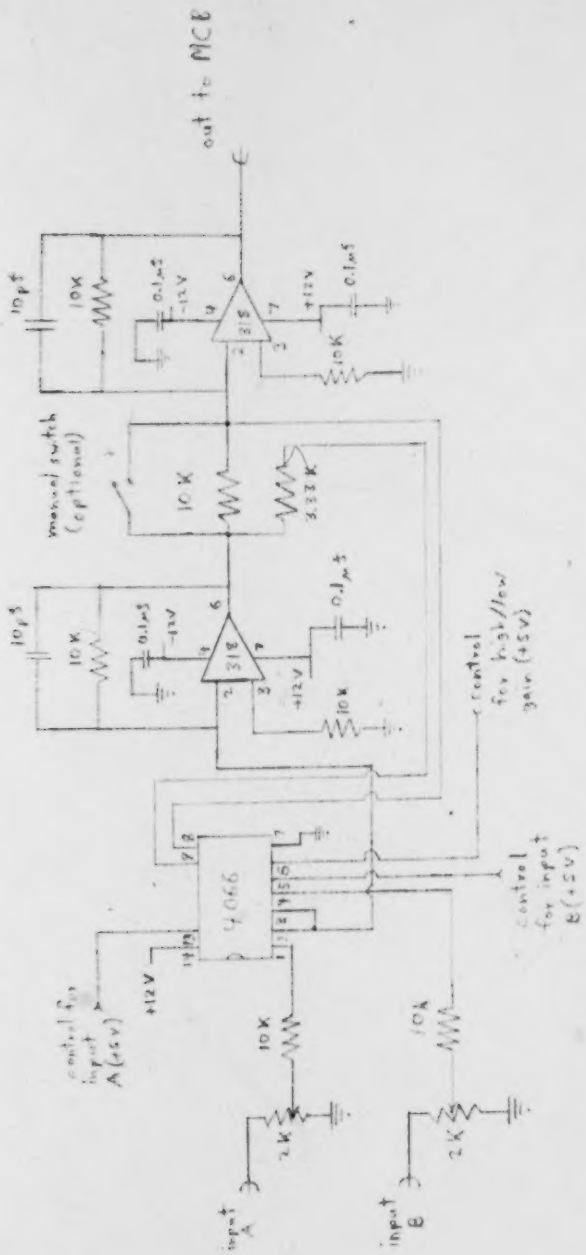

Schematic of one summing section of the summing NIM

One of two PC boards required for the summing NIM module - 8 summing circuits.

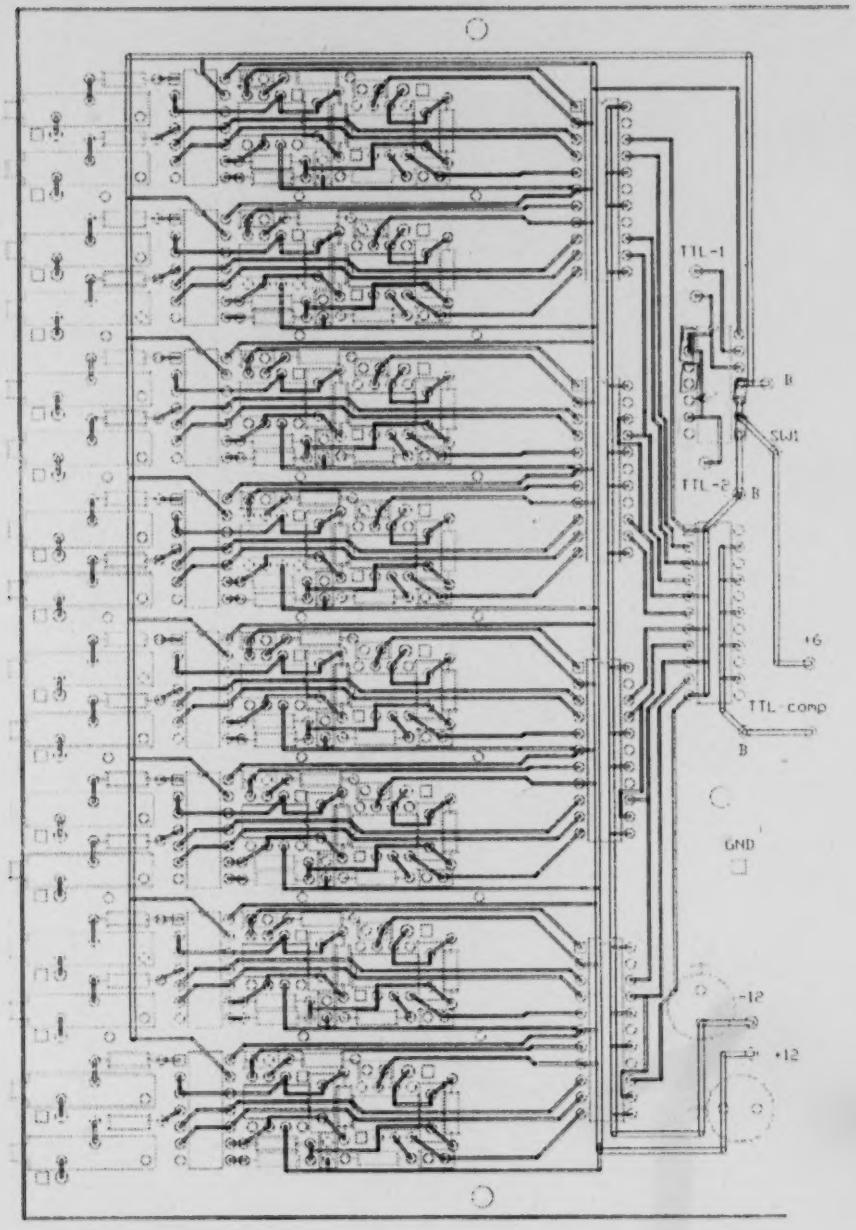

Both halves of the summing NIM module placed on one PC board.

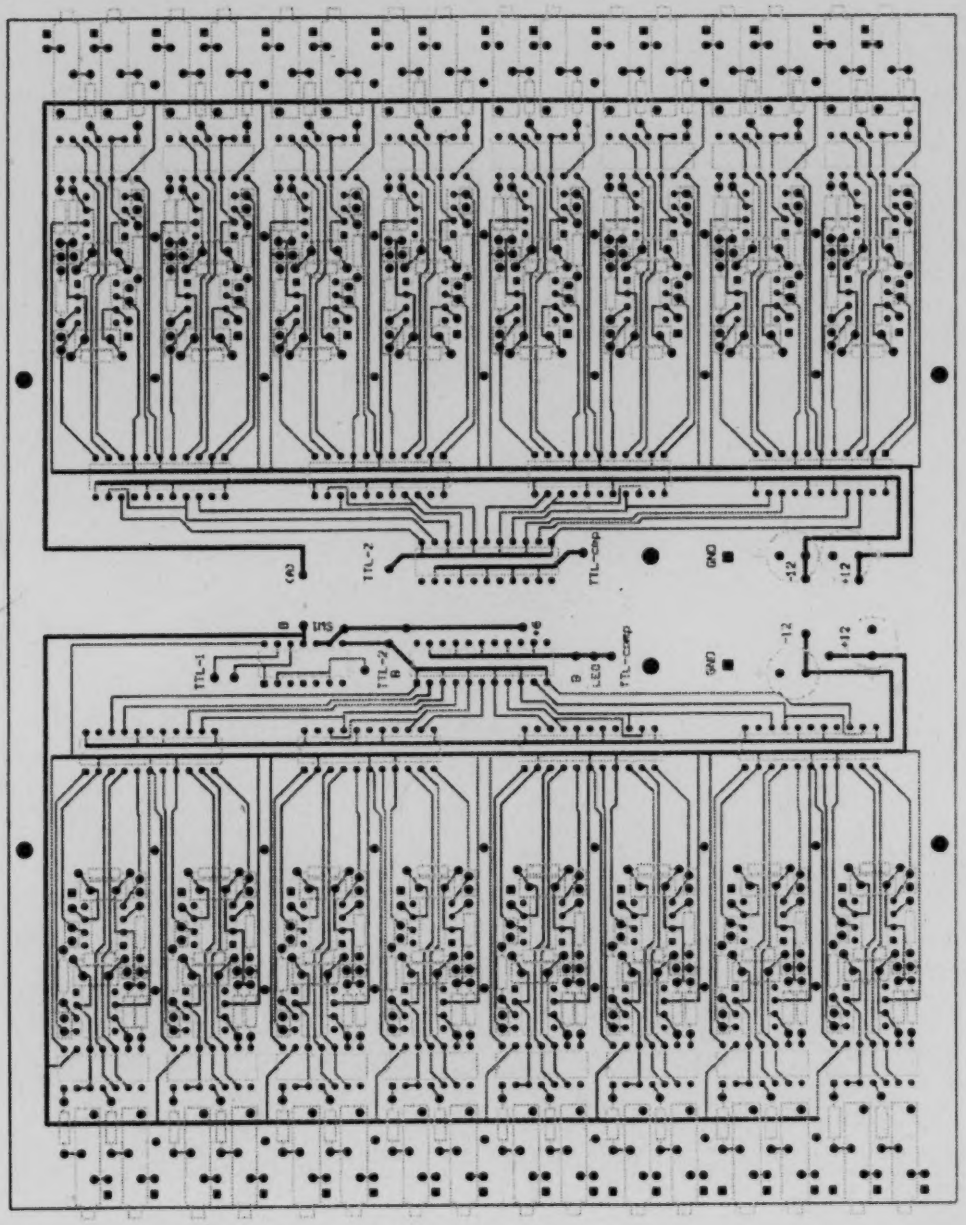

Appendix C

Program Listings

The programs presented in this appendix are the key programs that were used for simulations and data analysis for this thesis. All programs in this appendix were written in Matlab code.

AC.1 First-order Approximation Algorithm

```
% ***** first-order approximation sim *****
% All geometric and intrinsic efficiencies calculated and
% taken into account, as well as attenuation factors.
% This simulation is done for a point source.
%
% Bottle experiment (KCl bottle, one detector)
%
clear all
% create 11 x 11 matrix for cylindrical cross section
mat(1,:)=[0,0,0,1,1,1,1,1,0,0,0];
mat(2,:)=[0,0,1,1,1,1,1,1,1,0,0];
mat(3,:)=[0,1,1,1,1,1,1,1,1,1,0];
mat(4:8,:)=ones;
mat(9,:)=mat(3,:);
mat(10,:)=mat(2,:);
mat(11,:)=mat(1,:);
%
% determine activity from thoracic cylinder by
% expanding disk activity.
% note: one matrix body element=1.82 cm in width
% detector has 5X5 matrix, 0.744 cm element width
% layer distances=4.67 cm (15 sections for thorax)
% all distances in cm
%
xwidth=25.7;       %total width in x-direction
ywidth=25.7;       %total width in y-direction
dist=9.36;         % detector-start position distance
height=9.5;             % from bottom of cylinder (mid=35)
activity=6940.62;       % total c/s  304.6 for k-40
det=11.4;             % surface area of detector(11.4), 3.38X3.38
collhd=0.0;           % vertical collimation height
collwd=0.0;           % lateral collimation height
% mu values for 1.46 MeV photons K-40
muair=(5.27e-2)*(1.205e-3);
mubody=(5.86e-2)*0.99;
```

```
mucryst=0.176;
pttr=0.1851;%verified via MC and exp
%
%
av=activity/(15*sum(sum(mat))); %activity in one voxel (c/s)
% set voxel widths for elliptical cylinders
r=ywidth/2;
if ywidth>xwidth r=xwidth/2;end
jdiv=ywidth/11;
idiv=xwidth/11;
elldiv=2*r/11;
xstrch=xwidth/ywidth;
if xstrch<1 xstrch=1;end
ystrch=ywidth/xwidth;
if ystrch<1 ystrch=1;end
d=0;
v=0;
activ=0;
%ko=7.5;    % initial detector height
for ko=-8.3/2.286:4.6/2.286:19.3/2.286   %vertical detector movement
for io=6%(6-13.8/idiv):4.6/idiv:(6+13.8/idiv) % 7 detectors lateral
%for io=6%(6-16.1/idiv):4.6/idiv:(6+16.1/idiv) % 8 detectors
% determines activity from all sections making up the cylinder
for k=0.5:14.5
   % response from all voxels in slice
   for j=1:11
   for i=1:11
    % response over detector surface
    for ioo=-2:2
    for koo=-2:2
       % angles calculated, threshold values as well
       psih1=atan(collhd/((koo+2.5)*0.676+0.17));
       psih2=pi-atan(collhd/(3.55-(koo+2.5)*0.676));
       psiw1=atan(collwd/((ioo+2.5)*0.676+0.17));
       psiw2=pi-atan(collwd/(3.55-(ioo+2.5)*0.676));
       psilr=asin((dist-jdiv/2+j*jdiv)/sqrt((dist-...
       jdiv/2+j*jdiv)^2+((i-io)*idiv-ioo*3.38/5)^2));
       psiud=asin((dist-jdiv/2+j*jdiv)/sqrt((dist-...
       jdiv/2+j*jdiv)^2+((k-ko)*2.286-koo*3.38/5)^2));
       if (io+ioo*(0.676/idiv))<i psilr=pi-psilr; end
       if (ko+koo*(0.676/2.286))<k psiud=pi-psiud; end
       if psiud>psih1&psiud<psih2&psilr>psiw1&psilr<psiw2&mat(i,j)>0
        % attenuation distances determined
        ii=i+0.0001;
        jj=j-0.5;
        i1=ioo*3.38/5+((io-6)*elldiv); % detector point (x)
        i2=(ii-6)*2*r/11;  % source point (x,y)
        j2=(11/2-jj)*2*r/11;
        % finds intersection point nearest to detector
        m=((dist+r-j2)/(i1-i2));
        b=-m*i1+dist+r;
        p(1)=(1+1/(m^2));
        p(2)=-2*b/(m^2);
        p(3)=(b^2)/(m^2)-r^2;
        y=roots(p);
        if y(2)>y(1) y(1)=y(2); end
        intery=y(1);
```

```
        interx=(y(1)-b)/m;
        % finds distance and angle of activity from center
        leg=sqrt(i2^2+j2^2);
        theta1=-asin(j2/leg);
        % finds distance ray passes through
        theta2=asin(intery/r);
        body=sqrt(r^2+leg^2-2*r*leg*cos(theta1+theta2));
        % elliptical adjustment for body and air
        psiell=asin((dist-elldiv/2+j*elldiv)/sqrt((dist-...
        elldiv/2+j*elldiv)^2+((i-io)*elldiv-ioo*3.38/5)^2));
        body=sqrt((ystrch*body*cos(abs(psiell-pi/2)))^2+(xstrch*body...
        *sin(abs(psiell-pi/2)))^2);
        air=sqrt((dist-jdiv/2+j*jdiv)^2+((i-io)*...
        idiv-ioo*3.38/5)^2)-body;
        % k adjustment
        body=body/cos(abs(psiud-pi/2));
        air=air/cos(abs(psiud-pi/2));
        % distance through crystal
        if psilr<pi/2
           deep1=(1.69-(ioo*0.676))*tan(psilr);
           zeta1=pi/2-psilr;
        else
           deep1=(1.69+(ioo*0.676))*tan(pi-psilr);
           zeta1=psilr-pi/2;
        end
        if psiud<pi/2
           deep2=(1.69-(koo*0.676))*tan(psiud);
           zeta2=pi/2-psiud;
        else
           deep2=(1.69+(koo*0.676))*tan(pi-psiud);
           zeta2=psiud-pi/2;
        end
        deep=deep1;
        if deep2<deep1 deep=deep2; end
        if deep>7.62 deep=7.62; end
        lat1=deep*tan(zeta1);
        lat2=deep*tan(zeta2);
        crystal=sqrt(lat1^2+lat2^2+deep^2);
        % activity from all factors
        activ=activ+(((1/(4*pi))*(dist-jdiv/2+j*jdiv)*av)/...
        ((dist-jdiv/2+j*jdiv)^2+...
        ((i-io)*idiv-ioo*3.38/5)^2+((k-ko)...
        *2.286-koo*3.38/5)^2)^(3/2))*mat(i,j)*(1-exp(-
      mucryst*crystal))*...
        exp(-(muair*air+mubody*body))*det/25;
       end
      end
     end
    end
  end
k;
end
d=d+1
v(d)=activ*pttr
activ=0;
end
end
```

AC.2 Scanning Semi-Empirical-Regression Algorithm

The scanning semi-empirical-regression algorithm consists of a main program (one for each phantom size), and 50 functions that define the weighting factors for each bank FOV. The main program for the PM phantom is seen below, which is immediately followed by the bottom-end (foot) function.

PM Scan Algorithm

```
%mfile for PM bomab phantom results for all detectors
% scanns in 9.94 cm steps from head to toe
clear all
totscan=0;
ctganth=[20.65,20.65,20.65,20.65,20.65,20.65,20.65,19.68,19.68,19.68,14
.94];
cscanldist=[61.77,51.83,41.89,31.95,22.01,12,07,2.13,-7.81,-17.75,-
27.69,-37.63];
for scann=1:11
%
% **** ONLY TWO THINGS THAT NEED TO SET: ****
%
tganth=ctganth(scann)+1;  %top gantry height from table top (cm)
*require 1cm above subject*
scanldist=cscanldist(scann);  %scan line of the WBC.  Cm distance from
the ref line, head=+
%
% *** bottom-middle array *** botmid
%
%char('bottom-middle array')
% total width of ellipse in x direction
cxwidth=[19.5,14.76,29.84,36.19,9.52,9.52,16.18,16.18,12.55,12.55];
% total width of ellipse in y direction
cywidth=[14.61,13.69,20.65,19.68,9.52,9.52,14.94,14.94,12.13,12.13];
% total height of ellipse
czdepth=[19.68,9.52,41.6,20.17,58.11,58.11,39.7,39.7,39.83,39.83];
% distance of ellipse to detector array
cdist=[8.5,8.5,8.5,8.5,8.5,8.5,8.5,8.5,8.5,8.5];
%position of k reference line wrt bottom of gut
refheight=[-71.29,-61.77,-20.17,0,-3.66,-3.66,39.7,39.7,79.53,79.53];
refheight=refheight+scanldist;
% activity of ellipsoids (first entry in litres)
cactivity=[4.301,1.511,20.133,11.282,4.136,4.136,7.537,7.537,4.762,4.76
2];
cactivity=cactivity.*6.967;
% distace that cylinder is shifted wrt the center
cshift=[0,0,0,0,-(29.84/2+9.52/2),29.84/2+9.52/2,-16.18/2,16.18/2,-
16.18/2,16.18/2];
%
% *** bottom-end array (middle) *** botmid
%
```

```
botmid(scann,:)=bomab8bm(cxwidth,cywidth,czdepth,cdist,refheight,cactiv
ity,cshift);
%
% *** bottom-end array (foot side) *** botft
%
%char('bottom-end(ft) array')
cdist=cdist+1.64;
refheight=refheight-20.08;
botft(scann,:)=bomab7bf(cxwidth,cywidth,czdepth,cdist,refheight,cactivi
ty,cshift);
%
% *** bottom-end array (head side) *** bothd
%
%char('bottom-end(hd) array')
refheight=refheight+2*20.08;
bothd(scann,:)=bomab7bh(cxwidth,cywidth,czdepth,cdist,refheight,cactivi
ty,cshift);
%
% *** top-middle array *** topmid
%
%char('top-middle array')
%collhd & cdist self-adjusts. >25 dictated be end recession, and <25 by
middle extension
%
refheight=refheight-20.08;
if tganth > 25
   delta1=-5.96757863501484+(tganth+1.4+0.74)*14.82/67.4;
   cdist=tganth-cywidth+5.52+delta1;
else
   delta1=-1.54362289007822+(tganth+1.4+0.74+3.22)*(15.14-
10.2)/(86.96+10.2);
   cdist=tganth-cywidth+5.52+delta1;
end
delta=delta1-0.57;
% function and map function depends on delta, and directed to function
here
if delta <= -0.57
topmid(scann,:)=bomabm8n057(cxwidth,cywidth,czdepth,cdist,refheight,cac
tivity,cshift,delta);
elseif delta <= -0.13
topmid(scann,:)=bomabm8n013(cxwidth,cywidth,czdepth,cdist,refheight,cac
tivity,cshift,delta);
elseif delta <= 0
topmid(scann,:)=bomabm8n0(cxwidth,cywidth,czdepth,cdist,refheight,cacti
vity,cshift,delta);
elseif delta <= 0.37
topmid(scann,:)=bomabm8p037(cxwidth,cywidth,czdepth,cdist,refheight,cac
tivity,cshift,delta);
elseif delta <= 0.57
topmid(scann,:)=bomabm8p057(cxwidth,cywidth,czdepth,cdist,refheight,cac
tivity,cshift,delta);
elseif delta <= 0.87
topmid(scann,:)=bomabm8p087(cxwidth,cywidth,czdepth,cdist,refheight,cac
tivity,cshift,delta);
elseif delta <= 1.14
topmid(scann,:)=bomabm8p114(cxwidth,cywidth,czdepth,cdist,refheight,cac
tivity,cshift,delta);
```

```
elseif delta > 1.14
topmid(scann,:)=bomabm8p212(cxwidth,cywidth,czdepth,cdist,refheight,cac
tivity,cshift,delta);
end
%
% *** top-end arrays (Larger FOVs) *** topft1, tophd1
%
refheight=refheight-19.88;
cdist=cdist+1.32;
delta=delta1-0.13;
% function and map function depends on delta, and directed to function
here
if delta <= -1.23
topft1(scann,:)=bomab1f7n123(cxwidth,cywidth,czdepth,cdist,refheight,ca
ctivity,cshift,delta);
   refheight=refheight+2*19.88;
tophd1(scann,:)=bomab1h7n123(cxwidth,cywidth,czdepth,cdist,refheight,ca
ctivity,cshift,delta);
elseif delta <= -0.57
topft1(scann,:)=bomab1f7n057(cxwidth,cywidth,czdepth,cdist,refheight,ca
ctivity,cshift,delta);
   refheight=refheight+2*19.88;
tophd1(scann,:)=bomab1h7n057(cxwidth,cywidth,czdepth,cdist,refheight,ca
ctivity,cshift,delta);
elseif delta <= -0.13
topft1(scann,:)=bomab1f7n013(cxwidth,cywidth,czdepth,cdist,refheight,ca
ctivity,cshift,delta);
   refheight=refheight+2*19.88;
tophd1(scann,:)=bomab1h7n013(cxwidth,cywidth,czdepth,cdist,refheight,ca
ctivity,cshift,delta);
elseif delta <= 0
topft1(scann,:)=bomab1f7n0(cxwidth,cywidth,czdepth,cdist,refheight,cact
ivity,cshift,delta);
   refheight=refheight+2*19.88;
tophd1(scann,:)=bomab1h7n0(cxwidth,cywidth,czdepth,cdist,refheight,cact
ivity,cshift,delta);
elseif delta <= 0.37
topft1(scann,:)=bomab1f7p037(cxwidth,cywidth,czdepth,cdist,refheight,ca
ctivity,cshift,delta);
   refheight=refheight+2*19.88;
tophd1(scann,:)=bomab1h7p037(cxwidth,cywidth,czdepth,cdist,refheight,ca
ctivity,cshift,delta);
elseif delta <= 0.57
topft1(scann,:)=bomab1f7p057(cxwidth,cywidth,czdepth,cdist,refheight,ca
ctivity,cshift,delta);
   refheight=refheight+2*19.88;
tophd1(scann,:)=bomab1h7p057(cxwidth,cywidth,czdepth,cdist,refheight,ca
ctivity,cshift,delta);
elseif delta <= 0.87
topft1(scann,:)=bomab1f7p087(cxwidth,cywidth,czdepth,cdist,refheight,ca
ctivity,cshift,delta);
   refheight=refheight+2*19.88;
tophd1(scann,:)=bomab1h7p087(cxwidth,cywidth,czdepth,cdist,refheight,ca
ctivity,cshift,delta);
elseif delta <= 1.14
topft1(scann,:)=bomab1f7p114(cxwidth,cywidth,czdepth,cdist,refheight,ca
ctivity,cshift,delta);
```

```
   refheight=refheight+2*19.88;
tophd1(scann,:)=bomab1h7p114(cxwidth,cywidth,czdepth,cdist,refheight,ca
ctivity,cshift,delta);
elseif delta > 1.14
topft1(scann,:)=bomab1f7p212(cxwidth,cywidth,czdepth,cdist,refheight,ca
ctivity,cshift,delta);
   refheight=refheight+2*19.88;
tophd1(scann,:)=bomab1h7p212(cxwidth,cywidth,czdepth,cdist,refheight,ca
ctivity,cshift,delta);
end
%
% *** top-end arrays (Small FOVs) *** topft2, tophd2
%
refheight=refheight-2*19.88;
delta=delta1+0.37;
% function and map function depends on delta, and directed to function
here
if delta <= -1.23
topft2(scann,:)=bomab2f7n123(cxwidth,cywidth,czdepth,cdist,refheight,ca
ctivity,cshift,delta);
   refheight=refheight+2*19.88;
tophd2(scann,:)=bomab2h7n123(cxwidth,cywidth,czdepth,cdist,refheight,ca
ctivity,cshift,delta);
elseif delta <= -0.57
topft2(scann,:)=bomab2f7n057(cxwidth,cywidth,czdepth,cdist,refheight,ca
ctivity,cshift,delta);
   refheight=refheight+2*19.88;
tophd2(scann,:)=bomab2h7n057(cxwidth,cywidth,czdepth,cdist,refheight,ca
ctivity,cshift,delta);
elseif delta <= -0.13
topft2(scann,:)=bomab2f7n013(cxwidth,cywidth,czdepth,cdist,refheight,ca
ctivity,cshift,delta);
   refheight=refheight+2*19.88;
tophd2(scann,:)=bomab2h7n013(cxwidth,cywidth,czdepth,cdist,refheight,ca
ctivity,cshift,delta);
elseif delta <= 0
topft2(scann,:)=bomab2f7n0(cxwidth,cywidth,czdepth,cdist,refheight,cact
ivity,cshift,delta);
   refheight=refheight+2*19.88;
tophd2(scann,:)=bomab2h7n0(cxwidth,cywidth,czdepth,cdist,refheight,cact
ivity,cshift,delta);
elseif delta <= 0.37
topft2(scann,:)=bomab2f7p037(cxwidth,cywidth,czdepth,cdist,refheight,ca
ctivity,cshift,delta);
   refheight=refheight+2*19.88;
tophd2(scann,:)=bomab2h7p037(cxwidth,cywidth,czdepth,cdist,refheight,ca
ctivity,cshift,delta);
elseif delta <= 0.57
topft2(scann,:)=bomab2f7p057(cxwidth,cywidth,czdepth,cdist,refheight,ca
ctivity,cshift,delta);
   refheight=refheight+2*19.88;
tophd2(scann,:)=bomab2h7p057(cxwidth,cywidth,czdepth,cdist,refheight,ca
ctivity,cshift,delta);
elseif delta <= 0.87
topft2(scann,:)=bomab2f7p087(cxwidth,cywidth,czdepth,cdist,refheight,ca
ctivity,cshift,delta);
   refheight=refheight+2*19.88;
```

```
tophd2(scann,:)=bomab2h7p087(cxwidth,cywidth,czdepth,cdist,refheight,ca
ctivity,cshift,delta);
elseif delta <= 1.14
topft2(scann,:)=bomab2f7p114(cxwidth,cywidth,czdepth,cdist,refheight,ca
ctivity,cshift,delta);
   refheight=refheight+2*19.88;
tophd2(scann,:)=bomab2h7p114(cxwidth,cywidth,czdepth,cdist,refheight,ca
ctivity,cshift,delta);
elseif delta > 1.14
topft2(scann,:)=bomab2f7p212(cxwidth,cywidth,czdepth,cdist,refheight,ca
ctivity,cshift,delta);
   refheight=refheight+2*19.88;
tophd2(scann,:)=bomab2h7p212(cxwidth,cywidth,czdepth,cdist,refheight,ca
ctivity,cshift,delta);
end
%
% *** side-middle array *** sidmid
%
%char('side-mid array')
refheight=refheight-19.88;
cxwidth=cywidth;
cywidth=[19.5,14.76,29.84,36.19,9.52,9.52,16.18,16.18,12.55,12.55];
cdist=57/2-cshift-cywidth.*0.5+9.92;
cshift=10-cxwidth.*0.5;
sidmid(scann,:)=bomab4sm(cxwidth,cywidth,czdepth,cdist,refheight,cactiv
ity,cshift);
%
% *** side-end array (foot side)*** sidft
%
%char('side-end(ft) array')
cdist=cdist+2.02;
refheight=refheight-19.28;
sidft(scann,:)=bomab3sf(cxwidth,cywidth,czdepth,cdist,refheight,cactivi
ty,cshift);
%
% *** side-end array (head side) *** sidhd
%
%char('side-end(hd) array')
refheight=refheight+2*19.28;
sidhd(scann,:)=bomab3sh(cxwidth,cywidth,czdepth,cdist,refheight,cactivi
ty,cshift);
%
tottemp=sum(botmid(scann,:))+sum(botft(scann,:))+sum(bothd(scann,:))+su
m(topmid(scann,:))+...
sum(topft1(scann,:))+sum(topft2(scann,:))+sum(tophd1(scann,:))+sum(toph
d2(scann,:))+...
   2*sum(sidmid(scann,:))+2*sum(sidft(scann,:))+2*sum(sidhd(scann,:))
totscan=totscan+tottemp;
ctganth(scann)+1
cscanldist(scann)
end
totscan
totscan/11
save PMscan
```

Bottom-end (foot) Function

```
function
[v]=bomab7bf(cxwidth,cywidth,czdepth,cdist,refheight,cactivity,cshift)
%
% ***** BOMAB scanning, bottom-end (foot) *****
% ***** semi-empirical-regression sim *****
% All geometric and intrinsic efficiencies calculated and
% taken into account, as well as attenuation factors.
% This simulation is done for a point source.
%
%
% create 11 x 11 matrix for cylindrical cross section
mat(1,:)=[0,0,0,1,1,1,1,1,0,0,0];
mat(2,:)=[0,0,1,1,1,1,1,1,1,0,0];
mat(3,:)=[0,1,1,1,1,1,1,1,1,1,0];
mat(4:8,:)=ones;
mat(9,:)=mat(3,:);
mat(10,:)=mat(2,:);
mat(11,:)=mat(1,:);
%
% loop number of detectors in bank
v=zeros(1,7);
% determine activity from thorasic cylinder by
% expanding disk activity.
% note: one matrix body element=1.82 cm in width
% detector has 5X5 matrix, 0.744 cm element width
% layer distances=kdiv cm (15 sections for thorax)
% all distances in cm
%
% loop that determines activities from several different
% ellipsoids and sums the results into v
%
% cycle through 10 cylinders defining PM
for cylin=1:10
%
xwidth=cxwidth(cylin);      %total width in x-direction
ywidth=cywidth(cylin);      %total width in y-direction
zdepth=czdepth(cylin);      %total height in z-direction
dist=cdist(cylin);          % detector-start position distance
height=refheight(cylin);  % from BOTTOM of cylinder (mid=35 cm)
activity=cactivity(cylin);      % total c/s  304.6 for k-40
det=11.4;             % surface area of detector(11.4)
% mu values for 1.46 MeV photons K-40
muair=(5.27e-2)*(1.205e-3);
mubody=(5.86e-2)*0.99;
mucryst=0.176;
pttr=0.1851;%verified via MC and exp
%
%
av=activity/(15*sum(sum(mat))); %activity in a voxel (c/s)
% set voxel widths for elliptical cylinders
r=ywidth/2;
if ywidth>xwidth r=xwidth/2;end
jdiv=ywidth/11;
```

```
idiv=xwidth/11;
kdiv=zdepth/15;
elldiv=2*r/11;
xstrch=xwidth/ywidth;
if xstrch<1 xstrch=1;end
ystrch=ywidth/xwidth;
if ystrch<1 ystrch=1;end
d=0;
activ=0;
ko=height/kdiv;
%for ko=-70/kdiv:1.76:140/kdiv       % up-down movement
for io=(6-13.8/idiv):4.6/idiv:(6+13.8/idiv) % 7 detectors
%for io=(6-16.1/idiv):4.6/idiv:(6+16.1/idiv) % 8 detectors
   io=io+cshift(cylin)/idiv;
% determines activity from all sections making up the cylinder
for k=0.5:14.5
   % response from all voxels in slice
   for j=1:11
   for i=1:11
   % response over detector surface
    for ioo=-2:2
       for koo=-2:2
       % angles calculated, threshold values as well
       psilr=asin((dist-jdiv/2+j*jdiv)/sqrt((dist-...
       jdiv/2+j*jdiv)^2+((i-io)*idiv-ioo*3.38/5)^2));
       psiud=asin((dist-jdiv/2+j*jdiv)/sqrt((dist-...
       jdiv/2+j*jdiv)^2+((k-ko)*kdiv-koo*3.38/5)^2));
    if (io+ioo*(0.676/idiv))<i psilr=pi-psilr; end
    if (ko+koo*(0.676/kdiv))<k psiud=pi-psiud; end
    % theta defined for correction map
       thetalr=asin((dist-jdiv/2+j*jdiv)/sqrt((dist-...
       jdiv/2+j*jdiv)^2+((i-io)*idiv)^2));
       thetaud=asin((dist-jdiv/2+j*jdiv)/sqrt((dist-...
       jdiv/2+j*jdiv)^2+((k-ko)*kdiv)^2));
   % FOV cuttoff filter
    if (thetaud >= 0.7086)&(thetaud <= (pi-0.7158))&(thetalr >=
0.4149)&(thetalr <= (pi-0.4149))
       if ko<k  % towards head FOV
         map=-440.5735+603.194.*thetalr-
213.6436.*thetalr.^2+2236.523.*thetaud-3099.7289.*thetalr.*thetaud+...
         1108.1995.*thetalr.^2.*thetaud-
4419.0337.*thetaud.^2+6190.6519.*thetalr.*thetaud.^2-
2232.1701.*thetalr.^2.*thetaud.^2+...
         4232.3388.*thetaud.^3-
5989.3523.*thetalr.*thetaud.^3+2177.2033.*thetalr.^2.*thetaud.^3-
1959.9594.*thetaud.^4+2803.7378.*thetalr.*thetaud.^4-...
         1027.6193.*thetalr.^2.*thetaud.^4+351.977.*thetaud.^5-
509.3546.*thetalr.*thetaud.^5+188.2387.*thetalr.^2.*thetaud.^5;
       else % towards foot FOV
         map=-229.8275+324.02.*thetalr-
117.1557.*thetalr.^2+1180.5783.*thetaud-1632.7204.*thetalr.*thetaud+...
         583.4801.*thetalr.^2.*thetaud-
2340.897.*thetaud.^2+3169.4942.*thetalr.*thetaud.^2-
1119.368.*thetalr.^2.*thetaud.^2+...
         2227.4548.*thetaud.^3-
2951.1086.*thetalr.*thetaud.^3+1030.601.*thetalr.^2.*thetaud.^3-
1013.6358.*thetaud.^4+1316.6331.*thetalr.*thetaud.^4-...
```

```
        455.3596.*thetalr.^2.*thetaud.^4+177.3667.*thetaud.^5-
226.3703.*thetalr.*thetaud.^5+77.6505.*thetalr.^2.*thetaud.^5;
      end
       % attenuation distances determined
       ii=i+0.0001;
       jj=j-0.5;
       i1=ioo*3.38/5+((io-6)*elldiv); % detector point (x)
       i2=(ii-6)*2*r/11;  % source point (x,y)
       j2=(11/2-jj)*2*r/11;
       % finds intersection point nearest to detector
       m=((dist+r-j2)/(i1-i2));
       b=-m*i1+dist+r;
       p(1)=(1+1/(m^2));
       p(2)=-2*b/(m^2);
       p(3)=(b^2)/(m^2)-r^2;
       y=roots(p);
       if y(2)>y(1) y(1)=y(2); end
       intery=y(1);
       interx=(y(1)-b)/m;
       % finds distance and angle of activity from center
       leg=sqrt(i2^2+j2^2);
       theta1=-asin(j2/leg);
       % finds distance ray passes through
       theta2=asin(intery/r);
       body=sqrt(r^2+leg^2-2*r*leg*cos(theta1+theta2));
       % elliptical adjustment for body and air
       psiell=asin((dist-elldiv/2+j*elldiv)/sqrt((dist-...
       elldiv/2+j*elldiv)^2+((i-io)*elldiv-ioo*3.38/5)^2));
       body=sqrt((ystrch*body*cos(abs(psiell-pi/2)))^2+(xstrch*body...
       *sin(abs(psiell-pi/2)))^2);
       air=sqrt((dist-jdiv/2+j*jdiv)^2+((i-io)*...
       idiv-ioo*3.38/5)^2)-body;
       % k adjustment
       body=body/cos(abs(psiud-pi/2));
       air=air/cos(abs(psiud-pi/2));
       % distance through crystal
       if psilr<pi/2
          deep1=(1.69-(ioo*0.676))*tan(psilr);
          zeta1=pi/2-psilr;
       else
          deep1=(1.69+(ioo*0.676))*tan(pi-psilr);
          zeta1=psilr-pi/2;
       end
       if psiud<pi/2
          deep2=(1.69-(koo*0.676))*tan(psiud);
          zeta2=pi/2-psiud;
       else
          deep2=(1.69+(koo*0.676))*tan(pi-psiud);
          zeta2=psiud-pi/2;
       end
       deep=deep1;
       if deep2<deep1 deep=deep2; end
       if deep>7.62 deep=7.62; end
       lat1=deep*tan(zeta1);
       lat2=deep*tan(zeta2);
       crystal=sqrt(lat1^2+lat2^2+deep^2);
       % activity from all factors
```

```
        activ=activ+(((1/(4*pi))*(dist-jdiv/2+j*jdiv)*av)/...
        ((dist-jdiv/2+j*jdiv)^2+...
        ((i-io)*idiv-ioo*3.38/5)^2+((k-ko)...
        *kdiv-koo*3.38/5)^2)^(3/2))*mat(i,j)*(1-exp(-
mucryst*crystal))*...
        map*exp(-(muair*air+mubody*body))*det/25;
          end
         end
       end
     end
  end
k;
end
d=d+1;
v(d)=v(d)+activ*pttr;
activ=0;
end
%end   %for the height-varying sim (k direction)
d=0;
end  %advance from one cylinder to the next when using multiple
cylinders
```

AC.3 Cosine Transform Algorithm

The code below was used to splice specific parts from a spectrum, and then smooth it using the cosine transform. Once smoothed, beginning and end-points of a photopeak could then be selected and then the gross and net counts, including the net error were calculated.

```
%
%  This m-file is an interactive program, allowing the user
%  to select a region of interest, and then to specify
%  points for the net and net error to be calculated from
%
clear all
hold off
% load spectrum
load 8b4up %2b1offu
spect=X8b4up(:,2);
plot(spect)
% specify region to zoom into
[x1, y1] = ginput(2);
x1=round(x1);
% take cosine transform of the spectrum and filter
F=dct(spect);
F(100:2048)=0;
G=idct(F);
plot(spect(x1(1):x1(2)),'r')
hold on
```

```
plot(G(x1(1):x1(2)),'k')
% mark the two points for a linear fit for net
x = [];, y = [];
for j=1:2
   [x2(j), y2(j)] = ginput(1);
   x = [x; x2(j)];
   y = [y; y2(j)];
   plot(x, y, 'b')
end
hold off
elow=round((x2(1))+x1(1));        % min energy
ehi=round((x2(2))+x1(1));         % max energy
if x2(1)>x2(2)
   ehi=round((x2(1))+x1(1));         % min energy
   elow=round((x2(2))+x1(1));        % max energy
end
% make sure that any two points can be used
hiamp=y2(1);
loamp=y2(2);
if y2(1)<y2(2)
   hiamp=y2(2);
   loamp=y2(1);
end
% calculate gross, net, and net error
% amplitude from specified points are used
gross=sum(spect(elow:ehi))
back=(loamp*(ehi-elow))+((hiamp-loamp)*(ehi-elow)*0.5);
net=gross-back
nerror=(sqrt(gross+back)/net)*100
```

AC.4 Monte-Carlo Energy Spectrum Algorithm

The following code was required so that raw 'track' data from EGS4-Nova could be transformed into a deposited energy spectrum in a given voxel.

```
%
% ****************************************
% **  This m-file takes .trk output     **
% **  from xyznova, and outputs the     **
% **  loss of KE from beginning to end  **
% **  using an energy-flux model        **
% ****************************************
%
%
clear all
%
% *** user-defined variables: ***
%
load input.trk;          %data file to be loaded
xmin=11.3;             %limits of regions (x,y,z)
xmax=14.68;              %
```

```
ymin=11.3;              %
ymax=14.68;                %
zmin=11.3;              %
zmax=18.92;                %
%
%
%
long=size(input,1);
shower=input(long,1);
p=1;
maxe=0;
mine=0;
% fixes end of file problem (j+1)
input(long+1,1)=shower+1;
for j=2:long
   % if something is in region, go further
   if ((input(j,5)>=xmin)&(input(j,5)<=xmax)&(input(j,6)>=ymin)&...
         (input(j,6)<=ymax)&(input(j,7)>=zmin)&(input(j,7)<=zmax))
         % if track ENTERS the region then
      if (((input(j-1,5)<xmin)|(input(j-1,5)>xmax)|(input(j-
1,6)<ymin)|...
            (input(j-1,6)>ymax)|(input(j-1,7)<zmin)|(input(j-
1,7)>zmax))&...
            (input(j-1,1)==input(j,1))&(input(j,2)>=input(j-1,2)))
         maxe(p)=maxe(p)+input(j,8);
      end
      % if track LEAVES the region then
      if
(((input(j+1,5)<xmin)|(input(j+1,5)>xmax)|(input(j+1,6)<ymin)|...

(input(j+1,6)>ymax)|(input(j+1,7)<zmin)|(input(j+1,7)>zmax))&...
            (input(j+1,1)==input(j,1))&(input(j+1,2)>=input(j,2)))
         mine(p)=mine(p)+input(j,8);
      end
   end
   % advance shower count
   if input(j+1,1)>input(j,1)
      p=p+1;
      maxe(p)=0;
      mine(p)=0;
   end
end
fulle=input(1,8);
%clear input      % clear up some space
deposit=maxe-mine;
% clean up zeros and the odd undershoot for histogram
g=1;
h=0;
for w=1:(p-h)
   if (deposit(g)<=0)
      deposit(g)=[];
      h=h+1;
   else
      g=g+1;
   end
end
% show the fraction of energy deposited in the medium
```

```
fractiontot=sum(deposit)/(shower*fulle)
fractionvox=sum(deposit)/(sum(maxe))
%
%
%   *****  transform monoenergetic peaks to gaussian + convolve *****
%
%
maxch=1460;     %energy calibrated for 1460 keV photons max
ext=250;        %zero pad extention
spectr=hist(deposit,maxch);
% zero pad
spectail=zeros(1,ext);
%
% form gaussian for 8 % energy resolution (our NaI)
%
sigma=(0.08/2.35)*(1:(maxch+ext));
fhwidth=round(4.*sigma);
finspect=zeros(1,(maxch+ext));
for q=1:maxch
   if spectr(q)>0
      for x=(q-fhwidth(q)):(q+fhwidth(q))
         gaus(x)=((1/(sigma(q)*sqrt(2*pi)))*(exp((-(x-
q)^2)/(2*(sigma(q)^2)))));
         finspect(x)=finspect(x)+spectr(q).*gaus(x);
      end
   end
end
total=sum(finspect);
%low-energy cut-off
finspect(1:20)=0;
plot(finspect)
%
%
% give NET area between two energies (linear link)
%
%
elow=1295;          % min energy
ehi=1650;           % max energy
gross=sum(finspect(elow:ehi));
back=(finspect(ehi)*(ehi-elow))+((finspect(elow)-finspect(ehi))*(ehi-
elow)*0.5);
net=gross-back
pcntnerror=(sqrt(gross+back)/net)*100
%save the final spectrum
%finspect2=finspect';
%save spect-2 finspect2 -ascii
```